

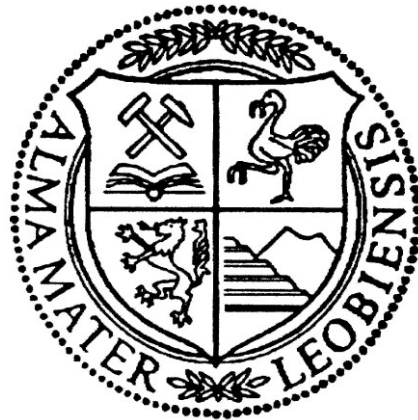
# Investigation on Peritectic Solidification using a Transparent Organic System

A thesis submitted to the University of Leoben  
for the degree of Doctor of montanistische Wissenschaften

Presented by

**Johann P. Mogeritsch**

Leoben, June 2012



Examiner: Univ.-Prof. Dipl.-Phys. Dr.rer.nat. Andreas Ludwig  
Chair for Simulation and Modelling of Metallurgical Processes  
Department of Metallurgy

Co-Examiner: Univ.-Prof. Dipl.-Ing. Dr.phil. Peter Schumacher  
Chair of Casting Research  
Department of Metallurgy

## **Eidesstattliche Erklärung**

Ich erkläre an Eides statt, dass ich diese Arbeit selbstständig verfasst, andere als die angegebenen Quellen und Hilfsmittel nicht benützt und mich auch sonst keiner unerlaubten Hilfsmittel bedient habe.

Leoben, 25.06.2012

\_\_\_\_\_

DI Johann Peter Mogeritsch

## **Affidavit**

I declare in lieu of oath, that I wrote this thesis and performed the associated research myself, using only literature cited in this volume.

Leoben, 25.06.2012

---

DI Johann Peter Mogeritsch

## **Danksagung**

Mit Dank möchte ich all die Hilfe und Unterstützung wertschätzen, die mir während der Erstellung meiner Doktorarbeit von meiner Familie, meinen Betreuern und Arbeitskollegen zuteil wurde. Besonders möchte ich meiner Lebensgefährtin Jacqueline danken, die mir immer mit ihrer Unterstützung und vor allem auch mit Ihrer Geduld zur Seite stand.

Speziell möchte ich mich bei Herrn Prof. Andreas Ludwig, dem Hauptbetreuer meiner Dissertation und meinem Chef am Lehrstuhl für Modellierung und Simulation metallurgischer Prozesse für die Möglichkeit der Verfassung der Dissertation danken. Seine fachliche Kompetenz, konstruktive Kritik aber auch Motivation haben in vielen Gespräche und Diskussionen sehr zum Gelingen dieser Doktorarbeit beigetragen. Vielen Dank auch Herrn Prof. Peter Schumacher als Zweitbetreuer der Doktorarbeit und seine Unterstützung durch experimentellen Messungen.

Viel Arbeit hatten auch meine beiden Betreuer, Frau Dr. Monika Grasser und Herr Dr. Sven Eck, denen ich für Ihre Unterstützung recht herzlich danke.

Mein Dank gilt aber auch der ESA und ASA die gemeinsam die Finanzierung der Dissertation ermöglicht haben und meinen Projektkollegen von METCOMP und DIRSOL.

Ich möchte aber auch meinen Arbeitskollegen für die gute und freundschaftliche Zusammenarbeit danken. Speziell sei hier auch das Sekretariat und die die EDV Abteilung erwähnt, denn ohne sie wäre diese Arbeit nicht möglich gewesen.

## Abstract

In the last decades the importance of metals and metallic alloys underlies an increasing importance, and with it the requirements on properties and quality of alloys. Important commercial alloys are for example steel, aluminum, copper, tin, and zinc alloys. Due to the fact that they show peritectic reactions in the phase diagram, it is of great importance to improve the understanding of a peritectic reaction and related morphologies leading to improved material properties of high quality. In the last century great efforts were made to gain deeper understanding of the microstructure formation in peritectic alloys during solidification, especially in cases where both phases solidify as a planar front.

The formation of a microstructure from the melt is influenced by convection in front of the solid/liquid interface, a consequence of the existing gravity on earth. Without gravity the natural convection does not operate, such as in the orbiting International Space Station (ISS). Therefore, the European Space Agency (ESA) supports investigations on peritectic solidification morphologies within the frame of the project “Metastable Solidification of Composites” (METCOMP).

To estimate the influence of natural convection on solidification morphologies the investigations within this project were divided into ground experiments, under normal gravity, and space experiments, under micro gravity. Due to a delay of the construction of the Bridgman-furnace for *in-situ* observation of direct solidification (DIRSOL) in space by ESA, the experiments in space had to be postponed to 2014. Thus the influence of the natural convection on the solidification morphologies remains to be elucidated in detail.

Investigations on peritectic metallic systems show a wide range of possible microstructures. Bands, tree-like microstructures, islands, and coupled growth were detected at a growth rate where both phases can solidify in form of a planar front. To improve the understanding of appearing morphologies during solidification transparent model systems for *in-situ* observation are an attractive option. Such systems offer the advantage that both, the morphology and the dynamics of solidification can be investigated by using optical diagnostic means. The organic phase diagram TRIS - NPG was selected for this study because temperature and concentration of the peritectic point are suitable for direct observation in a micro Bridgman-furnace setup. The organic compound TRIS is used for *in-situ* observation for the first time. Therefore, additional investigations to complete the physical properties of

TRIS and the alloys of TRIS - NPG had to be performed. Whereby, thermal instability of the organic compound TRIS was detected that constrains the processing window for *in-situ* observations.

The investigations on the organic phase diagram TRIS – NPG indicated a wide range of microstructures, whereby, well known structures as well as ones were found close to the limit of constitutional undercooling at the peritectic region. Oscillating behavior was found close to the peritectic concentration at pulling rates above the limit of constitutional undercooling. Here, both phases grow in a competitive manner in a way that oscillating solidification occurs. This kind of solidification was observed for the first time and no literature has been found up to now that describes this behavior. At a solidification rate close and below the limit of constitutional undercooling only a planar solidification front was found. In a few cases the growth of isothermal peritectic coupled growth (PCG) or banded growth which lead to isothermal PCG was observed. Evidence for this form of transformation were found in experiments with metals and supported with numerical simulation. Here, it was the first time that the transformation from banded to PCG is reported by direct observation.

# Contents

1	Introduction.....	5
2	State of the Art.....	8
2.1	Peritectic Solidification.....	8
2.1.1	Solidification Rate above the Critical Solidification Velocity $V_c$ , Cells and Dendrites .....	14
2.1.2	Solidification Rate below the Critical Solidification Velocity $V_c$ , Layered Structures .....	15
2.2	Organic Compounds .....	20
2.2.1	Organic Compound NPG.....	22
2.2.2	Organic Compound TRIS .....	22
2.2.3	Phase Diagram TRIS - NPG.....	24
3	Experimental Methods.....	27
3.1	Sample Preparation .....	27
3.1.1	Alloy Preparation.....	28
3.1.2	Sample Geometry .....	29
3.1.3	Sample Filling.....	29
3.2	Differential Scanning Calorimetry (DSC) .....	30
3.3	Bridgman Components .....	31
3.3.1	Micro Bridgman-furnace set up.....	32
3.3.2	Optical Observation System “DIOs” .....	34
4	Stability and Reproducibility of the NPG – TRIS System .....	36
4.1	Phase Diagram of TRIS – NPG .....	36
4.2	Available Physical and Chemical Properties of TRIS and NPG .....	41
4.3	Investigation on the Organic Material .....	42
4.3.1	Material Purification .....	42
4.3.2	Reproducibility of the Alloy Concentration .....	42
4.3.3	Thermal Stability .....	46
4.4	Corresponding Consequences .....	50
4.4.1	Conclusions from the Thermal Stability Investigation.....	50
4.4.2	Selection of Optimal Process Conditions .....	51
4.5	Selected Experimental Procedure .....	54
4.5.1	Experimental Type A: Unmoved Samples .....	55
4.5.2	Experimental Type B: Moved Samples .....	55
5	Results.....	56
5.1	Experimental Type A: Unmoved Samples.....	56
5.1.1	Samples with pure TRIS.....	56
5.1.2	Samples with pure NPG.....	59
5.1.3	Samples with Selected Concentrations.....	60
5.2	Experimental Type B: Moved Samples .....	63
5.2.1	Preparation of the Solid/Liquid Interface .....	63
5.2.2	Solidification Morphologies in the $[C_L]$ and the $[C_F]$ Phase Region.....	64
5.2.3	Layered Structure Morphologies .....	71
5.2.4	Oscillating Morphologies .....	80
5.2.5	Coupled Growth Morphologies .....	85
6	Discussion.....	90
6.1	Experimental Type A: Unmoved Samples.....	90
6.1.1	Thermal Stability .....	90
6.1.2	Wetting Angle and Nucleation Map .....	93
6.2	Experimental Type B: Moved Samples .....	95

6.2.1	Solidification Morphology in the TRIS-rich $[C_I]$ Phase for $x \leq 0.45$ .....	95
6.2.2	Solidification Morphology in the NPG-rich $[C_F]$ Phase for $x > 0.6$ .....	95
6.2.3	Band Formation Observed for Concentrations within the Peritectic Region .....	96
6.2.4	Oscillation Observed for Concentrations within the Peritectic Region and slightly above .....	98
6.2.5	Isothermal Coupled Growth Observed for Concentrations within the Peritectic Region .....	106
6.2.6	Microstructure Selection within the Peritectic Interval .....	111
7	Conclusions and Future Needs .....	114
8	Summary .....	116
9	References .....	117
10	Symbols .....	119
A	Appendix: Determination of Material Properties .....	1
A.1	Variation of Material Purifications .....	1
A.2	Material Colorization .....	4
A.3	Boiling Point .....	5
A.4	Raman Spectroscopy .....	7
A.5	Heat Conductivity .....	10
A.6	Vapor Pressure .....	15
A.7	Dynamic Viscosity .....	24
A.8	Temperature Gradient .....	30
A.9	Diffusion Coefficient .....	33
A.10	Refractive Index of Liquid with Peritectic Concentration .....	37



# 1 Introduction

The properties of pure metals are sometimes insufficient for special applications and in addition new applications require new materials with new properties. In this respect much interest is focused in producing new materials, which combine the properties of various compounds within one solid piece of matter.

Bronze, an alloy consisting of copper and tin, was the first alloy produced by the human spirit more than 5000 years ago. The importance of this history can be seen in the naming of entire human historical age like the Bronze and Iron Age. Since the Bronze Age mankind increased the applications of metals by alloying. The development of alloying techniques, casting and materials solidification processing improved physical, mechanical, and chemical properties of metallic materials. The handling of alloying techniques has been leading through the centuries from craft to science. Generally, alloying means mixing in the liquid state because normally only in the liquid state an ideal miscibility exists for different metals. Therefore, it is necessary to melt all components and then solidify the alloy again. During solidification, different possible phase reactions can take place, as for example monotectic, eutectic and peritectic reactions.

For the present study peritectic solidification is selected due to its complex and still not fully understood solidification morphologies. Commercially important alloys as Fe-C, Fe-Ni, Cu-Sn, and Cu-Zn show a peritectic reaction. The peritectic reaction is characterized by a phase transformation from liquid [L] and the primary solid [ $\alpha$ ] phase to the peritectic [ $\beta$ ] phase:  $[L + \alpha] \rightarrow [\beta]$  and is expected for all alloy compositions within the peritectic region  $C_\alpha$  to  $C_L$ , see Figure 1. The focus in this work is put on the occurring microstructure formation during solidification near the peritectic point at solidification rates where both phases might reveal a planar solid/liquid interface. Therefore, a micro Bridgman-furnace was used for *in-situ* observation of the solidification morphologies of transparent organic alloys. The usage of transparent organic alloys with a high temperature plastic phase (or non-faceted phase) is a quite attractive method to understand metallic solidification in detail. The micro Bridgman-furnace in combination with a microscope and a CCD camera enables *in-situ* observation and storage of the dynamic solidification morphology formation in real time.

The occurrence of different solidification morphologies are depending on nucleation conditions and diffusion in the liquid. Both are influenced by changes of the concentration field ahead of the solid/liquid interface, which is controlled by the growth dynamics of the interface and transport phenomena in the liquid due to thermal and solutal convection. Some solidification phenomena are not well understood in particular, because the solidification microstructure depends on convection which is always present under earth gravity conditions. To determine the influence of convection ahead of the solid/liquid interface on the formation of different solidification morphologies in peritectic systems microgravity experiments are planned.

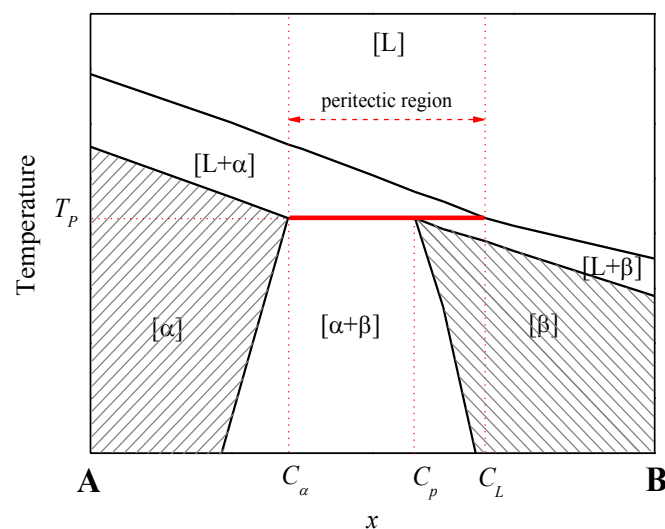


Figure 1: Schematic illustration of a phase diagram which shows a peritectic reaction. At the peritectic temperature  $T_p$  (red line) and the peritectic concentration  $C_p$  the primary [ $\alpha$ ] phase, the peritectic [ $\beta$ ] phase, and the liquid phase [L] are in equilibrium.

The experimental investigations under reduced gravity conditions are planned to take place on board of the ISS in 2014 within the frame of METCOMP project. The usage of beneficial conditions under microgravity in space may lead to a better understanding of the influences of gravitational related phenomena as natural convection and sedimentation on the solidification route. For that experimental results of solidification studies on earth will be compared with those obtained in space. The evaluation of such studies will lead to the construction of microstructure selection maps with convection and sedimentation as “process parameters”. This might serve industry as guidance to improve the qualities of materials and to increase the efficiency of production routes in order of saving energy and time concerning especially post

solidification treatment. In microgravity, thermo and solutal convection can be assumed to have a negligible effect on microstructure formation during peritectic solidification. The **Microgravity Science Glove box (MSG)** [1] in the Columbus module (see Figure 2a) on the **International Space Station (ISS)** represents a new perspective for the observation of peritectic solidification. The **DIRSOL** [1] instrument, a micro Bridgman-furnace, is developed to perform **DIR**ectional **SOL**idification experiments on transparent materials in the MSG on board of the ISS. The DIRSOL facility consists of three major flight parts: The experiment units with the micro Bridgman-furnace assemble and observation system, the facility control unit and the DIRSOL cartridges. The mounting configuration inside MSG is shown in Figure 2b. The main diagnostics element of DIRSOL is the optical observation system with high resolution. The camera can observe the changes in the sample between the hot and cold zones of the Bridgman assembly at fixed positions and angles.

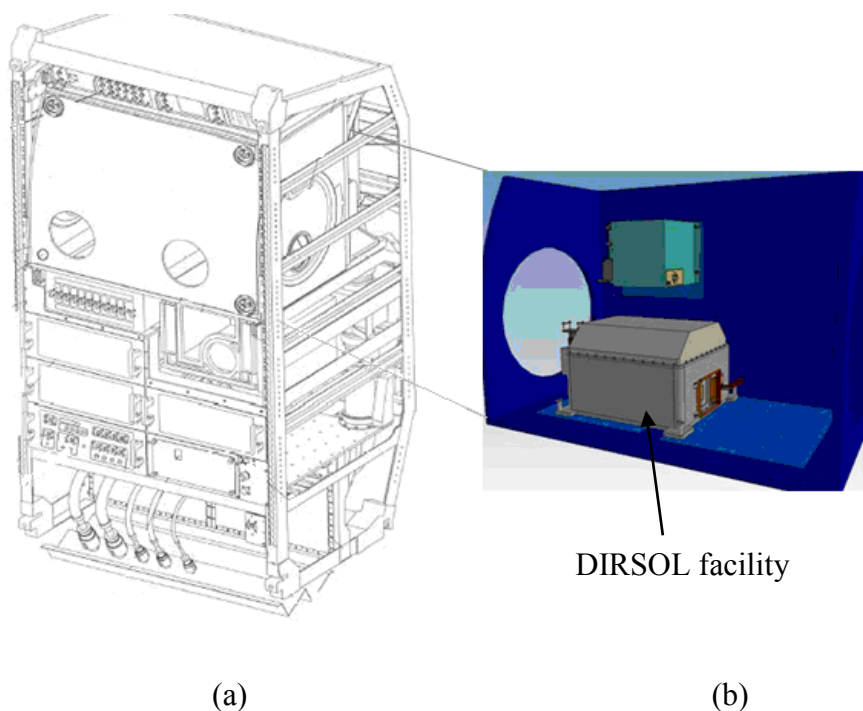


Figure 2: (a) MSG isometric view. (b) The DIRSOL facility in grey inside MSG work volume attached to DIRSOL experiment unit.

In this study, the background of peritectic solidification is reviewed, the suitability of the selected transparent organic alloy, selected material properties and the reproducibility of experiments are evaluated. Expected and unexpected solidification morphologies at solidification rates below the critical velocity are classified.

## 2 State of the Art

Peritectic solidification shows a variety of complex microstructures that is influenced by the competition between the nucleation and growth of different phases [2]. Investigations on directional solidification including *in-situ* observations with X-Ray techniques [3] of peritectic alloys have been performed on metals like Zn–Ag [4], Sn–Cd [5, 6, 7, 8], Cu–Sn [9], Pb–Bi [10, 11, 12, 13, 14], Zn–Cu [15, 16, 17], Sn–Sb [18, 19], Ti–Al [20, 21], Fe–Ni [22, 23, 24, 25, 26, 27, 28, 29, 30, 31], Ni–Al [32], YBCO [33] and Nd–Fe–B [34]. Wide spectrums of complex microstructures were found in directionally solidified alloys and discussed [17, 21, 22, 23, 24, 26, 27, 32, 35, 36, 37, 38] but an *in-situ* observations of peritectic reactions with organic compounds was not possible up to now.

### 2.1 Peritectic Solidification

A peritectic reaction in a binary system is in general the transformation of a liquid and an already existing primary solid phase  $[\alpha]$  to a peritectic solid phase  $[\beta]$  ( $[L + \alpha] \rightarrow [\beta]$ ) at the peritectic temperature  $T_p$ . Due to the necessary driving force for nucleation and growth of the peritectic  $[\beta]$  phase the peritectic reaction occur at  $\Delta T$  below the peritectic temperature (Figure 3a).

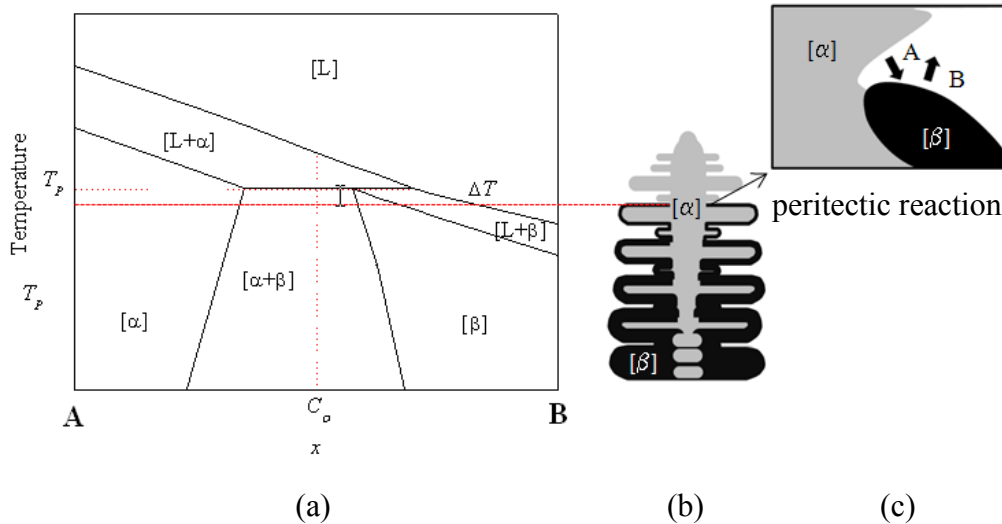


Figure 3: (a) Peritectic phase diagram. (b) Peritectic reaction during peritectic growth. (c) Diffusion pathway for the A and B element.

The peritectic phase diagram is described in detail in Figure 4. The corresponding concentrations  $x$  in mol fraction are  $C_\alpha$  for the  $[\alpha]$  phase,  $C_p$  or  $C_\beta$  for the peritectic  $[\beta]$  phase, and  $C_L$  for the liquid phase.

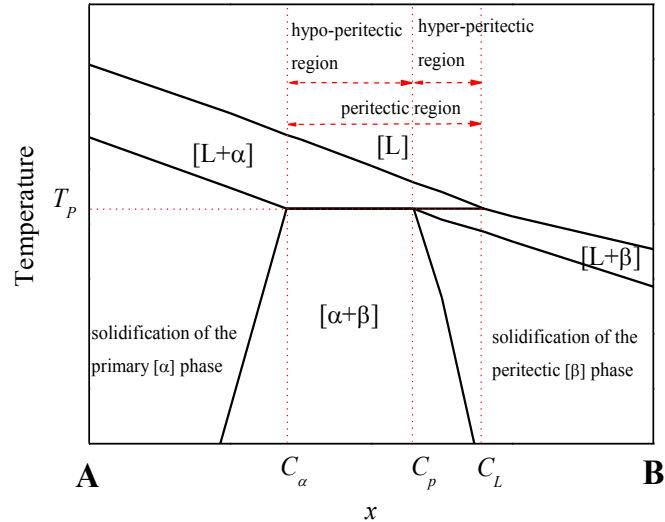


Figure 4: Detail of a peritectic phase diagram. At the peritectic temperature  $T_p$  and the peritectic concentration  $C_p$  the  $[\alpha]$ ,  $[\beta]$  and liquid phase are in equilibrium. The peritectic composition range  $C_\alpha$  to  $C_L$  can be divided in the hypo-peritectic range from  $C_\alpha$  to  $C_p$  and the hyper-peritectic range from  $C_p$  to  $C_L$ . At concentrations  $C_0 < C_\alpha$ , only the  $[\alpha]$  phase solidifies and for  $C_0 > C_L$  the  $[\beta]$  phase grows.

The region  $C_\alpha \leq x \leq C_L$  is divided in the hypo-peritectic region  $C_\alpha \leq x \leq C_p$  and the hyper-peritectic region  $C_p \leq x \leq C_L$ . Whereby, an alloy with a hypo-peritectic concentration  $C_0$  with  $C_\alpha \leq C_0 \leq C_L$  starts to solidify with the primary  $[\alpha]$  phase and transforms partly to the peritectic  $[\beta]$  phase when passing  $T_p$  [2]. For initial concentrations  $C_0 < C_\alpha$  only the  $[\alpha]$  phase solidifies and for  $C_0 > C_L$  the  $[\beta]$  phase solidifies. Possible variants for peritectic phase diagrams are given in Figure 5.

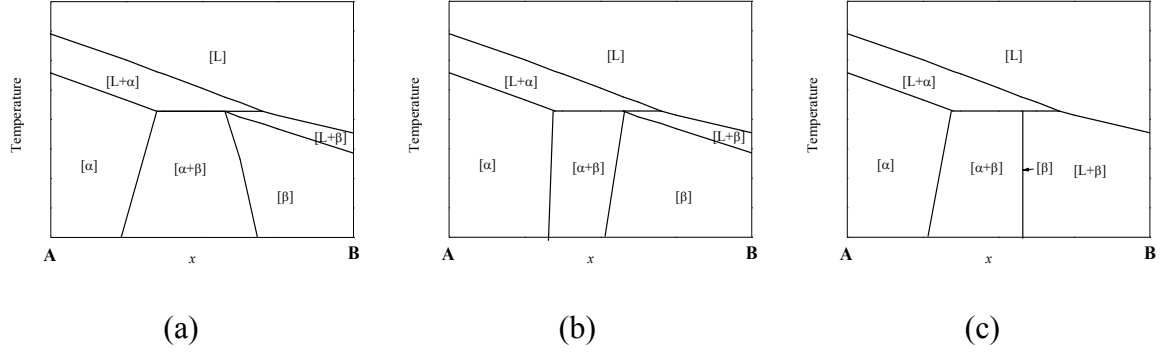


Figure 5: Peritectic phase diagrams which show different kinds of the two phase region  $[\alpha + \beta]$ . The proportion between the  $[\alpha]$  and the  $[\beta]$  phase for an initial hypoperitectic concentration, (a) remain equal, (b) shifted to a higher amount of  $[\beta]$  phase, or (c) show an increasing ratio of the  $[\alpha]$  phase with a constant concentration of the  $[\beta]$  phase during solidification below the peritectic temperature.

During solidification of an alloy, the solute accumulates ahead of the initial planar solid/liquid interface (Figure 6), because of the lower solubility of a compound (element in the case of metal alloys) in the solid phase in comparison to the liquid phase. The rejected solute will lead to a higher concentration of the other compound in the liquid boundary layer.

The concentration of the solute profile for steady-state conditions and  $V \leq V_c$  a planar solid/liquid interface is defined by [2]:

$$C_L(z) = C_0 + (C_L - C_S) \cdot \exp\left(-\frac{V \cdot z}{D_L}\right). \quad (\text{Eq. 1})$$

Here,  $C_L(z)$  is the concentration in the liquid in  $z$  direction ahead of the solid/liquid interface,  $C_0$  the initial concentration,  $C_L$  the liquid concentration at the solid/liquid interface,  $C_S$  the solid concentration at the solid/liquid interface,  $V$  the growth velocity, and  $D_L$  the diffusion coefficient in the liquid and  $z$  the distance in the liquid from the solid/liquid interface. The equivalent boundary layer thickness  $\delta$  is defined by [2]:

$$\delta = \frac{2 \cdot D_L}{V}. \quad (\text{Eq. 2})$$

The thickness of the boundary layer  $\delta$  depends on the diffusion coefficient  $D_L$  in the liquid and the growth velocity  $V$ . For a certain growth velocity  $V$  the concentration in the liquid  $C_L$  decreases from  $C_0/k$  to  $C_0$  with distance  $z$  as shown in Figure 6 and Figure 7a.  $k$  is the distribution coefficient defined as:

$$k = \frac{C_S}{C_L}. \quad (\text{Eq. 3})$$

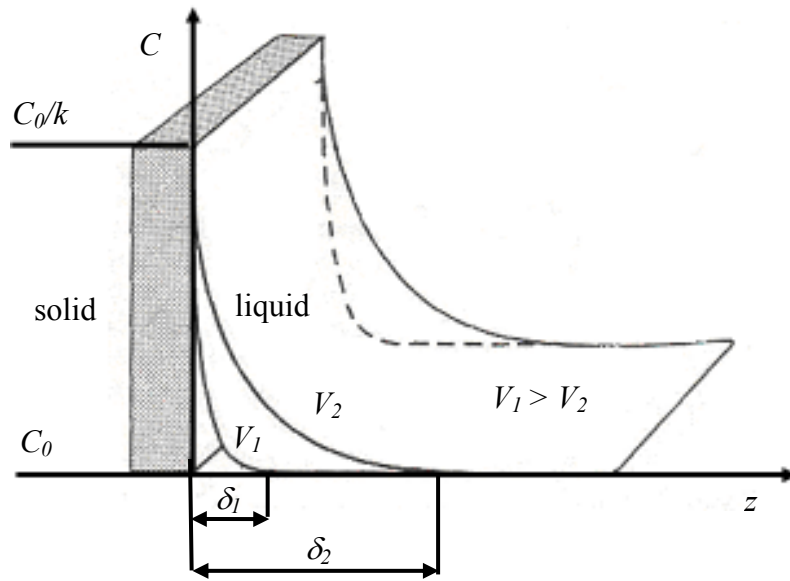


Figure 6: Boundary layer  $\delta$  at a planar solid/liquid interface. The layer increases with increasing diffusion coefficient  $D_L$  or decreasing growth velocity  $V$  (taken from [2]).

During solidification a temperature gradient  $G_T$  exists in the liquid ahead of the solid/liquid interface (Figure 7c). Whereby, the liquidus and solidus temperatures,  $T_L$  and  $T_S$ , are given by the phase diagram, see Figure 7b. Therefore, for each concentration ahead of the solid/liquid interface (Figure 7a) the corresponding liquidus temperatures can be taken from the phase diagram (Figure 7b). Depending on the magnitude of the temperature gradient, a zone of constitutional undercooling occur [2] (gray shaded in Figure 7c) ahead of the planar solid/liquid interface when:

$$G_T \leq \frac{-m_L \cdot \Delta C_0 \cdot V}{D_L}. \quad (\text{Eq. 4})$$

Here,  $m_L$  is the liquidus slope and  $\Delta C_0$  the concentration difference between the solidus concentration  $C_0$  and the liquidus concentration  $C_L$ .

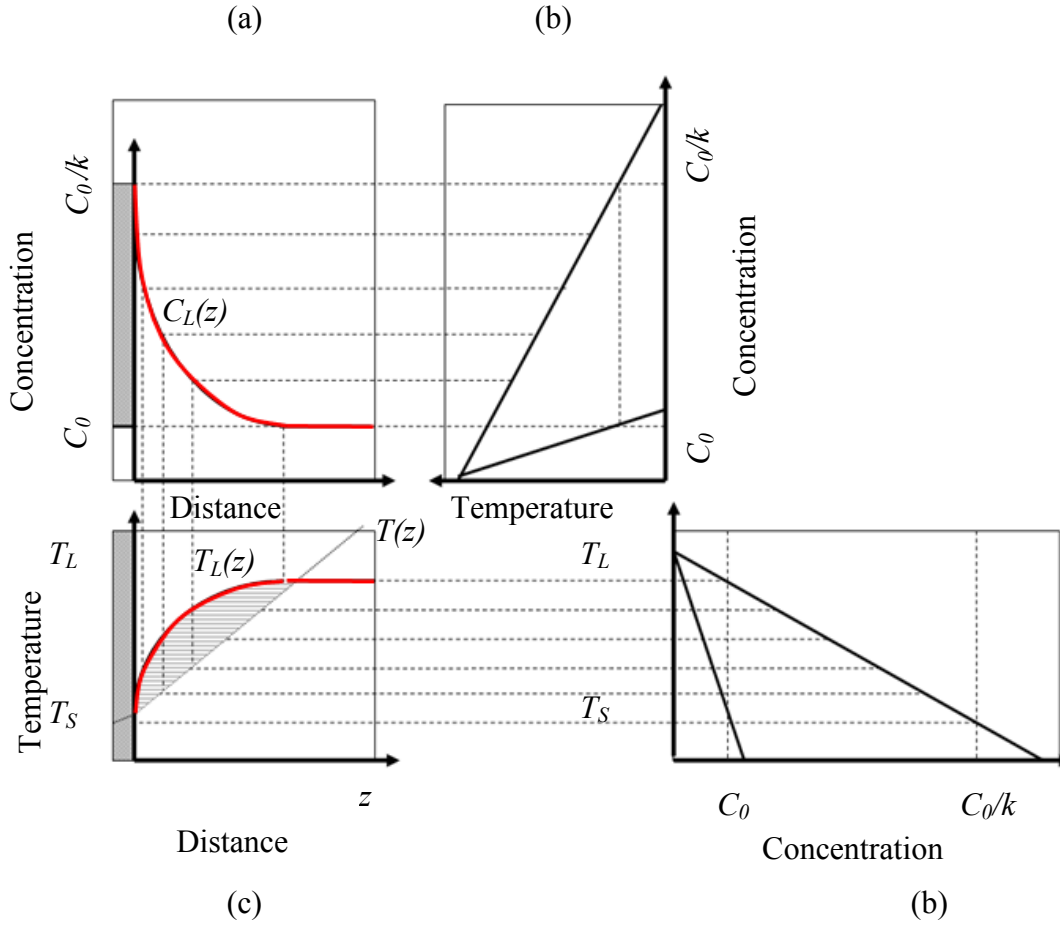


Figure 7: Constitutional undercooling in an alloy which grows with a planar front. The region where constitutional undercooling is expected is marked grey.

Having a zone of constitutional undercooling ahead of the solid/liquid interface, the planar solidification front will always become unstable and cells or dendrites will start to grow. For controlled directional solidification the temperature gradient  $G_T$  is implemented by a Bridgman-furnace whereby the solidification velocity  $V$  is equal to the pulling rate  $V_p$  under steady state condition. Furthermore, the liquidus slope and the concentration difference can be expressed by the temperature difference:

$$-m \cdot \Delta C_0 = (T_L - T_S) = \Delta T_0. \quad (\text{Eq. 5})$$

Here,  $\Delta T_0$  is the temperature difference between the liquidus temperature  $T_L$  and the solidus temperature  $T_S$ . Therefore, the limit of constitutional undercooling can be expressed by:



$$\frac{G_T}{V_c} = \frac{\Delta T_0}{D_L} \quad \text{or} \quad V_c = \frac{D_L \cdot G_T}{\Delta T_0}. \quad (\text{Eq. 6})$$

Here,  $V_c$  is the critical solidification velocity. At limit of constitutional undercooling, for  $V \leq V_c$ , a stable planar front grows at the corresponding solidus temperature  $T_S$  of the alloy [2]. Otherwise, if  $V > V_c$ , the planar interface becomes unstable and transforms to cells and/or dendrites to reduce the zone of constitutional undercooling. Whereby, cells and dendrite tip are growing undercooled in respect to the liquidus temperature  $T_L$ .

In the peritectic region the values of the two temperature differences,  $\Delta T_\alpha$  and  $\Delta T_\beta$ , are dissimilar (see Figure 8), therefore, for a definite solidification velocity  $V$  it is possible that one phase grows above the limit of constitutional undercooling where the other one grows below the limit of constitutional undercooling ( $V_c^\alpha < V < V_c^\beta$  for  $\Delta T_\alpha > \Delta T_\beta$ ).

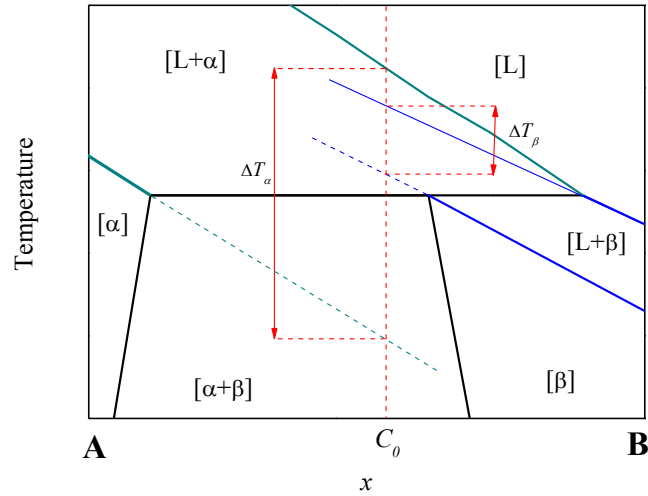


Figure 8: Temperature difference  $\Delta T_\alpha$  and  $\Delta T_\beta$  between the liquidus and solidus line of the primary  $[\alpha]$  phase and the peritectic  $[\beta]$  phase within the peritectic region. For a given concentration  $C_0$  the temperature difference  $\Delta T$  depends on the phase with  $\Delta T_\alpha \neq \Delta T_\beta$ .

In this case that the  $[\alpha]$  phase grows above the limit of constitutional undercooling only the  $[\beta]$  phase grows planar and the  $[\alpha]$  phase shows cellular or dendritic solidification

morphology. The solidification morphology changes to a planar front as soon as the solidification velocity ( $V < V_c^\alpha$  and  $V_c^\beta$ ) is below the critical velocities of both phases.

The development of the pill-up during the initial transient requires a certain distance of solidification until the solid/liquid interface can grow under steady-state condition. As a rule of thumb the necessary transition distance for a planar front to reach steady-state growth conditions [2] is:

$$z_{tr} \approx \frac{6 \cdot D_L}{V_p \cdot k}. \quad (\text{Eq. 7})$$

Here,  $z_{tr}$  is the transition length. To determine the time necessary for the solidification front to reach steady-state the equation above can be transferred to:

$$t_{tr} \approx \frac{6 \cdot D_L}{V_p^2 \cdot k}. \quad (\text{Eq. 8})$$

Here,  $t_{tr}$  is the transition time. Thereafter, the solidification morphology grows under steady-state condition and forms a diffusion boundary layer with a characteristic length  $\delta$  as shown in Figure 6. In case of cellular or dendritic growth at  $V_p > V_c^{\alpha,\beta}$ , steady-state is reached much faster than in case of a planar solidification front.

### 2.1.1 Solidification Rate above the Critical Solidification Velocity $V_c$ , Cells and Dendrites

A peritectic reaction requires the solidification of liquid and the transformation from the primary phase  $[\alpha]$  to the peritectic phase  $[\beta]$ . The change from the  $[\alpha]$  phase to the  $[\beta]$  phase is a solid to solid transformation while the transformation from melt to the peritectic  $[\beta]$  phase occurs by solidification. Generally, the solidification and transformation is controlled by thermal and solute diffusion. Since the thermal diffusion is faster than the solute diffusion, the solute diffusion is the limiting factor. Besides, the solute diffusion in the liquid is approximately 1000 times higher than in the solid.

For fast growth conditions ( $V > V_c^{\alpha,\beta}$ ) the peritectic phase can solidify directly from the melt or nucleate at the solid/liquid interface, see Figure 9a and b. Another possibility is the

solid/solid transformation of the primary  $[\alpha]$  phase to the peritectic  $[\beta]$  phase at temperatures below the peritectic temperature, see Figure 9c. In Figure 9a the primary  $[\alpha]$  phase forms cells or dendrites whereas the peritectic  $[\beta]$  phase forms a cellular or dendritic morphology in the interdendritic or intercellular region. Both phases either grow at the same isotherm or the peritectic phase is lagging behind the primary phase [39]. As the solidification velocity  $V$  decreases the peritectic solid in between the primary dendrites undergoes a transition from dendritic to cellular growth and finally to a planar front. For  $V > V_c^\alpha$  and  $V \leq V_c^\beta$ , the primary  $[\alpha]$  phase solidifies still dendritic or cellular while the peritectic  $[\beta]$  phase may grow planar.

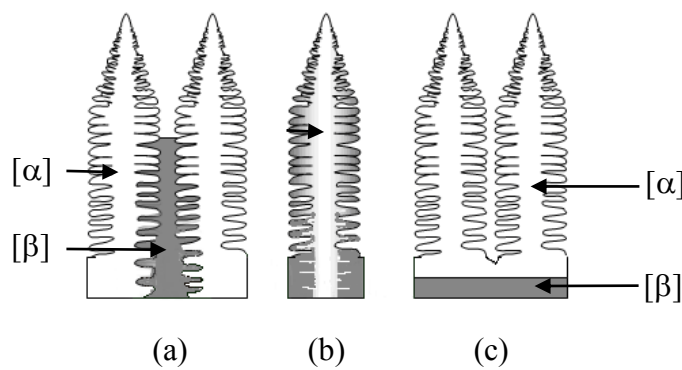


Figure 9: Solidification of the peritectic phase for fast growth conditions. (a) The peritectic phase  $[\beta]$  grows directly from the melt. (b) The peritectic phase (gray colored) solidifies on the solid/liquid interface of the primary phase (white colored). (c) A solid phase transformation takes place at lower temperature.

Although a microstructure map (depending on temperature gradient  $G_T$ , pulling velocity  $V_p$ , and initial concentration  $C_0$ ) based on the change in microstructure encountered with single-phase solidification was proposed by Hunzinger et al. [40], the situation is more complex since the formation of the  $[\beta]$  phase in the intercellular or interdendritic region is controlled by the diffusion field influenced by the solidifying primary phase.

### 2.1.2 Solidification Rate below the Critical Solidification Velocity $V_c$ , Layered Structures

The process conditions for possible band formations are a planar interface for one of the phases and the absence of convection in the liquid as described in Trivedi [41]. Here, two metastable two-phase microstructures occur (Figure 10).

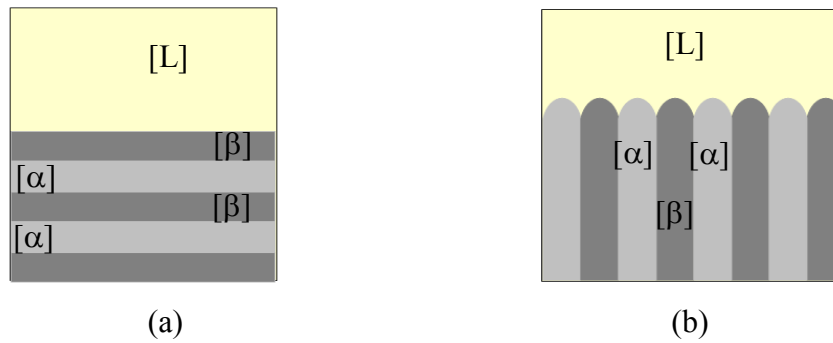


Figure 10: (a)  $[\alpha]$  and  $[\beta]$  bands grow parallel to the solidification front. (b) Coupled growth of  $[\alpha]$  and  $[\beta]$  phase in the form of lamellae.

Precise interpretations of experimental studies at low velocities have been difficult due to the presence of convection. Most peritectic alloy systems are composed of dissimilar metals possessing large density differences that cause convection. This alters the stability of the primary growth front by altering diffusion fields ahead of the peritectic phase and thereby modifying the morphology of the peritectic solid.

The process which leads to the formation of bands is described in detail in Figure 11.

Figure 11, no. 1: For concentrations within the peritectic region ( $C_\alpha < C_0 < C_L$ ) the  $[\alpha]$  phase grows during the initial solidification for low growth rates.

Figure 11, no. 2: Simultaneously to the growth of the  $[\alpha]$  phase, a solute enriched boundary layer is built in front of the planar solid/liquid interface. The solid/liquid interface temperature decreases from the liquidus temperature  $T_L$  to the solidus temperature  $T_S$  as soon as the liquid concentration at the solid/liquid interface reaches  $C_L$ .

Figure 11, no. 3: The temperature of the interface follows the solidus line and, if the temperature decreases beyond the peritectic temperature  $T_p$ , the liquid becomes undercooled in respect to the  $[\beta]$  phase. In this case, Boettinger [5] and Trivedi et al. [6] predicts the growth of the peritectic  $[\beta]$  phase in front of the planar growing primary  $[\alpha]$  phase within the concentration region of  $C_b$ . The undercooled liquid in respect to the  $[\beta]$  phase enables the peritectic  $[\beta]$  phase to nucleate in front of the primary  $[\alpha]$  phase.

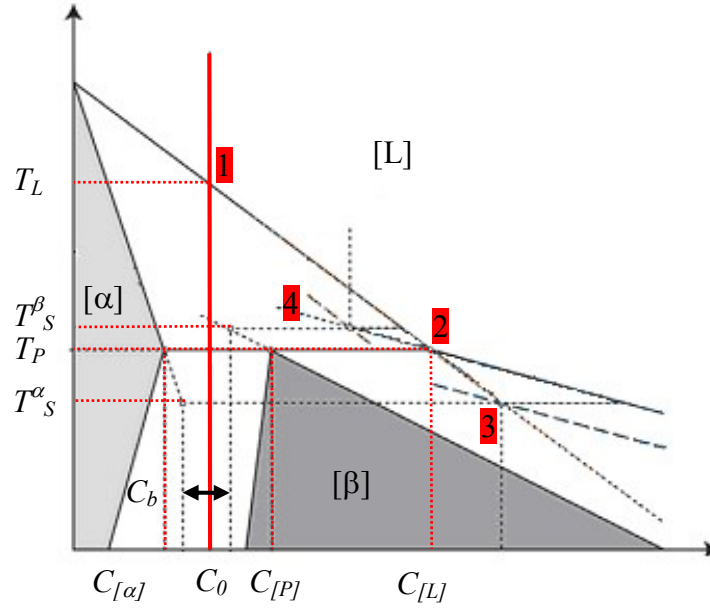


Figure 11: Illustration of the banding process, published in [9], predicted by Trivedi [41] for concentrations  $C_0$  within the concentration region of  $C_b$ .

Figure 11, no. 4: Now, with the growth of the peritectic phase the solid composition follows the solidus line of the  $[\beta]$  phase to a higher temperature. Once the temperature of the liquid in front of the peritectic phase is above the peritectic temperature the  $[\alpha]$  phase can nucleate before a steady-state condition for  $[\beta]$  growth is obtained. This process leads to the formation of bands with alternating phases which grow in the form of an oscillating planar front at temperatures between  $T_S^\alpha$  and  $T_S^\beta$  (Figure 11, no. 3 and 4).

Trivedi [41] published an equation which can be used to calculate the thickness of bands. The width of each individual lamella  $A_{[\alpha]}$  and  $A_{[\beta]}$  of the  $[\alpha]$  and  $[\beta]$  layers is given by:

$$A_{[\alpha]} = \frac{1 - \frac{C_{[\alpha]}}{C_0} \cdot \left(1 - \frac{\Delta T_N^{[\alpha]}}{C_{[L]} \cdot (m_i^{[\beta]} - m_i^{[\alpha]})}\right)}{1 - \frac{C_{[\alpha]}}{C_0} \cdot \left(1 + \frac{\Delta T_N^{[\beta]}}{C_{[L]} \cdot (m_i^{[\beta]} - m_i^{[\alpha]})}\right)} \quad (\text{Eq. 9})$$

$$A_{[\beta]} = \frac{1 - \frac{C_{[\beta]}}{C_0} \cdot \left(1 + \frac{\Delta T_N^{[\beta]}}{C_{[L]} \cdot (m_i^{[\beta]} - m_i^{[\alpha]})}\right)}{1 - \frac{C_{[\beta]}}{C_0} \cdot \left(1 - \frac{\Delta T_N^{[\alpha]}}{C_{[L]} \cdot (m_i^{[\beta]} - m_i^{[\alpha]})}\right)} \quad (\text{Eq. 10})$$

$$\lambda = \frac{D_L}{V \cdot k_{[\alpha]}} \cdot \ln A_{[\alpha]} + \frac{D_L}{V \cdot k_{[\beta]}} \cdot \ln A_{[\beta]} \quad (\text{Eq. 11})$$

Here,  $\Delta T_N^i$  ( $i = [\beta]$  or  $[\alpha]$ ) is the undercooling. The assumption of this model is that the growth of the new nucleated phase in lateral direction  $V_L$  is rapidly enough to form a new band before the existing phase overgrow the new nucleated phase, see Figure 12. Note, that in contrast to Figure 3c on page 8 which shows a peritectic reaction, here, both phases  $[\alpha]$  and  $[\beta]$  are growing independent.

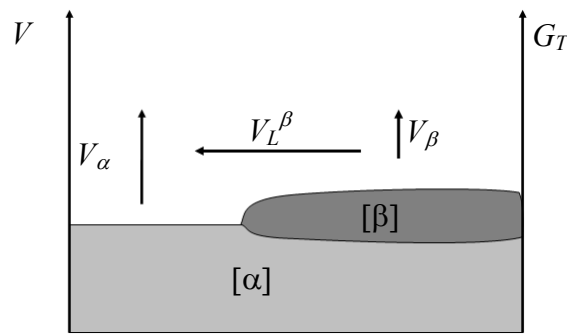


Figure 12: Competing growth between the primary  $[\alpha]$  phase and the lateral growth of the peritectic  $[\beta]$  phase in solidification direction. Banded solidification occurs only if the lateral velocity  $V_L^\beta$  of the new phase  $[\beta]$  is faster than the solidification speed of the existing phase  $[\alpha]$ . Otherwise island bands or coupled growth is possible.

The growth competition between the nucleated phase and the preexisting phase leads to new solidification dynamics like coupled growth in a eutectic system (Figure 10b). Dobler [27] observed such coupled growth in Fe-Ni peritectic alloys.

Prima facie, the coupled growth of a lamellar eutectic system is equal to the solidification morphology of a coupled growth peritectic system. In both cases, the  $[\alpha]$  phase grows side by side with the  $[\beta]$  phase. However, in details the coupled growth in a eutectic system differs from the lamella growth in peritectic systems, see Figure 13. During solidification in eutectic system the rejected solute in front of the solidifying  $[\alpha]$  phase is needed by the solidifying  $[\beta]$  phase (Figure 13a). In contrast, solidification in the peritectic system requires similar alloy elements in the solid  $[\alpha]$  and  $[\beta]$  phase. Therefore, the rejected solute in front of the primary

[ $\alpha$ ] phase is not needed to form the peritectic [ $\beta$ ] phase (Figure 13b). This difference leads to a much larger boundary layer  $\delta$  in front of the solidification front of a peritectic coupled growth,  $\delta_c \approx 2 \cdot D_L/V$ , compared to the eutectic solidification with  $\delta \approx \lambda$ . Furthermore, all solidification morphologies are highly influenced by the presence of convection and nucleation ahead of the growing interface [6, 27, 39, 42, 43].

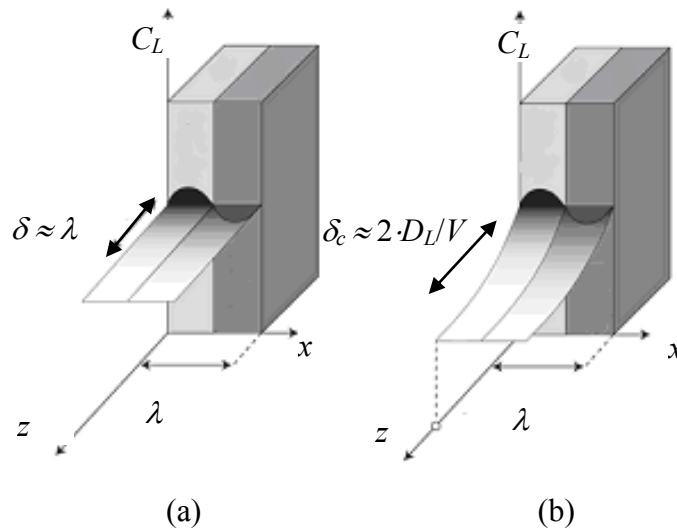


Figure 13: Formation of the solute layer in front of the solid/liquid interface, published in [9].

(a) Eutectic coupled growth with a solute layer equal to  $\lambda$ . (b) Peritectic coupled growth with a much thicker solute layer of  $2 \cdot D_L/V$ .

## 2.2 Organic Compounds

Several organic compounds show an **orientationally disordered crystal phase** (short form ODIC), usually called plastic crystals [44, 45, 46, 47] or a non-faceted phase (see Figure 14). Such molecules consist of a pseudo-spherical or globular shape with weakly angle-dependent interactions usually by *van der Waals* forces or hydrogen bonds. Plastic crystals can be considered as an intermediate stage between solid and liquid. They do not have any orientation order but the positional order still exists, therefore, the molecules are able to reorient on their lattice site. In a plastic crystal there is a solid lattice with long range translation symmetry inside which is indicated by sharp Bragg reflections. Molecules in these phases are more or less free to rotate around their center so that they do act as stacked spherical objects, therefore, plastic crystals are optically isotropic. The plastic phase is usually highly symmetrical (etc. cubic) [47, 48].

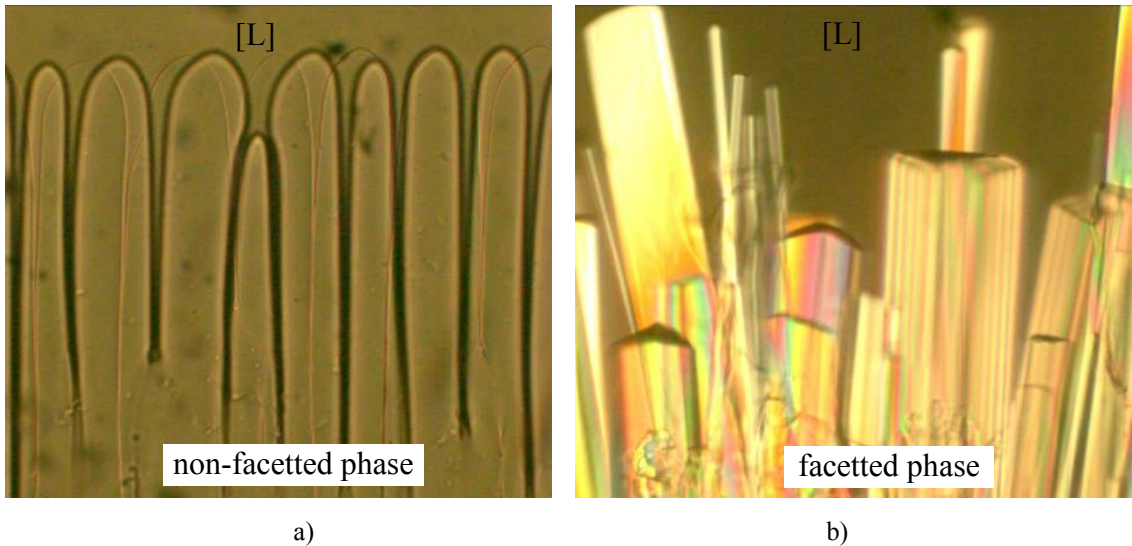


Figure 14: The difference between the solid/liquid interface morphologies for solidification of a non-faceted phase and a faceted phase can be seen in the growth structure. a) Solidification of a plastic phase (ODIC) or non-faceted phase happens in the form of cells similar to metals. b) Growth of a faceted phase or orientationally ordered crystal. In both cases the pictures show observation results of TRIS ultra-pure [49].

A convenient criterion for predicting a plastic phase or a faceted phase is the dimensionless entropy  $\alpha$  :

$$\alpha = \frac{\Delta S_f}{R}. \quad (\text{Eq. 12})$$



Here,  $\Delta S_f$  is the entropy of fusion and  $R$  the gas constant. Values of  $\alpha \leq 2$  imply non-faceted crystal growth or plastic crystal [2]. The name plastic crystal refers to the same soft plastic mechanical properties like waxes. This kind of material is very soft and ductile and can be easily deformed. The molecules reorientate on their lattice position and act in the same way as metals do [50, 51]. The solidification of the plastic phase follows the same behavior as observed in metals, namely in form of a planar front, cells, or dendrites depending on the solidification conditions. Therefore, organic compounds with a plastic phase are quite attractive to study solidification morphologies with *in-situ* observation technique. A number of transparent organic compounds and their alloys have been investigated in [50, 52, 53, 54, 55, 56] to find model substances that allow *in-situ* and real time observation of metal-like solidification phenomena such as planar, cellular or dendritic growth. Barrio et al. [57] and Sturz et al. [52] reported a peritectic reaction for the organic model alloy NPG (Neopentylglycol)-TRIS (Tris(hydroxymethyl)aminomethane) and for TRIS (Tris(hydroxymethyl)aminomethane) – PE (Pentaerythritol), see Figure 15.

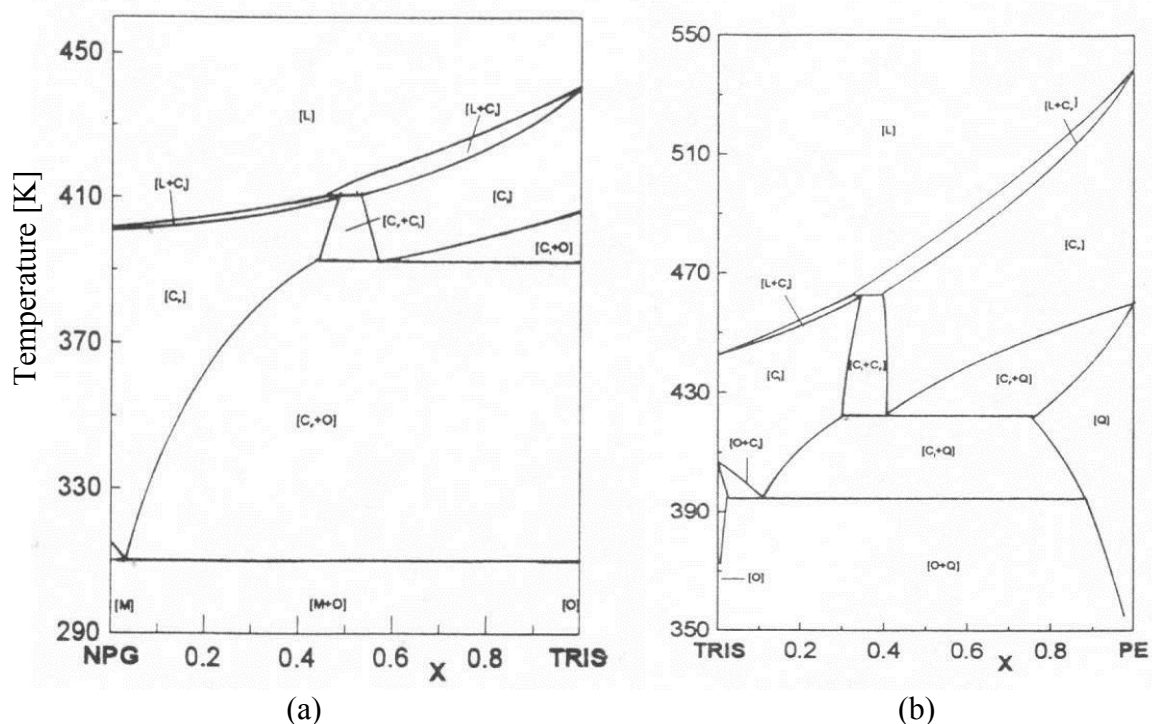


Figure 15: (a) The phase diagram of NPG - TRIS (b) The phase diagram of TRIS - PE [57].

All compounds show a plastic phase at high temperature. This fact permits the *in-situ* investigation of a non-faceted/non-faceted peritectic phase diagram with the Bridgman technique. In both diagrams the organic substance TRIS is part of the alloy, a material which

was never used before for *in-situ* investigations. Since the temperature range of the peritectic reaction TRIS – NPG is lower than in the phase diagram TRIS – PE, the phase diagram TRIS – NPG was chosen in the present thesis for *in-situ* investigations with the Bridgman technique.

The binary phase diagram TRIS - NPG was investigated by DSC measurement and X-Ray patterns and the results are published by Lopez et al. [57, 58]. Also Chandra et al. [59] investigated the binary phase diagram TRIS – NPG and calculated the binary phase diagram with the *CALPHAD* approach and investigated with DSC measurement. All phase diagrams show differences in the concentrations for the peritectic line and the exact position of the liquidus and solidus temperatures. Especially, the liquidus line of the pure substance NPG in the published phase diagram [59] is higher.

Sturz et al. [52] published the thermodynamic data for several organic compounds including TRIS and NPG. Available information about the physical and chemical properties of TRIS and NPG are given in Table 7 on page 41.

### 2.2.1 Organic Compound NPG

Neopentylglycol (formally known as 2,2-dimethyl-1,3propanediol)  $(\text{CH}_3)_2\text{C}(\text{CH}_2\text{OH})_2$  has already been used for this kind of research for a long time and its chemical as well as physical properties are well known [49]. At  $314.6 \pm 1.0$  K this organic substance transforms from an ordered low temperature faceted solid phase (phase II) to an orientationally disordered solid phase (phase I) which is stable up to the melting point at  $401.3 \pm 1$  K. The crystal structure of the low temperature phase II is monoclinic [M],  $Z = 4$ , space group  $P2_1/n$ . Phase I, the plastic phase (see Figure 14a, page 20), has a face centered cubic structure and is called [C<sub>F</sub>] with  $Z = 4$ , [57, 58]. The organic substance as delivered from commercial companies has a purity of 99 % [49]. It is mentioned that thermal decomposition occurs in contact with a strong base at temperatures higher than 393 K and its decomposition products are methanol, isobutanol, isobutyl aldehyde, formaldehyde etc. [60]. NPG is very hygroscopic and thus, it usually contains residual water [61]. This fact requires in any case a pretreatment before it can be used for further investigations.

### 2.2.2 Organic Compound TRIS

Tris(hydroxymethyl)aminomethane  $\text{H}_2\text{NC}(\text{CH}_2\text{OH})_3$  is a widely used buffering agent in the pH range 7 to 9. It is important for studies of physiological media and seawater and

commonly known as TRIS or THAM, but formally named 2-amino-2-hydroxymethyl-1,3-propanediol. With an acid dissociation constant,  $pK_a$  of 8.3, TRIS is a strong base and has a good buffer capacity between 7.2 – 9.0 pH. The  $pK_a$  decreases with approximately 0.03 units/K with increasing temperature [62], therefore, at 393 K TRIS is just a medium strong base. TRIS is highly hygroscopic, soluble in water and insoluble in alcohol and ether. The low temperature phase shows an orthorhombic lattice [O] with space group  $Pn2_1a$  and  $Z = 4$  [57, 58]. It is a faceted phase and appears under polarized light multi-colored (see Figure 14b, page 20) [61]. The solid/solid transition occurs at  $406.8 \pm 1.0$  K. The high temperature phase (plastic phase) is body centered cubic [ $C_1$ ], space group  $Im3m$  with  $Z = 2$  and not optical active [57, 58]. Phase II, the low temperature phase, shows strong hydrogen bonds in the layer and weak hydrogen bonds between the layers. The plastic phase [ $C_1$ ] differs from other pseudo spherical compounds due to its strong extensive hydrogen bonds. Hydrogen bonding plays a dominant role in the plastic phase of TRIS and hence the rotational activation energy is 10 times higher in TRIS than in other plastic crystals [51]. Tamarit et al. [63] investigated the influence of the dynamic hydrogen bonds on the packing coefficient. It was shown that the hydrogen bonds control the packing of the molecular crystals and mixed crystals in the plastic phases. Eilerman et al. [51] investigated the low [O] and high temperature phase [ $C_1$ ] of the organic substance. The occurrence of plastic phase stability [ $C_1$ ] is quite sensitive to impurities and the sample volume [51]. For three impurities  $Y-C(CH_2OH)_3$  different circumstances were observed [51], for  $Y =$

- (i)  $C(CH_2OH)_3 - CH_2OH$  A reversible transformation to the fcc phase [O] was reported.
- (ii)  $C(CH_2OH)_3 - CH_2CH_3$  A glassy state was reported.
- (iii)  $C(CH_2OH)_3 - CH_3$  A syrup was formed prior to melting.

This is important because impurities are most likely always present. Wasylishen et al. [64] investigated the plastic and liquid phase of TRIS and detected an influence of the thermal history of the sample (with carbon-13 nuclear magnetic resonance spectra). Furthermore, decomposition of the liquid phase of TRIS was observed [64] indicated by a change from transparent color to light yellow on. The chemical company DOW reported in their material safety data sheet (MSDS) [65] that a temperature above 422 K can cause decomposition of TRIS.

In contrast to metals, organic compounds consist of molecules, therefore, they can be thermal instable and decompose. Thermal instability arises through one of the two mechanisms: (i) molecular decomposition or self-reaction or (ii) reaction with the molecule with the environment especially with oxygen [66]. However, TRIS is commercial used at room temperature, therefore, its properties at higher temperatures are not well studied. Here, TRIS is used the first time for *in-situ* observations of solidification morphologies at temperature above the melting point.

### 2.2.3 Phase Diagram TRIS - NPG

Barrio et al. [50] published 1995 a thermodynamic phase diagram showing a peritectic reaction for the organic model alloy NPG (Neopentylglycol)-TRIS(Tris(hydroxymethyl)aminomethane). Both compounds have an orientationally disordered crystalline phase at high temperature (see Figure 16).

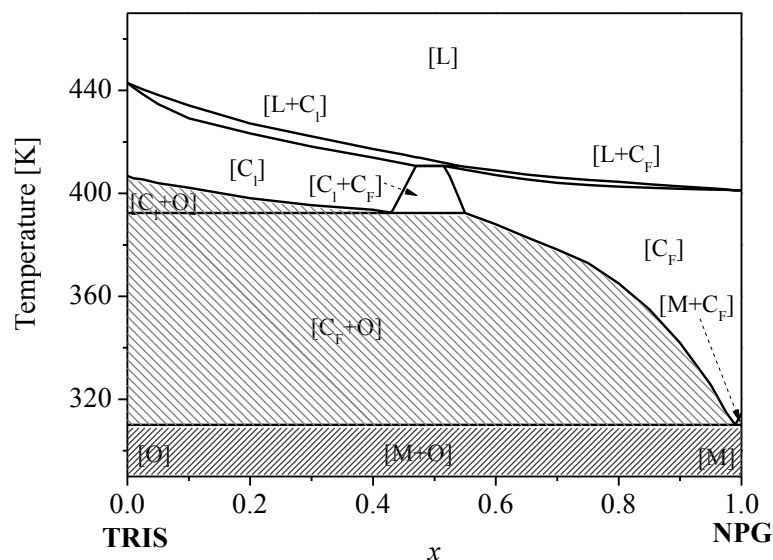


Figure 16: Phase diagram of TRIS - NPG. The regions where a faceted phase is present are shadowed.

The low temperature phases [O] and [M] of the organic compounds are faceted and not miscible. At approximately 310 K, the faceted phase [M] disappears and transforms into the plastic phase [C<sub>F</sub>]. Close to pure NPG ( $0.95 \leq x \leq 1$ ) the phase diagram shows a eutectoid reaction. The dissolution of the faceted phase [O] at low temperatures ( $\leq 392$  K) is very slow and needs up to 60 minutes and more to reach equilibrium [50]. At high temperature the dissolution of the faceted phase [O] is much faster. The amount of the faceted phase [O] decreasing with increasing temperature. The faceted phase of TRIS [O] coexists with the

NPG-rich plastic phase  $[C_F]$  up to  $T = 392$  K and  $0 \leq x \leq 0.56$ . The plastic phase  $[C_F]$  is stable up to the melting point between  $0.54 \leq x \leq 1$ . At temperatures higher than 392 K, the plastic phase  $[C_F]$  transforms to the new plastic phase  $[C_I]$  within  $0 \leq x \leq 0.43$  which is stable up to the melting point. Whereby, the faceted phase  $[O]$  disappears above 410 K. Between  $0.43 \leq x \leq 0.56$  and above 392 K both plastic phases  $[C_I]$  and  $[C_F]$  coexist and form a peritectic plateau at  $T_p = 410$  K and  $0.47 \leq x \leq 0.54$ .

The reported phase diagram was constructed from DSC measurements [50] and the evaluation of the lattice parameters is based on x-ray diffractometry [50]. Figure 17 shows the peritectic region of the TRIS - NPG phase diagram in detail.

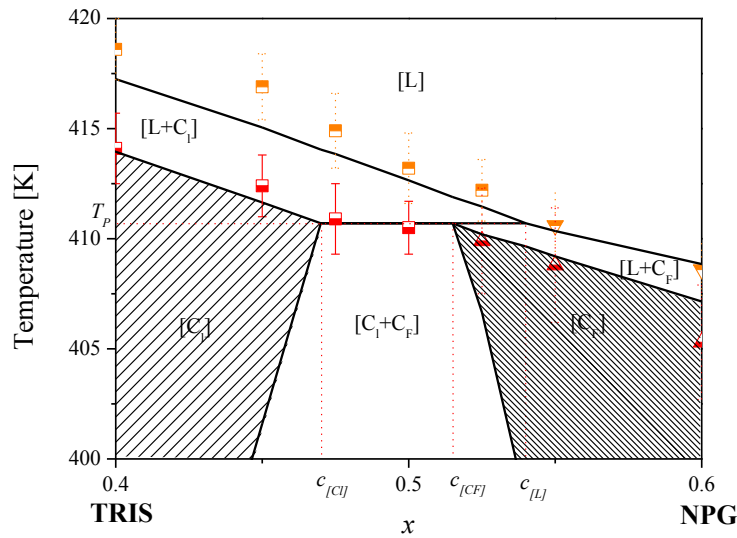


Figure 17: Peritectic region of the system TRIS - NPG. The squares show the liquidus (orange), the solidus (red) temperature and the peritectic temperature  $T_p$  for the TRIS-rich side published by [50]. The triangles show the corresponding situation for the NPG-rich side. The black lines are used to approach the phase diagram by smooth bended lines and to calculate the distribution coefficient  $k$  and the liquidus slope  $m$ .

The published differences between the solidus temperature and the liquidus temperature are small and the error bands of both temperatures partly overlap [50]. For calculations the solidus- and liquidus line have to be approached by smooth bended lines. The calculated values of the entire phase diagram are given in chapter 4.1 for the distribution coefficient  $k$  (Table 4), the liquidus slope  $m$  (Table 5) and the solidus- and liquidus temperature  $T$  (Table 2). The red and orange symbols with error bars (Figure 17) are measurements published in

[50] and the black lines are the interpolation based on the measurements. Based on the phase diagram with smooth banded lines, the solute distribution coefficient  $k$  and the liquidus slope  $m_L$  at the peritectic temperature  $T_P$  are  $k_{[CF]} = 0.97 \pm 0.01$  and  $m_{[CF]} = -31.0 \pm 0.1$  K/mol.%, and also  $k_{[CI]} = 0.86 \pm 0.01$  and  $m_{L[CI]} = -47.9 \pm 1.4$  K/mol.%. The concentrations of the peritectic plateau  $C_{[CI]}$ ,  $C_{[CF]}$ , and  $C_{[L]}$  and the peritectic temperature are given in Table 1.

Table 1: Characterization of the peritectic plateau [50].

<b>Peritectic plateau of the phase diagram TRIS - NPG</b>			
	concentration		temperature
	$C_0$	$x$	$T_p$
	%	mol fraction	K
$C_{[L]}$	54	0.54	$410.7 \pm 2.0$ K
$C_{[CF]}$	51.5	0.515	$410.7 \pm 2.0$ K
$C_{[CI]}$	47	0.47	$410.7 \pm 2.0$ K

### 3 Experimental Methods

#### 3.1 Sample Preparation

The two compounds TRIS and NPG had to be handled in an inert protection atmosphere. Consequently, the entire preparation was performed within a glove box, consisting of a main chamber with a removable side wall, two valves for pumping, an argon inlet, and a gate to a smaller cylindrical flood chamber (Figure 18). The flood chamber itself had two valves for flooding and pumping. The glove box was filled with Argon 5.6. In order to reduce the humidity an open container with silica gel was used in order to keep the water humidity below  $10^4$  ppm. Several cycles of short evacuation and slow flooding with Argon 5.6 were performed to reduce the oxygen content from 21 vol.% to a value below  $2 \cdot 10^3$  ppm. Both values were estimated with a hygrometer. These conditions are kept within the glove box for all further operations. Experiments outside of the glove box are especially mentioned in the corresponding chapters.



*A* side wall

*B* hygrometer

*C* main chamber

*D* gloves

*E* silica gel

*F* flood chamber

Figure 18: Glove box and equipment used for the sample preparation of TRIS - NPG alloys.

### 3.1.1 Alloy Preparation

For the same temperature and atmospheric pressure the vapor pressure of NPG and TRIS is quite different (appendix A.6). Thus, NPG starts to sublime where TRIS does not. Therefore, alloy preparation in an open container would lead to a permanent shift in concentration. As a consequence, it is necessary to prepare the alloys in a small, closed container (diameter 1 cm, height 5 cm) where it is not possible to lose material by evaporation. The whole alloy preparation was performed within a glove box, except the heating and cooling procedure which took place outside the glove box. The accuracy of concentration of each alloy was checked by DSC measurements.

For the preparation of the different initial alloy compositions, the pure compounds are weighted (3g) and joined in a small cylindrical glass container closed with a plastic cap (see Figure 19).

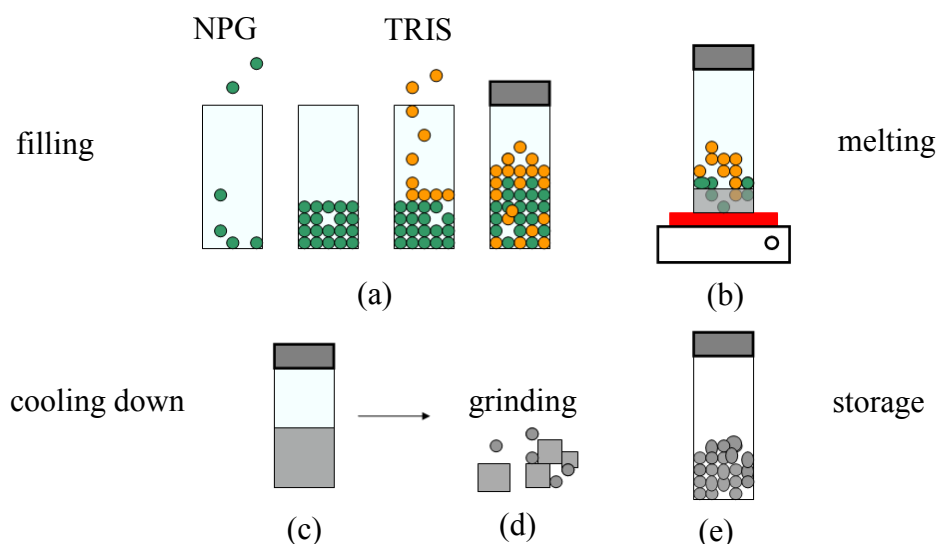


Figure 19: The sketch shows the different steps of the alloy preparation. (a) Total filling of the empty glass container with NPG and TRIS. (b) Melting of both organic compounds close to the expected melting temperature. (c) Cooling down and detach from the glass container. (d) Cut and grinding. (e) Finally, storing for future use.

Since NPG has a lower melting point than TRIS, NPG was filled into the container first. This sequence of filling hindered NPG from sublimating before TRIS becomes liquid. The glass container was heated outside the glove box on a hot plate and as a consequence NPG melts and TRIS goes partly in solution. Now, the altitude of the liquid alloy was approximately



1 cm and solid parts of TRIS swam on the liquid surface. Impurities with a boiling temperature below the melting temperature of NPG were evaporated during melting and solidified on the cap of the glass container. Then the sample was removed from the heater and carefully slowly shaken to improve mixing till the last solid part of TRIS was entirely molten. Subsequently, the solidification started and the sample was slowly cooled down (~ 1 hour). Finally, the material formed a compact cylindrical alloy within the glass container. The glass container was crushed in the glove box and a fine thin layer at the top of the cylindrical alloy was removed. This was done to remove possible impurities from the former liquid surface. Finally the alloy was ground and filled into a new storage container at atmospheric pressure.

### **3.1.2 Sample Geometry**

Due to the relatively high temperature of the hot zone, 453 K, which is needed to investigate the solid/liquid interface, all self-produced samples sealed with UV hardening glues and silica-based glues started leaking after some hours of investigation in the Bridgman-furnace. Only industrial produced long capillary tubes with glued ends outside of the micro Bridgman furnace stayed sealed. Samples with an extra-large ratio rectangle tube ( $100 \times 1800 \mu\text{m}^2$  inner diameter and 100  $\mu\text{m}$  wall thickness [67]) are used to ensure an optimum of observation area and a minimum of convection. The sample itself has a length of more than 20 cm and so 10 cm observation length can be used. For simultaneous investigations of samples with different or equal concentrations square capillary tubes of  $0.4 \times 0.4 \text{ mm}^2$  with a wall thickness of 0.1 mm were used.

### **3.1.3 Sample Filling**

The sample preparation is performed within a glove box filled with Argon as shown in Figure 18. For the sample filling one end of the glass tube is fixed with a UV hardening glue on a flat glass plate (60 x 40 x 1 mm). A closed border of glue on the glass plate around the open end of the tube serves as reservoir for filling as shown in Figure 20. The glass sample is laid on a hot plate so that the side with the reservoir is heated and the open side freely protrudes the heated plate. As soon as small amounts of the alloy grains within the reservoir melt the liquid is dragged into the tube by capillary forces until it reaches the colder end of the tube where it solidifies. Next, the capillary is slowly dragged off the hot plate and the material solidifies directionally whereby it shrinks. Consequently, a small part at the end of the sample is unfilled. The tube is now removed from the glass plate and finally the unfilled ends of the tube are sealed by gluing. During the investigation in the Bridgman-furnace, both ends of the capillary tubes extended the hot zone of the furnace and are thus kept close to room

temperature. Hence, the solid alloy seals further both ends of the capillary tube and additionally protects the liquid alloy from any contact with ambient air. After filling, one end of the tube is glued again on a  $2 \times 2 \text{ cm}^2$  glass plate which serves as handhold. Finally, the filled and sealed sample is transferred out of the glove box.

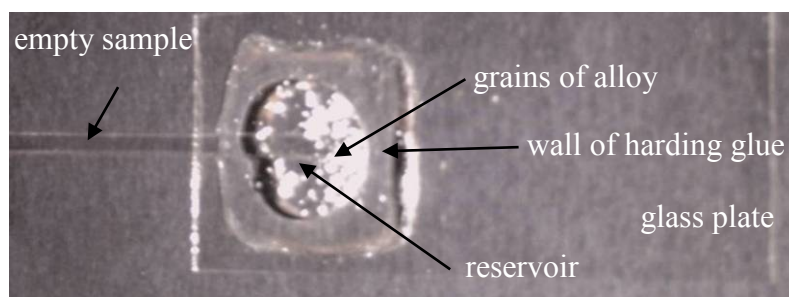


Figure 20: Glass plate with glued sample, reservoir and grains of the alloy.

### 3.2 Differential Scanning Calorimetry (DSC)

For the different scanning Calorimetry (DSC) measurements, 5 mg of each alloy was filled into small Al pans that were hermetically sealed within the glove box. Next, these DSC samples were investigated using a Perkin-Elmer Diamond DSC instrument equipped with Pyris7 Software and calibrated with In and Zn [68]. A similar instrument had been used by Barrio et al. [50]. The Perkin-Elmer Diamond DSC instrument is a power compensation DSC. The measuring system consists of two equal micro furnaces. Both furnaces contain a temperature sensor and a heating resistor (Figure 21).

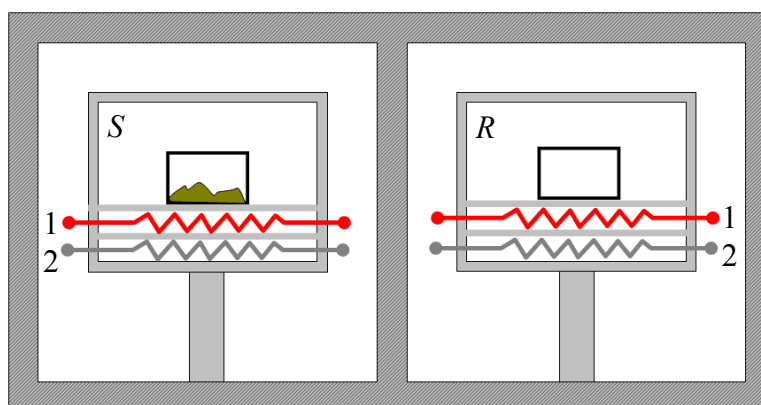


Figure 21: Power compensation DSC [68]. Set-up of the measuring system. *S*: sample measuring system with sample, micro-furnace. *R*: reference sample system. 1: heating wire, 2: resistance thermometer. Both systems are in a surrounding block at constant temperature.

In one furnace, there is an Al pan with the sample while in the second one there is an empty Al pan as a reference. During heating-up the same heating power is applied to both micro furnaces. If a reaction occurs in one of the pans a slight temperature change occurs only in the sample furnace. Now, the DSC regulation starts to compensate this difference by heating or cooling. This effect is visible as a peak in the heat flux plot (DSC curve, see Figure 29 on page 43). The used scanning rate was the same as reported in Ref. [50], i.e. 2 K/min. In the follow interpretation of the DSC curves will be performed according to the procedure described in Ref. [68, 69].

### 3.3 Bridgman Components

The solidification experiments performed within this study were performed in a horizontal Bridgman-furnace, fixed on the stage of a ZEISS microscope. The furnace consists of a heating and a cooling zone departed by a small adiabatic zone. The hot parts of the Bridgman-furnace are controlled by electrical resistant heaters where the cold part is cooled by circulating water. A device controls the linear movement of the sample(s) through the furnace. For the optical investigations, the microscope is connected to a self-developed recording system, called **Dynamic Imaging of Solidification (DIOs)**. During solidification, this system records images simultaneously with relevant temperatures from the furnace. Figure 22 shows the experimental set-up as used.

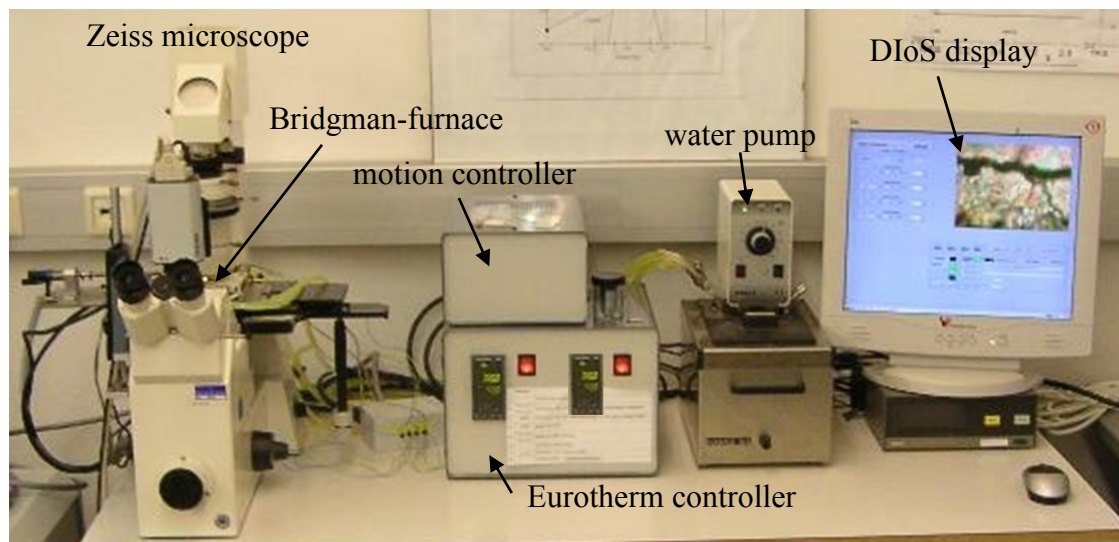


Figure 22: Experimental set up.

### 3.3.1 Micro Bridgman-furnace set up

The horizontal micro Bridgman-furnace is constructed to study directional solidification of transparent alloys in rectangle or square sample tubes with an observation length of  $3.6 \pm 0.1\text{mm}$ .

The movement of the capillary tubes through the furnace is PC-controlled using a FAULHABER DC stepper motor [70] connected to a drive spindle which allows withdrawal velocities between 0.01 and 115  $\mu\text{m/s}$ . The spindle moves a sledge on which the sample is fixed. For an experiment a total sample length of 40 mm can be pulled through the adiabatic gap. Movements in pulling directions are given in the text as a positive value and movements in the opposite direction as a negative one.

The main parts of the furnace consist of two ceramic plates, each covering a fixed cold and hot brass block, as shown in Figure 23.

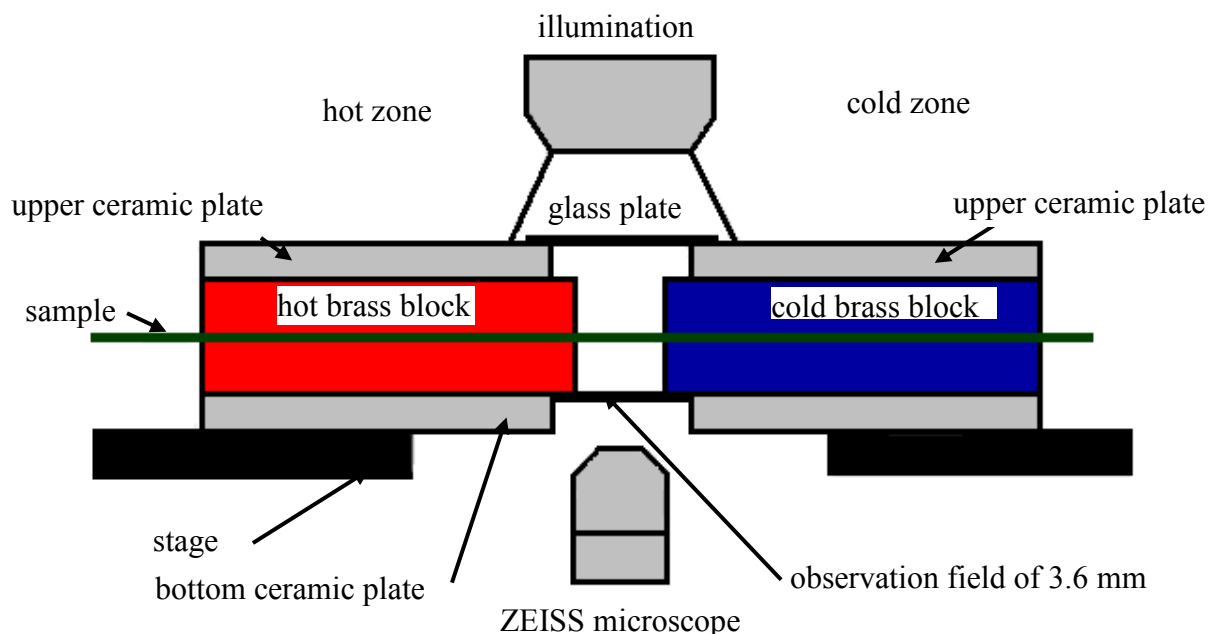


Figure 23: Sketch of the directional solidification apparatus (Bridgman-furnace) used for the optical investigation of the organic peritectic alloys.

The ceramic plates act in two ways, firstly as thermal isolation, and secondly as a frame to hold the hot and cold brass blocks. One hot and one cold brass block with a distance of 3.6 mm are permanently mounted within ceramic plates. The bottom plate is permanently

connected with the stage of the microscope. The ceramic plate is fixed to the stage only at four points to reduce the heat conductivity to the microscope. The top plate is placed plane on top of the bottom plate with a simple plug system. This design allowed a quick change of samples in the preheated furnace. The hot blocks can be heated up to a maximum temperature of 523 K using an electric resistant heater. The cold blocks are cooled by a water circuit. Therefore, the temperature range is limited by the freezing and boiling temperature of water. The temperatures of the hot zone were measured with Pt-100 temperature sensors placed inside each brass block and regulated independently by a EUROTHERM 2408 controller [71] with an accuracy of  $\pm 0.1$  °C. The temperature of the cold zone was measured with a Pt-100 temperature sensor placed between the brass blocks and regulated by a water cooling system with an accuracy of  $\pm 0.5$  °C measured within the water tank of the pump. A slot of  $0.4 \times 2$  mm<sup>2</sup> is milled in the hot and cold brass block of the bottom ceramic plate to host the samples. The width of the slot allows the investigation of a rectangular glass capillary  $0.3 \times 2$  mm<sup>2</sup> ( $0.1 \times 1.8$  mm<sup>2</sup> with 100  $\mu$ m wall thickness) or simultaneous investigation of up to five square capillaries of  $0.4 \times 0.4$  mm<sup>2</sup> ( $0.2 \times 0.2$  mm<sup>2</sup> with 100  $\mu$ m wall thickness). Additionally, two parallel slots are at the bottom part of the brass blocks. During the experiments, two short filled glass samples ( $0.4 \times 0.4$  mm<sup>2</sup>) with pure NPG and pure TRIS laid unmoved in the additional slots because the phase transition boundaries, solid/liquid for NPG and solid/solid for TRIS, were used to check the stability of the temperature gradient (see chapter A.8). Figure 24 gives detailed information about the construction.

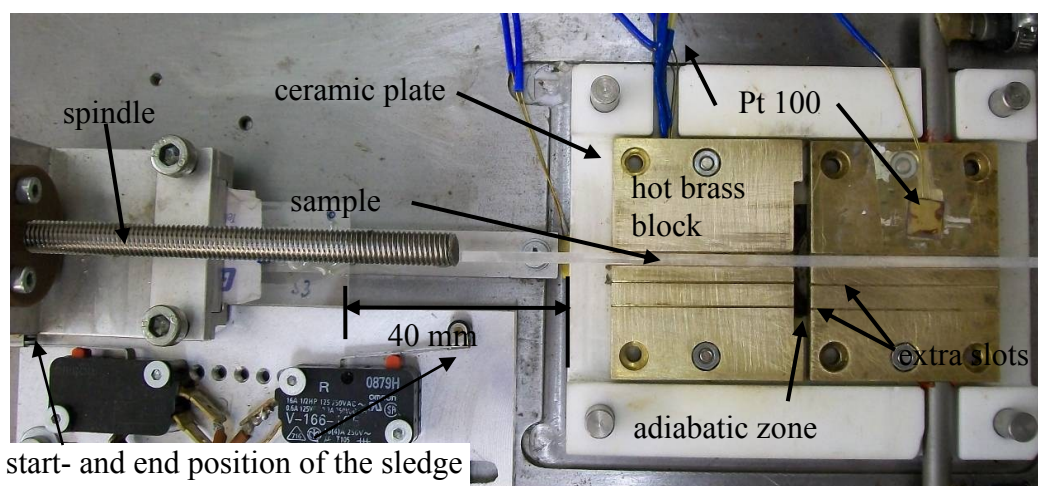


Figure 24: Picture of the bottom ceramic plate, the hot and cold brass blocks, a filled rectangular glass sample, and the pulling system.

The size of the glass sample hinders the usage of micro temperature sensors to estimate the temperature gradient within the adiabatic zone. With additional spacers on the hot and cold brass block, the furnace is also suitable for a  $0.8 \times 3.5 \text{ mm}^2$  rectangular tube. The larger sample shape enables the application of temperature sensor.

### 3.3.2 Optical Observation System “DIOs”

The ZEISS microscope was equipped with a CCD camera and two crossable polarization filters. The filters are used to distinguish between the optical active and inactive solid phases as described in Figure 14. Without the usage of the filters all phases are visible but with two  $90^\circ$  crossed filters only the optically active phases can be seen. A self-developed software records and stores images and the corresponding temperature data with a frame rate of up to 10 images per second. In the gap (3.6 mm) between the hot and the cold brass blocks the samples were illuminated from the bottom and observed from the top with the used ZEISS microscope. The construction of the Bridgman-furnace enables a large Field of View (FOV) of  $3180 \times 2760 \mu\text{m}^2$ , for a better overview, or a small FOV of  $636 \times 552 \mu\text{m}^2$ , for more details. Figure 25 shows the visual difference between the two FOV. In Figure 25a, the formation of a band over the entire solid/liquid interface is visible. The picture gives a good overview of the solidification morphology of the solid/liquid interface. The rectangular field in Figure 25a marked with black broken lines the size and position of Figure 25b. Figure 25b shows more details of the solidification morphology at the solid/liquid interface.

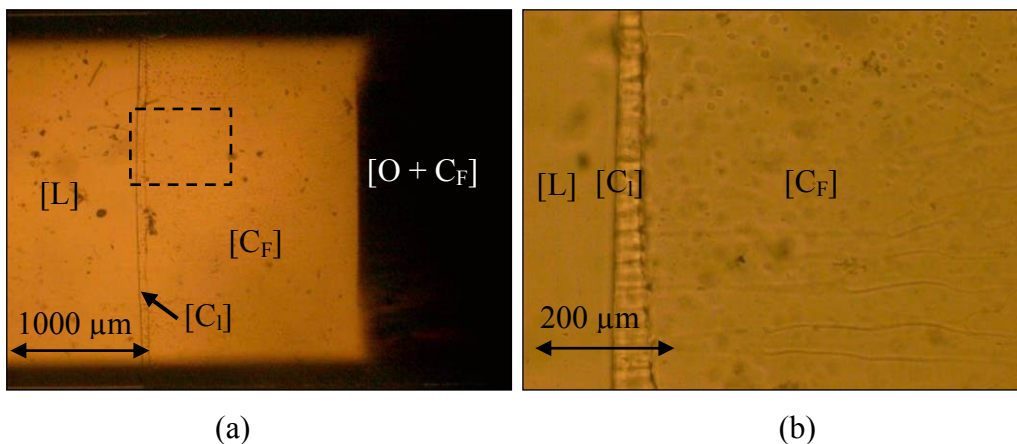


Figure 25: Comparison of the Field of View (FOV) with (a)  $3180 \times 2760 \mu\text{m}^2$  and the (b) FOV with  $636 \times 552 \mu\text{m}^2$ . The black frame in (a) shows the size and position of the picture displayed in (b). Note that the time of recording of both pictures is different.

In this work, pictures with the larger field of view are aligned to thick red (hot) and blue (cold) lines for the indication of the position of the corresponding copper blocks of the Bridgman-furnace. The small construction of the adiabatic gap limits the optical magnification.

A measurement facility was developed to enable the recording of digital images and the corresponding temperatures. The DIoS system was assembled by the Institute for Automation at the University of Leoben [72]. It is equipped with 4 PT-100 temperature resistances, a 1/2” Pulnix TMC-6700 digital camera. The camera itself has a resolution of 648 x 484 pixels and the software was programmed in MATLAB [72]. Figure 26 shows the display of the recording system. On the right side, the area of observation (FOV) and on the left side, the reading of up to 4 Pt-100 temperature sensors can be displayed and triggers can be set. It is possible to trigger the recording of images and temperatures via a start or end temperature.

recording of the temperature in the hot and cold zone of the cooper block

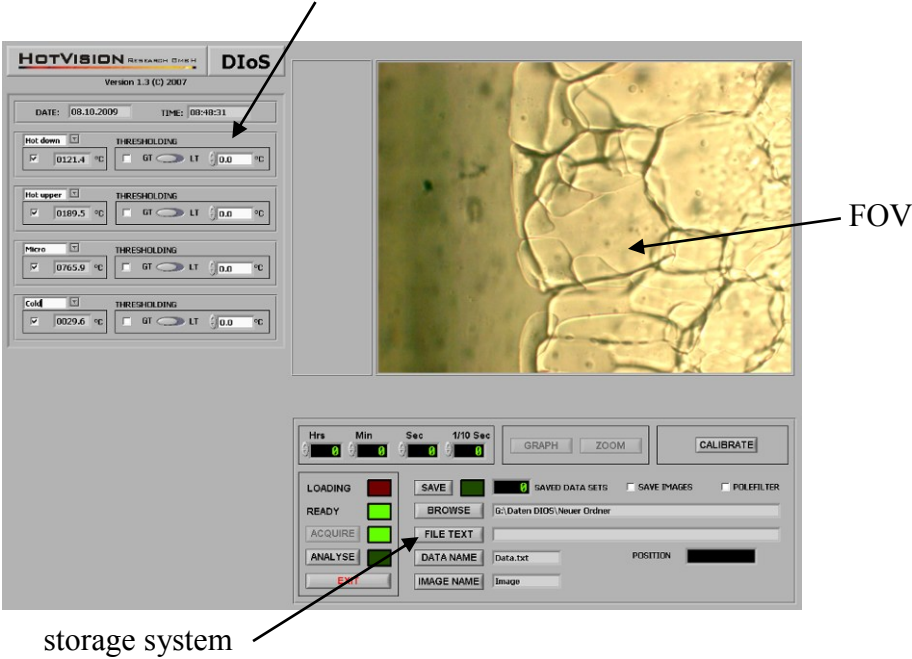


Figure 26: Display of the DIoS system and the field of view (FOV) of the microscope.

Below the image display the timescale of the recordings can be chosen from images taken every tenth of a second up to hours. The software stores up to 3000 pictures per run. Furthermore the software allows the setting of measurement positions in the field of view, which in combination with the fixed temperature gradient, can be used to estimate the temperature on a certain position.

## 4 Stability and Reproducibility of the NPG – TRIS System

NPG was already investigated in several *in-situ* experiments and has been used for years without any problems. TRIS is known to be a buffer agent but in literature up to now nothing has been reported about its application for *in-situ* observation experiments. The present thesis is based on studies which was performed in order to define process conditions for *in-situ* observations of peritectic solidification morphologies in a micro Bridgman-furnace for the system TRIS - NPG. The qualities of organic substances differ between several production charges. Therefore, experiments were done to compare published values. The appendix includes the effect of different material purification and the colorization of the phases for better visual observations, the determination of the boiling point, the Raman spectra, the heat conductivity, the vapor pressure, the viscosity, and the diffusion coefficient in the liquid.

This section contains the collection of all available material safety data sheets (MSDS) of the pure compounds, details of the phase diagram TRIS – NPG, the stability and reproducibility of the NPG – TRIS alloys, possible operation conditions and the selected experimental procedure.

### 4.1 Phase Diagram of TRIS – NPG

The published phase transition temperatures at selected concentrations from Barrio et al. [50] include error bars which are not shown in the diagrams in the presented study. For simplification, the published phase diagram [50] was changed from NPG – TRIS (Figure 15 on page 21) to TRIS – NPG (Figure 16 on page 24). Furthermore the published solidus and liquidus temperatures intervals were connected by smoother lines. From these lines the average solidus and liquidus temperatures (Table 2), also the distribution coefficient  $k_\alpha$  and  $k_\beta$  (Figure 27, Table 4) and the liquidus and solidus slopes  $m_l^\alpha$ ,  $m_s^\alpha$ ,  $m_l^\beta$  and  $m_s^\beta$  (Figure 28, Table 5) were calculated. Table 6 shows the estimated values of the diffusion coefficient  $D_L$  in the liquid from chapter A.9 and the calculated critical velocity  $V_c$ .



Table 2: Liquidus temperature, solidus temperature and  $\Delta T$  estimated by smoothing of information of the phase diagram published in [50]. Values in bracket show metastable extensions.

$x$	liquidus temperature	solidus temperature	$\Delta T$	liquidus temperature	solidus temperature	$\Delta T$
	phase [ $C_F$ ]	phase [ $C_F$ ]		phase [ $C_I$ ]	phase [ $C_I$ ]	
mol fraction	K	K	K	K	K	K
0.000				442.95	442.95	0.00
0.010				441.85	441.05	0.80
0.025				440.45	438.55	1.90
0.050				438.25	434.65	3.60
0.100				434.15	429.15	5.00
0.200				427.15	423.35	3.80
0.300				422.20	418.15	4.05
0.400				417.25	413.95	3.30
0.450				415.05	411.65	3.40
0.470				414.05	410.70	3.35
0.475				413.85	(410.50)	(3.35)
0.500	(411.80)	(411.40)	(0.40)	412.65	(409.50)	(3.35)
0.515	(411.40)	(410.70)	(0.70)	411.89	(408.80)	(3.35)
0.525	(410.90)	(410.20)	(0.70)	411.46	(408.40)	(3.35)
0.540	410.7	409.65	1.05	410.70	(407.70)	(3.35)
0.550	410.35	409.2	1.15			
0.600	408.85	407.15	1.70			
0.650	407.35	405.4	1.95			
0.700	406.2	404.05	2.15			
0.750	405.25	403.25	2.00			
0.800	404.45	402.65	1.80			
0.850	403.55	402.25	1.30			
0.900	402.75	401.8	0.95			
0.950	401.95	401.35	0.60			
0.975	401.55	401.25	0.30			
0.990	401.15	401.15	0.00			
1.000	401.15	401.15	0.00			

Table 3: Liquidus temperature, solidus temperature and  $\Delta T$  estimated by own DSC measurement.

$x$	liquidus temperature	solidus temperature	$\Delta T$	$x$	liquidus temperature	solidus temperature	$\Delta T$
	phase [ $C_I$ ]	phase [ $C_I$ ]			phase [ $C_F$ ]	phase [ $C_F$ ]	
mol fraction	K	K	K	mol fraction	K	K	K
0.000		441.6		0.6	410.9	406.2	4.7
0.100	434.9	429.1	5.8	0.7	408.6	404.1	4.5
0.200	428.2	421.6	6.6	0.75	407.3	403.1	4.2
0.300	423.6	418.6	5	0.8	406.3	402.1	4.2
0.400	419	414.1	4.9	0.85	405	401.6	3.4
0.450	416.4	409.1	7.3	0.9	403.7	400.1	3.6
0.470	415.3	409.1	6.2	0.95	403.7	401.1	2.6
0.460	415.6	411.6	4	1		400.9	
0.500	412.5	408.6	3.9				
0.520	412.8	409.6	3.2				

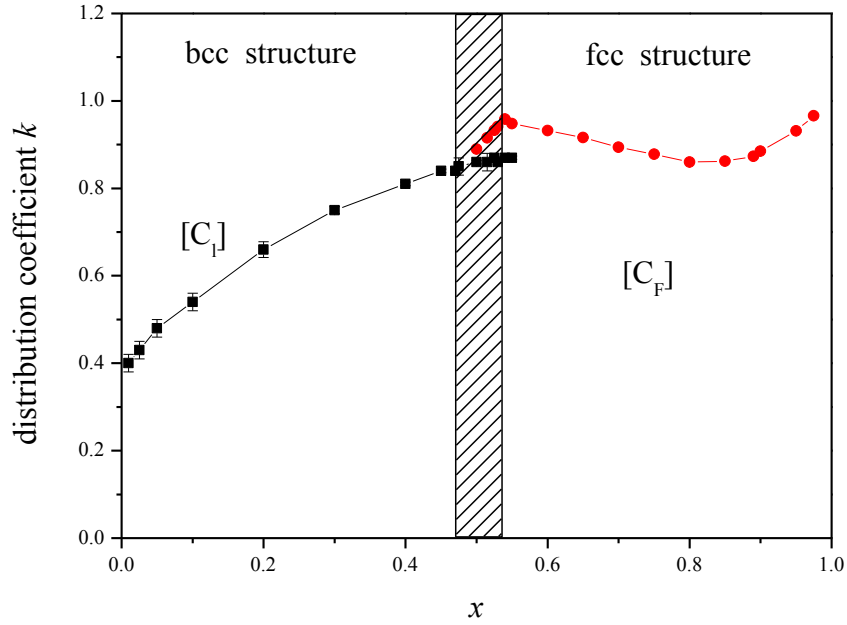


Figure 27: Calculated solute distribution coefficient  $k_i$  of the phase diagram TRIS - NPG depending on the mol fraction  $x$ .

Table 4: Calculated values of the solute distribution coefficient  $k_i$  of the phase diagram TRIS - NPG as shown in Figure 27. Values in bracket show metastable extensions.

bcc structure (TRIS rich)			fcc structure (NPG rich)		
$x$	$k_L$	$\pm$	$x$	$k_L$	$\pm$
mol fraction			mol fraction		
0.010	0.40	$2.0 \cdot 10^{-02}$	0.500	(0.89)	$1.0 \cdot 10^{-02}$
0.025	0.43	$2.0 \cdot 10^{-02}$	0.540	0.96	$1.0 \cdot 10^{-02}$
0.050	0.48	$2.0 \cdot 10^{-02}$	0.550	0.95	$1.0 \cdot 10^{-02}$
0.100	0.54	$2.0 \cdot 10^{-02}$	0.600	0.93	$1.0 \cdot 10^{-02}$
0.200	0.66	$2.0 \cdot 10^{-02}$	0.650	0.92	$1.0 \cdot 10^{-02}$
0.300	0.75	$1.0 \cdot 10^{-02}$	0.700	0.89	$1.0 \cdot 10^{-02}$
0.400	0.81	$1.0 \cdot 10^{-02}$	0.750	0.88	$1.0 \cdot 10^{-02}$
0.450	0.84	$1.0 \cdot 10^{-02}$	0.800	0.86	$1.0 \cdot 10^{-02}$
0.470	0.84	$1.0 \cdot 10^{-02}$	0.850	0.86	$1.0 \cdot 10^{-02}$
0.475	0.85	$2.0 \cdot 10^{-02}$	0.890	0.87	$1.0 \cdot 10^{-02}$
0.500	0.86	$1.0 \cdot 10^{-02}$	0.900	0.89	$1.0 \cdot 10^{-02}$
0.515	0.86	$2.0 \cdot 10^{-02}$	0.950	0.93	$1.0 \cdot 10^{-02}$
0.525	0.87	$1.0 \cdot 10^{-02}$	0.975	0.97	$1.0 \cdot 10^{-02}$
0.530	0.86	$1.0 \cdot 10^{-02}$			
0.540	0.87	$1.0 \cdot 10^{-02}$			

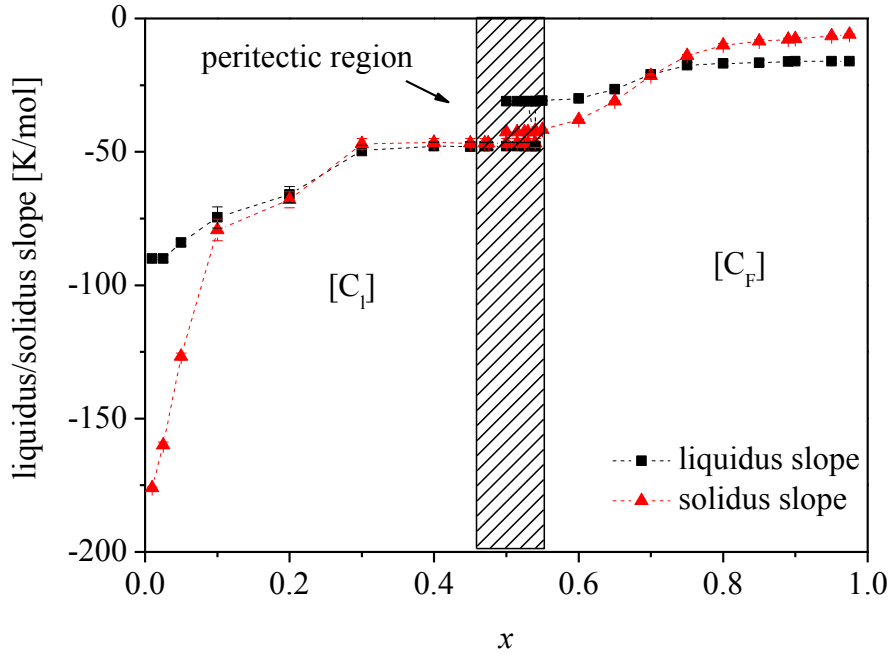


Figure 28: Liquidus and solidus slope  $m_i$  of the phase diagram TRIS - NPG depending on the mole fraction.

Table 5: Data of the liquidus and solidus slopes  $m$  of the phase diagram TRIS - NPG. Values in bracket show metastable extensions.

bcc structure (TRIS rich)					fcc structure (NPG rich)				
$x$	$m_l$	$\pm$	$m_s$	$\pm$	$x$	$m_l$	$\pm$	$m_s$	$\pm$
K/mol					K/mol				
0.010	-90.0	0.4	-176.0	0.4	0.500	(-31.0)	(0.1)	(-42.6)	(0.1)
0.025	-90.0	1.3	-160.0	1.2	0.525	(-31.0)	(0.1)	(-42.6)	(0.1)
0.050	-84.0	1.3	-126.7	1.3	0.530	(-31.0)	(0.1)	(-42.6)	(0.1)
0.100	-74.6	4.0	-79.3	4.0	0.540	-31.0	0.1	-42.0	0.1
0.200	-66.0	3.0	-68.0	3.0	0.550	-30.8	0.1	-41.7	0.1
0.300	-49.5	2.0	-47.0	2.0	0.600	-30.0	0.2	-38.0	0.1
0.400	-47.9	1.5	-46.5	1.5	0.650	-26.5	0.3	-31.0	0.2
0.450	-48.0	1.8	-46.7	1.7	0.700	-21.0	0.9	-21.5	0.4
0.470	-47.9	1.4	(-46.7)	(1.7)	0.750	-17.5	1.0	-14.0	0.5
0.475	-47.9	1.4	(-46.7)	(1.7)	0.800	-16.9	1.0	-10.0	0.6
0.500	-47.9	1.4	(-46.7)	(1.7)	0.850	-16.6	1.0	-8.5	0.5
0.515	-47.9	1.4	(-46.7)	(1.7)	0.890	-16.1	0.1	-7.8	0.4
0.525	-47.9	1.4	(-46.7)	(1.7)	0.900	-16.0	0.7	-7.6	0.4
0.530	-47.9	1.4	(-46.7)	(1.7)	0.950	-16.0	0.7	-6.6	0.2
0.540	-47.9	1.4	(-46.7)	(1.7)	0.975	-16.0	0.6	-6.0	0.2

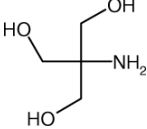
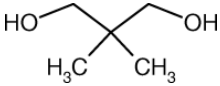
Table 6: Corresponding to Eq.6 in chapter 2.1 the estimated values of the critical velocity  $V_c$  of the binary phase diagram TRIS - NPG. Values in bracket show interpolated values.

$x$ mol fraction	phase [C <sub>I</sub> ] (TRIS rich)			phase [C <sub>F</sub> ] (NPG rich)		
	$D_L$	$G/V$	$V_c$	$D_L$	$G/V$	$V_c$
NPG	m <sup>2</sup> /s	s·K/m <sup>2</sup>	μm/s	m <sup>2</sup> /s	s·K/m <sup>2</sup>	μm/s
0.050	4.0·10 <sup>-11</sup>	9.0·10 <sup>-11</sup>	0.16			
0.100	3.4·10 <sup>-11</sup>	1.5·10 <sup>-11</sup>	0.10			
0.200	3.8·10 <sup>-11</sup>	1.0·10 <sup>-11</sup>	0.15			
0.300	3.0·10 <sup>-11</sup>	1.3·10 <sup>-11</sup>	0.11			
0.400	3.2·10 <sup>-11</sup>	1.0·10 <sup>-11</sup>	0.14			
0.450	2.8·10 <sup>-11</sup>	1.2·10 <sup>-11</sup>	0.12			
0.470	2.9·10 <sup>-11</sup>	1.2·10 <sup>-11</sup>	0.13			
0.475	(2.8·10 <sup>-11</sup> )	1.2·10 <sup>-11</sup>	0.12			
0.500	2.0·10 <sup>-11</sup>	1.7·10 <sup>-11</sup>	0.09	2.0·10 <sup>-11</sup>	2.0·10 <sup>-10</sup>	0.73
0.515	(1.7·10 <sup>-11</sup> )	1.9·10 <sup>-11</sup>	0.08	1.7·10 <sup>-11</sup>	(4.1·10 <sup>-10</sup> )	0.35
0.525	1.6·10 <sup>-11</sup>	2.1·10 <sup>-11</sup>	0.07	1.6·10 <sup>-11</sup>	(4.3·10 <sup>-10</sup> )	0.33
0.540	(1.3·10 <sup>-11</sup> )	2.6·10 <sup>-11</sup>	0.06	1.3·10 <sup>-11</sup>	8.0·10 <sup>-10</sup>	0.18
0.550				1.3·10 <sup>-11</sup>	(8.7·10 <sup>-10</sup> )	0.17
0.600				1.4·10 <sup>-11</sup>	1.2·10 <sup>-11</sup>	0.12
0.650				2.0·10 <sup>-11</sup>	(9.7·10 <sup>-10</sup> )	0.15
0.700				2.6·10 <sup>-11</sup>	8.3·10 <sup>-10</sup>	0.18
0.750				2.8·10 <sup>-11</sup>	(7.1·10 <sup>-10</sup> )	0.20
0.800				3.0·10 <sup>-11</sup>	6.0·10 <sup>-10</sup>	0.24
0.850				3.4·10 <sup>-11</sup>	(3.8·10 <sup>-10</sup> )	0.38
0.900				4.4·10 <sup>-11</sup>	(2.1·10 <sup>-10</sup> )	0.68

## 4.2 Available Physical and Chemical Properties of TRIS and NPG

Table 7 shows published chemical and physical properties of the organic compounds TRIS and NPG. Some data are only available online [49, 65] whereby other information are based on direct contact with the producing company.

Table 7: Published chemical and physical properties of TRIS - NPG.

	TRIS	NPG
Formula [49]	$\text{H}_2\text{NC}(\text{CH}_2\text{OH})_3$	$(\text{CH}_3)_2\text{C}(\text{CH}_2\text{OH})_2$
Formula, summed up [49]	$\text{C}_4\text{H}_{11}\text{NO}_3$	$\text{C}_5\text{H}_{12}\text{O}_2$
CAS-Nr. [49]	77-86-1	126-30-7
Structure [49]		
Sigma Aldrich Prod. Nr. [49]	T1503	53.825-6
Purity as delivered [49]	99.9+ %	99 %
Density at room temperature [49]	1.353 g/cm <sup>3</sup>	0.980 g/cm <sup>3</sup>
Molar mass [62]	121.14 g/mol	104.15 g/mol
$T_m$ (as delivered) [49]	445 - 446 K	398 - 403 K
Low temperature phase [57]	Orthorhombic [O]	Monoclinic [M]
Lattice constants [57]	$a = 8.853 \text{ \AA}$ $b = 7.804 \text{ \AA}$ $c = 8.800 \text{ \AA}$	$a = 6.019 \text{ \AA}$ $b = 10.881 \text{ \AA}$ $c = 10.132 \text{ \AA}$ $\beta = 100.160 \text{ \AA}$
$T_{SST}$ (s.-s. transition) [57]	$406.8 \pm 1.0 \text{ K}$	$314.6 \pm 1.0 \text{ K}$
$\Delta H_{SST}$ [57]	$34.0 \pm 1.7 \text{ kJ/mol}$	$12.8 \pm 0.6 \text{ kJ/mol}$
$\Delta S_{SST}$ [63]	$83.7 \text{ J/mol}\cdot\text{K}$	$40.6 \text{ J/mol}\cdot\text{K}$
$\Delta V_{SST}$ [63]	$5.07 \text{ cm}^3/\text{mol}$	$4.86 \text{ cm}^3/\text{mol}$
$\Delta H_{SST}$ [57]	$3.7 \pm 0.2 \text{ kJ/mol}$	$4.4 \pm 0.2 \text{ kJ/mol}$
High temp phase [57]	bcc [C <sub>i</sub> ]	fcc [C <sub>F</sub> ]
Lattice constant [57]	$6.8888 \text{ \AA}$ (at 408 K)	$8.854 \text{ \AA}$ (at 353 K)
$T_m$ (purified) [57]	$442.7 \pm 1.0 \text{ K}$	$401.3 \pm 1.0 \text{ K}$
$\Delta H_m$ [57]	$3.7 \pm 0.2 \text{ kJ/mol}$	$4.4 \pm 0.2 \text{ kJ/mol}$
$\Delta S_m$ [63]	$7.12 \text{ J/mol}\cdot\text{K}$	$10.8 \text{ J/mol}\cdot\text{K}$
$\Delta V_m$ [63]	$6.63 \text{ cm}^3/\text{mol}$	$4.86 \text{ cm}^3/\text{mol}$
$T_b$ (as delivered) [49]	492 - 493 K (at 13 hPa)	481 - 482 K
$\Delta S_f$ [73]	$1.06 \cdot 10^5 \text{ J/K}\cdot\text{m}$	

### **4.3 Investigation on the Organic Material**

This section includes the effect of material purification and experiments to determine the reproducibility of the phase diagram, and thermal stability for long time experiments,

#### **4.3.1 Material Purification**

NPG and TRIS were delivered with a purity of 99 % and 99.9+ %, respectively. Efforts were made to increase the level of purity of both organic substances, see appendix A.1. The organic substance NPG was treated in two ways, by a drying process and by sublimation and deposition. The achieved purity was tested by DSC measurements. The change of the melting temperature was marginal and within the error of the DSC evaluation. Therefore, NPG was purified only by a long time drying process within the glove box, similar to the work described in [50].

TRIS is reported to be a hygroscopic material [61] and the plastic phase of the organic substance TRIS is quite sensitive to impurities [51, 64] and decomposes after several hours. A drying process at 310 K shows no optically visible effect within 24 hours. At a temperature of 373 K, the solid material becomes soft and liquid after 24 hours, whereby the published melting temperature is 445 K [50]. This could be an indicator for the reported thermal instability of TRIS at higher temperature [51, 64, 65]. A purification of TRIS by sublimation and subsequent solid deposition is not possible because TRIS decompose visible by long brown/white faceted organic crystals. Since TRIS as delivered has already a purity of 99.9+ %, TRIS ultra-pure [49] and to avoid decomposition, TRIS was used as delivered without any further purification.

#### **4.3.2 Reproducibility of the Alloy Concentration**

In order to check the reproducibility of the alloy concentration, DSC measurements were performed. Various alloy compositions were prepared in the glove box and stored in glass containers.

The top of Figure 29 shows the original heat flow plot where the peak represents the change in the heat flux curve due to a phase transition (e.g. from a solid to the liquid phase), the curve below shows its first derivative.

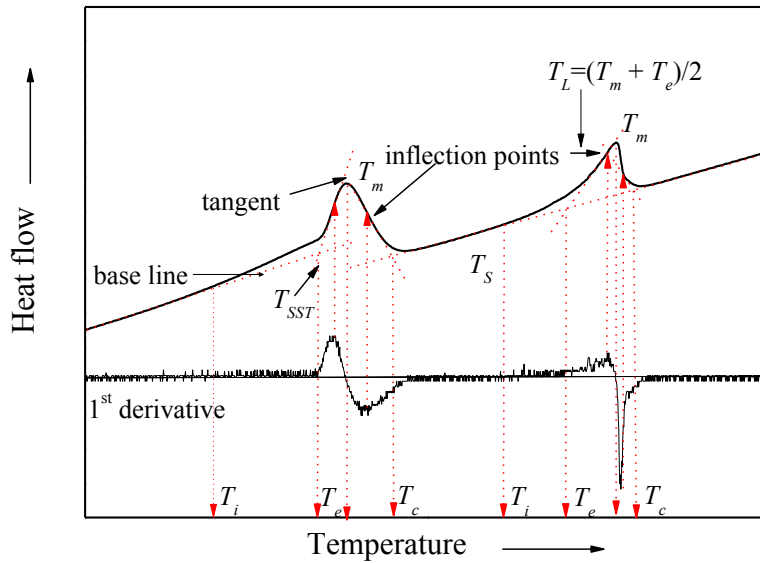


Figure 29: Sketch illustrating how transition temperatures have been extracted from a DSC heating curve,  $T_i$ : Initial peak temperature,  $T_e$ : extrapolated peak onset temperature,  $T_c$ : extrapolated peak completion temperature,  $T_{SST}$ : solid state transformation temperature,  $T_S$ : solidus temperature and  $T_L$ : liquidus temperature.

Without a phase transition (i.e. in the regions before and after the peaks) the heating curve corresponds to the heat absorbed by the corresponding phase. Since the applied heat increases linearly, the corresponding heat flow curves before and after the transitions are resulting in two different baselines, whereby, the difference in the baselines is caused by the different heat capacities of the phases.  $T_i$  defines the beginning of the first melting, the maximum and the minimum of the first derivative give the inflection points of the phase transition peak. The inflection point of the first derivative defines the maximum of the phase transition peak  $T_m$ . The intersection points between the baselines and the corresponding tangents are the points where the phase transition starts ( $T_e$ ) and ends ( $T_c$ ).

Sturz et al. [52] obtained the solid transformation temperature and the melting point for the organic substance TRIS from the extrapolated peak onset temperature  $T_e$ . Due to the relatively small liquidus/solidus separation, the DSC measurements reveal only single peaks for the transition from liquid to solid. Boettinger et al. [69] showed that for small freezing ranges the maximum peak temperature lies above the liquidus temperature with an error increasing as the

freezing interval decreases. Therefore, it can be concluded that the true liquidus temperature lies between the lower temperature onset point and the maximum peak temperature. This is reflected in the error bar for the liquidus temperature (see Figure 31). The solidus temperature was taken at the first deviation from the base line of the DSC curve performed identically in [69]. For a solid state transformation ( $T_{SST}$ ) the first onset point  $T_e$  was taken. Furthermore, the transition curves for the solid/solid transition often show shoulders indicating a superposition of multiple peaks. In these cases the onset of the phase transition was taken from the lowest temperature peak. Due to the overlap of the peaks, the transition temperature of the next peak segment was approximated with a tangent from the top of the shoulder peak segment. Samples taken from the same alloy preparation showed a standard deviation of  $\pm 0.7$  K for the liquidus temperature and  $\pm 1.1$  K for the solidus.

In Figure 30, DSC tracers for the different regions of the peritectic phase diagram are presented. The solid/liquid transition generally showed a clearly distinguishable single peak. Therefore, this transition was the best for a direct comparison with the phase diagram published by Barrio et al. [50].

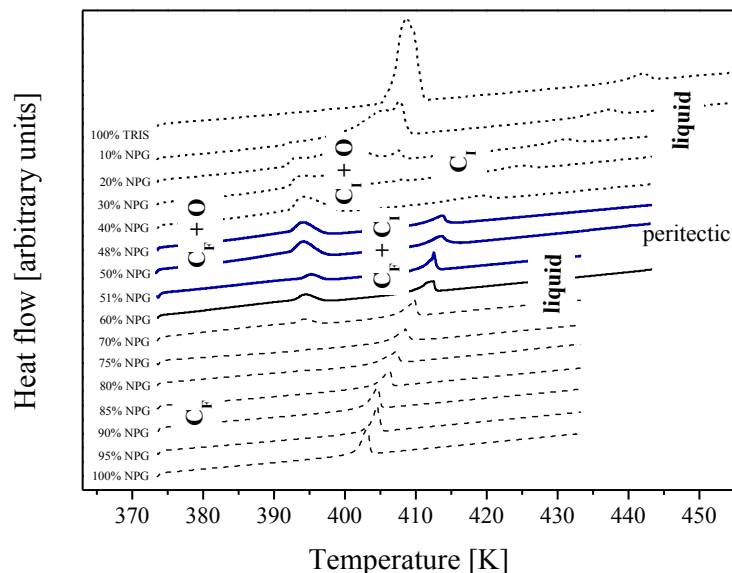


Figure 30: DSC heating curves obtained with various alloy compositions and a heating rate of 2 K/min for the binary phase diagram TRIS – NPG.



Compositions ranging from  $0 \leq x \leq 0.48$  mol fraction NPG showed overlapping peaks for the solid/solid transition and a clearly detached solid-liquid transition peak. The compositions at the peritectic plateau showed clearly distinguishable single solid/solid and solid-liquid transition peaks. The compositions from  $0.65 \leq x \leq 1$  mol fraction NPG showed no clearly distinguishable solid/solid transition but a clear solid/liquid transition peak.

The comparison of the phase diagram derived from these DSC measurements (Figure 31) with the phase diagram that was elaborated by X-ray diffraction and DSC measurements and published by Barrio et al. [50] gives good agreement for the liquidus line and the lowest temperature solid/solid transition line which was denoted as the  $[C_F+O]$  to  $[C_I+O]$  phase transition by Barrio et al. [50]. The reported phase diagram could be confirmed by our DSC measurement.

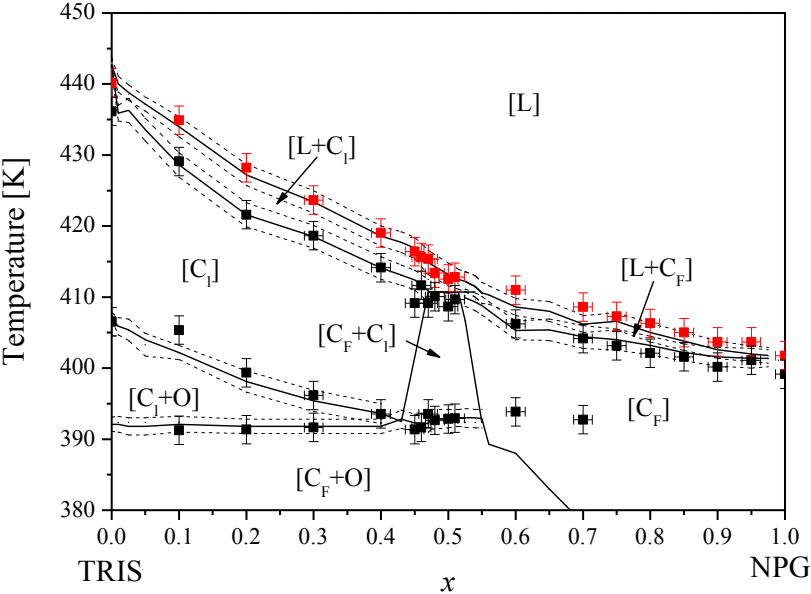


Figure 31: Phase diagram derived from DSC measurements (points with error bars) and comparison with the diagram published in [50] (lines with dotted error bands).

### 4.3.3 Thermal Stability

Up to now, no other organic model alloy with a non-faceted/non-faceted peritectic reaction was investigated. Trivedi et al. [41] presented experimental evidence for banded structure formation during directional peritectic solidification in metals. These experiments required several hours for the formation of alternating bands [6, 39, 42]. Unfortunately, the Dow Chemical Company [65] propose a decomposition temperature for TRIS at 422 K. Depending on the liquidus temperature of the phase diagram TRIS - NPG, alloys with a concentration of  $x > 0.3$  mol fraction NPG (including concentrations within the peritectic region), melt below this temperature. Whereas alloys with a higher TRIS content,  $x \leq 0.3$  mol fraction NPG melt above the decomposition temperature. To clarify a possible decomposition of TRIS during solidification experiments, annealing DSC measurements, heating cycles DSC measurement and annealing investigations in a furnace were performed [66]. In addition, the influence of heating of TRIS was investigated by Raman spectroscopy.

#### Annealing DSC measurements

To establish the thermal stability of the molecules of NPG and TRIS separate DSC measurements have been performed. A thermal stability investigation DSC with a very fast heating rate of  $16.6 \cdot 10^{-2}$  K/s (10 K/min) was selected. At the selected temperatures (473, 463 and 453 K) the pure materials and the representative alloys ( $x = 0.3, 0.5,$  and  $0.7$  mol fraction NPG) were exposed to the temperature for several hours. As long as no reaction occurs, the DSC curve should be a straight line. In the case of a chemical reaction a peak appears.

Figure 32 summarizes the isothermal DSC measurement obtained for pure NPG, pure TRIS, and an alloy with  $x = 0.50$  mol fraction NPG within the peritectic region. The flat DSC lines for pure NPG (dotted red lines in Figure 32) indicate that NPG is stable up to 473 K, which correspond to 10 K below the boiling point of NPG, for more than 4 hours. The DSC curves for pure TRIS (continuous solid line) show that some changes occur after 60 minutes in TRIS when it is exposed to a temperature of 473 K (i.e. 20 K below the boiling point). Upon reducing the exposure temperature to 463 K and 453 K (10 K above its melting point) the stability time of TRIS gradually increased to 3 and more than 4 hours, respectively.

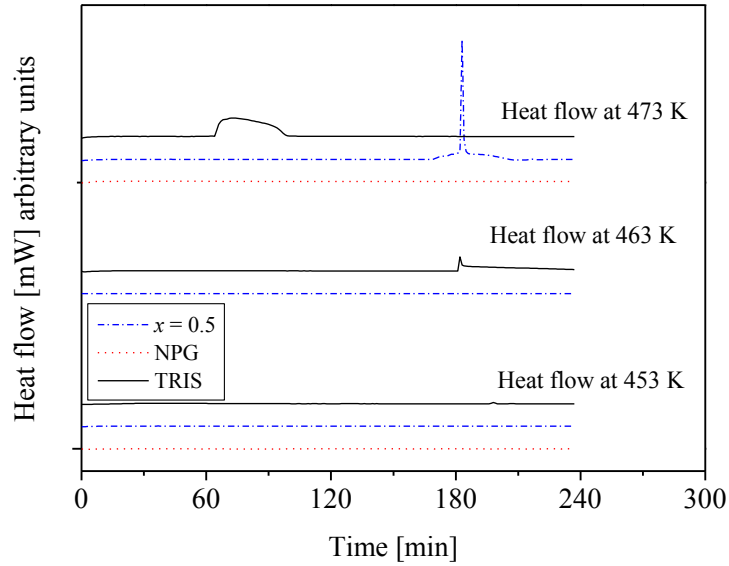


Figure 32: DSC measurement curves of a peritectic alloy ( $x = 0.5$ ), pure NPG and pure TRIS at different temperatures. The graph shows heat flow versus time after reaching the selected annealing temperature.

It is important that the DSC curves indicate decomposition after 3 hours for the representative alloy composition of  $x = 0.50$  mol fraction NPG (dash-dot line) at 473 K whereas no decomposition was found for 4 hours at an exposure of 453 K. Note that the peritectic temperature is at  $T_p = 410$  K. Further investigations on pure TRIS showed a thermal stability of more than 8 hours when held at 438 K.

#### Heating cycles DSC measurements

To check the influence of several heating-up cycles, two Al-pans were filled with the powder of NPG and TRIS in the desired concentration ( $x = 0.15$ , 0.5 and 0.52 mol fraction NPG). The samples with selected alloys were directly heated up to 453 K and cooled down to 373 K four times. The heating and cooling rate was 2 K/min and the entire experiment needed 340 minutes (85 minute for each cycle), 80 minutes longer than the investigated DSC measurements at constant temperatures. Figure 33 shows the effect of heating-up and cooling down for an alloy with  $x = 0.15$  mol fraction NPG for four heating cycles.

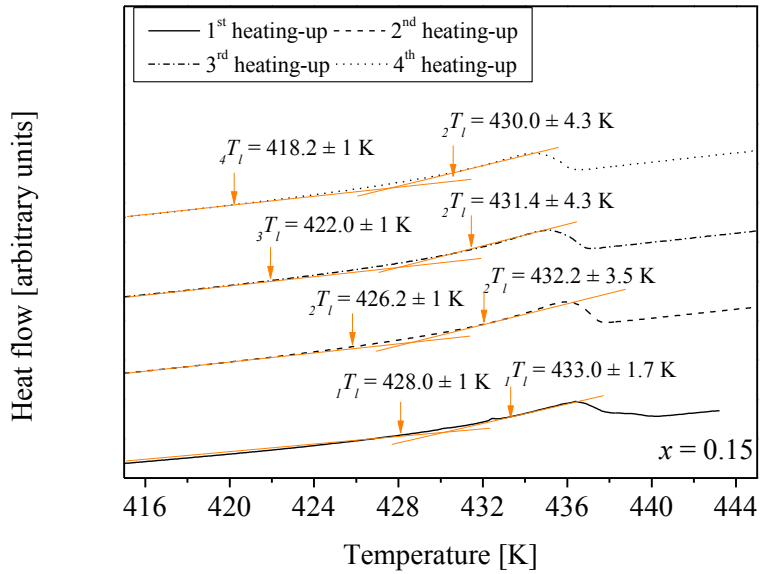


Figure 33: DSC curve of a sample with  $x = 0.15$  mol fraction NPG. The sample was heated up and cooled down four times. The liquidus and solidus temperature decreased after each cycle.

The estimated liquidus and solidus temperature decreased for each DSC measurement cycle. In combination the variance increased from 1.7 K to 4.3 K. The variance can be used as an indication for the amount of impurities within the sample [68]. The same happens with other tested concentrations. The decreasing solidus and liquidus temperatures illustrate an increasing amount of impurities. Since the samples were sealed, the additional impurities are thought to be caused by thermal instability of the organic substances TRIS and/or NPG. As a consequence samples can be used only for a single experimental run and should not be longer investigated than 4 hours at a temperature of 453 K otherwise the investigation results are questionable.

### Annealing furnace investigations

For the annealing experiments several glass bottles (5 cm diameter, 5 cm high) were filled with 25 g TRIS, sealed and kept for 24 hours at 435 K, 425 K, 415 and 405 K. The error bars for all temperatures are smaller than 1 K. The first three selected temperatures are in the plastic phase region whereas the last one is below the solid/solid transition. All samples kept above the solid/solid transition temperature transformed from the faceted phase to the plastic phase and the samples kept at an annealing temperature at 435 K and 425 K became finally

liquid. The sample kept at an annealing temperature of 415 K became waxier (softer) and then liquid. During the investigations, the color of the material changed from transparent to opaque and finally to brown. Only the sample at the annealing temperature below the solid/solid transition temperature stayed solid within 24 hours.

#### Raman spectroscopy

Raman spectroscopy (see appendix A.4) was used to investigate the decomposition because each material shows a typical vibration band, like a finger print. Therefore, pure TRIS and an alloy with a high concentration of TRIS were prepared and investigated. Subsequently, TRIS and the alloy were heated and hold for selected temperatures for several hours. During this time the color of TRIS and the alloy changed from opaque to brown. After cooling, the spectrum of TRIS and the alloy were again determined. Pure unheated TRIS shows a Raman spectrum without fluorescence but used TRIS, prepared alloy, and the in solidification experiments used alloy show in their Raman spectra a strong fluorescence. Furthermore, the Raman spectra show small differences in the Raman intensity between the molten substance and the substance as delivered. This indicates that TRIS is affected after melting.

#### Summary

DSC isothermal annealing showed that NPG was stable for more than 4 hours at temperatures up to 473 K. TRIS, on the contrary, showed decomposition depending on the applied temperature. At a hot zone temperature of 453 K selected samples were chemically stable for 4 hours. Investigations of heating and cooling cycles show a small declination of the liquidus and solidus temperature after each cycle. As a consequence samples can be used only for a single experimental run and should not be longer investigated than 4 hours at a temperature of 453 K or lower.

## 4.4 Corresponding Consequences

### 4.4.1 Conclusions from the Thermal Stability Investigation

Based on the investigation it can be stated that TRIS restricts the solidification studies in this work. The duration of thermal stability depends on the selected temperature and is the main limitation for *in-situ* observations.

Long time annealing investigations (24 hours) in a furnace show that TRIS decomposes in the liquid state and in the plastic phase, too. The decomposition of TRIS is visible in a change of the material color from transparent to opaque and finally to dark brown. Investigations with Raman spectroscopy shows that TRIS is affected as soon as it is heated up into the liquid phase for the first time. TRIS and alloys with a high content of TRIS change their color from white to brown in the liquid state.

DSC measurements show an increasing thermal stability with decreasing temperature and a decreasing of the liquidus and solidus temperature after subsequent cooling and melting of TRIS and selected alloys. Based on these investigations, it can be concluded that TRIS and alloys should not be evaluated after 4 hours at a temperature of maximum 453 K. Hence, the selected temperature in the hot zone of the micro Bridgman-furnace has to be as low as possible to increase the time for thermal stability and investigations.

For the *in-situ* observation, the solid/liquid interface should lie between the hot and the cold zone of the furnace. Unfortunately, the melting temperature for alloys at the peritectic concentration is close to the thermal stability temperature. Therefore, with a fixed temperature in the hot zone the temperature in the cold zone has to be as hot as possible to bring the solid/liquid interface between the hot and the cold zone of the furnace. The selection of the hot and cold temperature of the Bridgman-furnace establishes the temperature gradient  $G_T$ :

$$G_T = \frac{T_{hot} - T_{cold}}{X}. \quad (\text{Eq. 13})$$

Here,  $T_{hot}$  is the temperature in the hot zone,  $T_{cold}$  the temperature in the cold zone of the Bridgman-furnace, and  $X$  the length of the adiabatic zone between the hot and the cold zone.

To increase the temperature gradient  $G_T$ , the adiabatic gap should be kept as small as possible. Later, it will be shown that the size of the adiabatic zone has further restrictions, see chapter 4.4.2.

#### 4.4.2 Selection of Optimal Process Conditions

##### Selection of the optimal temperature gradient $G_T$

The object of the *in-situ* observation is the investigation of different solidification morphologies. Therefore, the solid/liquid interface has to be close to the middle of the adiabatic zone of the Bridgman-furnace. Whereby, the decomposition of TRIS requires a temperature in the hot zone  $T_{hot}$  as low as possible. A low temperature in the hot zone leads to a flat temperature gradient  $G_T$  and this reduce linear the pulling rate  $V_p$  and extended quadratic the transition time  $t_r$  to reach steady state, see chapter 2.1. A short observation time is only achievable for a fast pulling rate coupled with a steep temperature gradient. From chapter 4.4.1, it is known that the thermal stability is given only for the first 4 hours at a temperature of 453 K and increases with lower temperatures. The time to establish initial planar solid/liquid morphology within the Bridgman-furnace is assumed with max. 1 hour. Therefore, the observation time where thermal stability is assumed is reduced to three hours. With an average diffusion coefficient of  $D_L \approx 2.1 \cdot 10^{-11} \pm 0.6 \text{ m}^2/\text{s}$  within the peritectic concentration range of  $0.47 < x < 0.54$  (see chapter A.9), the required temperature gradient  $G_T$  in a Bridgman-furnace can be calculated from the boundary conditions of the thermal stability  $t$ , the temperature difference  $\Delta T$ , and the distribution coefficient  $k$  to be:

$$G_T = \sqrt{\frac{6 \cdot \Delta T_0^2}{k \cdot D_L \cdot t}} \quad (\text{Eq. 14})$$

The distribution coefficient  $k$  for a concentration of  $x = 0.5$  mol fraction NPG is given in Table 4 on page 38 and the temperature difference  $\Delta T$  between the liquidus- and solidus temperature, for this concentration, is given in Table 2 on page 37. Thus, the temperature gradient necessary for reach a steady state planar growth in 3 hours can be estimated to be:

$$G_T = \sqrt{\frac{6 \cdot 3.35^2}{0.86 \cdot 2.1 \cdot 10^{-11} \cdot 3600 \cdot 3}} \frac{\text{K}}{\text{m}} = 18.6 \cdot 10^3 \frac{\text{K}}{\text{m}}. \quad (\text{Eq. 15})$$

It has to be mentioned that the temperature gradient in a Bridgman-furnace shows a smooth transition from the adiabatic gap to the hot zone and the cold one. Thus, the selected temperature gradient should be more than  $18.6 \cdot 10^3$  K/m.

#### Selection of the optimum pulling velocity $V_p$

The pulling rate  $V_p$  during the *in-situ* experiments has to be lower than the critical velocity  $V_c$  which is defined as the speed limit where the solid/liquid interface of phase  $[\alpha]$  and phase  $[\beta]$  solidifies planar. With a speed higher than  $V_c$  the solid/liquid interface becomes unstable and starts to solidify in the form of cells and dendrites. The predicted bands [10, 41] for an alloy with peritectic concentration form at a solidification speed below the critical velocity  $V_c$ . The critical speed itself depends on the diffusion coefficient  $D_L$ , the thermal gradient  $G_T$ , and the temperature difference  $\Delta T_0$  between the solidus- and the liquidus temperature [40] defined by:

$$V_c = \frac{G_T \cdot D_L}{\Delta T_0}. \quad (\text{Eq. 16})$$

During solidification with  $V_p \leq V_c$  a pill-up [2] is established and the solidification morphology is already stable even during the initial transient. With  $G_T = 18.6 \cdot 10^3$  K/m and  $\Delta T_\alpha = 3.35$  K (with  $\Delta T_\alpha > \Delta T_\beta$ , see chapter 4.1) we get:

$$V_c = \frac{18.6 \cdot 10^3 \cdot 2.1 \cdot 10^{-11}}{3.35} \frac{\text{m}}{\text{s}} = 8.3 \cdot 10^{-8} \frac{\text{m}}{\text{s}}. \quad (\text{Eq. 17})$$

With a selected pulling rate  $V_p \leq 8.3 \cdot 10^{-2}$  mm/s we obtain a planar solidification front for both phases. The calculated critical velocity  $V_c$  for each concentration is given in Table 6, page 40, for the final selected process conditions.

#### Selection of the optimal adiabatic gap $X$

The melting temperatures for alloys within the peritectic composition of the phase diagram TRIS - NPG lay between 415 K and 410 K (see Table 2, page 37) and the maximum desired



temperature for the hot zone is 453 K. To be able to observe the solidification morphology in the middle of the adiabatic gap, the adiabatic gap is given by:

$$G_T = \frac{\Delta T}{X} \rightarrow X = \frac{2 \cdot (453 - 415)}{18.6} \text{ mm} = 4.1 \text{ mm}. \quad (\text{Eq. 18})$$

Therefore, the adiabatic gap  $X$  should be equal or less than 4.1 mm but wide enough to enable the observation with a microscope. With the temperature in the hot zone, the calculated length of the adiabatic zone and the temperature gradient the temperature in the cold zone has to be 377 K.

#### Summary of possible operation conditions

TRIS is affected by a possible decomposes at high temperature [51, 65]. DSC investigations show a thermal stability of organic alloys within 4 hours and a temperature of 453 K in the hot zone. A possible operation window for the *in-situ* observation is given in Table 8.

Table 8: Possible process conditions for an *in-situ* observation.

<b>Window for Process Conditions</b>		
temperature $T_{hot}$ hot zone Bridgman-furnace	453	K
temperature $T_{cold}$ in the cold zone of the Bridgman-furnace	377	K
adiabatic gap $X$ (distance between hot and cold zone)	4.15	mm
pulling rate $V_p$ to obtain a planar solidification front	$8.3 \cdot 10^{-2}$	$\mu\text{m/s}$
maximum experimental time $t$ for $T_{hot} = 453$ K	4	hours

Despite of all these approximations, the exact range for the *in-situ* experiments has to be determined in experiments in the micro Bridgman-furnace itself.

## 4.5 Selected Experimental Procedure

The general experimental procedure is described in the following. The micro Bridgman-furnace is preheated to bring the entire system, furnace and microscope, in a thermal equilibrated stage. The selected process conditions are given in Table 9.

Table 9: Selected process conditions for the *in-situ* observations.

Window for Process Conditions		
temperature $T_{hot}$ hot zone Bridgman-furnace	453	K
temperature $T_{cold}$ in the cold zone of the Bridgman-furnace	353	K
adiabatic gap $X$ (distance between hot and cold zone)	3.6	mm
field of view	636 x 552 or 3180 x 2760	$\mu\text{m}^2$

The sledge which moves the sample through the Bridgman-furnace is at its end position (close to the hot zone of the Bridgman-furnace). After 1 hour the temperature gradient in the furnace is stable. The upper plate of the micro Bridgman-furnace is removed and a sample is placed into the furnace and connected with the sledge. Then the upper plate is put back and the furnace is closed again. At the beginning, only an empty part of the sample tube is in the hot zone and the solid material within the capillary tube is approximately 1 mm outside of the hot plate. That allows the material to expand during melting into the unfilled tube when it is moved into the hot zone. The whole sample is now moved with relatively high speed ( $V_p = 100$  mm/s) into the hot zone to the start position of the sledge. Now, the sample is ready for the solidification experiment, the predefined pulling velocity is set and the DIoS system is started to record pictures and temperatures. Table 10 shows the number of evaluated experiments, the prepared concentrations and the applied pulling rates.

Table 10: Implemented experimental setups

$V_p$	Concentration in mol fraction															
$\mu\text{m/s}$	0	0.1	0.2	0.3	0.4	0.45	0.47	0.48	0.5	0.52	0.6	0.7	0.75	0.8	0.9	1
1.28					1			1			1	1	1			
1.02											1		1	1	1	
0.89	1			1	1	1	2		2		2	1	1			2
0.83									2							
0.64				1	2	1	1		1		2	2	1	2	1	1
0.51									1		2	1	1	1	2	
0.38				1	2	1	1		2	1	1	1	1		1	2
0.26					1		1		1	1	1	1				
0.19					1	2	1	1	2	1	1	1				
0.13	2	1	1	2	3	1	3		8		2	1	2	21		1
0.10									1							
0.06	1			1	2	2	1	1	1		2	1	1	1	1	

The stability of the temperature gradient has been evaluated during the solidification experiments. Two 12 mm long square samples ( $0.2 \times 0.2 \text{ mm}^2$ ) were filled, one with NPG and one with TRIS. The samples were placed in the two extra slots in the micro Bridgman-furnace next to the measured sample, see Figure 24 on page 33. During the experiment the two glass samples stayed unmoved and the position of the phase transition (solid/solid for TRIS and solid/liquid for NPG) of the pure organic compounds was used to determine the stability of the temperature gradient.

#### **4.5.1 Experimental Type A: Unmoved Samples**

For the stability investigations samples remained immobile in the Bridgman-furnace for several hours. The DIoS system took every 10 minutes a picture and recorded the temperatures. A large FOV ( $3180 \times 2760 \text{ }\mu\text{m}^2$ ) was selected to observe most of the entire adiabatic gap.

#### **4.5.2 Experimental Type B: Moved Samples**

The sample was held in the start position at least 30 minutes to prepare a planar solid/liquid interface. Afterwards, the sample was moved with a constant pulling rate for several hours through the Bridgman-furnace. The solid/liquid interface morphology was observed with the DIoS system, taking a picture every 30 or 60 seconds.

To see the entire adiabatic gap, a large FOV was preferred for the first experiments. To see the microstructures of the solidification morphology in more detail, a small FOV was preferred for further experiments with the same concentration and the same pulling rate. In a few cases experiments were started at a certain pulling rate which was then changed during experiments to a higher, lower or reverse pulling rate to complete the information on the dynamic of the solidification morphology.

## 5 Results

For a structured description of the investigations, the results were divided in experiments with unmoved samples and moved samples. The tests with unmoved samples were necessary to observe changes of the solid/liquid interface position in a steep temperature gradient over a time period of hours. The experiments with moved samples are applied to investigate the solidification morphologies of the solid/liquid interface close to the critical velocity. Barrio et al. [50] reported that the phase [O] is optically active while the other two phases [C<sub>I</sub>] and [C<sub>F</sub>] are optically inactive. Based on this, the optically active solid phase [O] in the TRIS-rich region can be clearly distinguished from the inactive phases even without using the polarization filters. When illuminated with subdued white light, the optically inactive phases, [C<sub>I</sub>] and [C<sub>F</sub>], appear in the micro-Bridgman furnace in light brown color depending on the illumination intensity while the optically active phase [O] appears with short colored strands or simply dark brown or black. On the other hand, it was not possible to distinguish in terms of color between the two optically inactive phases [C<sub>I</sub>] and [C<sub>F</sub>]. For a better understanding of the selected pictures a schematic sketch is added to most of the figures. This sketch and the definition of the phase region are the basis for the discussion. It has to be mentioned that the sketch and the interpretation are based on experimental observations on more than the presented pictures.

### 5.1 Experimental Type A: Unmoved Samples

Samples were investigated in long time annealing experiments with alloys and pure compounds. This chapter gives an overview of the solid/liquid interface of selected samples staying unmoved in the Bridgman-furnace.

#### 5.1.1 Samples with pure TRIS

In the present work TRIS is used for the first time as a model substance for *in-situ* observation of solidification morphologies. Investigations show for TRIS a temperature depending stability, see chapter 4.3.3. Figure 34 shows the migration of the solid/liquid interface of TRIS (unmoved in the Bridgman-furnace) within 18 hours. Initially only the plastic phase and the solid/solid interface between the plastic phase and the faceted phase is visible, Figure 34a. The selected temperature of 453 K in the hot copper block hinders the observation of the solid/liquid interface at 442 K. After approximately 8 hours the solid/liquid interface appears on the hot side of the Bridgman-furnace (Figure 34b).

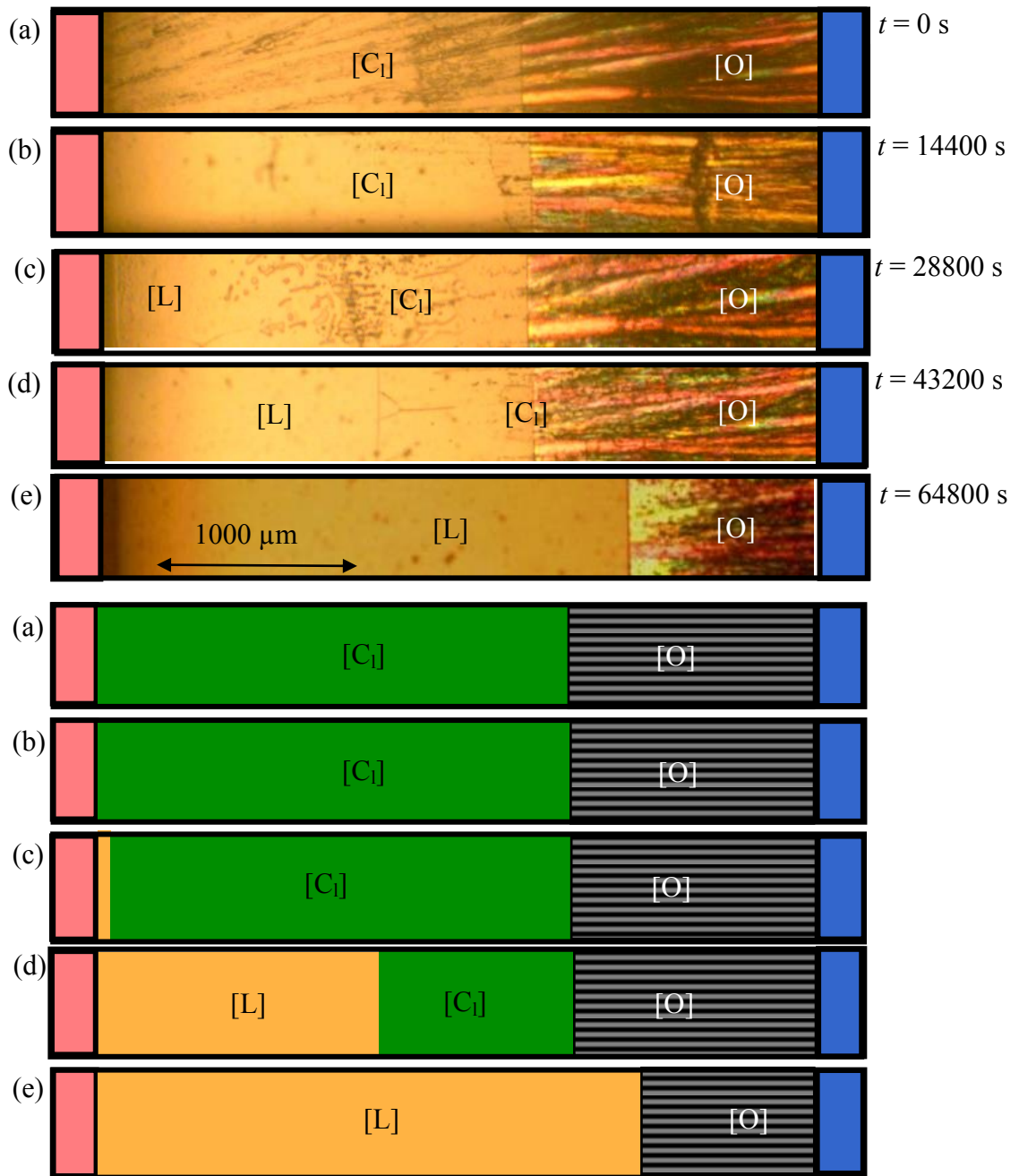


Figure 34: Pictures with corresponding sketches. Decomposition of TRIS indicated by the solid/liquid interface. The figure shows the time depending position of the solid/liquid interface in a pure TRIS sample (a) Initial situation at  $t = 0$  seconds. (b) after 4 hours (14400 s) and (c) after 8 hours (28800 s) unmoved. The solid/liquid interface is for the first time visible. (d) The situation after 12 hours (43200 s). (e) Finally, the plastic phase disappears after 18 hours (64800 s) completely and the faceted phase is in contact with the liquid.

During the following 10 hours, the boundary between the liquid and the plastic phase moves from the left to the right (Figure 34c and d), till the liquid is in contact with the faceted phase (Figure 34e). Afterwards, the faceted phase starts to dissolve.

However, after cooling and heating-up in the Bridgman-furnace the plastic phase [C<sub>1</sub>] and the faceted phase [O] are re-established again. The sample is kept again unmoved in the furnace and the plastic phase [C<sub>1</sub>] disappears again and the liquid is coming in contact with the faceted phase [O] after 16 hours.

Figure 35 shows the time depending solid/liquid interface temperatures of the experiments described above. Both temperature lines are parallel except for the positions where the liquid phase reached the faceted phase.

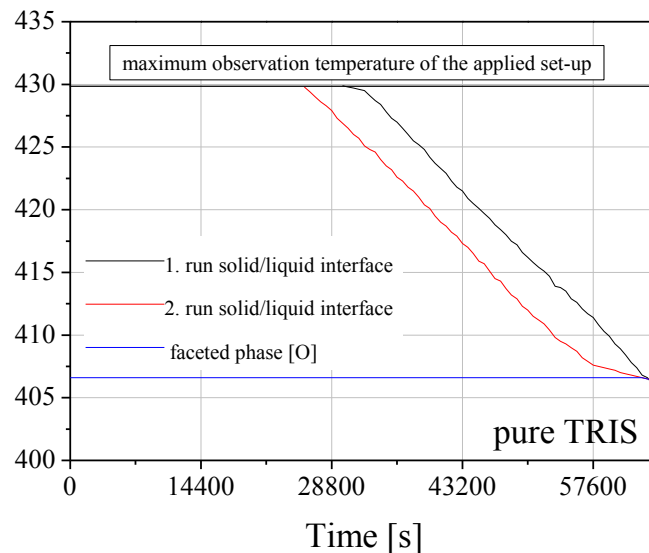


Figure 35: The graph shows the temperature of the solid/liquid interface and the non-faceted/faceted transition temperature for pure TRIS depending on the observation time. The plastic phase dissolves with  $1.9 \pm 0.6$  K/h. After 18 hours the liquid is in contact with the faceted phase.

### 5.1.2 Samples with pure NPG

NPG was used as a model substance in various published experiments [53, 56, 74] as a component in a eutectic phase diagrams. Whereby, eutectic alloys of NPG solidify below the melting temperature of pure NPG. In this work, the organic substance is used as a component in a peritectic phase diagram, therefore, alloys solidify above the melting point of pure NPG. Furthermore, the selected temperature in the hot zone of the furnace is close to the boiling temperature of the organic substance at atmospheric pressure, see chapter A.3. Hence, the stability of NPG close to the boiling point has to be investigated.

During the first minutes, the solid/liquid interface showed a mushy zone which disappeared, Figure 36a and b. For the next 18 hours the solid/liquid interface showed a planar solid/liquid interface and no bubbles were observed.

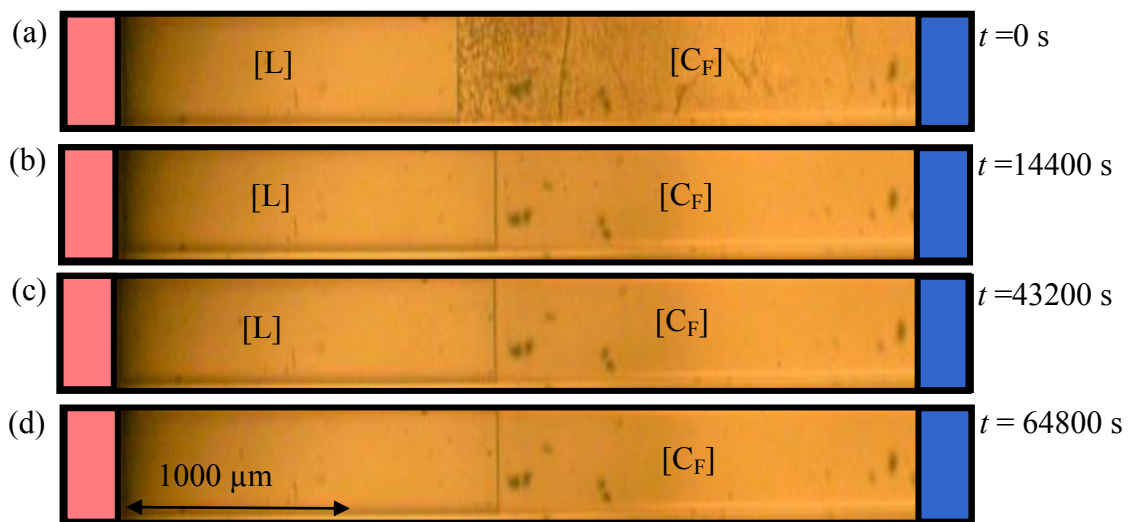


Figure 36: Solid/liquid interface of pure NPG within the first 4 hours (a-d).

Figure 37 shows the temperature of the solid/liquid interface of pure NPG within the fixed temperature gradient. The solid/liquid interface stays planar at a temperature of  $400.6 \pm 0.2$  K for 18 hours.

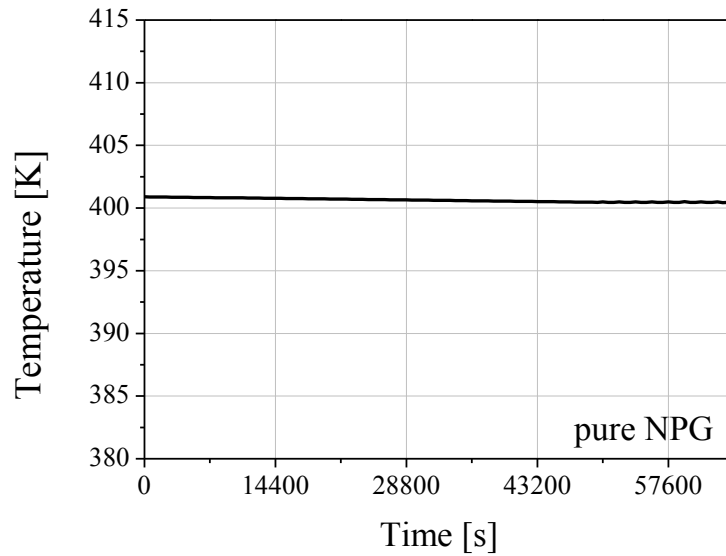


Figure 37: The graph shows the temperature of the solid/liquid interface for pure NPG depending on the observation time. The sample stays unmoved for 18 hours in the Bridgman-furnace with a temperature gradient of 14 K/mm.

### 5.1.3 Samples with Selected Concentrations

The thermal stability is investigated for selected concentrations at the same time ( $x = 0, 0.1, 0.2, 0.3, 0.4, 0.45, 0.48, 0.5, 0.6, 0.75, 0.8, 0.95, \text{ and } 1$ ). Six samples ( $x = 0, 0.3, 0.45, 0.5, 0.6, 0.75, \text{ and } 1$ ) are shown together in Figure 38. Each sample was investigated on its own. Afterwards, the pictures were merged together. The investigations reveals that after several hours the plastic phase  $[C_I]$  dissolves and the solid/liquid interface temperature in the TRIS-rich region of the phase diagram is constantly shifted to a lower temperature (see Figure 38). The NPG rich  $[C_F]$  phase seems to be stable but a shift of the solid/liquid interface to lower temperature is observed after 12 hours, too. Whereby, the solid/solid interface of the alloy stays at the same position.



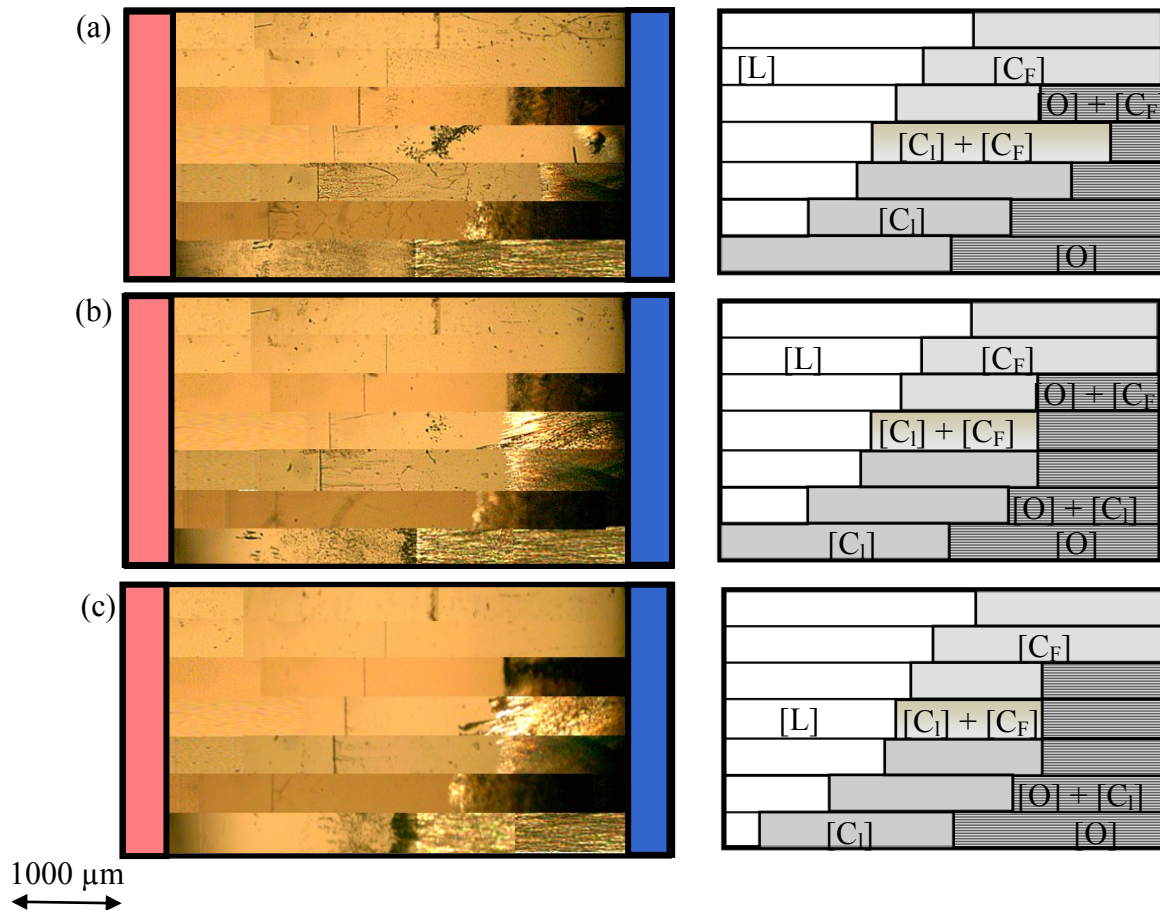


Figure 38: Micrographs of stationary samples of various compositions after several hours within the micro Bridgman setup at a constant temperature gradient. In each picture the concentration starts at the bottom with  $x = 0$  (TRIS), 0.3, 0.45, 0.5, 0.6, 0.75 and 1 (NPG). The left side shows the pictures and the right side the interpretation of the phases. (a) Situation after 1 hour within the furnace. (b) Same samples after 4 hours. (c) Position of the solid/liquid interface after 8 hours unmoved in the furnace.

The interface temperatures were estimated from the position within the adiabatic gap and the temperature gradient. In Figure 39 the results of the evaluation of the interface temperatures after 1 hour have been plotted as points within the phase diagram (as published by Barrio et al [50]). The points show no error bars because they correspond to single experiments with a systematic error (measurement error of the temperature and positions) smaller than the point size. Taking the measurement accuracy into account, the phase transition temperatures confirm the published phase diagram by Barrio et al. [50].

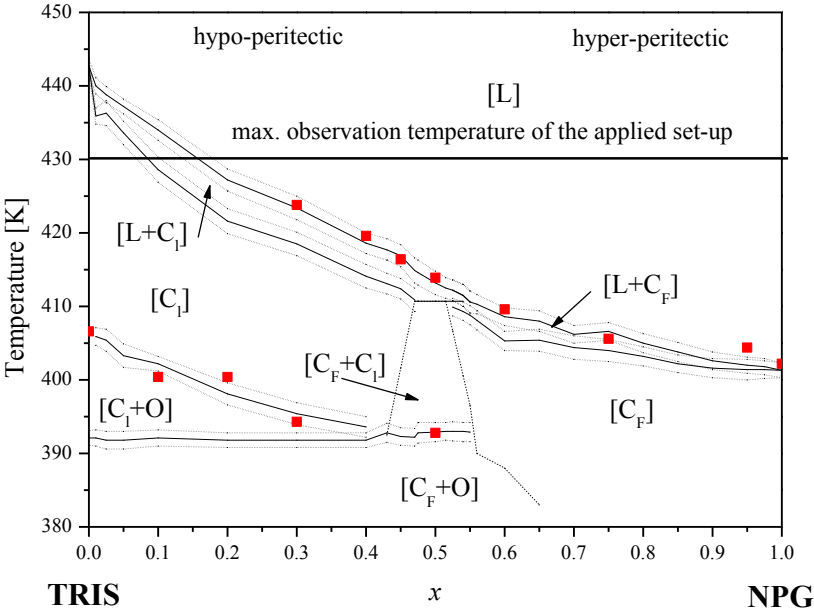


Figure 39: Comparison of the reported phase diagram [50] (lines with dotted error bands) with optical investigation (red points) for  $x = 0, 0.1, 0.2, 0.3, 0.4, 0.45, 0.5, 0.6, 0.75, 0.95$  and 1. The maximum temperature observable in the chosen Bridgman-furnace is shown as a line at 430 K.

## 5.2 Experimental Type B: Moved Samples

The entire phase diagram TRIS – NPG was investigated in certain concentration steps. Table 10 on page 54 gives an overview of the concentrations which were investigated. The most expressive pictures of the experiments are used to show the evolution of the solid/liquid interface. In the peritectic region where both phases  $[C_L]$  and  $[C_F]$  coexist the terminus  $[\alpha]$  and  $[\beta]$  is used.

### 5.2.1 Preparation of the Solid/Liquid Interface

Directly after the sample was placed in the preheated the micro Bridgman-furnace, the material started to melt and after approx. 20 to 30 minutes a stable planar solid/liquid interface indicated that a stable temperature gradient in the samples was reached. Figure 40 shows images of an unmoved sample with  $x = 0.6$  mol fraction NPG during the start up. The initially faceted phases  $[M + O]$ , indicated by a colorfully structure, disappear and transform to liquid  $[L]$  and the plastic phase  $[C_F]$ . The plastic phase close to the solid/liquid interface shows a mushy zone with a solid matrix and fine channels of liquid (Figure 40b and c).

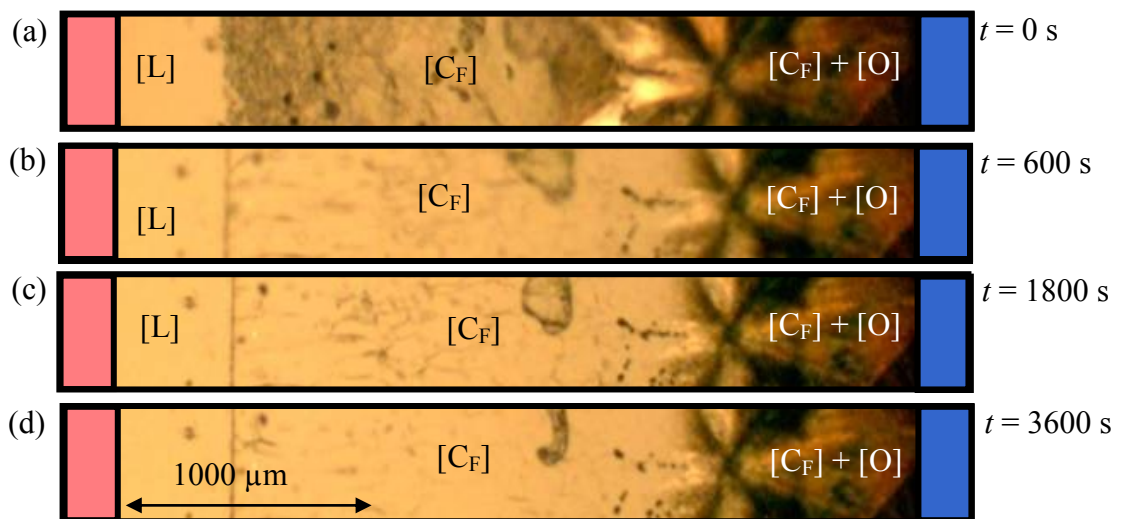


Figure 40: Evolution of the solid/liquid interface in sample of  $x = 0.6$  within 30 minutes (1800 s) after the sample was put into the preheated Bridgman furnace. (a) Initial situation  $t = 0$  s with liquid phase  $[L]$ , non-faceted phase  $[C_F]$  and faceted phase  $[O]$ . (b) 10 minutes (600 s) after the sample was brought into the furnace. (c) and (d) Sample after 30 minutes (1800 s) and 60 minute (3600 s).

Figure 41 shows the temperature of the solid/liquid interface within the first 3600 s from Figure 40. The interface temperature declined and reached the position which corresponds to the liquidus temperature within 30 minutes. The mushy zone disappeared and the solid phase is in equilibrium with the liquid phase.

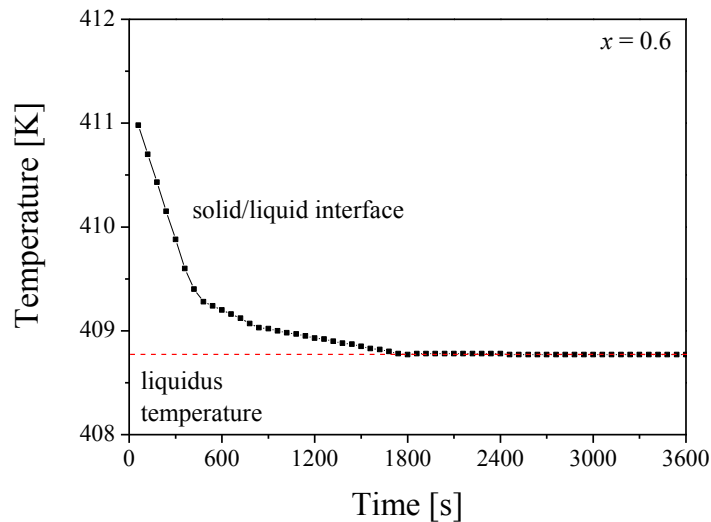


Figure 41: The graph shows the evolution of the solid/liquid interface temperature within the first hour. The black squares are measurement results with an error of 0.3 K. The solid/liquid interface reaches a stable liquidus temperature after approximately 30 minutes.

## 5.2.2 Solidification Morphologies in the [C<sub>I</sub>] and the [C<sub>F</sub>] Phase Region

### Solidification morphologies of TRIS at a pulling rate of $V_p > 0.13 \mu\text{m/s}$

For the start-up, the solid/liquid interface stays unmoved during the first 30 minutes and only the plastic phase [C<sub>I</sub>] and the faceted phase [O] is visible, Figure 42a. Afterwards, the sample was pulled through the Bridgman-furnace with  $V_p = 0.89 \mu\text{m/s}$ . During the direct solidification experiment the organic substance showed initially planar solidification morphology, see Figure 42b. The solid/liquid interface became unstable and transformed first to cells and then to dendrites. The low temperature phase grew in the form of facets. Simultaneously, liquid appeared in front of the faceted phase (Figure 42c) and departs the two solid phases (plastic phase and faceted phase). The gap of liquid between the faceted phase and the plastic phase increased until the interdendritic liquid got in contact (Figure 43).

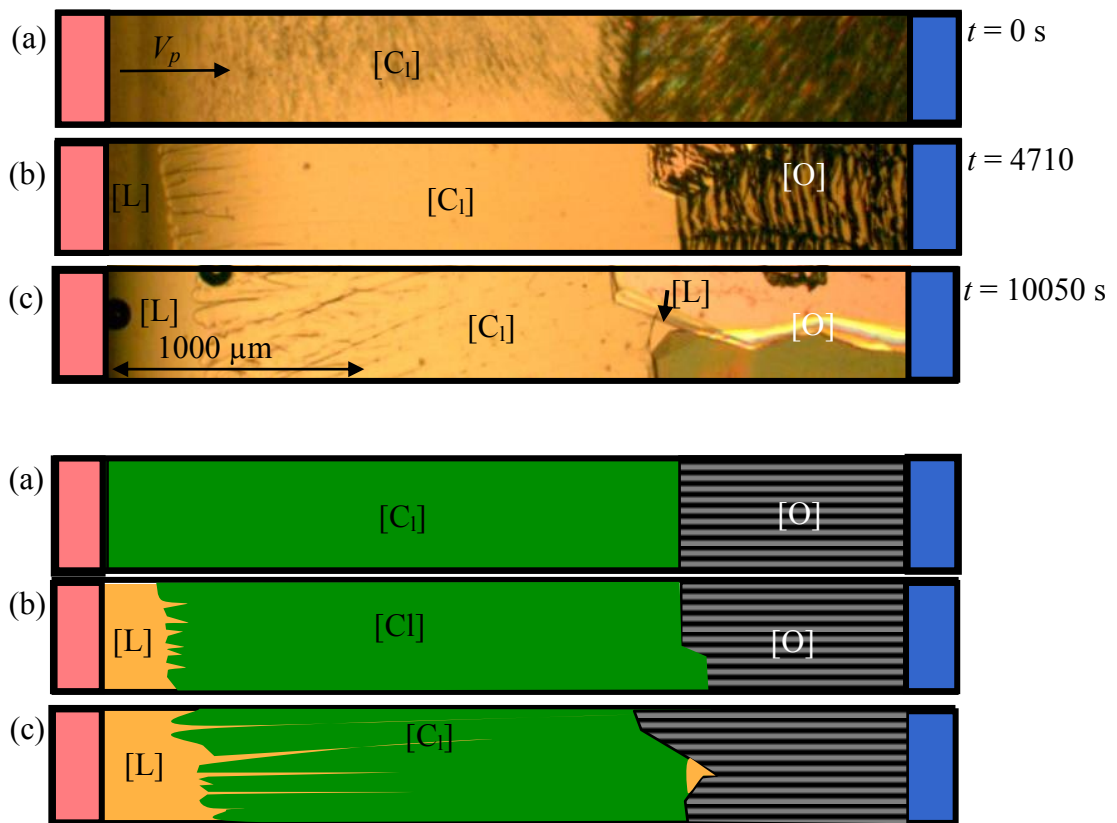


Figure 42: Pictures with corresponding sketches of the evolution of the optical solidification morphology of pure Tris at a pulling rate of  $V_p = 0.89 \mu\text{m/s}$ . (a) Initial situation where only the plastic phase and the faceted phase are visible. (b) TRIS shows a cellular solid/liquid front on the left side and a straight line for the non-faceted/faceted transition interface. (c) The initially cellular front becomes unstable and transforms into dendrites. Simultaneously, the liquid phase appears in front of the faceted phase and departs both solid phases while the faceted phase grows in the form of small facets.

The channels and the gap between the faceted phase [O] and the plastic phase [C<sub>1</sub>] increased with time. Finally, the plastic phase somehow appeared in form of small dendrites in front of the faceted phase until it dissolves and disappears completely.

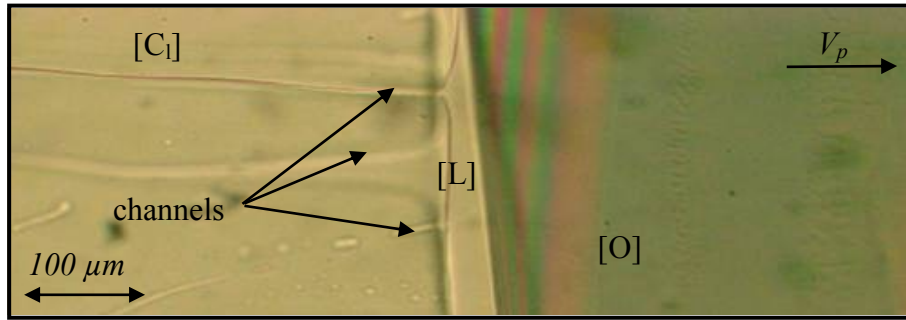


Figure 43: Liquid between the faceted phase on the right side and the plastic phase on the left side of the picture. The plastic phase shows fine channels which connects the liquid region with the liquid in front of the solidification front.

Solidification morphologies of the TRIS-rich phase [C<sub>1</sub>] at a pulling rate of  $V_p > 0.13 \mu\text{m/s}$

The experimental results of the moved samples show cellular and dendritic solidification morphology for all concentrations with  $x < 0.47$  mol fraction NPG. It is assumed that in this region of the phase diagram only the plastic phase [C<sub>1</sub>] occurs. The picture in Figure 44 shows solidification morphologies for different times for an alloy with a concentration of  $x = 0.3$  mol fraction NPG as example for all other experiments within this concentration range. Starting with a planar front at  $t = 0$  s the solidification morphology becomes unstable (Figure 44b) and changes within a few minutes to a dendritic solidification front (Figure 44c) and changes within a few minutes to a dendritic solidification front (Figure 44c).

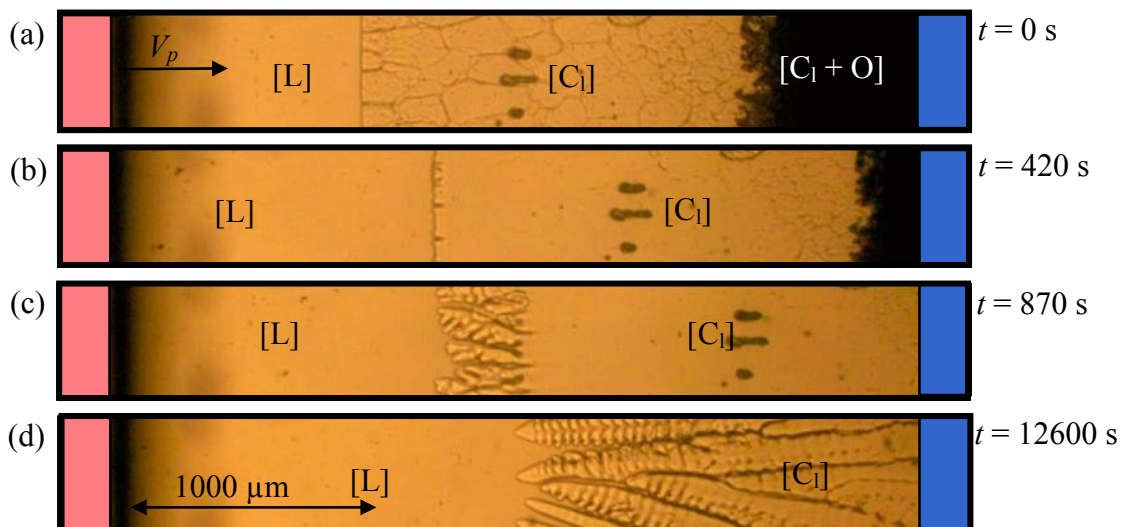


Figure 44: During solidification ( $V_p = 0.89 \mu\text{m/s}$ ) the solid/liquid interface changes for an alloy with  $x = 0.3$  mol fraction NPG from (a) the initial planar front to dendrites within (b) 7 minutes, (c) 14 minutes and finally (d) after 3.5 hours.

It is known from literature that tips of dendrites grow below the liquidus temperature and above the solidus temperature. Here, a constant shift of the dendrites tips to lower temperature was always observed in all experiments performed (like Figure 44c and d). Furthermore, the mushy zone got more extended while the solid/liquid interface moves. In Figure 44d the tip of the dendrites are  $4.7 \pm 1$  K below the nominal solidus line. Finally, after 10 to 14 hours, depending on the selected concentration, the entire FOV shows only liquid, therefore, the solid/liquid interface grows below 353 K.

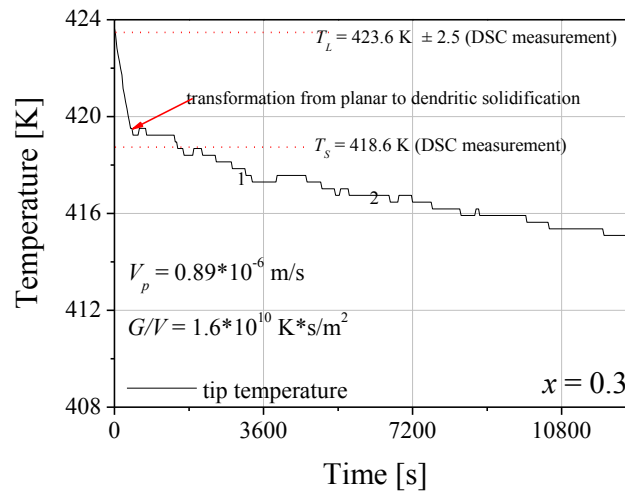


Figure 45: The graph shows the temperature of the dendrite tips from Figure 44 as a function of time ( $x = 0.3$  mol fraction NPG and a pulling velocity  $V_p = 0.89 \mu\text{m/s}$ ). The red dotted lines show the detected liquidus and solidus temperature by DSC measurement.

#### Solidification morphologies of the NPG-rich phase $[C_F]$ at a pulling rate of $V_p > 0.13 \mu\text{m/s}$

The solidification morphology of alloys with the NPG-rich  $[C_F]$  phase,  $x \geq 0.7$  mol fraction, shows a planar front, before the morphology of the solidification front changes to cells or dendrites.

Figure 46 shows the solidification morphology of an alloy with  $x = 0.75$  mol fraction NPG and a pulling velocity of  $0.89 \mu\text{m/s}$ . After more than 4 hours it can be assumed that phases  $[C_F]$  grows in steady-state manner because the theoretical transition time is exceeded. The initial planar front becomes unstable and changes to a cellular solidification morphology. Note that the cellular solidification front in Figure 46d is undercooled relative to the initial

solid/liquid interface in Figure 46a by approximately 3.5 K. The solidification morphology stays constant even for more than 4 hours.

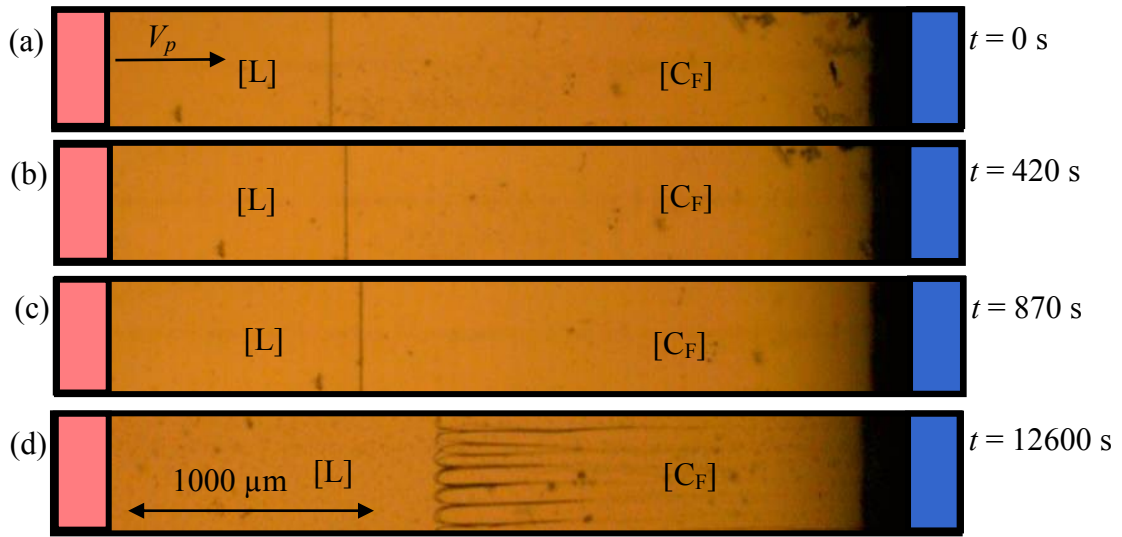


Figure 46: The solidification morphology of an alloy with  $x = 0.75$  mol fraction NPG and a pulling velocity of  $0.89 \mu\text{m/s}$ . (a) The initial planar front, (b) the solidification morphology after 7 minutes, and (c) after 14 minutes and finally (d) cells after 3.5 hours.

Figure 47 shows the temperature of the solid/liquid interface and the cell tips within the first 3.5 hours. During the first 3000 s the position of the planar front moves from the liquidus temperature close to the solidus temperature. Whereby, the cellular solidification morphology occurs approximately after the first 1500 s. To a better comparability both graphs in Figure 45 and Figure 47 show the same time and temperature scale. It illustrates that under the same process conditions the TRIS-rich  $[C_1]$  phase dissolves faster than the NPG-rich phase  $[C_F]$ . Additionally, the  $[C_1]$  phase grows dendritic where the  $[C_F]$  phase grows cellular (compare Figure 44d and Figure 46d).



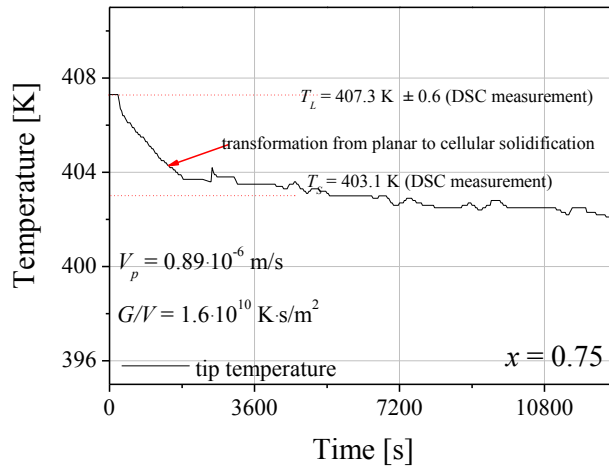


Figure 47: The graph shows the solid/liquid interface temperature of an alloy with  $x = 0.75$  mol fraction NPG and a pulling velocity of  $0.89 \mu\text{m/s}$ . The corresponding liquidus and solidus temperature are taken from the DSC measurement.

#### Solidification morphology at a pulling rate of $V_p \leq 0.13 \mu\text{m/s}$

The solidification morphology for alloys  $0 \leq x \leq 1$  with a pulling rate equal or slower than  $V_p = 0.13 \mu\text{m/s}$  shows a planar front for all concentrations. Exceptions are presented in the next chapter. The steady decreasing of the solid/liquid interface temperature is visible by the change of the position of the solid/liquid interface which moves to lower temperature. The solid/solid interface is only visible within the adiabatic gap for concentrations  $x \leq 0.52$  mol fraction NPG and stays constant at the same position, a clear indication for a constant temperature gradient. As shown in chapter 2.1, the solid/liquid interface of an alloy grows at the corresponding solidus temperature for  $V_p \leq V_c$ . Here, the solid/liquid interface grows planar and goes even below the solidus temperature. We assume this phenomenon as a consequence of the beginning of the decomposition of the organic substance TRIS. It has to be stated that the plastic phase disappears for all concentrations depending on the observation time and that the solid/liquid interface temperature goes below the melting temperature of NPG.

Figure 48 shows the solid/liquid interface of a TRIS-rich alloy with a concentration of  $x = 0.3$  mol fraction NPG. Bubbles which cross the solid/liquid interface influence the solidification morphology locally, but in general the solidification morphology stays planar. Hence, it can be stated that the liquid is not constitutionally undercooled.

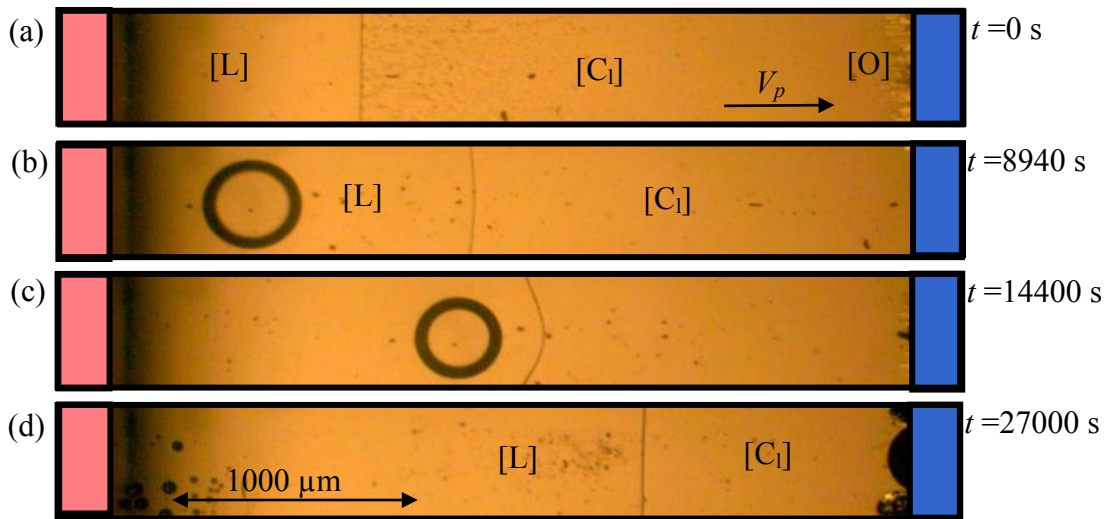


Figure 48: Solidification morphology of an alloy with  $x = 0.3$  mol fraction NPG and  $V_p = 0.13$  m/s. The interface shows clearly a planar solid/liquid interface even when a bubble crosses the solid/liquid interface. The faceted phase can be seen at the right side.

The evolution of the temperature of the planar solid/liquid interface can be seen in Figure 49. The graph shows the change of the interface temperature within the first 4 hours. Long time investigations ( $t > 4$  hours) show that the interface stays planar until the plastic phase disappears completely.

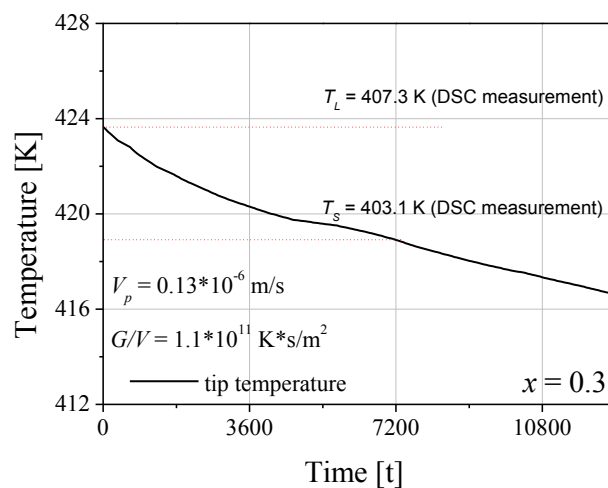


Figure 49: The morphology of an alloy with  $x = 0.3$  mol fraction NPG solidification occurs as a planar solid/liquid interface. The graph shows the temperature of the solid/liquid interface as a function of time,  $V_p = 0.13$   $\mu\text{m/s}$ .

### 5.2.3 Layered Structure Morphologies

Layered structures were observed during the preparation of the solid/liquid interface for  $x = 0.5$ , 0.51 and 0.6 mol fraction NPG and during solidification experiments for  $x = 0.48$ , 0.5, and 0.51 mol fraction NPG. For pulling rates  $V_p > 0.38 \mu\text{m/s}$  some layered structures leads to an oscillation solidification morphology (see chapter 5.2.4) and for  $V_p \leq 0.38 \mu\text{m/s}$  to some banded solidification and finally to peritectic coupled growth (see chapter 5.2.5).

#### NPG-rich phase [C<sub>F</sub>] with $x = 0.6$ mol fraction NPG at a pulling rate of $V_p = 0.38 \mu\text{m/s}$

Figure 50 shows solidification morphologies for the concentration  $x = 0.6$  mol fraction NPG (peritectic region:  $0.47 \leq x \leq 0.54$ ). Within the preparation time to establish a planar solid/liquid interface of the  $[\beta]$  phase, the solid/liquid interface was overgrown by the  $[\alpha]$  phase (visible in Figure 50a as a small black line behind the solid/liquid interface). The  $[\alpha]$  phase grows with a lateral velocity of  $19.0 \pm 6 \mu\text{m/s}$ . During solidification with  $V_p = 0.38 \mu\text{m/s}$ , the  $[\alpha]$  phase grows with  $0.11 \mu\text{m/s}$  against the pulling direction until the phase  $[\beta]$  nucleates in front of the interface, Figure 50b, and overgrows the  $[\alpha]$  phase with  $6 \pm 2 \mu\text{m/s}$ , see Figure 50c. The  $[\beta]$  phase grows stable with  $0.25 \mu\text{m/s}$  against the pulling direction and the band of the  $[\alpha]$  phase stays unchanged (Figure 50d). During the initial time of the experiment (Figure 50a to c) the faceted phase [O] disappeared till only a small part was visible close to the cold part (Figure 50a to c).

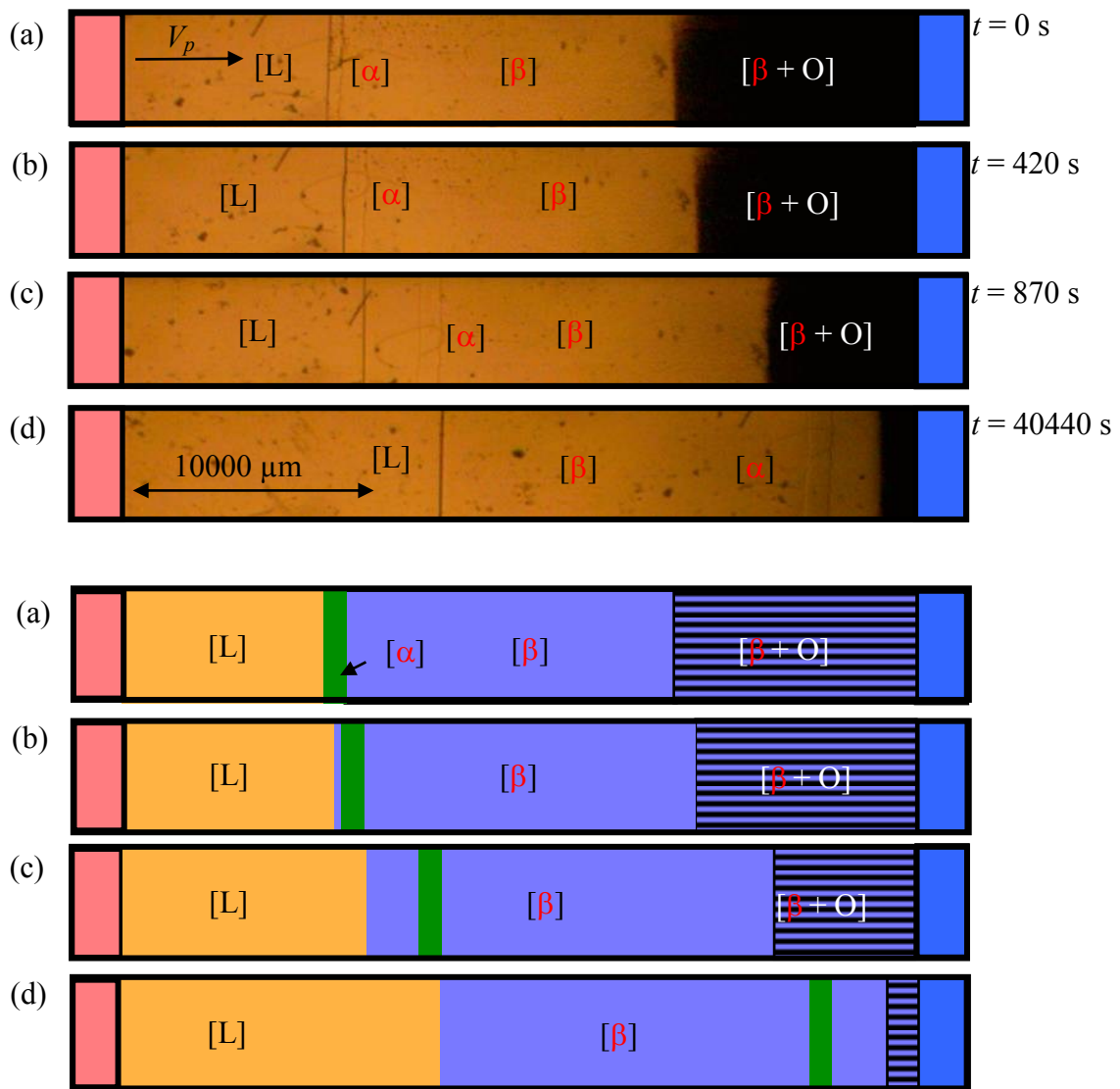


Figure 50: (a) The initial phase  $[\beta]$  is overgrown by the phase  $[\alpha]$ . (b) The phase  $[\alpha]$  is again overgrown by the phase  $[\beta]$  and (c-d) remains as a band in the  $[\beta]$  phase matrix ( $x = 0.6$  mol fraction NPG and  $V_p = 0.38 \mu\text{m/s}$ ).

NPG-rich phase  $[C_F]$  with  $x = 0.5$  mol fraction NPG at a pulling rate of  $V_p = 0.13 \mu\text{m/s}$

For a concentration of  $x = 0.5$  the growth of a second phase was observed during the initial investigations, see Figure 51. The second phase grows in front of the solid/liquid interface which is indicated by a slightly different optical impression, see Figure 51a. During solidification the faceted phase  $[O]$  starts to grow and after approximately 7.5 hours (Figure 51c) the sample shows just a small region of  $[C_F]$  phase.

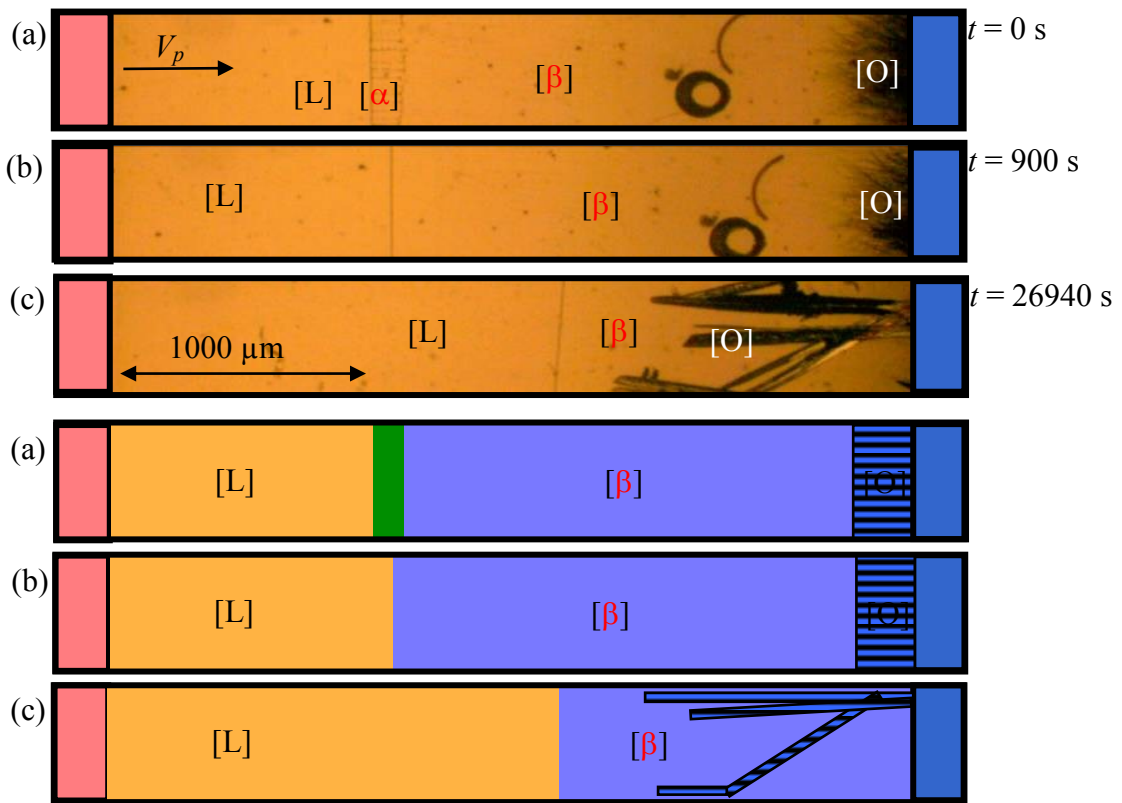


Figure 51: Pictures with corresponding sketches for  $x = 0.5$ . (a) The interface shows the growth of the primary phase  $[\alpha]$  and the secondary phase  $[\beta]$ . (b) After approximately 15 minutes the secondary phase disappeared. (c) After 7.5 hours the faceted face  $[O]$  grows needle like.  $V_p = 0.13 \mu\text{m/s}$ .

Peritectic concentration  $x = 0.5$  mol fraction NPG at a pulling rate of  $V_p = 0.83 \mu\text{m/s}$

After melting, the initial solid/liquid interface, see Figure 52a, changes the position from a lower temperature level to a higher temperature level within 30 seconds, see Figure 52b. On the fine black thread outside the glass sample, the movement of the sample from the left side to the right side or respectively the movement of the solidification front from the right side to the left side is visible. As soon as the solid/liquid interface reaches the higher temperature level a new phase grows (Figure 52c, d). Afterwards, the  $[\beta]$  phase grows envelop the  $[\alpha]$  phase and the solid/liquid interface temperature decreases.

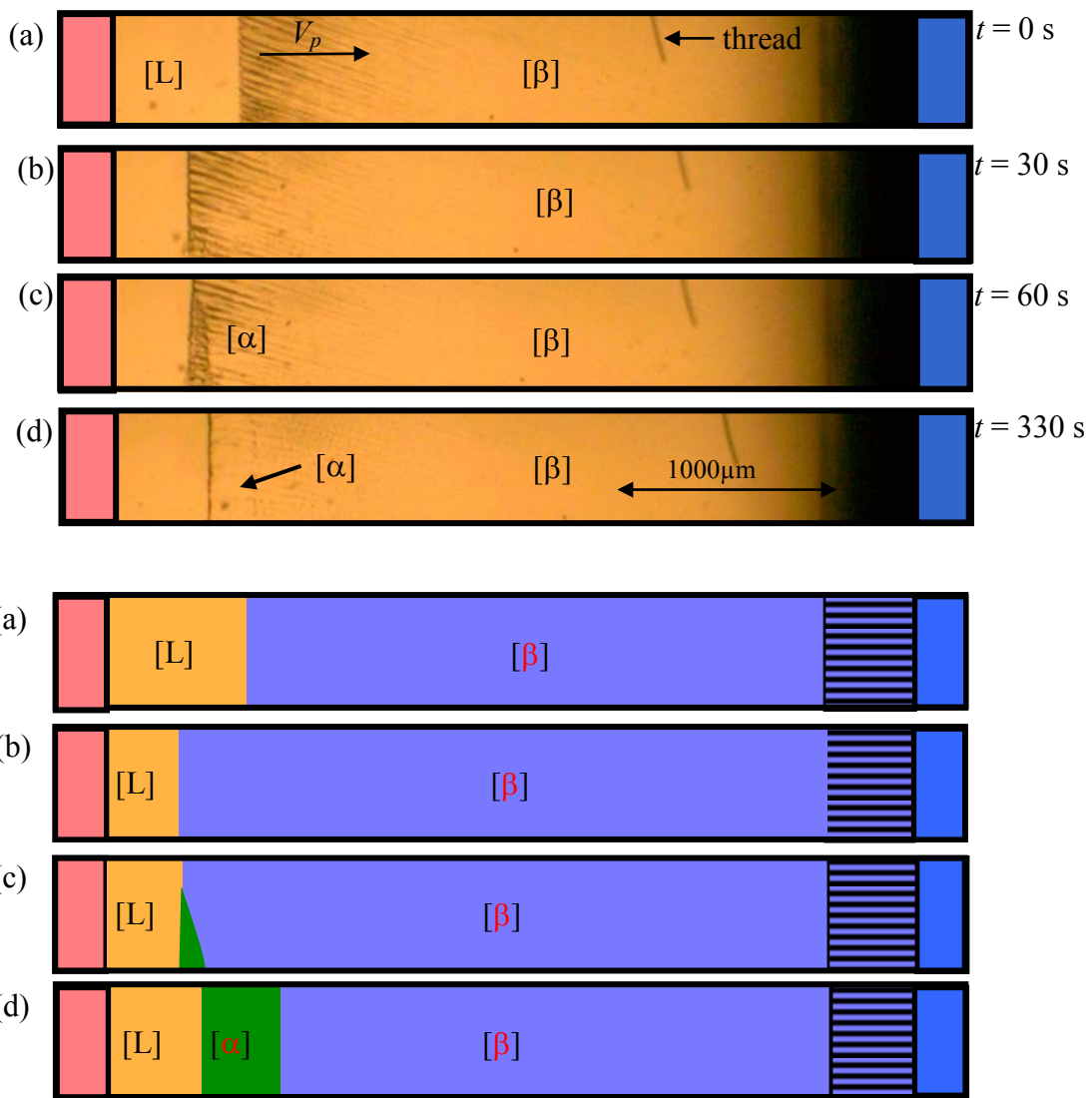


Figure 52: (a – b) After melting, the initial cellular solid/liquid interface of the peritectic [β] phase ( $x = 0.5$  mol fraction NPG) moves from a lower temperature level to a higher one. (c - d) At this temperature level the phase [α] starts to grow. During solidification the [α] phase is stable and the solid/liquid interface changes to a planar front.  $V_p = 0.83 \mu\text{m/s}$ . The thread is outside the sample.

Peritectic concentration  $x = 0.51$  mol fraction NPG at a pulling rate of  $V_p = 0.26 \mu\text{m/s}$

Figure 53a to Figure 53f shows the formation of banded structures at a pulling rate of  $0.26 \mu\text{m/s}$ . The initial situation is shown in Figure 53a. The sample is in rest and the first [α] phase starts to melt in front of the [β] phase. With a pulling rate of  $0.26 \mu\text{m/s}$  the [α] phase starts to grow and forms a layered structure between the melt and the [β] phase, shown in Figure 53b to d. As soon as the [α] phase is  $6.8 \pm 0.1$  K below the liquidus temperature,

$T_L = 410.06 \pm 2.8$  K for  $x = 0.48$  mol fraction NPG, the  $[\beta]$  phase starts to grow at a temperature of 403.5 K. The  $[\alpha]$  phase builds a 152  $\mu\text{m}$  broad layer but further phase transitions or layered structures are not observed.

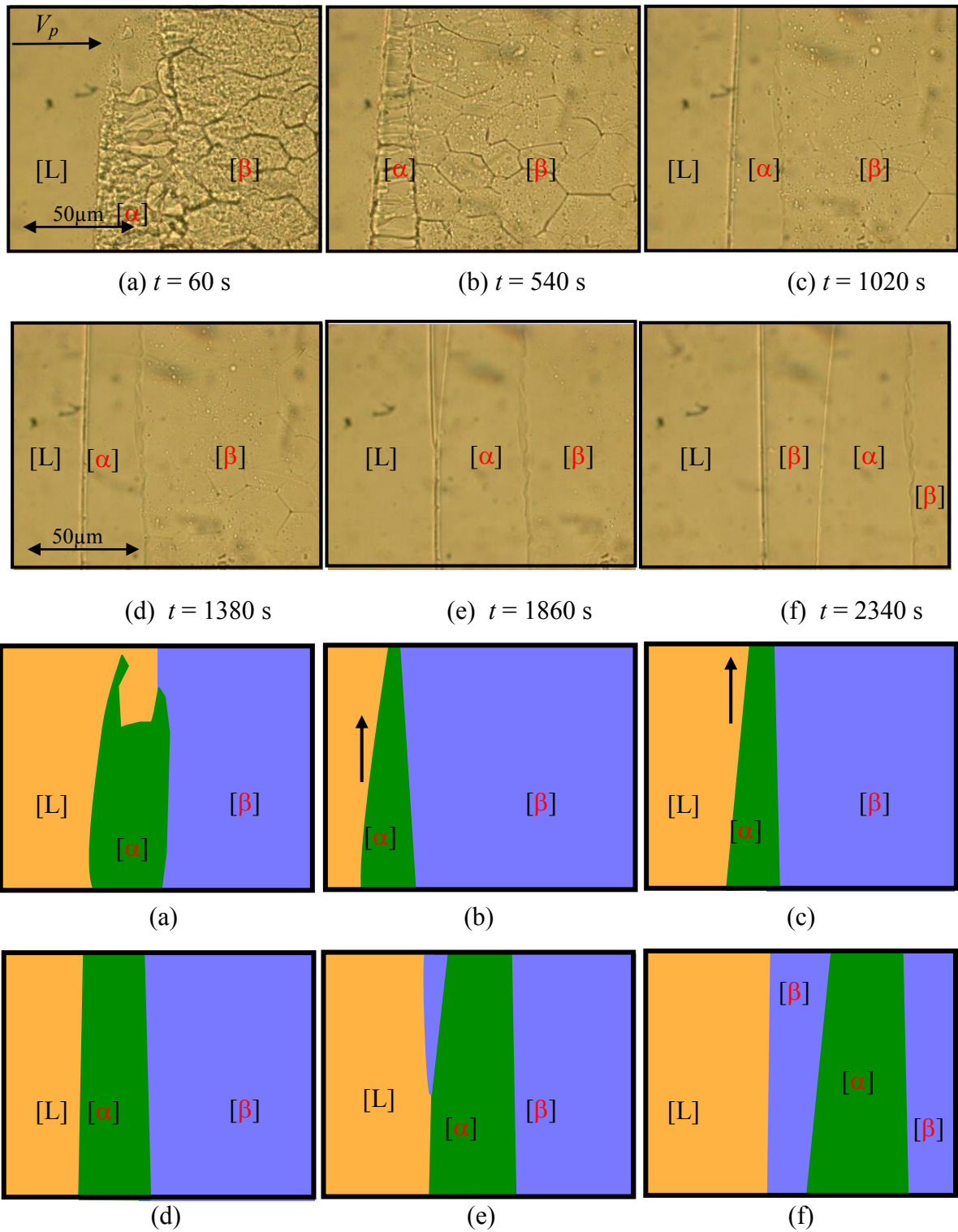


Figure 53: Formation of banded structures for an alloy with  $x = 0.51$  mol fraction NPG. (a) The initial situation with the sample in rest. (b) to (d) The  $[\alpha]$  phase grows in front of the  $[\beta]$  phase. (e) and (f) growth of the  $[\beta]$  phase in front of the  $[\alpha]$  phase.



Peritectic concentration  $x = 0.51$  mol fraction NPG at a pulling rate of  $V_p = 0.19 \mu\text{m/s}$

The initial phase  $[\beta]$  is expected during the development of a banded solidification structure. Immediately after the partially melting of the alloy the remaining solid close to the interface shows a mushy zone, see Figure 54a and in front of the solid/liquid interface there are still small solid parts.

As soon as the sample is pulled with  $0.19 \mu\text{m/s}$  through the Bridgman-furnace, the coarse solid/liquid interface tries to create a planar front. During the change of the interface from a coarse morphology to a planar front the  $[\alpha]$  phase starts to grow in front of the  $[\beta]$  phase. Figure 54b shows the growth of the  $[\alpha]$  phase from the outside toward the center of the sample and simultaneously the  $[\beta]$  phase overgrows the  $[\alpha]$  phase and merge in the center of the sample (Figure 54c). As soon as the  $[\beta]$  phase cuts the  $[\alpha]$  phase from the liquid, only the  $[\beta]$  phase grows (Figure 54d) and the  $[\alpha]$  phase forms a lenticular embedding within the  $[\beta]$  phase matrix with a thickness of  $137 \pm 3 \mu\text{m}$ . After the growth of the  $[\beta]$  phase neither a new solidification of the  $[\alpha]$  phase in front of the  $[\beta]$  phase is observed nor a phase transition from  $[\beta]$  to  $[\alpha]$  or  $[\alpha]$  to  $[\beta]$ , respectively.

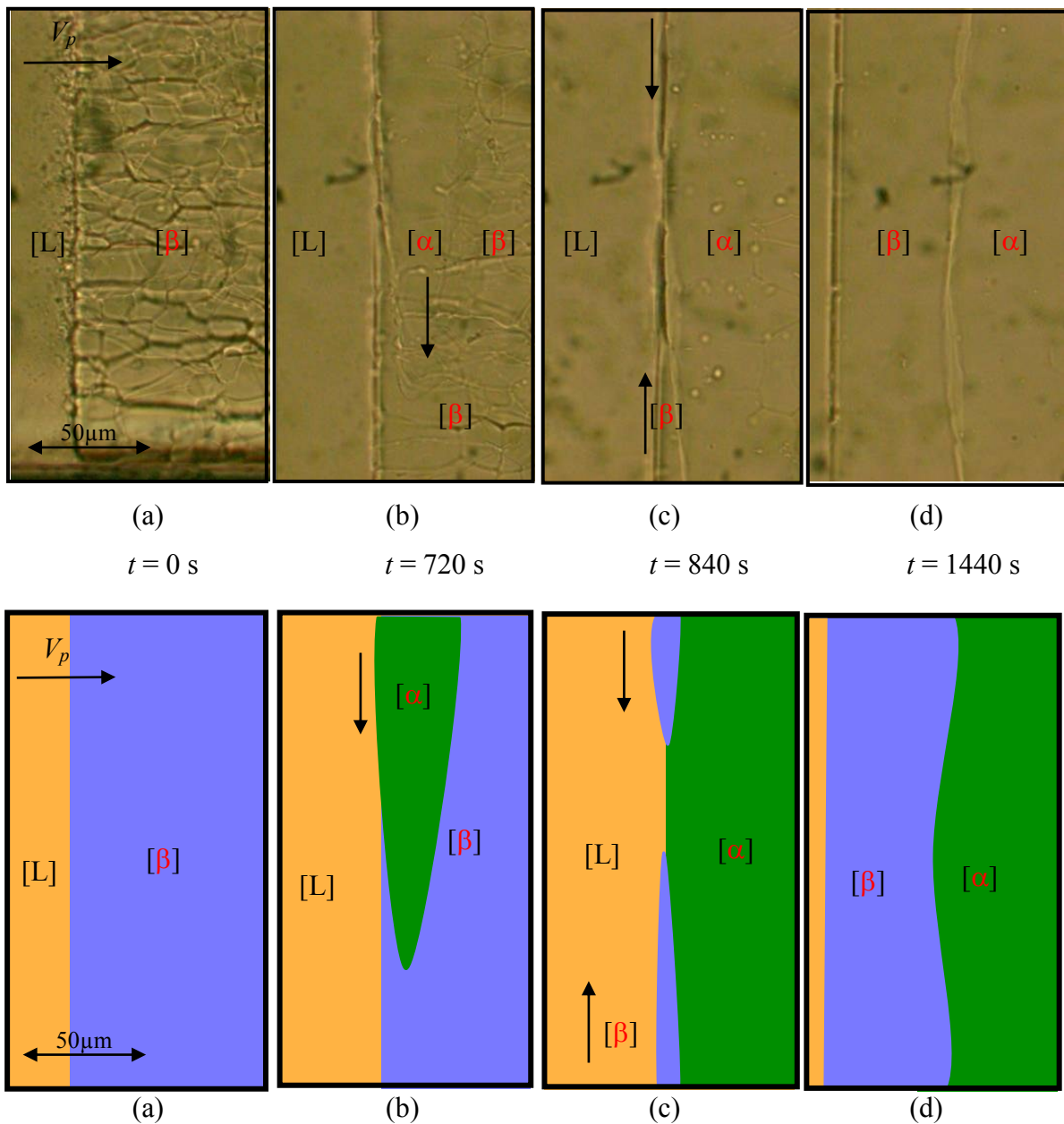


Figure 54: Development of a banded structure for an alloy with  $x = 0.51$  mol fraction NPG. (a) Initial situation after melting. (b) Growth of the  $[\alpha]$  phase from the outside to the center. (c) Now, the  $[\beta]$  overgrow the  $[\alpha]$  phase and merge in the center of the sample. Note that the position of the focus between picture (b) and (c) is lateral shifted from the corner of the sample to the center. (d) Final solidification structure with bands of  $[\beta]$  and  $[\alpha]$  phase.

To investigate the solidification structure in detail the sample is pulled reverse with  $5.11 \mu\text{m/s}$  and with that the  $[\beta]$  phase starts to melt. The end of the lenticular embedding of the  $[\alpha]$  phase is observed in Figure 55a together with a melting of  $[\beta]$  phase matrix. In addition to  $[\beta]$  phase melting a phase transition from  $[\beta]$ - to  $[\alpha]$  was observed in form of small grains which grow discontinuously, see Figure 55b. Whereby, the  $[\beta]$  phase matrix and the grains of the  $[\alpha]$  phase melted at different temperature levels with  $\Delta T = 0.2 \pm 0.05 \text{ K}$  (Figure 55c).

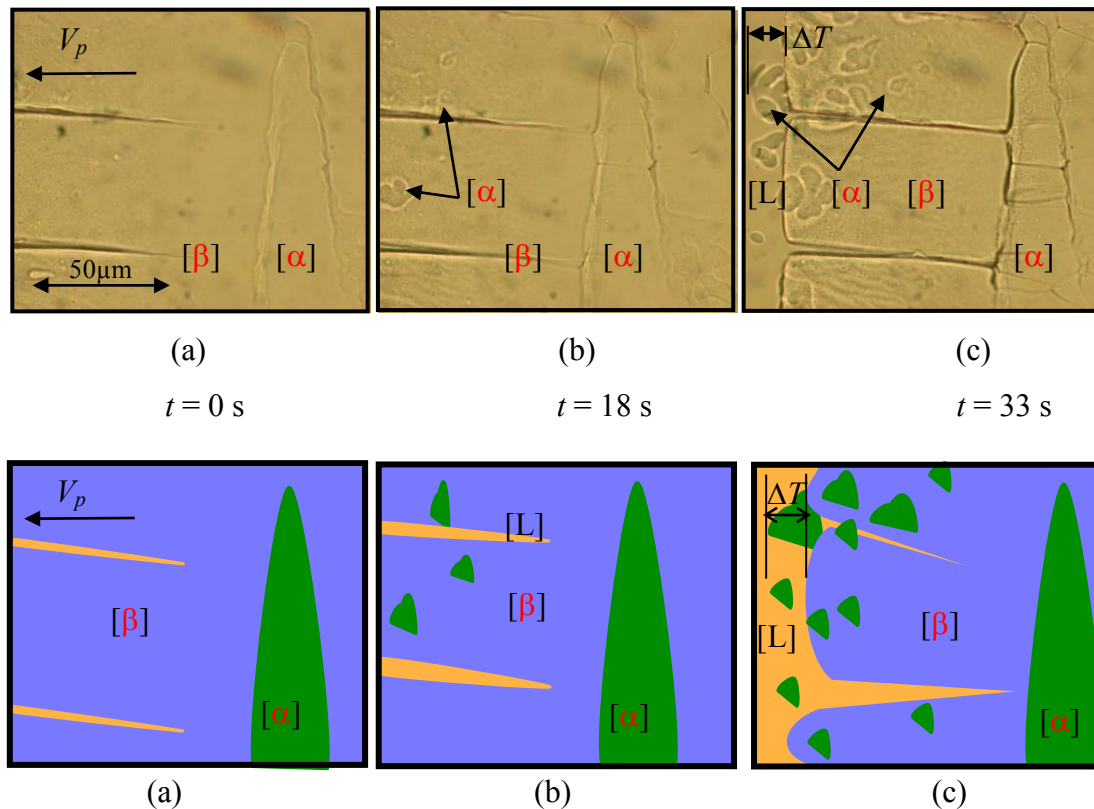


Figure 55: Melting of the  $[\beta]$  phase matrix ( $x = 0.51$  mol fraction NPG). (a)  $[\beta]$  phase matrix with the lenticular embedding  $[\alpha]$  phase. (b) Phase transition  $[\beta]$  to  $[\alpha]$  within the  $[\beta]$  phase matrix. (c) Different melting temperatures ( $\Delta T$ ) between the  $[\beta]$  phase and the  $[\alpha]$  phase.

#### 5.2.4 Oscillating Morphologies

The solid/liquid interface shows strong oscillations for concentrations of  $x = 0.5$  and  $0.6$  mol fraction NPG at a pulling rate of  $V_p = 0.89 \mu\text{m/s}$  coupled with a change in morphology from dendritic to cellular/planar and backwards. In all cases the initial solid/liquid interface was overgrown by a new phase during the time to establish a planar solid/liquid interface, like in Figure 50 on page 72.

##### Oscillating morphology for $x = 0.5$ mol fraction NPG

An overview of a cycle of an oscillation is shown in Figure 56. The oscillatory growth turned out to be different from the formation of an alternating sequence of  $[\alpha]$  and  $[\beta]$  bands parallel to the solidification front. The starting point for the present oscillations is a side-by-side growth of arrays of  $[\alpha]$ - and  $[\beta]$ -cells. Both arrays of cells try to form a more or less planar growth front, until a sudden instability leads to the formation of fine cells of both types, which are now able to grow faster. Afterwards, the tips thicken again and thus the interface/tip temperature starts to drop. Close to a “planar” growth of the two cellular arrays the oscillation starts again. The described mechanism for an oscillatory growth has, to the authors’ knowledge, never been observed before.

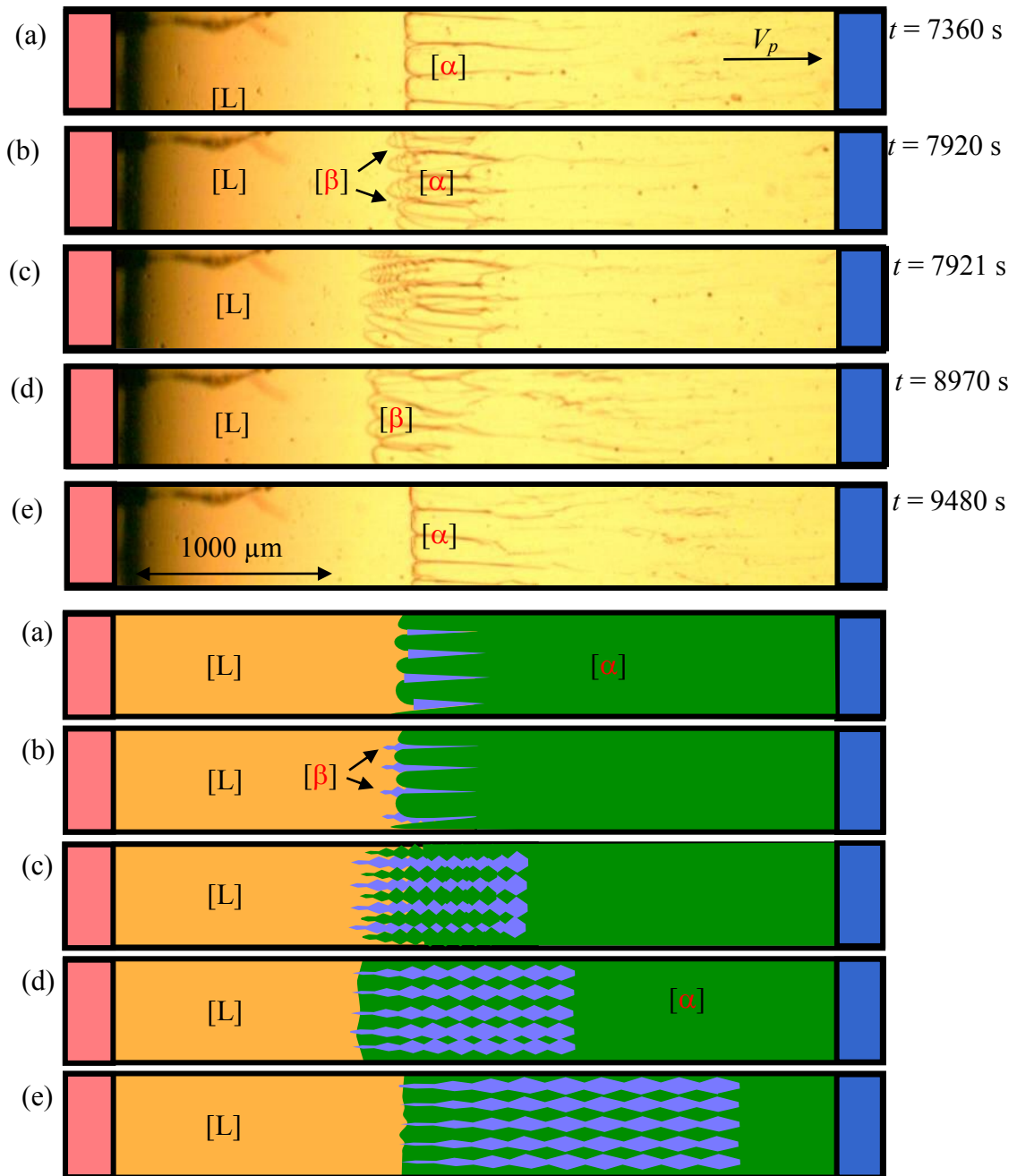


Figure 56: The pictures and the sketches show the oscillation of the solid/liquid interface as a function of time. Both phases  $[\beta]$  and  $[\alpha]$  grow at the same time in a competitive manner. (a) The primary phase  $[\alpha]$  grows in form of cells with the peritectic phase  $[\beta]$  between the cells. (b) The peritectic phase  $[\beta]$  starts to solidify as dendrites. (c) The primary phase starts to grow within the interdendritic liquid. (d) The peritectic phase  $[\beta]$  overgrows the primary phase and forms a cellular solid/liquid interface. (e) The primary phase tries to grow at the solidus line whereas the peritectic phase  $[\beta]$  starts to grow again.  $V_p = 0.89 \mu\text{m/s}$ .

The strong oscillation of the solid/liquid interface from Figure 56 is clear visible in Figure 57.

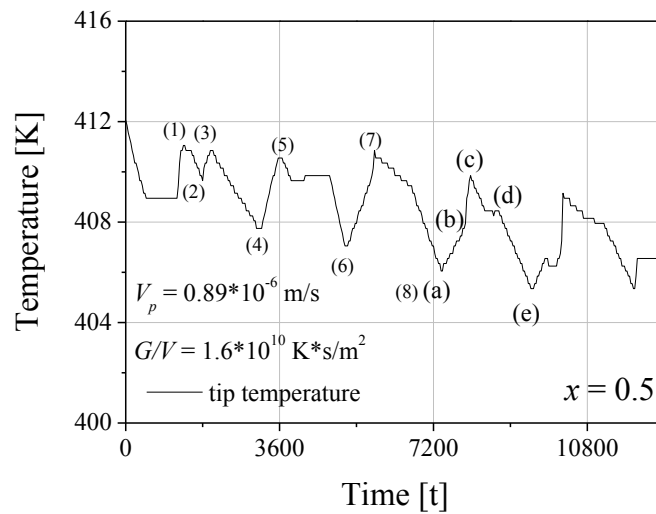


Figure 57: The graph shows the oscillation of the cell tips temperature from Figure 56 as a function of time.

Another form of oscillation for the same concentration and the same boundary conditions are shown in Figure 58. Like in Figure 56, the solid/liquid interface altered from dendrites to a planar/cellular morphology.

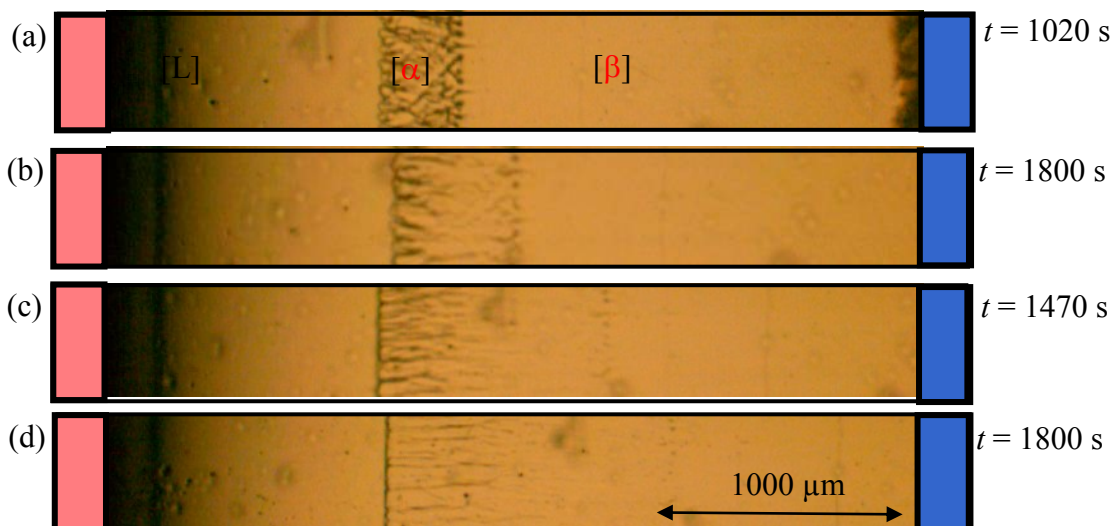


Figure 58: Solidification morphologies of the solid/liquid interface with  $x = 0.5$  mol fraction NPG and  $V_p = 0.89 \mu\text{m/s}$ .

Here, only two peaks are observed, see Figure 59. Furthermore, the estimated initial solid/liquid interface temperature is below the expected temperature for the selected alloy, see Figure 57 and Figure 59.

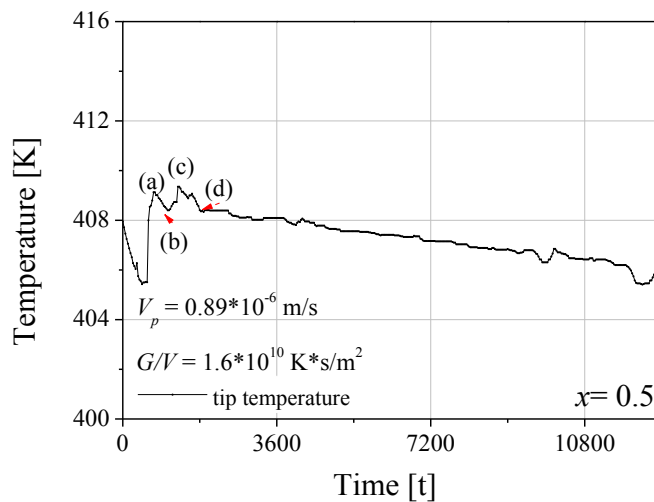


Figure 59: The graph shows the temperature at the position of the tips for the concentration  $x = 0.5$  and a pulling rate of  $V_p = 0.89 \mu\text{m/s}$ . In the first hour the interface oscillates, grows stable for 2 hours and starts to oscillate again. The extremes marked with letters correspond to Figure 58.

#### Oscillating morphology for $x = 0.6$ mol fraction NPG

An oscillating solid/liquid interface was also observe for an alloy with  $x = 0.6$  mol fraction NPG, which is clearly outside the peritectic region ( $0.47 \leq x \leq 0.54$ ). The initial planar front moves from the liquidus temperature towards the solidus temperature. Suddenly, the planar interface changes to dendrites and starts to grow at a higher temperature, see Figure 60.

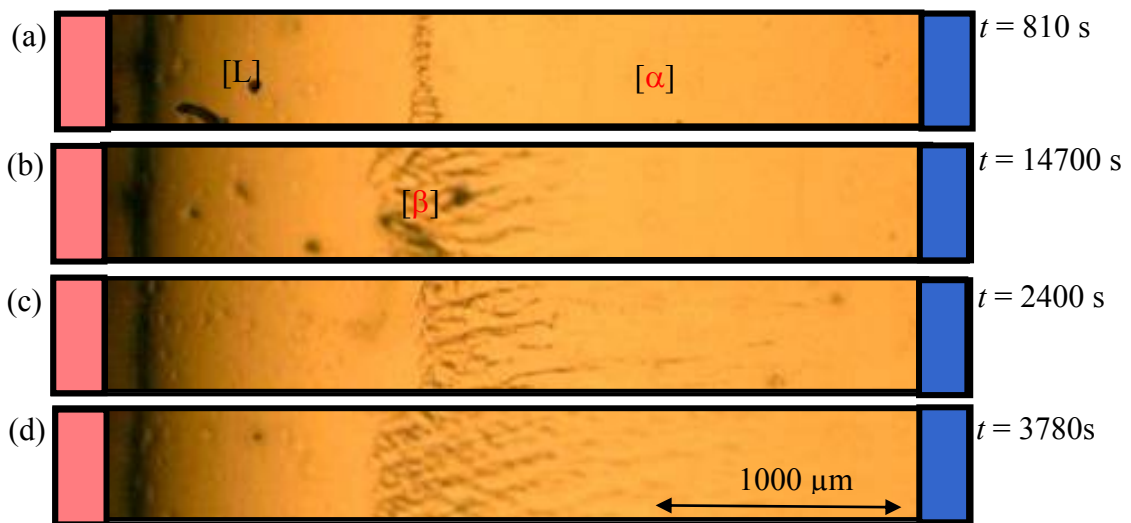


Figure 60: The pictures show the solidification morphologies occurring at each extreme in Figure 61 (marked with letters).

As soon as the dendrites reached the position at a higher temperature the dendritic solid/liquid interface decrease again to a lower temperature. From this position the dendrites moves again forward and grows as dendrites without any further oscillating morphology.

The corresponding temperature of the tip temperature versus time is given in Figure 61. The oscillation shows only 2 peaks, like in Figure 59, but the form is more like in Figure 57.

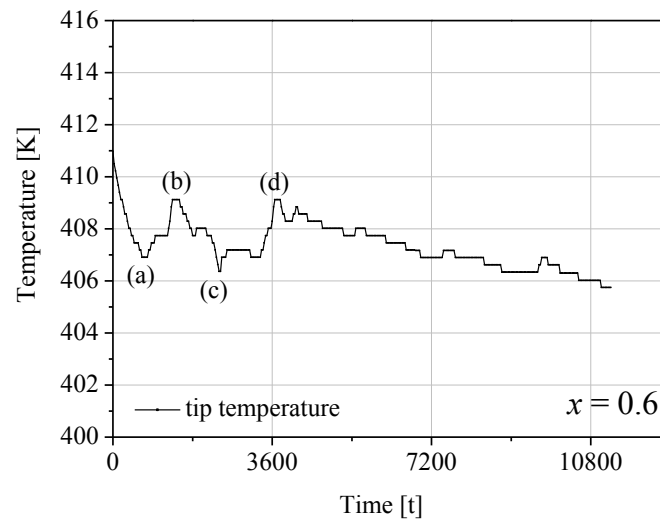


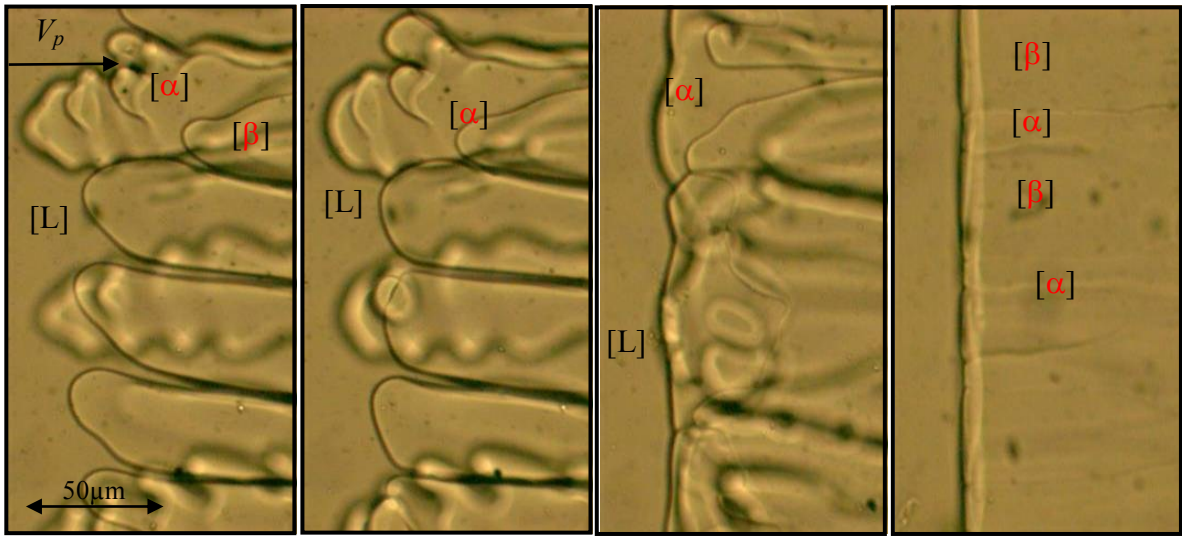
Figure 61: The graph shows the temperature of cell/dendrite tips for the alloy with  $x = 0.6$  mol fraction NPG. Compared to the phase diagram, the concentration is clearly outside of the region where a peritectic reaction or layered structures are expected (Figure 17 on page 25). The experiment is finished after 3 hours.



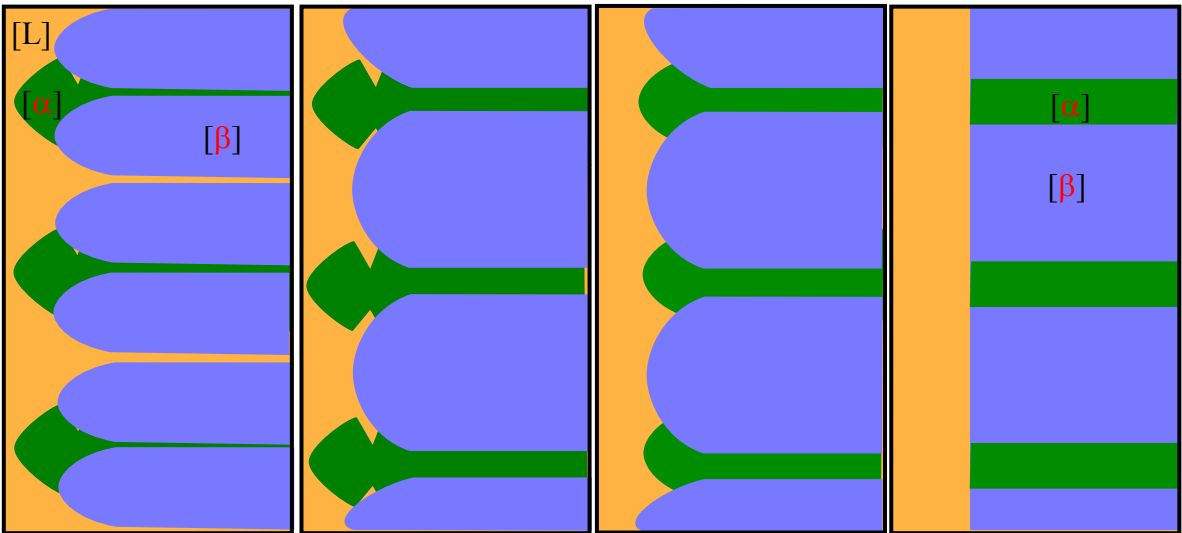
### 5.2.5 Coupled Growth Morphologies

Peritectic concentration  $x = 0.5$  mol fraction NPG at a pulling rate of  $V_p = 0.19 \mu\text{m/s}$

The formation of the isothermal coupled peritectic growth starts from simultaneous growth of the primary  $[\alpha]$  phase and the peritectic  $[\beta]$  phase. Figure 62 shows  $[\alpha]$ -dendrites ahead of  $[\beta]$ -cells (see also Figure 77 on page 105). By reducing the withdrawal speed, the phases tend to form two planar solid/liquid interfaces,  $[\alpha]$  in background and  $[\beta]$  in front. As the  $[\alpha]$  and  $[\beta]$  interface morphologies get closer and closer to planarity they approach each other. By careful observations in corresponding video sequences it becomes obvious that the  $[\alpha]$ -phase starts to form islands at the planar liquid/ $[\beta]$  interface (not shown here), which then form lamella which grow side-by-side with  $[\beta]$ -lamella.



(a)  $t = 0$  s  
 (b)  $t = 120$  s  
 (c)  $t = 510$  s  
 (d)  $t = 2430$  s



(a) (b) (c) (d)

Figure 62: Development of coupled peritectic growth morphologies by reducing the pulling velocity from  $0.64 \mu\text{m/s}$  down to  $0.19 \mu\text{m/s}$  ( $x = 0.5$ ). The transition from a dendritic/cellular interface to planar solidification morphology took around 900 s. Note that the  $[\alpha]$  phase grows as dendrites and cells ahead of the  $[\beta]$  cells. (a-b) The dendritic structure of phase  $[\alpha]$  transforms to a cellular morphology. (c-d) Both phases change from cellular to planar solid/liquid interface. The sketches of the solidification morphology show only a rough overview.

Peritectic concentration  $x = 0.51$  mol fraction NPG at a pulling rate of  $V_p = 0.19 \mu\text{m/s}$

The solidification morphology with  $x = 0.51$  mol fraction NPG shows a transformation from banded solidification to coupled growth.

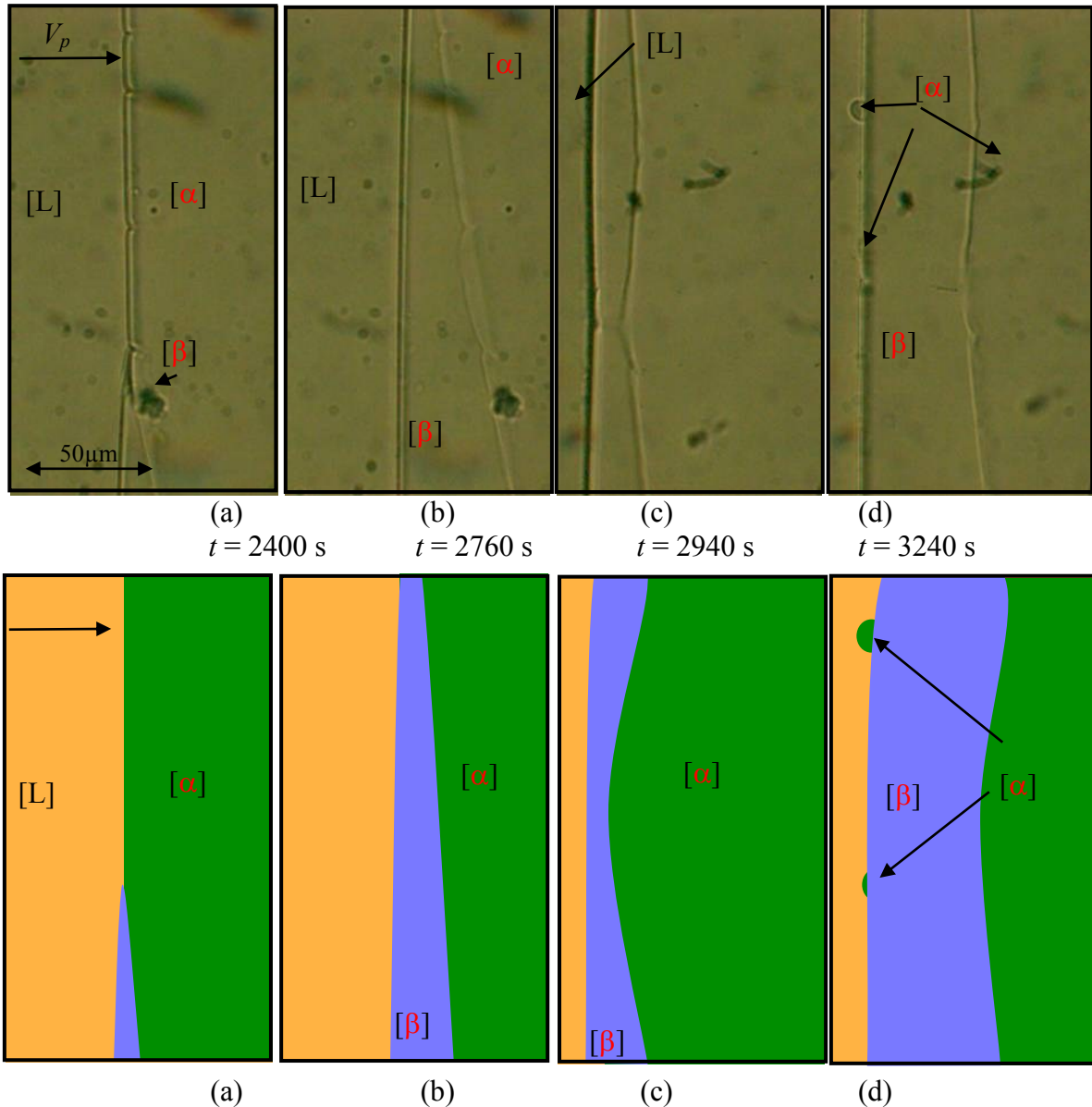


Figure 63: (a - b) Growth of the  $[\beta]$  phase in front of the  $[\alpha]$  phase ( $x = 0.51$  mol fraction NPG). (c) The  $[\beta]$  phase overgrows the  $[\alpha]$  phase. (d) Obviously, the  $[\alpha]$  phase starts to solidify in front of the solid/liquid interface of the  $[\beta]$  phase.

The evolution of the banded structure can be seen in Figure 63. The solid/liquid interface of the  $[\alpha]$  phase, was overgrown by the  $[\beta]$  phase after 40 minutes after the beginning of the experiment (Figure 63a and Figure 63b). The  $[\beta]$  phase grows laterally from both solid/liquid/wall junctions of the sample. The entire  $[\alpha]$  phase was overgrown after

approximately 10 minutes. The planar solidification front of the  $[\beta]$  phase grows stable until the  $[\beta]$  phase nucleates again in front of the solid/liquid interface (Figure 63a, 2 minutes later).

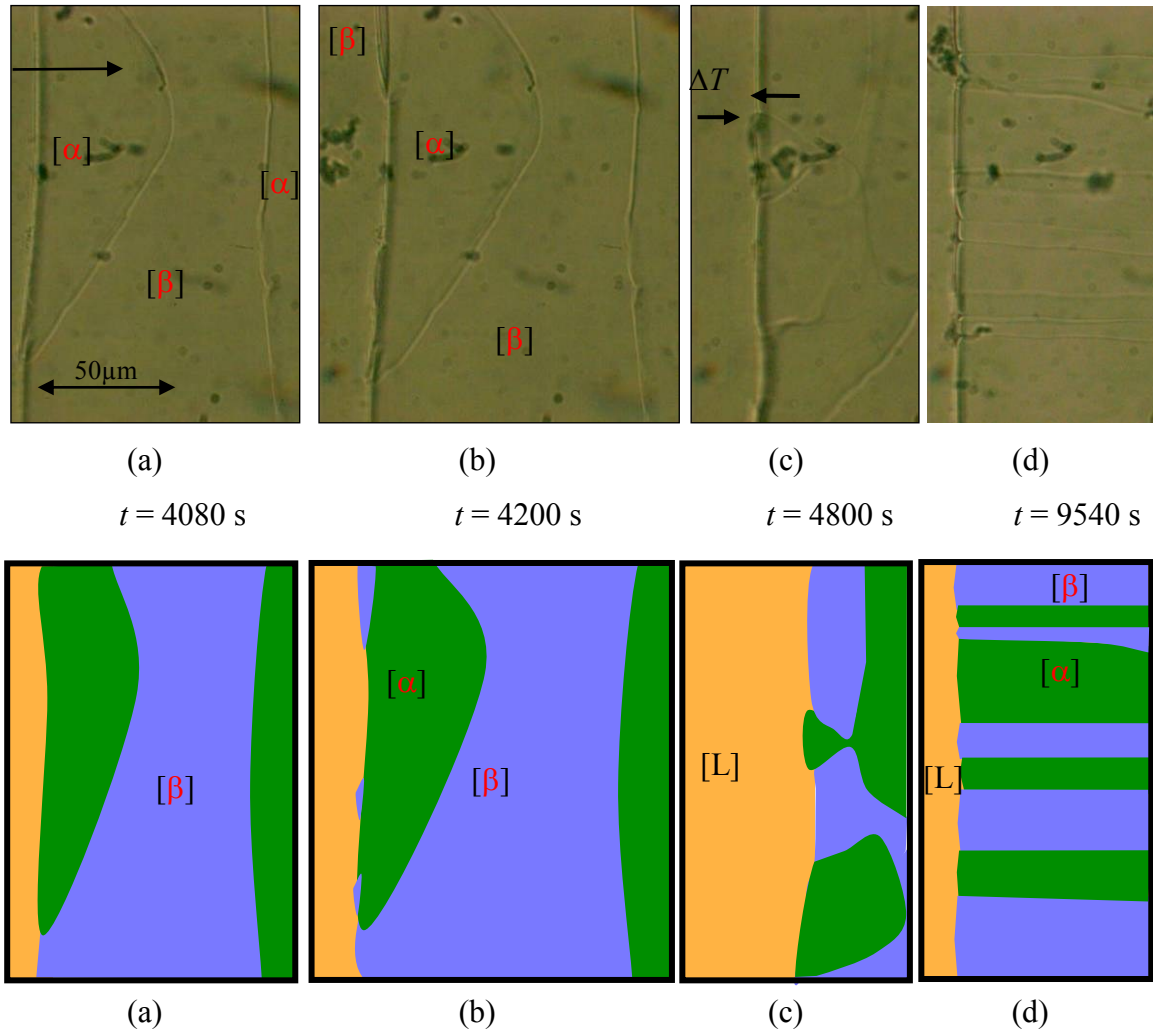


Figure 64: Alternating growth of the  $[\alpha]$  and  $[\beta]$  phases and the evolution from banded to couple growth. The phases are intertwined and the sketches below the pictures give only a rough overview: (a) growth of solidification bands; (b) nucleation of the  $[\beta]$  phase ahead of the  $[\alpha]$  phase; (c) lateral growth of the phase leads to a local undercooling ahead of the phase and to a somewhat chaotic growth behavior; (d) finally a stable coupled peritectic growth occurs.

The  $[\beta]$  phase grows laterally and in solidification direction, as shown in Figure 64a. Since the  $[\beta]$  phase grows at a lower solid/liquid interface temperature compared to the  $[\alpha]$  phase, the  $[\alpha]$  nucleates on various positions in front of the interface of phase  $[\beta]$ , 15 minutes later as shown in Figure 64b. The nucleation of the  $[\alpha]$  phase on various positions ahead of the  $[\beta]$

phase doesn't lead to a new band, see Figure 64b. Instead the nucleation frequency increases and growth becomes chaotic (Figure 64c) and changes within 20 minutes to coupled growth. Figure 64d shows the coupled growth alternating a phase with larger  $\lambda_\beta$  lamella width and smaller  $\lambda_\alpha$  lamella width. The coupled solidification was stable for more than 7 hours.

Peritectic concentration  $x = 0.48$  mol fraction NPG at a pulling rate of  $V_p = 0.19 \mu\text{m/s}$

The transformation from banded solidification to isothermal coupled growth for a peritectic concentration with  $x = 0.48$  is shown in Figure 65. The solid/liquid interface of the  $[\alpha]$  phase was overgrown by the  $[\beta]$  phase after 36 minutes. Like in Figure 64 nucleation on various positions in front of the interface leads to coupled growth solidification structure.

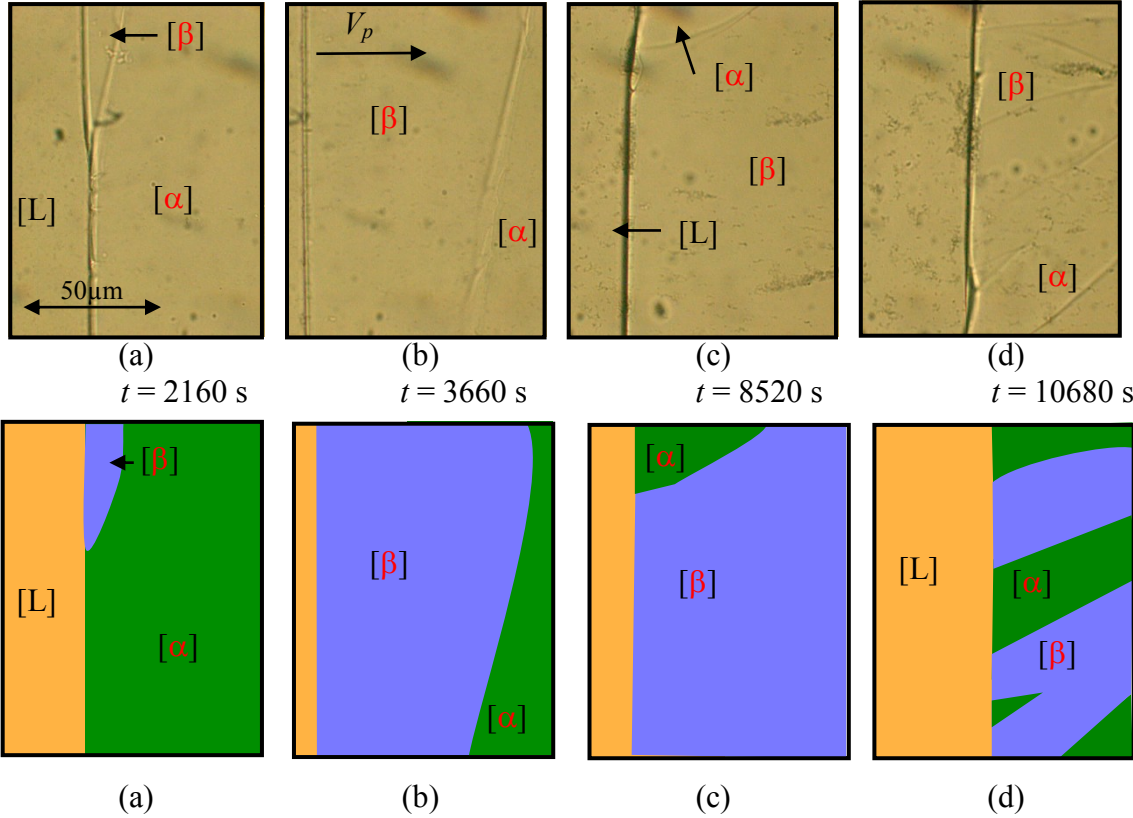


Figure 65: (a - d) Solidification sequence from  $[\alpha]$  phase to  $[\beta]$  phase and finally to peritectic coupled growth.

## 6 Discussion

During directional solidification of peritectic systems, layered solidification structures are expected for near peritectic concentrations and solidification rates where the primary and peritectic phase solidify with a planar solid/liquid interface. Based on the results of the experiments for the binary organic system TRIS – NPG the expected layered solidification morphologies were found. Furthermore, the results for this system show a wide range of layered solidification morphologies and permit a detailed study at how layered solidification structures occur. Parts of the results are published in [75, 76].

Principally it is not possible to optically distinguish between the primary phase [ $C_1$ ] and the peritectic phase [ $C_F$ ]. Therefore, the interpretation of the phases is based on the whole experimental observation of the entire phase diagram. Additionally, solidification morphology of the solid/liquid interface close to the critical velocity for [ $C_1$ ] and [ $C_F$ ] phases are used as a cross check (see Figure 44 and Figure 46 on page 66 and 68).

### 6.1 Experimental Type A: Unmoved Samples

#### 6.1.1 Thermal Stability

The thermal stability of the organic substances TRIS and NPG were investigated by DSC measurements (see chapter 4.3.3.). A thermal stability for 4 hours was detected at the selected process conditions (see chapter 4.4.1). Nonetheless, the thermal stability of (i) TRIS and NPG and (ii) selected alloy concentrations were investigated within the constant temperature gradient. While the sample stayed unmoved within the Bridgman-furnace, the positions of the phase transitions were recorded.

(i) For TRIS, the selected temperature in the hot zone of the Bridgman-furnace has to be kept close to the liquidus temperature of TRIS to avoid decomposition [61] (see chapter 4.4.2). As a consequence, only the plastic phase [ $C_1$ ], the solid/solid interface and the faceted phase [O] were visible within the adiabatic gap (see Figure 34a on page 57). The solid/solid transition interface stayed at a fixed position so that the corresponding interface temperature remains stable and constant. After 8 hours the solid/liquid interface was visible and another 10 hours later it reached the solid/solid interface, see Figure 34e. Subsequently, 18 hours after the start of the experiment the plastic phase [ $C_1$ ] disappeared totally and the liquid was in direct contact with the faceted phase [O].

The decomposition of the plastic phase  $[C_1]$  was measurable by the change of the position of the solid/liquid interface within the adiabatic zone. The position of the solid/liquid interface changes by  $1.9 \pm 0.6$  K/h, see Figure 35 on page 58.

After the experiment the sample was removed from the Bridgman-furnace and cooled down to room temperature. The part of the sample which has been within the hot zone stayed transparent while the rest of the sample became faceted. The sample was stored at room temperature, whereby, the transparent part of the sample remains optically unchanged. After one month the sample was used again for a new non-moving experiment. The transparent part of the sample was put again into the hot zone of the furnace. The experiment showed the same behavior as described above. Additionally, the transparent part of the sample was now light brown and full of small bubbles, properly consisting of TRIS (vaporization),  $\text{NH}_3$ , and  $\text{H}_2\text{O}$ , similar indicating behavior was observed in chapter A.3. The optical investigations of TRIS confirms the results of the DSC measurements, therefore, TRIS can be used only with great care.

NPG shows only a small shift of  $0.4 \pm 0.1$  K of the solid/liquid interface during the solidification experiments within 18 hours, see Figure 37 (page 60). Therefore, NPG can be used without care at the selected process conditions.

(ii) Selected alloy compositions were prepared in different steps of 10 % to investigate the entire phase diagram. In the peritectic region additional concentrations are selected. The solid/liquid interfaces became stable within the first 30 minutes and stay unchanged for the next hours, see Figure 38a and b on page 61. Approximately after 4 to 5 hours the solid/liquid interfaces of the  $[C_1]$  phase were constantly shifted to lower temperatures. Note that the observed solid/liquid interface temperature goes even below the solidus temperature. This effect of decomposition is enhanced for very TRIS-rich concentrations (Figure 38c).

The evolution of the solid/liquid interface temperatures of the pure organic substances and the alloy with time are shown in Figure 66. The shaded region shows the solid (plastic) phase and the dots for the solid/liquid interface. Figure 66a shows the situation after 1 hour. The solid/liquid interface temperatures are approximately at the same level as the temperatures of the liquidus line of the phase diagram. Within the first 4 hours the solid/liquid interface stayed fixed (Figure 66b). Afterwards, the decomposition of the TRIS-rich  $[C_1]$  phase becomes

visible. After 8 hours (Figure 66c), the solid/liquid interface temperature for concentrations of  $x \leq 0.3$  is below the solidus temperature of the phase diagram. 12 hours after the beginning of the experiment the solid/liquid interface temperature for  $x \leq 0.5$  is below the corresponding solidus temperature of the phase diagram (Figure 66d).

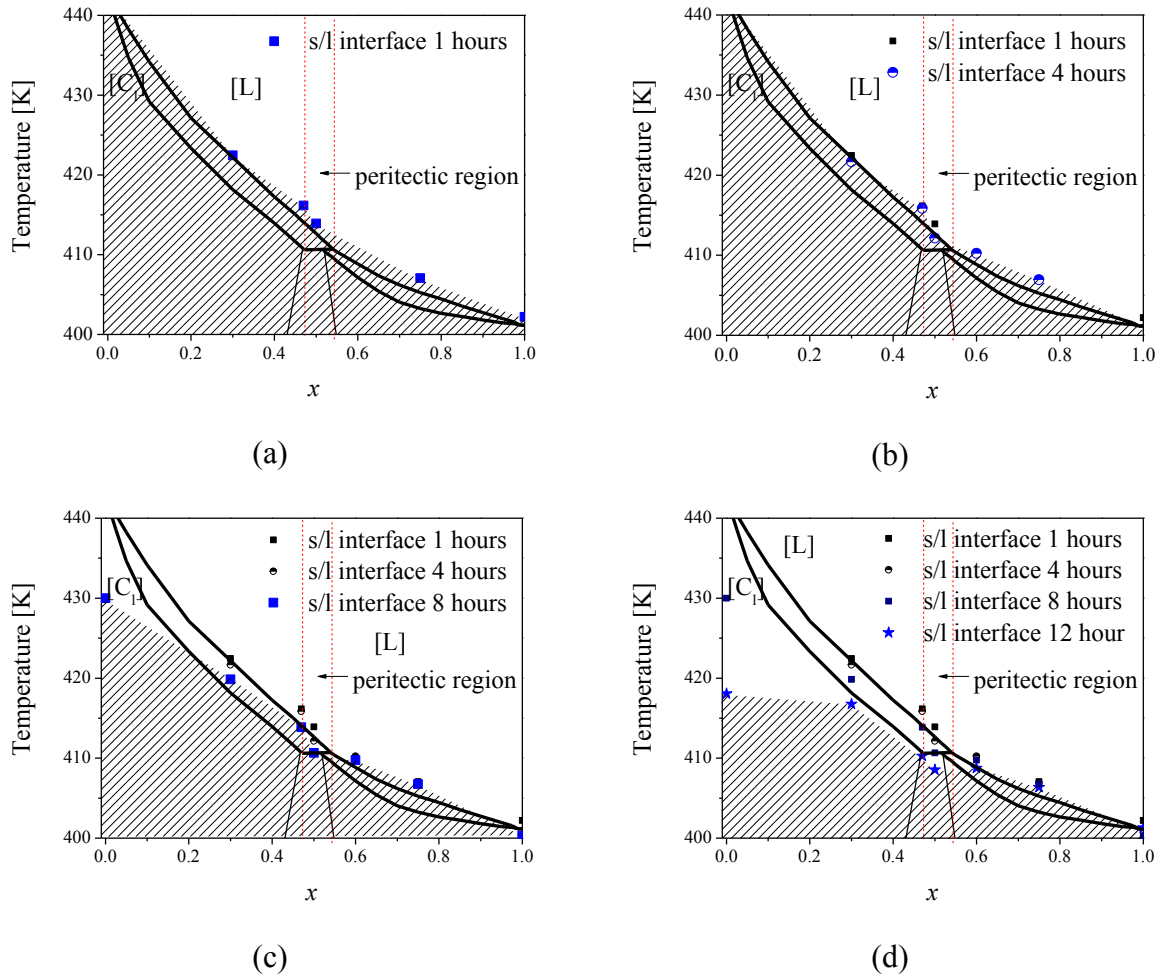


Figure 66: Effect of the decomposition of TRIS on the solid/liquid interface within 12 hours. The solid phase is shaded and the solid/liquid interface is shown as blue dots. (a) Temperature of the solid/liquid interface after 1 hour unmoved in the temperature gradient. (b) The solid/liquid interface temperatures after 4 hours. (c) after 8 hours and (d) after 12 hours. The thermal instability of the plastic phase of TRIS leads to a change of the solid/liquid interface to much lower temperatures compared to the equilibrium one.

As a consequence of the thermal stability investigations, after 4 hours the solidification morphologies are no longer used for the interpretation in combination with the phase diagram. The determination of the microstructure map requires the solidification morphology under steady state growth conditions. Whereby, solidification morphologies within the peritectic



region need more than 4 hours transition time to reach steady state conditions at a higher  $G_T/V_p$  ratio of  $1.7 \cdot 10^{-11} \text{ s} \cdot \text{K}/\text{m}^2$  (according to Eq. 8 on page 14). However, we found out that at this  $G_T/V_p$  ratio (and for higher values) the solid/liquid interface temperature shows a planar solid/liquid interface.

### 6.1.2 Wetting Angle and Nucleation Map

The precise interpretation of the experimental studies requires knowledge about the process conditions for nucleation. Trivedi [44] published a model for nucleation of the peritectic phase depending on the wetting angle. The nucleation conditions and the lateral growth rate set the process conditions for discrete bands, partial bands or coupled growth.

Nucleation at the wall–solid–liquid interface supports the growth of bands for fast spreading rate, whereas nucleation at the solid/liquid interface supports the formation of bands. Therefore, the contact angles between the wall and the phases were estimated. The plastic phase  $[C_I]$  shows a wetting angle with the glass wall of approximately  $\phi_{[C_I]} = 105 \pm 5^\circ$  and the  $[C_F]$  phase of  $\phi_{[C_F]} = 150 \pm 10^\circ$  (not shown here). To estimate the wetting angle between both plastic phases, here, the nucleation of phase  $[C_F]$  in front of the solid/liquid interface  $[C_I]$  has been investigated (see Figure 67). The observations imply a wetting angle of about  $\Phi = 40 \pm 10^\circ$ .



Figure 67 : Wetting angle  $\Phi$  between the secondary and the primary phase. The solid/liquid interface is indicated by the red broken lines.

The investigation on the wetting angles allows a general prediction for the location of nucleation [43]. Figure 68 shows the nucleation map as described by Trivedi [43]. Generally, for TRIS - NPG alloys, the nucleation map predicts nucleation at the wall-solid/liquid interface. The result of the investigation suggests the growth of particular bands and coupled growth. However, bands can only grow if the lateral growth rate is fast enough.

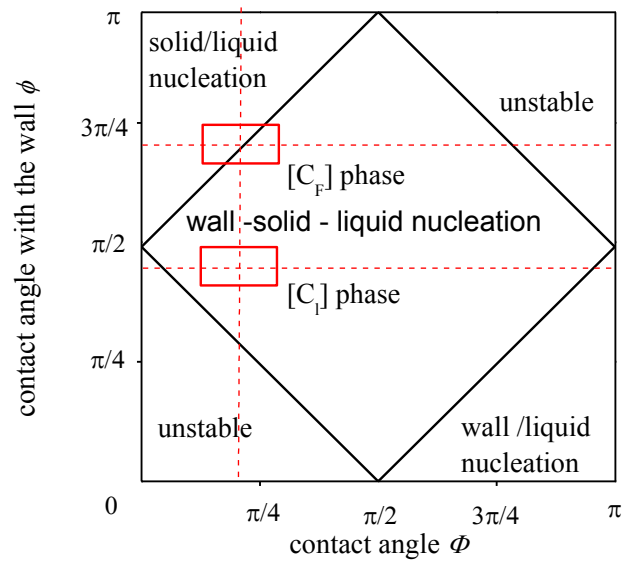


Figure 68: Possible nucleation for both phases depending on the contact angle with the wall  $\phi$  and the angle between both phases  $\Phi$ . The red square considers the possible state of nucleation for the TRIS - NPG alloys. The red broken line indicates the expected nucleation for the determined values.

## 6.2 Experimental Type B: Moved Samples

### 6.2.1 Solidification Morphology in the TRIS-rich [C<sub>I</sub>] Phase for $x \leq 0.45$

For concentrations smaller than  $x \leq 0.45$  mol fraction NPG ( $x = 0.1, 0.2, 0.3, 0.4,$  and  $0.45$ ) and for pulling rates  $V_p > 0.13 \mu\text{m/s}$ , the initial planar front changes after a certain time into a dendritic solidification morphology. Figure 44 on page 66 is representative for the solidification morphology of the [C<sub>I</sub>] phase and shows the evolution of the solid/liquid interface during the solidification experiments for the concentration of  $x = 0.3$  mol fraction NPG at  $V_p = 0.89 \mu\text{m/s}$  within the first 4 hours (see also Figure 45 on page 67).

During the solidification experiments the solid/liquid interface temperature of the planar front or the cell/dendritic tips changed from the liquidus to the solidus temperature. The solid/liquid interface transformed from a planar to dendritic solidification morphology close to the solidus temperature or above. It is expected that the tips of the dendrites are growing at a constant temperature. Here, the temperature at the dendritic solid/liquid interface decreased constantly (see Figure 45). This indicates that the plastic phase [C<sub>I</sub>] dissolves during solidification experiments as under the non-moving conditions.

The solidification morphology of samples with a pulling rate of  $V_p \leq 0.13 \mu\text{m/s}$  show a planar solid/liquid front until the plastic phase disappears ( $t \gg 4$  hours). At this point the faceted phase gets in contact with the liquid, see Figure 48 on page 70.

### 6.2.2 Solidification Morphology in the NPG-rich [C<sub>F</sub>] Phase for $x > 0.6$

The solidification morphology of alloys with  $x > 0.6$  mol fraction NPG ( $x = 0.7, 0.75, 0.8, 0.85, 0.9,$  and  $0.95$ ) and for pulling rates  $V_p > 0.13 \mu\text{m/s}$  were investigated. The solid/liquid interface grows planar until the interface reached a temperature close to the solidus temperature or even lower. In contrast to the dendritic solidification morphology in the [C<sub>I</sub>] phase, here the [C<sub>F</sub>] phase solidified cellular (Figure 46 on page 68). The cell tip temperature of the [C<sub>F</sub>] phase decreases below the solidus temperature and for very long time investigations ( $t > 24$  hours) even below the melting point of pure NPG.

Like the solidification morphology of the [C<sub>I</sub>] phase the solid/liquid interface of the [C<sub>F</sub>] phase solidify in a planar manner at a pulling rate of  $V_p \leq 0.13 \mu\text{m/s}$ .

### 6.2.3 Band Formation Observed for Concentrations within the Peritectic Region

In some experiments partial layered structure formation, see Figure 50 on page 72, or a phase transforming was observed, see Figure 52 on page 74. Only in a few experiments the formation of more than one band was detected. But in none of the experiments a peritectic reaction was observed. The investigations show banded structures for the alloy with  $x = 0.48$  and  $x = 0.51$  mol fraction NPG, see Figure 69.

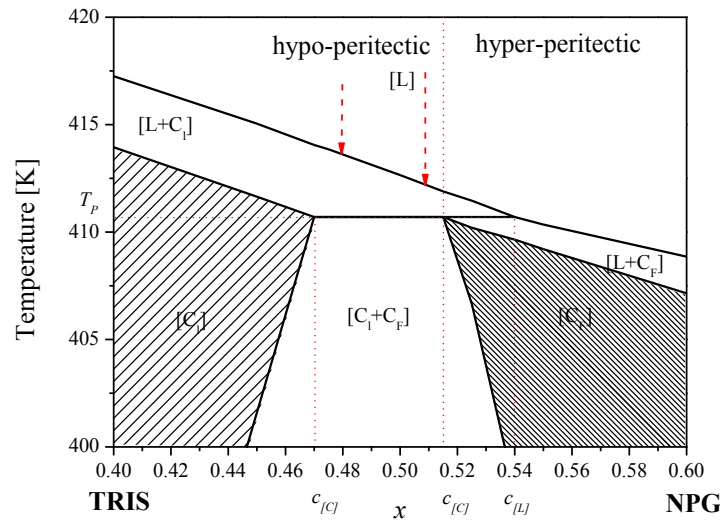


Figure 69: Peritectic region of the system NPG-TRIS. The arrows mark the concentration where bands were observed.

Since the solidification morphology of layered structures depends on the absence of convection, only a low reproduction rate was obtained. Moreover, as both phases are transparent, it is not possible to distinguish between the two phases clearly.

The following observations help to indirectly identify the correctly growing phase:

- The investigations in the  $[C_i]$  and  $[C_p]$  phase region revealed that under the same process conditions the TRIS-rich phase  $[C_i]$  shows dendritic solidification morphology (see Figure 44 on page 66), whereby the NPG-rich  $[C_p]$  phase shows cellular solidification morphology (see Figure 46 on page 68).
- The dissolving of the plastic phase  $[C_p]$  is significantly slower (Figure 47, page 69), compared to the dissolving of the  $[C_i]$  phase in Figure 45 on page 67.

- Furthermore, it is assumed that, independently from the initially growing phase, the phase that grows corresponds finally to the phase diagram.

Banded growth requires an oscillating planar solid/liquid interface due to the difference in the liquidus temperatures of the  $[C_I]$  and  $[C_F]$  phases (see Figure 11 on page 17). The solid/liquid interface of the primary  $[C_I]$  phase prefers to grow at the  $[C_I]$  solidus temperature which is at a lower temperature compared to the  $[C_F]$  one. The movement is in pulling direction, therefore, the solidification velocity of the solid/liquid interface increases. The opposite applies for the peritectic phase  $[C_F]$  which is undercooled in respect to the primary phase  $[C_I]$ . As soon as the peritectic phase  $[C_F]$  starts to solidify it prefers to grow at the solidus temperature of the  $[C_F]$  phase which is at a higher temperature. Thus, the solid/liquid interface grows against the pulling direction and the solidification velocity decreases. Therefore, during banded solidification the growth velocity of the planar solid/liquid interface with respect to the pulling velocity helps to indicate the correct phases.

Under this assumption, the determination of the  $[C_I]$  and  $[C_F]$  phase during lateral growth in chapter 5.2.5 is possible. Table 11 shows the growth velocity (parallel to the solidification direction for both plastic phases) compared to the pulling rate  $V_P$ .

Table 11: Comparison of the growth rate and the pulling rate  $V_P$  for  $x = 0.48$  and  $x = 0.51$ .

$x$	$V_p$	$[\alpha]$	error	$[\beta]$	error
	$\mu\text{m/s}$	$\mu\text{m/s}$	$\mu\text{m/s}$	$\mu\text{m/s}$	$\mu\text{m/s}$
0.48	0.19	0.21	0.03	0.13	0.03
0.51	0.19	0.21	0.03	0.14	0.03
0.51	0.19	0.21	0.04	0.18	0.02

The  $[\alpha]$  phase is indicated as the  $[C_I]$  phase because the solid/liquid interface of the  $[\alpha]$  phase moves faster than the selected pulling rate. Consequently, the  $[\beta]$  phase is the peritectic  $[C_F]$  phase.

The calculation of the expected lamella distances requires the knowledge of the undercooling  $\Delta T_N$  of both phases which is due to the constant shift of the solid/liquid interface experimentally not determinable. For an alloy of  $x = 0.51$  mol fraction NPG it is only possible to measure the width of two bands, namely which is  $76 \pm 10 \mu\text{m}$  for the  $[C_F]$  phase and  $190 \pm 10 \mu\text{m}$  for the  $[C_I]$  phase. These values agree with equation 10 and 11 (see chapter 2.1.2) if the following nucleation undercooling is chosen:  $\Delta T_N^{[C_I]} = 0.12 \text{ K}$  and  $\Delta T_N^{[C_F]} = 0.44 \text{ K}$ .

#### **6.2.4 Oscillation Observed for Concentrations within the Peritectic Region and slightly above**

As described in chapter 5.2.4 oscillating solidification morphologies are observed for concentrations of  $x = 0.5$  and  $0.6$  mol fraction NPG for  $V_p > V_c$ . Note, that the oscillatory growth, as described here, is different from the formation of an alternating sequence of  $[C_I]$  and  $[C_F]$  bands parallel to the solidification front (banded microstructures) where alternative bands grow at velocities below the limit of constitutional undercooling (planar front growth), whereas here the growth velocity is definitely larger.

The oscillations discussed in this section occur for growth velocities above the limit of constitutional undercooling. To discuss this oscillating solidification event we refer to the observations for  $x = 0.6$  mol fraction, presented in Figure 60 and Figure 61 on page 83. Detailed investigation shows the nucleation of the  $[C_F]$  phase. The initial planar solid/liquid interface of the  $[C_I]$  phase became unstable. Within the perturbations of the solid/liquid interfaces the  $[C_F]$  phase nucleated. The new phase  $[C_F]$  (red circles) differs from the perturbations of the existing phase  $[C_I]$  (blue circles) by a solid/solid interface, visible as a small black line, see Figure 70. Both phases start to grow but only the dendrites of the  $[C_I]$  phase overgrow the  $[C_F]$  phase.

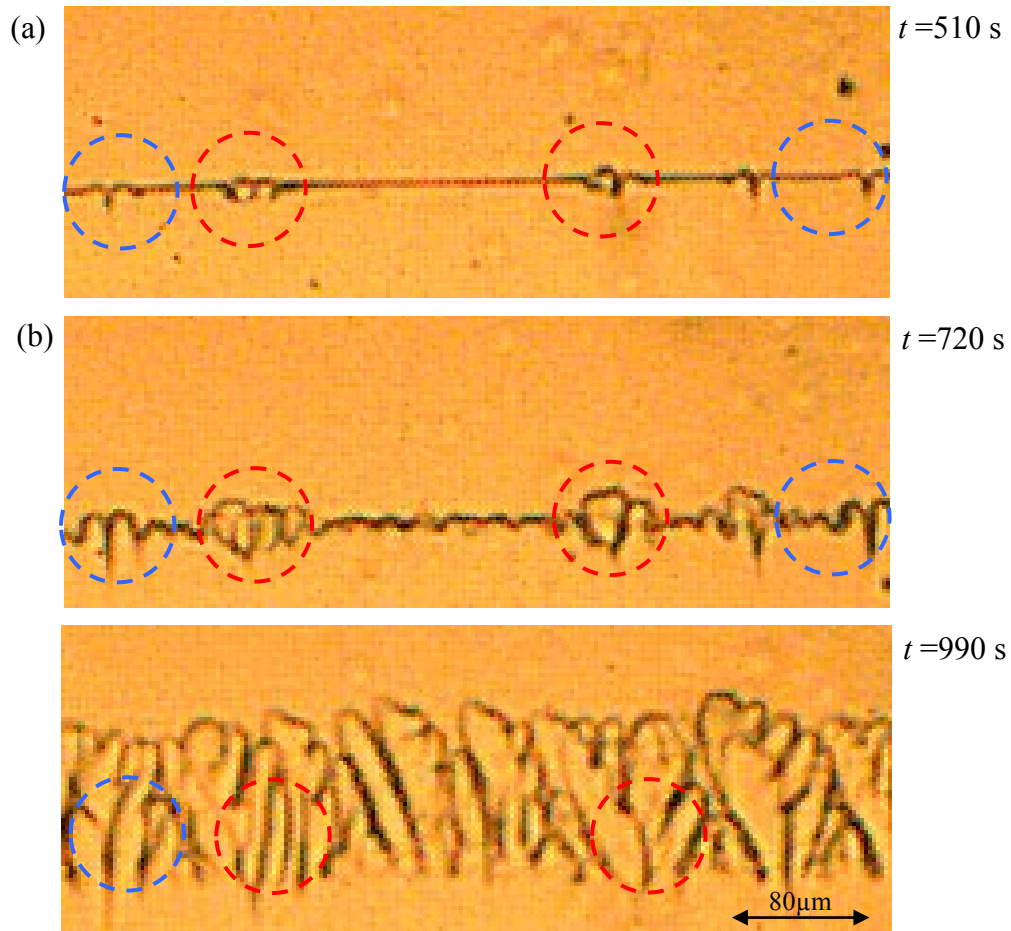


Figure 70: The figure shows the solid/liquid interface of  $x = 0.6$  mol fraction NPG in detail. (a - b) The interface becomes instable. Parts of the interface show instability (blue circle) where other parts show the nucleation of the primary  $[C_F]$  phase (red circle). (c) The  $[C_F]$  phase becomes partly overgrown by the  $[C_I]$  phase.

Figure 61 (page 84) shows the oscillation of the solid/liquid interface within first hours for  $x = 0.6$  mol fraction NPG. The dendritic interface oscillated with a 15 minutes cycle. After one hour of oscillation the solidification front grows as dendrites. The growth of dendrites under the present conditions identifies the grow phase as the  $[C_I]$  phase. It has to be noted, that in other cases when no oscillation solidification was observed (under the same boundary conditions) the solidification morphology shows instead a cellular interface.

For an alloy with  $x = 0.5$  mol fraction NPG different strong oscillations were observed. In Figure 59 (page 83) the oscillation shows only two cycles. Remarkable is the change from the initial solidification temperature at 408 K to a higher solid/liquid interface close to 409 K.

In Figure 57 on page 82 the oscillation shows 7 peaks during more than 4 hours. One oscillation time period is approximately  $2109 \pm 169$  s and the alloy solidifies over a length of  $1.89 \pm 0.15$  mm. The time period and the width of one period remain constant in this experiment. Originally started with the presence of a band and a planar solid/liquid interface, the solidification morphology changes its morphology from a dendritic front to dendrites with a higher growth velocity. The dendrites grow against the pulling direction until the interdendritic liquid starts to solidify. Meanwhile the dendrite tips reach the maximum temperature and the tip radius increases. Now the solidification stops and the dendrites transform to cells and to a cellular/planar front which falls back to lower temperature until the oscillation starts again.

Unfortunately, the increasing undercooling of the TRIS-rich  $[C_I]$  phase over time makes it difficult to compare the results of these investigations with the phase diagram. The first observed dendrites grow below the peritectic temperature and the following cycle of the oscillation grows at an even lower temperature.

Since this oscillatory solidification sequence has never been reported before, the oscillation from Figure 57 is described in more details in Figure 71 to Figure 77. The following facts limit the interpretation of the observation. Both plastic phases are transparent, therefore, it is not possible to distinguish the two phases optically. Published and measured errors of the liquidus and solidus temperature are close to the temperature difference between solidus and liquidus line. Furthermore, the TRIS-rich phase tends to decompose slightly with time.

Two ways of interpretations for the oscillating morphology are given: (i) competitive growth of both phases in comparison to the modified phase diagram and (ii) oscillation as a consequence of the solutal layer in front of the leading phase.

#### Competitive growth of both phases explained by the modified phase diagram

The assumption of a competition in growth of both phases, in comparison with the phase diagram, considers the fact that the solidus and liquidus line of both phases,  $[C_I]$  and  $[C_F]$ , decrease in each cycle. Figure 71 shows the modification of the solidus and liquidus line after 1800 s.



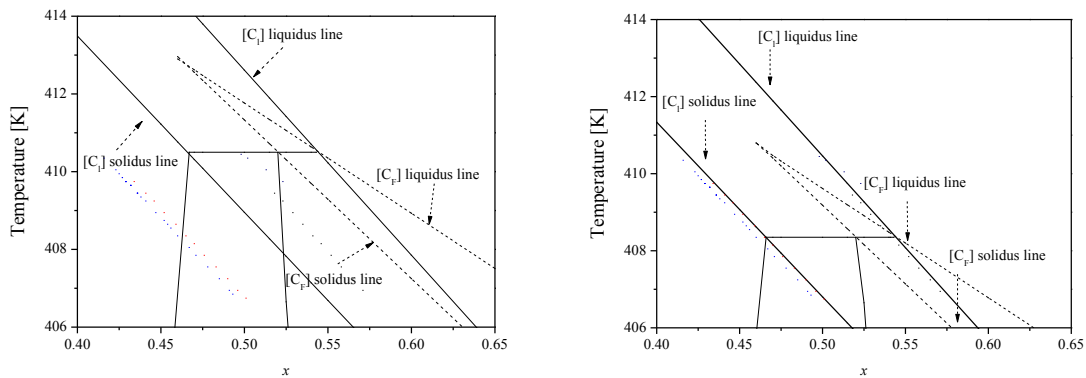


Figure 71: The graph shows a possible variation of the solidus and liquidus line to lower temperatures during solidification experiments as a consequence of the decomposition of TRIS.

Figure 73 covers the time period from the peak 3 to peak 6 as defined in Figure 57. From peak 3 to peak 6 the corresponding concentration of each cycle is given in the phase diagram, see Figure 72.

The explanation starts with the situation in peak 3 in Figure 57 on page 82. The solid/liquid interfaces of both phases ( $[C_I]$  and  $[C_F]$ ) follow the solidus line and try to reach a stable planar front (see Figure 72a, red broken arrow 1 for phase  $[C_I]$ ) Now, the solid/liquid interface is constitutional undercooled and changes its morphology from a cellular/planar front (like Figure 73a) to shallow cells and dendrites (like Figure 73b). This change of the solidification morphology is equal to the arrow 2 and 3 in Figure 72b. The dendrite tips grow against the pulling direction, see Figure 72 red broken arrow 3, to reach equilibrium at the initial concentration of  $x = 0.5$  mol fraction NPG. The shallow  $[C_F]$  cells changes to deep cells and grow behind the  $[C_I]$  dendrites.

Shortly afterwards, the concentration in the liquid reaches the concentration where the peritectic phase  $[C_F]$  can grow and the intercellular liquid again solidifies (compare Figure 73c-d). Now, both phases grow isothermally (see arrow 5 in Figure 72c). As soon as the dendrite tips of the  $[C_I]$  and  $[C_F]$  phase reach the maximum temperature the tip radii increase (Figure 73e - f). The morphology changes from dendrites to a cellular/planar front (see Figure 72 red broken arrow 6). The dendrites transform to cells (Figure 73i) and both phases then to a cellular/planar front (Figure 73j). The solid/liquid interface temperature increases, see Figure 72 red broken arrow 7 and 8. Afterwards, the solidification cycle starts again.

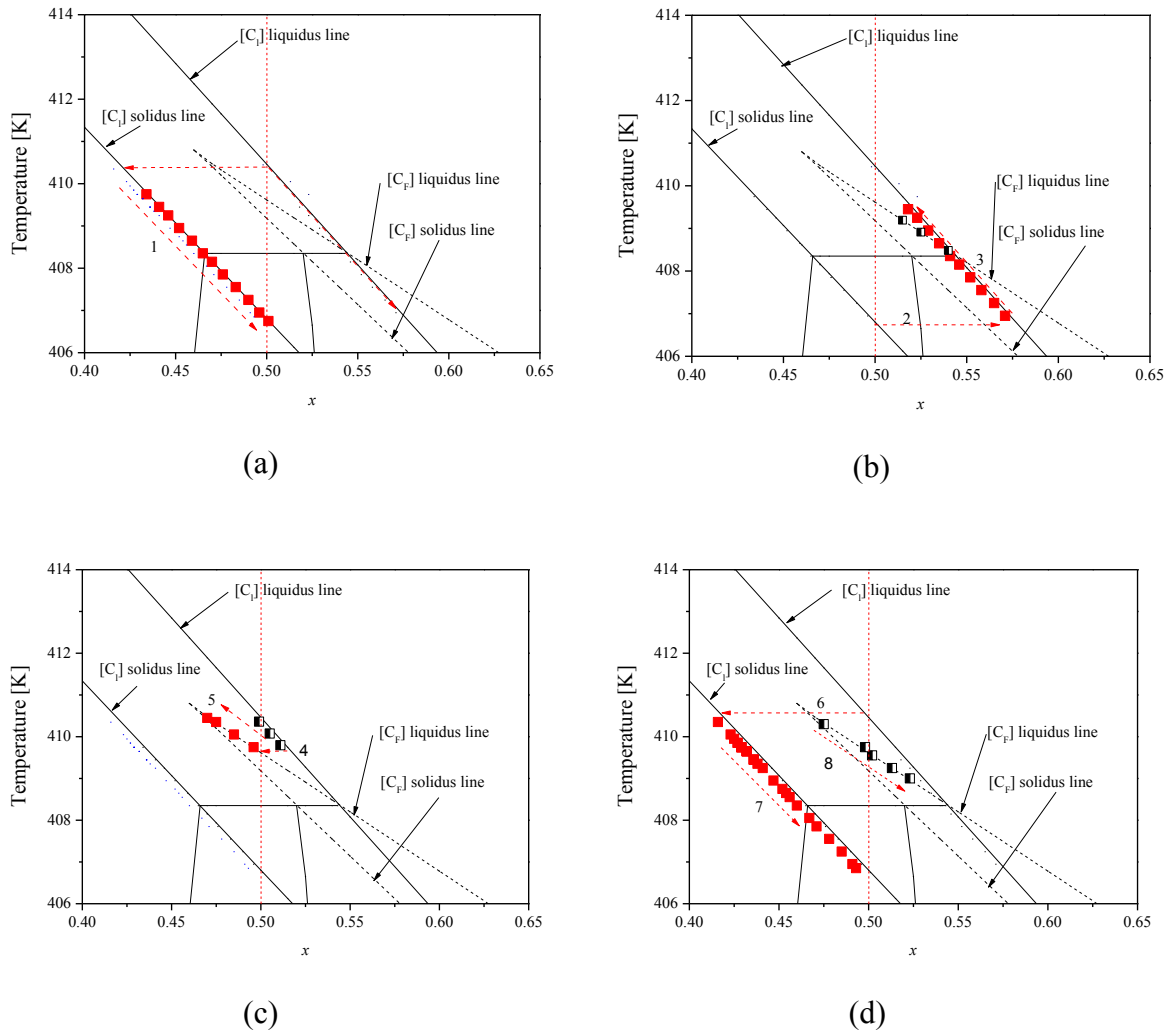


Figure 72: Cooperative oscillation growth of both phases from the peaks 3 to 6 as defined in Figure 57, whereby in each oscillation cycle the solidus and liquidus line decrease. (a) The [C<sub>I</sub>] phase (red dots) starts to grow as a nearly planar front along the [C<sub>I</sub>] solidus line (arrow 1). (b) Close to the final concentration the planar front becomes unstable (arrow 2) and grows as a dendritic [C<sub>I</sub>] and cellular [C<sub>F</sub>] solidification front back to the initial concentration (arrow 3). (c) Close to the initial concentration the undercooling in the interdendritic liquid is sufficient so that the peritectic phase [C<sub>F</sub>] (black dots) can grow (arrow 4) in addition to the primary phase [C<sub>I</sub>] (arrow 5). (d) Both phases try to grow as a planar front (arrow 6 – 8) and the loop starts again.

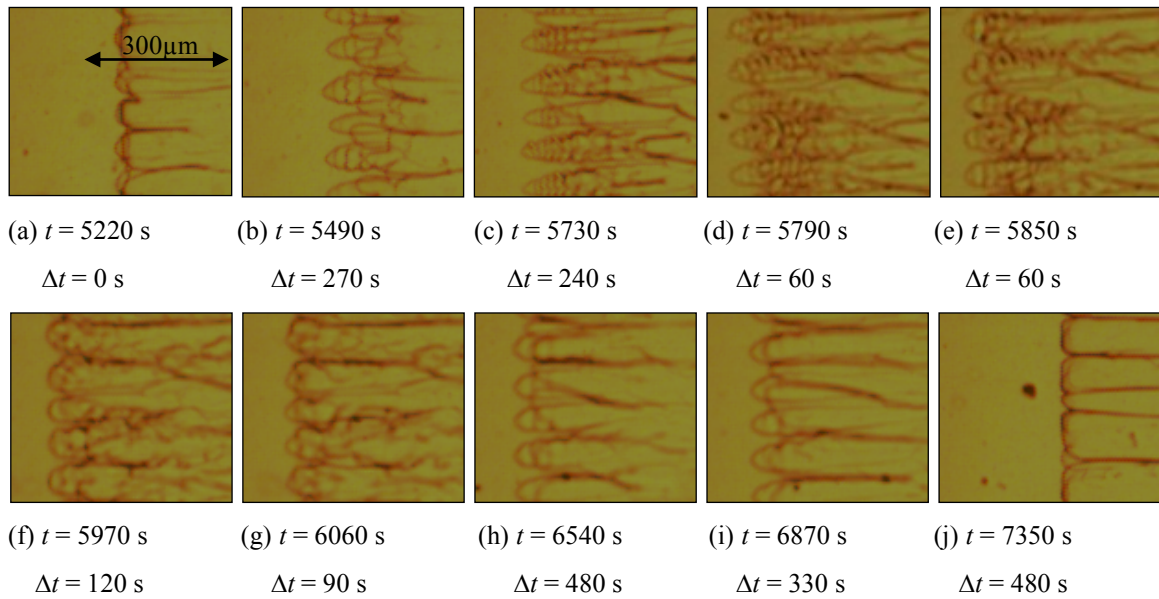


Figure 73: Details of one oscillation period from point 7 to 8 in Figure 57.  $t$  shows the absolute time position in Figure 57.

#### Oscillation as a consequence of the solutal layer in front of the leading phase

The second explanation is based on oscillation as a consequence of the solutal layer in front of the leading phase, (Figure 74 to Figure 77). Here the evolution of the growth morphology for the cycle peak 7 to peak 9 in Figure 57 ( $t = 5520$  s after start pulling to  $t = 8160$  s) is shown.

The cycle starts shortly before the minimum at  $t = 7.350$  s occurs. The morphology evolution at the minimum is shown in Figure 74 in more details. In Figure 74a, two cellular arrays can be seen, one slightly ahead of the other. In corresponding magnified pictures (Figure 62) it becomes clear that the two arrays grow at different depth in the sample.

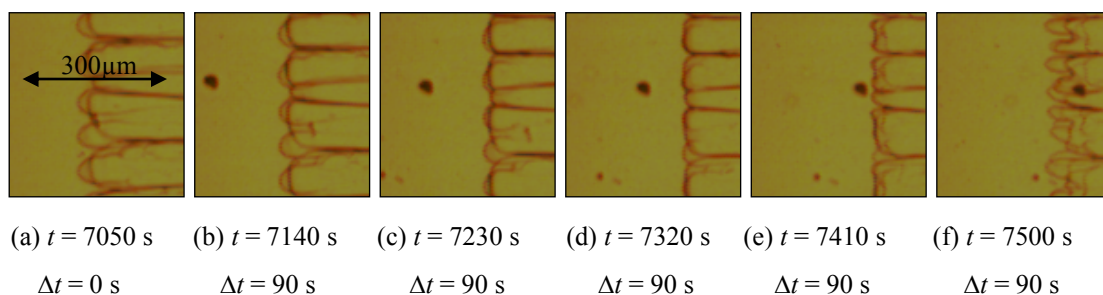


Figure 74: Growth of two cellular arrays close to the minimum interface/tip temperature. The front instability goes along with a minimum in interface/tip temperature.

In order to understand the subsequent morphological transitions, let's assume that the leading array consists of  $[C_I]$ -cells and the following of  $[C_F]$ -cells. Figure 74a-d shows that the

advance of the  $[C_I]$ -cells gradually disappears until both cellular arrays grow with the same interface temperature. However, this “side-by side” growth is obviously inherently unstable and leads to a sudden advance of smaller cells of both phases. Careful observation of morphological details makes it obvious that after the advance of the small cells of both phases the  $[C_I]$ -cells once more move ahead of the  $[C_F]$ -cells (see Figure 75).

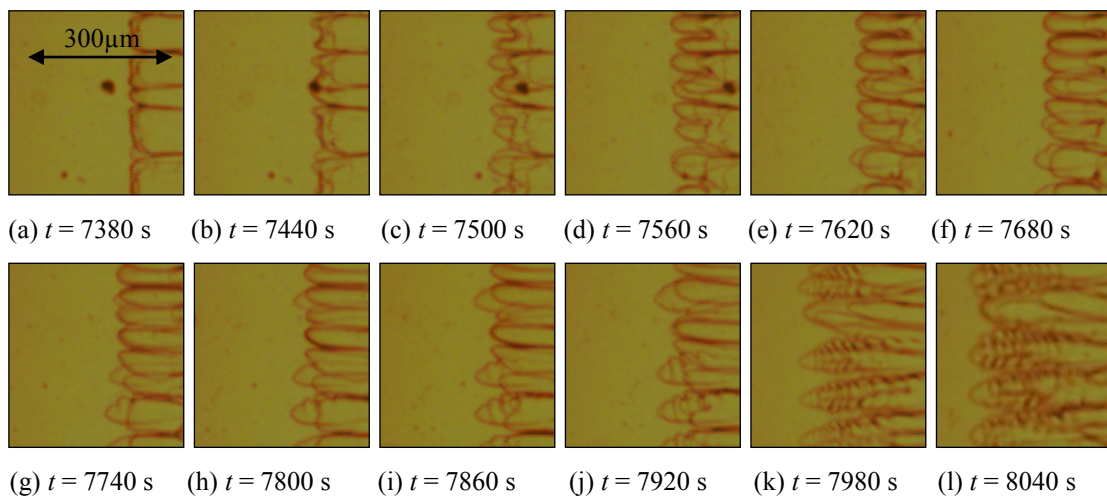


Figure 75: Two examples which show that after new finer cells of both phases occur, the fine  $[C_I]$ -cells are leading against the fine  $[C_F]$ -cells. In pictures (f) and (l)  $[C_I]$  is again the leading phase. The pictures are taken at  $t = 7.380$  s after starting pulling with a time increment of  $\Delta t = 60$  s.

The leading fine  $[C_I]$ -cells further develop into dendrites, as can be seen in Figure 76a. These isolated dendrites grow clearly ahead of the cellular front which might now consist mostly of  $[C_F]$ -cells. One might expect that the  $[C_I]$ -dendrites now gradually try to reach steady-state. Suddenly all growing objects,  $[C_I]$ -dendrites and  $[C_F]$ -cells, shot forwards, as shown in Figure 76b - d. This can be understood by considering the fact that a flat growth front which consists of deep cells (as shown in Figure 75) does have a large solute layer  $\delta = 2 \cdot D/V$  similar to a planar front. After the sudden occurrence of the fine cellular growth, these cells have to grow right into the solute boundary layer. With  $V_p = 0.89 \mu\text{m/s}$  and  $D_L = 2.0 \cdot 10^{-11} \text{ m}^2/\text{s}$  for  $x = 0.5$  mol fraction NPG (see chapter 4.1) the boundary layer can be calculated to be  $\delta = 45 \mu\text{m}$  in thickness, 2 times smaller as the observed growth length. The weakness here is that the exact solute boundary layer of each phase is unknown. Due to the fact that the tip radius of the fine cells is much smaller than that of the former larger cells, the corresponding growth diffusion field is more or less localized around the tips. Therefore, the growth velocity can increase for both, the leading  $[C_I]$ -cells/dendrites as well as the following  $[C_F]$ -cells. This leads to a

gradual forward motion of the front until the front reaches the end of the boundary layer. Here, the corresponding tips feel the initial melt composition and can further accelerate until they reach a temperature close to the related steady-state tip temperature for the fast growth.

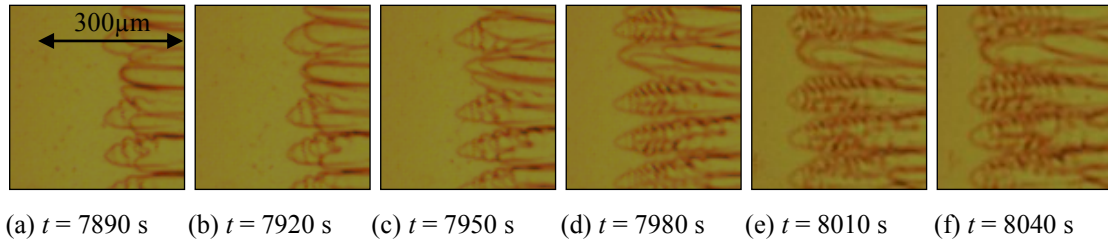


Figure 76: The leading  $[C_I]$ -dendrites as well as the following  $[C_F]$ -cells advance gradually until they reach the end of the solute boundary layer which has been formed previously. Feeling the initial melt concentration further acceleration of the tips occur until the tip temperatures are close to the related steady-state tip temperature for the fast growth. Then the tip velocity adapts to the pulling speed and tip thickening occurs. The pictures are taken  $t = 7.890$  s after starting pulling with a time increment of  $\Delta t = 30$  s.

However, now the tips have to adapt to the pulling speed, therefore, the tip radii gets larger and larger (Figure 76d - f). Note that the  $[C_I]$ - and  $[C_F]$ -tips do thicken at slightly different temperatures. The reason for that is that due to the higher liquidus temperature of  $[C_I]$ , compared to  $[C_F]$ , and due to an approximately similar tip undercooling, the tip temperature of  $[C_I]$  is higher than that of  $[C_F]$ . This argument confirms that the assumption of  $[C_I]$  being the leading phase is reasonable. It is important to notice that as soon as the tips adapt to the pulling velocity, the maximum of the interface/tip temperature cycle is reached.

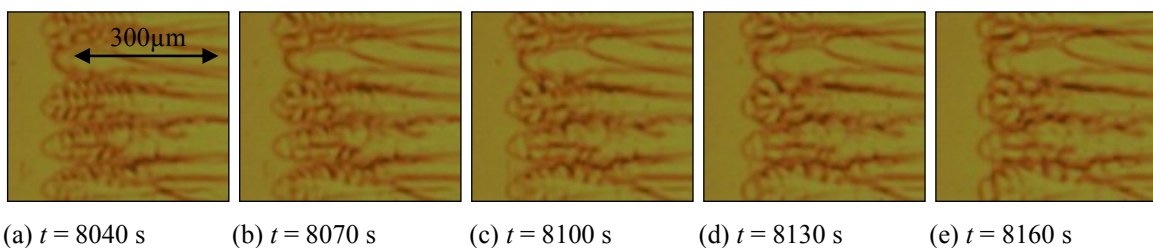


Figure 77: After reducing the growth velocity in order to adapt the pulling speed, tip thickening results in a transition from dendrite-like into cell-like growth. With that the interface/tip temperature decreases. Note that the  $[C_I]$ -cells/dendrites keep being ahead of the subsequently  $[C_F]$ -cells. The pictures are taken with a time increment of  $\Delta t = 30$  s.

With the following tip thickening (see Figure 76e - f) a change from isolated-tip-growth to a diffusion-field-overlapping-growth occurs. In consequence the tip temperatures decrease again. The difference in tip temperatures between the  $[C_I]$ -cells and  $[C_F]$ -cells remains, while the interface/tip temperature further drops. Figure 77 shows the evolution of the interface morphology from the maximum of the interface/tip temperature to its minimum. Note that Figure 77e, taken at the end of the corresponding cycle, is similar to Figure 73a, which represent the beginning of the cycle.

The solidification morphology shows that the oscillation occurs at a  $G_T/V_p$  ratio where both phases solidify not planar (above the limit of constitutional undercooling). In this region the primary phase  $[C_I]$  solidifies as dendrites where the secondary phase  $[C_F]$  forms cells ( $V_p = 0.89 \mu\text{m/s}$ ), therefore, they did not accomplish the assumptions for layered structure formation formulated in [50]. Nucleation is unnecessary because already both phases are present and solidify in a competitive manner.

### **6.2.5 Isothermal Coupled Growth Observed for Concentrations within the Peritectic Region**

Isothermal peritectic coupled growth (PCG) was discussed in literature and experimental evidences were found in [17, 22, 26, 27]. Additionally, simulation shows a wide range of different solidification within the peritectic region [26]. In this thesis, isothermal peritectic coupled growth (PCG) is observed for alloys with  $x = 0.48, 0.50$  and  $0.51$  mol fraction NPG. Within the hypo-peritectic region, see Figure 4 on page 9, close to the  $[C_\alpha]$  concentration, the peritectic  $[\beta]$  phase solidifies in form of islands within the primary  $[\alpha]$  phase. Whereby, in the hyper-peritectic region close to the  $[C_\beta]$  concentration the primary  $[\alpha]$  phase is imbedded in the peritectic  $[\beta]$  phase. In between, both phases solidify in a lamella form, like eutectic coupled growth.

In the present thesis, PCG was reached under two different conditions (i) by long-time growing with a constant velocity below the critical value for morphological stability of both solid phases, or by (ii) reducing the growth velocity from above the critical value for morphological stability of both solid phases to a value below the limit of constitutional undercooling. In both cases island banding was observed, where nucleation and lateral growth of the peritectic phase compete with growth of the primary phase. Interphase spacing and the

widths of  $[\alpha]$  and  $[\beta]$  lamellae were measured as function of growth velocity for a fixed composition and as function of composition for a fix growth velocity.

#### Isothermal PCG by competition between lateral growth and nucleation via island bands

A hypo-peritectic sample with  $x = 0.51$  mol fraction NPG transforms from discrete bands via island bands to isothermal PCG at a pulling rate  $V_p = 0.19 \mu\text{m/s}$ . The transition from banded solidification via island bands to isothermal PCG is shown in Figure 78. This overview is created by overlapping all pictures from the experiment shown in Figure 64 on page 88. The transparent appearance of both plastic phases makes the phase distinguish difficult. Whereby, the different solid phases can indirectly be differentiated by growth velocities and careful observations of the dynamic of changes in combination with the phase diagram, see chapter 6.2.3.

The *in-situ* study starts by an overgrowth of a planar  $[\text{L}]-[\alpha]$  interface by the  $[\beta]$  phase (see Figure 63, page 87). The peritectic phase grows along the solid/liquid interface and the glass wall. The planar  $[\beta]$  solidification front grows stable till the primary  $[\alpha]$  phase nucleates again at various positions at the  $[\text{L}]-[\beta]$  interface (see Figure 63d). Careful observation of the pictures reveals that the  $[\alpha]$  phase is more or less embedded in the  $[\beta]$  phase. During the lateral growth of the  $[\alpha]$  phase both phase,  $[\alpha]$  and  $[\beta]$ , solidify parallel to the solidification direction. The solid/liquid interface of both phases moves in the same direction as the sample is pulled, which means to a lower tip temperature. Whereby, the  $[\alpha]$  phase moves faster to a lower temperature than the  $[\beta]$  phase. During this, the  $[\beta]$  phase also nucleate on various positions at the  $[\text{L}]-[\alpha]$  interface, the beginning of island bands [27]. The nucleated  $[\beta]$  phase grows in lateral direction and is additional overgrown by the preexisted  $[\alpha]$  phase. Now, the forward growth of the two solid phases leads to an isothermal PCG. During the PCG, the single lamellae of the  $[\alpha]$  and  $[\beta]$  phases grow interlaced.

Studies of the solidification velocity shows a lower movement in pulling direction for the  $[\beta]$  phase compare to the  $[\alpha]$  phase and the  $[\text{C}_1]$  phase grows preferred in the peritectic region. Both findings lead to the assumption that the initial  $[\alpha]$  phase is the primary  $[\text{C}_1]$  phase and the first  $[\beta]$  phase band is the peritectic  $[\text{C}_F]$  phase, see Figure 78.

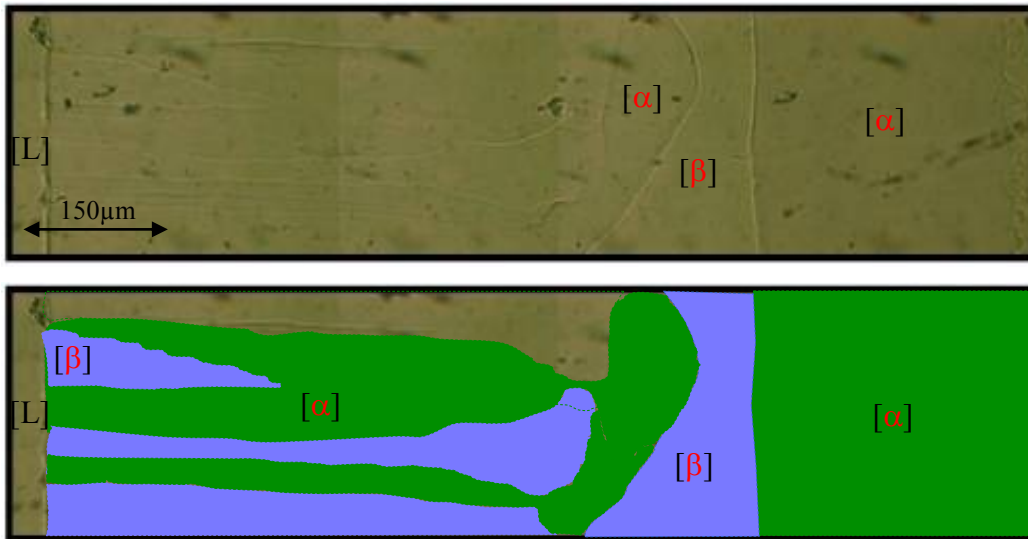


Figure 78: Banded to peritectic coupled growth via island banding. The figure gives an overview and an interpretation of the individual phases from Figure 64 on page 88.

#### Isothermal PCG by reducing the growth velocity

PCG was achievable for a hypo-peritectic alloy with  $x = 0.5$  mol fraction NPG if both phases were present. During solidification close to the limit of constitutional undercooling both phases grow at different layers. According to the peritectic phase diagram the dendrites of the primary  $[C_I]$  phase grow in front of the cells of the peritectic  $[C_F]$  phase. Here, isothermal PCG could be achieved by reducing the growth velocity from above the critical value ( $V_p = 0.64 \mu\text{m/s}$ ) for morphological stability of both solid phases to a value below ( $V = 0.19 \mu\text{m/s}$ ).

Figure 62 on page 86 shows that the array of  $[\alpha]$  dendrites and the array of  $[\beta]$  cells grow at different depth in the sample. By reducing the growth velocity the dendrites and the cells tend to form two separate planar solid/liquid interfaces. As the two interfaces come closer and closer, the  $[\alpha]$  dendrites become broader and transform into cells, see Figure 62c. Additionally, the  $[\beta]$  phase starts to form islands at the  $[L]$ - $[\alpha]$  interface, which then transform into  $[\beta]$  lamellae which grow side-by-side with  $[\alpha]$  lamellae (Figure 62d). According to the definition in chapter 6.2.3 the  $[\alpha]$  dendrites are the primary  $[C_I]$  phase and the  $[\beta]$  cells are the peritectic  $[C_F]$  phase. The entire sequence of the transformation from a simultaneous growth at different layers to PCG is visible in Figure 79.



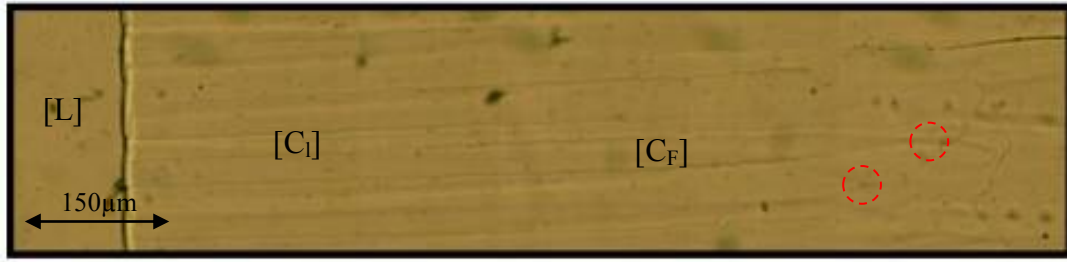


Figure 79: PCG of an alloy with  $x = 0.5$  mol fraction NPG at  $V_p = 0.19 \mu\text{m/s}$ . Selected pictures after the reducing of the growth velocity were merged together to illustrate the evolution from island banding to PCG. The beginning of the island banding of the peritectic  $[C_F]$  phase is shown by red circles.

#### Interphase spacing and width of the $[C_I]$ and $[C_F]$ lamellae

During isothermal PCG the lamellae of the  $[C_I]$  and  $[C_F]$  phase are mostly parallel and straight. Only in a few cases short wavelength oscillatory instabilities which are reminiscent to  $1 - \lambda$  instabilities occur.

Figure 80 shows the oscillatory of lamella size of the  $[C_I]$  and  $[C_F]$  phases for  $x = 0.5$  mol fraction NPG. The first 9000 s are required to form PCG. However, due the lack of sufficient results no systematical studies on this topic were possible.

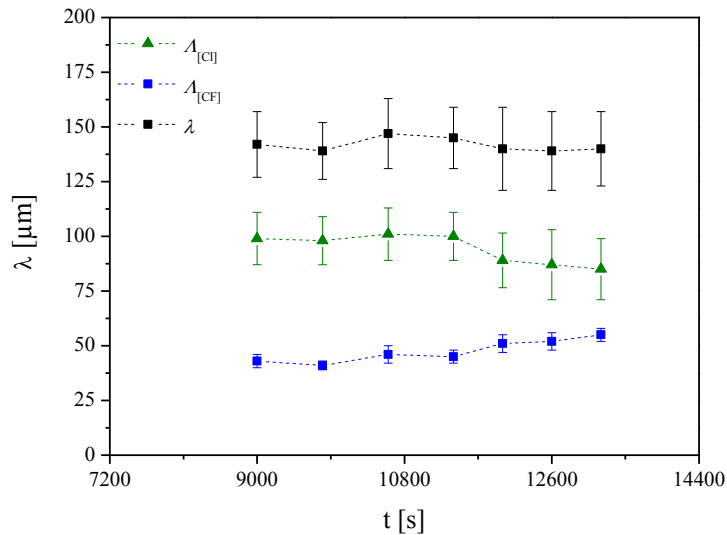


Figure 80: Lamella distance  $\lambda$  for  $x = 0.5$  mol fraction NPG and  $V_p = 0.19 \mu\text{m/s}$ . Within the first hour the distance seems to be constant. After more than 4 hours experimental time,  $A_{[C_I]}$  becomes smaller and the size of  $A_{[C_F]}$  becomes larger.

The width of the  $[C_I]$  and  $[C_F]$  lamellae as well as the interphase spacing has been estimated in an averaged manner for different moments in time and at different positions. Both phases are transparent and intertwined.

In Figure 81 the interphase spacing and width of  $[C_I]$  and  $[C_F]$  lamellae are shown as function of pulling rate for a hyper-peritectic concentration  $x = 0.5$  mole fraction NPG. From eutectic solidification it is known that the interphase spacing  $\lambda$  decreases with increasing pulling rate. Interpretation suggests here that this might be different for peritectic solidification. Although the error bar at  $V_p = 0.07 \mu\text{m/s}$  is quite large the decrease of  $\lambda$  for smaller growth velocity seems significant. Otherwise, an imbedded  $[C_F]$  phase within a  $[C_I]$  matrix would influence the measurement.

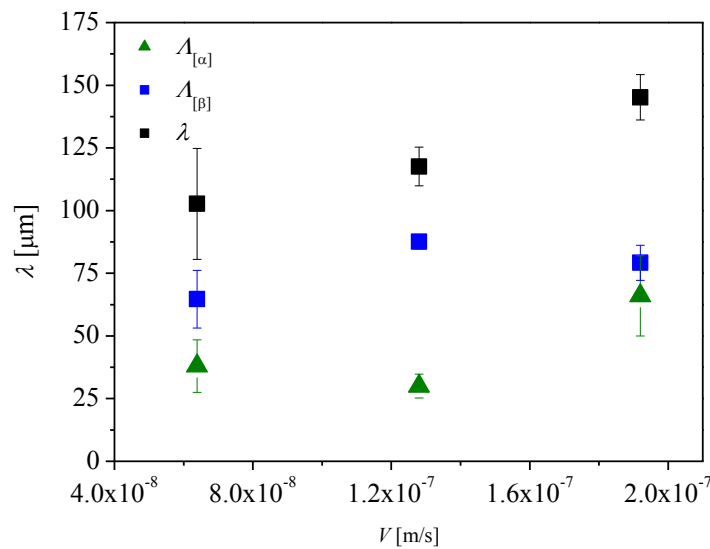


Figure 81: Estimated interphase spacing  $\lambda_{[CI]}$  and  $\lambda_{[CF]}$  and lamellar spacing  $\lambda$  for different pulling rates  $V_p$  and a concentration  $x = 0.5$  mol fraction NPG.

The context between concentration and lamella spacing  $\lambda$  is shown in Figure 82. The lamella spacing has a minimum at the concentration of  $x = 0.5$  mol fraction NPG.

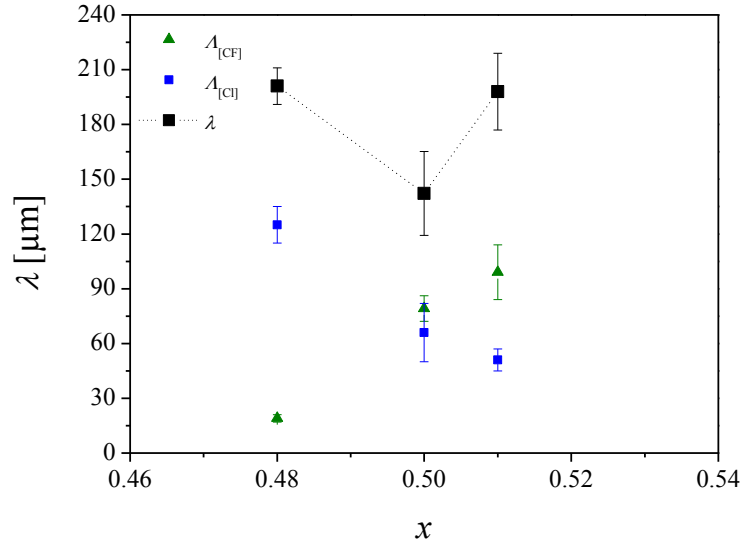


Figure 82: The interphase spacing and width of  $[C_I]$  and  $[C_F]$  lamellae are shown as function of concentration for  $V_p = 0.19 \mu\text{m/s}$ .

Finally, it is worth mentioning that the ratio of lamella width to interphase spacing is in good agreement with the position of  $x$  within the peritectic interval.

### 6.2.6 Microstructure Selection within the Peritectic Interval

Hunziker et al. [37] published equations to calculate the microstructure map of the metallic peritectic systems Ni – Cu under the assumption that constitutional undercooling ahead of the solid/liquid interface exists and with diffusion in the liquid [2]. Based on the experiments the calculated microstructure map and the experimental results for the peritectic region of the binary organic phase diagram NPG - TRIS are shown in Figure 83. The microstructure map is calculated with the measured diffusion coefficient and the difference between the calculated solidus and the liquidus temperature (see chapter 4.1). It has to be mentioned that solidification morphologies at a higher  $G_T/V_p$  ratio of  $1.7 \cdot 10^{-11} \text{ s} \cdot \text{K/m}^2$  need more than 4 hours to reach steady state conditions. The calculations predict the appearance of mixed bands for concentrations between  $x = 0.475$  and  $0.505$  mol fraction NPG.

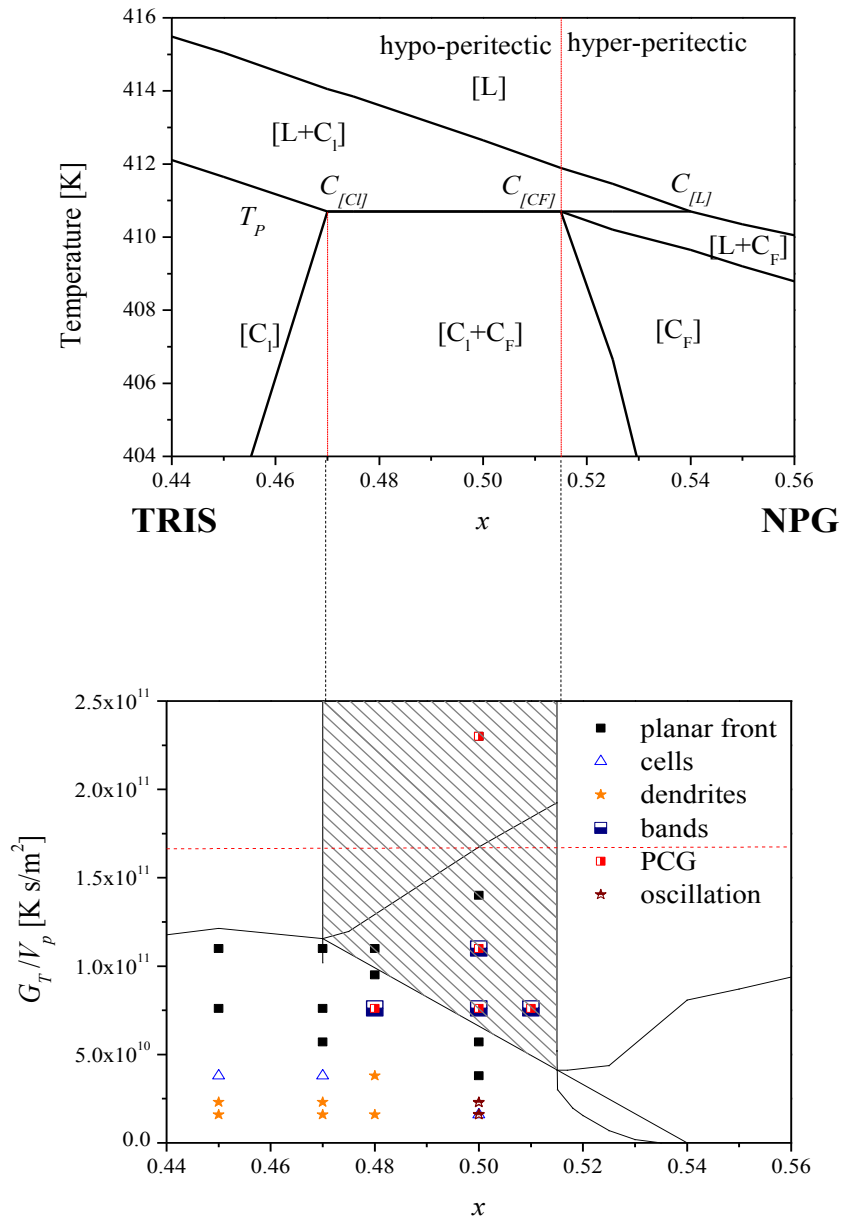


Figure 83: Peritectic region of the phase diagram and calculated microstructures depending on the applied  $G_T/V_p$  and the mol fraction NPG  $x$  as full lines. The region where layered structure formation is possible is shaded in grey. The dots show the experimental solidification morphology for dendrites, cells and planar front after having reached theoretically stable growth conditions. Metastable solidification morphologies are shown in the graph even before the reach of steady state growth conditions. Note that the experimental points below the dotted line represent experiments taken at less than 4 hours.

For all concentrations below that region the change from planar to dendritic growth is predicted for a nearly constant ratio  $G_T/V_p \leq 1.2 \cdot 10^{11} \text{ s} \cdot \text{K}/\text{m}^2$ , for concentrations above that region the change is situated at about  $G_T/V_p \leq 4 \cdot 10^{10} \text{ s} \cdot \text{K}/\text{m}^2$ . The experimental  $G_T/V_p$  microstructure map has been established with several different concentrations and pulling rates. Figure 83 shows the measured  $G_T/V_p - x$  microstructure map with the estimated diffusion coefficient from chapter A.9.

Since the TRIS rich  $[C_I]$  plastic phase is stable for only 4 hours at the selected process conditions, the solidification morphology at the calculated steady-state time was selected if smaller than 4 hours. These investigations reproduce the predicted step in the  $G_T/V_p$  microstructure map between the  $[C_I]$  and  $[C_F]$  phase as a consequence of the different  $\Delta T_0$  at the same concentration [40] in the far hypo- and hyper-peritectic region. It shows the oscillating solidification morphology along the region where the cellular solidification changes to a planar front. Furthermore, the region where coupled growth occurs is within the peritectic region. Both solidification morphologies have in common an initial unstable banded structure.

## 7 Conclusions and Future Needs

In the present work, solidification morphologies in the hypo- and hyper-peritectic region were studied. The investigations were done at solidification rates close to the limit of constitutional undercooling in a binary organic system which shows a peritectic reaction. The work includes additional investigations such as estimation of viscosity, heat coefficient, vapor pressure and DSC measurements to identify necessary physical and chemical properties. The results of the experiments show the following insights:

- Annealing experiments indicate a thermal instability for pure TRIS and its alloys if the material is kept at a temperature above the solid/solid transition at 406 K.
- DSC measurements show a thermal stability for pure TRIS and its alloys if the material is kept at a temperature of 453 K no longer than 4 hours.
- The reported phase diagram by Barrio et al. [50] has been confirmed by DSC measurements within the expected measurements errors in a fixed temperature gradient. Also good agreement was achieved by studying the corresponding solid/liquid interface positions of various alloys.

The main investigation focuses on controlled solidification at selected concentrations within a micro Bridgman-furnace. Rectangular glass samples were filled with an alloy and pulled through the furnace. *In-situ* solidification morphology was observed with a microscope in combination with a CCD camera. The solidification morphologies were recorded and stored for further investigation. The following can be stated:

- The determined melting points of the selected concentrations were confirmed by *in-situ* observations.
- When holding a sample with a TRIS - NPG alloy stationary within a constant temperature gradient the plastic phase is stable for 4 hours. Afterwards, the TRIS-rich phase [ $C_I$ ] gradually disappears and the faceted phase [O] contacts with the liquid phase after 18 hours. The NPG-rich [ $C_F$ ] phase appears to be more stable.
- After full dissolution, the plastic phase can be re-established by cooling the entire sample and re-starting the experiment. In this case, the decomposition is faster.

- Under pulling conditions the thermal instability of TRIS lowers permanently the melting temperature due to the long expose time at high temperature during the experiments.
- The effective diffusion coefficient  $D_{eff}$  is estimated for the entire phase diagram although the plastic phase disappears. This is done by the determination of the migration of droplets through the matrix phase. The measured diffusion coefficient  $D_L$  is in the average order of  $2.1 \cdot 10^{-11} \pm 0.6 \text{ m}^2/\text{s}$  for concentrations  $0.47 \leq x \leq 0.54$  mol fraction NPG.
- Bands, oscillating growth, and coupled growth solidification morphologies were found in the hypo-peritectic region. The results are partly reproducible. In the most cases partial layered structure formation were observed which is predicted under the presents of convection. The position agrees with theoretical predictions for solidification morphologies in the presence of convection.
- Investigation in the hypo-peritectic composition regions shows an oscillatory behavior of the dendritic/planar liquid-solid interface for a constant pulling velocity. This behavior is not predicted for the formation of layered structures and it is for the first time observed *in-situ*.
- Both plastic phases which participate at a peritectic growth, namely  $[C_I]$  and  $[C_F]$ , are optically undistinguishable. To distinguish between the plastic phases  $[C_I]$  and  $[C_F]$ , concentrations in the TRIS-rich and in the NPG-rich regions are investigated under the same process conditions. In order to indicate which growth mode occurs for a given concentration  $C_0$ , temperature gradient  $G_T$ , pulling velocity,  $V_p$  and the corresponding morphology is mapped as a function of alloy composition and  $G_T/V_p$  ratio.
- Up to now no evidence has been found for peritectic reaction during coupled growth solidification.
- The intended experiments on ISS to determine the effect of the natural convection on the solidification morphologies wasn't investigated. This will not be done before 2014.

The collected information improves the understanding of peritectic solidification, however, the results are influenced by decomposition and convection. Further investigations are required without convection. For that, experiments in space are highly desired. Additionally investigations of further organic phase diagrams which also show a peritectic reaction are proposed to increase the understanding of the observed solidification morphologies.

## 8 Summary

In the last century investigations on peritectic metallic systems show a wide range of possible microstructures. Bands, islands, tree-like microstructures and coupled growth were detected at growth rates where both phases can solidify with a planar front. The investigations were done by experiments and numerical simulations. Whereby, all these microstructures are highly influenced by convection and undercooling in front of the solid/liquid interface.

In the present study, the organic compound TRIS - NPG was used as a model substance for *in-situ* observation of peritectic solidification. It is the first time that peritectic solidification is directly observed at velocities close to the limit of constitutional undercooling. Both organic compounds have high temperature non-faceted phases which solidify in the same manner as metals do. Non-faceted phases, called plastic phase, occur with almost the same transparent color. Therefore, they are optically undistinguishable and only the solid/solid interface between the transparent plastic phases [C<sub>I</sub>] and [C<sub>F</sub>] and the solid/solid interface with the faceted phase [O] is visible. Due to the high temperature of the Bridgman-furnace and the long observation time the plastic phase [C<sub>F</sub>] of TRIS can be used only limited within a tight experimental border conditions.

For hypo-peritectic concentrations the growth of bands with thickness from 76  $\mu\text{m}$  to 190  $\mu\text{m}$  were observed. The observed banded solidification was not stable and led to coupled growth. Evidence for this form of transformation were found previously in experiments with metals and supported with numerical simulation. The transformation from a banded structure to coupled growth is discussed in literature. Here, it was the first time that the transformation from banded to coupled growth could be directly observed. Unexpected, unstable oscillating behavior was found where both phases grow in a competitive manner at the same time. This observed solidification pattern occurs for process conditions where layered structures are not discussed in literature. Beside the oscillatory growth mode, direct isothermal coupled peritectic growth was observed. This eutectic-like solidification pattern is stable and shows a typical spacing of  $\lambda = 142$  to 201  $\mu\text{m}$ . Investigations near the peritectic concentration, where mixed bands are predicted, require finer adjustment in the variation of the alloy composition. However, this is postponed to further research work.



## 9 References

- [1] European Space Agency Contract DRD-E18, “*DIRSOL Preliminary Design Report*”, (2008) 235.
- [2] W.Kurz, D.J.Fischer, “*Fundamentals of solidification*”, Trans tech Publications Ltd 1998 [ISBN 0-87849-804-4].
- [3] S.T. Mixture, D.P. Matheis, R.L. Snyder, T.N. Blanton, G. M. Zorn, B. Seebacher, *Physica C: Superconductivity*, **250** (1995) 175-183.
- [4] D.R. Uhlmann and G.A. Chadwick, *Acta Metall.* **9** (1961) 835–840.
- [5] W.J.Boettinger, *Metall. Trans.* **5** (1974) 2023 - 2031.
- [6] R.Trivedi and J.S.Park, *J. Cryst. Growth* **235** (2002) 572 - 588.
- [7] R. Trivedi and J.H. Shin, *Mater. Sci. Eng. A* **413–414** (2005) 288–295.
- [8] H.Yasuda, N.Notake, K.Tokieda and I.Ohnaka, *J. Cryst. Growth* **210** (2000) 637–645.
- [9] F.Kohler, L.Germond, J.D. Wagnière and M.Rappaz, *Acta mater* **57** (2009) 56-68.
- [10] A.Karma, W.J.Rappel, B.C.Fuh and R.Trivedi, *Metall. Trans.* **29A** (1998) 1457–1470.
- [11] K.Tokieda, H.Yasuda and I.Ohnaka, *Mater. Sci. Eng.* **A262** (1999) 238–245.
- [12] T.A.Lograsso, B.C.Fuh and R.Trivedi, *Metall. Trans.* **36A** (2005) 1287–1300.
- [13] S.Liu and R.Trivedi, *Metall. Trans.* **37A** (2006) 3293–3304.
- [14] X.W.Hu, S.M.Li, W.J.Chen, S.F.Gao, L.Liu. and H.Z.Fu, *J. Alloys and Compounds* **484** (2009) 631-636.
- [15] D.Ma, Y.Li, S.C.Ng and H.Jones, *Acta Mater.* **48** (2000) 1741–1751.
- [16] D.Ma, Y.Li, S.C.Ng and H.Jones, *Acta Mater.* **48** (2000) 419–431.
- [17] Y.Li, S.C.Ng and H.Jones, *Scripta Mater.* **39** (1998)7–11.
- [18] X.W.Hu, S.M.Li, L.Liu and H.Z.Fu, *China Foundry* **5** (2008) 167–171.
- [19] A.P.Titchener and J.A.Spittle, *Acta Metall.* **23** (1975) 497–502.
- [20] Y.Q.Su, C.Liu, X.Z.Li, J.J.Guo, B.S.Li, J.Jia and H.Z.Fu, *Intermetallics* **13** (2005) 267–274.
- [21] P.Busse and F.Meissen, *Scripta Mater.* **36** (1997) 653–658.
- [22] L.S.Luo, Y.Q.Su, J.J.Guo, X.Z.Li, S.M.Li, H.Zhong, L.Liu and H.Z.Fu, *J. Alloys Compd.* **461** (2008) 121–127.
- [23] Y.Q.Su, L.S.Luo, X.Z.Li, J.J.Guo, H.M.Yang and H.Z.Fu, *Appl. Phys. Lett.* **89** (2006) 2319181-2319183.
- [24] L.S.Luo, Y.Q.Su, X.Z.Li, J.J.Guo, H.M.Yang and H.Z.Fu, *Appl. Phys. Lett.* **92**, (2008) 0619031-0619033.
- [25] M.Vandyoussefi, H.W.Kerr and W.Kurz, *Acta Mater.* **48** (2000) 2297–2306.
- [26] T.S.Lo, S.Dobler, M.Plapp, A.Karma, and W.Kurz, *Acta Mater.* **51** (2003) 599-611.
- [27] S. Dobler, T.S.Lo, M.Plapp, A.Karma and W.Kurz, *Acta Mater.* **52** (2004) 2795-2808.
- [28] Massaki Sumida, *Journal of Alloys and Compounds* **349** (2003) 302-310.
- [29] Z.Feng, J.Shen, Z.Min, L.Wang and H.Fu, *Materials Letters* **64** (2010) 1813-1815.
- [30] M.Vandyoussefi, H.W.Kerr and W.Kurz, *Acta Mater.* **45** (1997) 4093-4105.
- [31] L.S.Luo, Y.Q.Su, J.J.Guo, X.Z.Li and H.Z.Fu, *Sci China-Phys mech. Astron* **50** (2007) 442-450.
- [32] J.H.Lee and J.D.Verhoeven, *J. Cryst. Growth* **144** (1994) 353–366.
- [33] Q.L.Rao, X.L.Fan, D.Shu and C.C.Wu, *J. Alloys Compd.* **461** (2008) L29–L33.
- [34] H.Zhong, S.M.Li, H.Y.Lü, L.Liu, G.R.Zou and H.Z.Fu, *J. Cryst. Growth* **310** (2008) 3366–3371.
- [35] H.W.Kerr and W.Kurz, *Int. Mater. Rev.* **41** (1996) 129–164.
- [36] W.Luo, J.Shen, Z.Min and H.Fu, *J. Cryst. Growth* **24** (2008) 5441–5446.
- [37] O.Hunziker, M.Vandyoussefi and W.Kurz, *ActaMater* **46** (1998) 6325–6336.
- [38] W.Z. Luo, J. Shen, Z.X. Min and H.Z. Fu, *Mater. Lett.* **63** (2009)1419–1421.
- [39] T.A. Lagrasso, B.C. Fuh and R. Trivedi, *Met. Mat. Trans. A* **36A** (2005) 1287 – 1300.
- [40] O.Hunzinger, M.Vandyoussefi and W.Kurz, *Acta mater* **46** (1998). 6325-6336.
- [41] R. Trivedi, *Metall. Mater. Trans.* **26A** (1995) 1583-1590.
- [42] P.Mazumder, R.Trivedi and A.Karmer, *Met. Mat. Trans.* **31A** (2000) 1234-1246.
- [43] R.Trivedi, *Scripta Mat.* **53** (2005) 47-52.
- [44] R.Rudman, *Solid State Commun.* **29** (1979) 785-787.
- [45] J.Timmermans, *J.Phys.Chem.Solids.* **18** (1961) 1 - 8.
- [46] L.A.K.Staveley, *Annu. Rev. Phys. Chem.* **13** (1962) 351 - 368.
- [47] P.R.Sahm, I.Egry, T. Volkmann, “*Schmelze, Erstarrung, Grenzflächen*”, Vieweg Verlag [ISBN 3-528-06979-1].
- [48] W.J. Dunning, *J.Phys.Chem.Solids.* **18** (1961) 21.
- [49] [http:// www.merck.de](http://www.merck.de)
- [50] M.Barrío, D.O.Lopez, J.L.Tamarit, P.Negrier and Y.Haget, *J. Mater. Chem.* **5** (1995) 431 - 439.
- [51] D.Eilerman and R.Rudman, *J.Chem.Phys.* **72** (1980) 5656-5666.
- [52] L.Sturz, V.T.Witusiewicz, U.Hecht and S.Rex, *J. Crystal Growth* **270** (2004) 273 - 282.

- [53] V.T.Witusiewicz, L.Sturz., U.Hecht and S. Rex, *Acta Mater.* **53** (2005) 173 - 183.
- [54] S.Akamatsu and G.Faivre, *Phys. Rev. E* **58** (1998) 3302. – 3314.
- [55] S.Akamatsu, M.Plapp, G.Faivre and A.Karma, *Phys. Rev. E* **66** (2002) 0305011 - 0305014.
- [56] V.T.Witusiewicz, L.Sturz, U.Hecht and S.Rex, *Acta Mater.* **52** (2004) 5071 - 5081.
- [57] M.Barrio, D.O.Lopez, J.L.Tamarit, P. Negrier and Y .Haget, *J. Solid State Chem.* **124** (1996) 29-38.
- [58] D.O.Lopez, J.Van Braak, J.L.Tamarit and H.A.J.Oonk, *Calphad* **19** (1995) 37 - 47.
- [59] D.Chandra and R.Chellappa, W.M.Chien, *J. Phys.Chem. Solids* **66** (2005) 235 – 240.
- [60] <http://www.chem.unep.ch>
- [61] J.P.Mogeritsch, A.Ludwig, S.Eck, M.Grasser and B.J.McKay, *Scripta Mat.* **60** (2009) 882-885.
- [62] <http://en.wikipedia.org/wiki/Tris>
- [63] J.Ll.Tamarit, *Mol. Cryst. Liq. Cryst.* **250** (1994) 347-358.
- [64] R.E.Wasylishen, P.F.Barron and D.M.Doddrell, *Aust. J. Chem.* **32** (1979) 905 -909.
- [65] <http://www.dow.com/>
- [66] S.M.Rowe, *Org. Proc. Research & Dvelop.* **6** (2002) 877-883.
- [67] <http://www.vitrocom.com>.
- [68] G.W.H.Höhne, W.Hemminger, H.-J.Flammerheim, “*Differential Scanning Calorimetry*”, Springer-Verlag Berlin [ISBN 3-540-59012-9].
- [69] W.J.Boettinger, U.R.Kattner, K.-W.Moon, J.H. perepezko, “DTA and Heat-flux DSC Measurements of Alloy Melting and Freezing“, National Institute of Standards and Technology [Spec.Publ. 960-15].
- [70] <http://www.faulhaber.com/>
- [71] <http://www.eurotherm.com>
- [72] Prof. Paul O’Leary, Institute for Automation, University of Leoben, Peter-Tunnerstraße 27, Leoben
- [73] Y.Ocak, S.Akbulut,K.Keslioglu and N.Marasli, *J. Colloid and Interface Science* **320** (2008) 555-562.
- [74] V.T.Witusiewicz, L.Sturz, U.Hecht and S.Rex, *Acta Mater.* **52** (2004) 5519 - 5527.
- [75] A.Ludwig, J.Mogeritsch and M.Grasser, *Trans. Ind. Inst. Metals* **62** (2009) 433-36.
- [76] J.P.Mogeritsch, S.Eck, M.Grasser and A.Ludwig, *Mater. Sci. Forum* **649** (2010) 159-64.
- [77] <http://lb.chemie.uni-hamburg.de>
- [78] <http://www.sigmaaldrich.com>
- [79] N.N.Brandt, A.Y.Chikishev and I.K.Sakodinskaya, *J.Molc. Str.* **648** (2003) 177-182.
- [80] B.Granzow, P. Klæboe and V. Sablinskas, *J.Molc. Str.* **349** (1995) 153-156.
- [81] Z.Zhang and Y.Xu, *Solar Energy* **71** (2001) 299-303.
- [82] Z.Zhang, Y.Xu and M.Yang, *J. Chem. Data* **45** (2000) 1060-1063.
- [83] S.Akbulut, Y.Ocak, K.Keslioglu and N. Marasli, *J. Phy. Chem. Solid* **70** (2009) 72-78.
- [84] S.Divi, R.Chellapa and D.Chandra, *J.Chem. Thermodynamics* **38** (2006) 1312-1326,
- [85] D.Chandra, W.Chien, V.Gandikotta and D.W. Lindle, *Z. Phys. Chem.* **216** (2002) 1433-1444.
- [86] Z.Z.Ying and Y.M.Lin, *J. Chem. Thermodynamics* **22** (1990) 617-622.
- [87] <http://www.weblo.com/domain/available/bestvibes.com>
- [88] <http://www.astm.org/DATABASE.CART/HISTORICAL/D5930-97.htm>
- [89] <http://www.carlroth.ch/catalogue>
- [90] <http://www.kayelaby.npl.co.uk/chemistry>
- [91] G.M.Barrow, “*Physical Chemistry*”, McGraw-Hill Inc., 1973 [ISBN 3-528-23806-2].
- [92] <http://www.chemic.org/kdb/kdb/hcprop/showcoef.php?cmpid=922&prop=PVP>
- [93] <http://chem.sis.nlm.nih.gov/chemidplus/>
- [94] [www.perstorp.com/layouts/ViewFile.aspx?prodid=66&langid=1&filetype=msds](http://www.perstorp.com/layouts/ViewFile.aspx?prodid=66&langid=1&filetype=msds) –
- [95] J.Font and J.Muntasell, *Mat. Research Bulletin.* **30** (1995) 479-489.
- [96] <http://web.grcc.edu/Pr/msds/Biology/Tris%20Base%20-%20Genomic%20Solutions.pdf>
- [97] <http://www.koeichem.com/english/index.htm>
- [98] <http://www.brookfieldengineering.com/products/viscometers/laboratory.asp>
- [99] <http://en.wikipedia.org/wiki/Viscometer>
- [100] <http://www.basf.com/group/corporate/de/index>
- [101] S.Liu, J.Teng and J.Choi, *Metall. Mat. Trans.* **38A** (2007) 1555-1562.
- [102] E.Hecht, A.Zajac, “*Optics*“, Fourth Edition. Pearson Higher Education. [ISBN 9780321188786].

## 10 Symbols

Symbol	Meaning	Definitions	Units
$C$	concentration	$C = x \cdot 100 \%$	mol.% wt.%
$C_0$	initial concentration		mol.%
$C_L$	liquidus concentration		mol.%
$C_S$	solidus concentration		mol.%
$C_p$	peritectic concentration		mol.%
$D$	diffusion coefficient		$m^2/s$
$D_L$	diffusion coefficient in the liquid		$m^2/s$
$G_T$	temperature gradient		K/m
$M$	molar mass		g/mol
$N$	Avogadro number	$6.022 \cdot 10^{23}$	$mol^{-1}$
$Q$	heat flow		W
$Q^*$	heat stream		W/s
$R$	gas constant	8.314	J/K·mol
$T_b$	boiling temperature		K
$T_c$	temperature in the cold zone of the Bridgman-furnace		K
$T_{cold}$	extrapolated peak completions temperature of a DSC curve		K
$T_e$	extrapolated peak onset temperature of a DSC curve		K
$T_f$	finish peak temperature of a DSC curve		K
$T_{hot}$	temperature in the hot zone of the Bridgman-furnace		K
$T_i$	initial peak temperature of a DSC curve		K
$T_L$	liquidus temperature		K
$T_m$	melting temperature		K
$T_m$	maximum peak temperature of a DSC curve		K
$T_p$	peritectic temperature		K
$T_S$	solidus temperature		K
$T_{SST}$	transition temperature solid/solid		K
$T_S^\alpha$	solidus temperature of the $[\alpha]$ phase		K
$T_S^\beta$	solidus temperature of the $[\beta]$ phase		K
$V$	growth or solidification velocity		m/s
$V_c$	critical solidification velocity		m/s
$V_L$	lateral solidification velocity		m/s
$V_p$	pulling rate		$m^2/s$
$V_s$	molar volume,		$m^3/mol$
$V_\alpha$	solidification velocity of the $[\alpha]$ phase		m/s
$V_\beta$	solidification velocity of the $[\beta]$ phase		m/s
$X$	length of the adiabatic gap		m
$Z$	atoms per cell		-
$[C_F]$	face center cubic, non-faceted phase , optical inactive phase or high temperature phase of NPG and NPG rich alloys		-
$[C_I]$	body center cubic, non-faceted phase , optical inactive phase or high temperature phase of TRIS and TRIS rich alloys		-
$[M]$	monocline, faceted phase , optical active phase or low temperature phase of NPG		-
$[O]$	orthorhombic, faceted phase , optical active phase or low temperature phase of TRIS		-

Symbol	Meaning	Definitions	Units
a	lattice		$\text{\AA}$
a	Sensor constant		
b	lattice		$\text{\AA}$
c	lattice		$\text{\AA}$
con.	constant		wt. %
cp	heat capacity		J/K·mol
i	index		-
k	distribution coefficient	$k = C_S/C_L$	-
$m_L$	liquidus slope	$m = \Delta T_L/\Delta C$	K/mol
$m_s$	solidus slope		
n	refractive index		
p	pressure		Pa
$pk_a$	dissociation constant		
r	curvature between solid and liquid		m
t	time		s
$t_{tr}$	transition time		s
x	mol fraction	$x = C/100 \%$	-
z	length in solidification direction		m
$z_{tr}$	transition length to reach steady-state		m
$\Delta C_b$	concentration range where bands can occur		Mol %
$\Delta H_m$	enthalpy of melting		J/mol
$\Delta H_{SST}$	enthalpy of transition		J/mol
$\Delta H_V$	enthalpy of vaporization		J/mol
$\Delta S_f$	entropy of fusion		J/K·mol
$\Delta S_m$	entropy of melting		J/K·mol
$\Delta S_{SST}$	entropy transition solid/solid		J/K·mol
$\Delta S_V$	entropy of vaporization		J/K·mol
$\Delta T_0$	temperature difference between $T_L$ and $T_S$		K
$\Delta T_N$	Nucleation undercooling		K
$\Delta t$	time difference		s
$\Delta V_m$	molar volume contraction		$\text{m}^3/\text{mol}$
$\Delta V_{SST}$	volume difference due to phase transition		$\text{m}^3$
$\Gamma$	Gibbs-Thompson coefficient		K·m
$\alpha$	dimensionless entropy of fusion		
$\delta$	boundary layer thickness		m
$\eta$	dynamic viscosity		Pa·s
$\kappa$	heat conductivity		W/K m
$\tau$	cell structure coefficient	0.34	-

## **A Appendix: Determination of Material Properties**

### **A.1 Variation of Material Purifications**

#### Introduction

In this part of the thesis the effect of different material purifications on the organic substances TRIS and NPG was tested. Barrio et al. [50] reported that the purity of NPG can be increased by applying a drying process at about 310 K for several hours. NPG is very hygroscopic and contains as delivered usually residual water. Therefore, a pretreatment of the organic compounds seems to be necessary for further use in his studies [61].

#### Experimental investigations

To improve the purity of the organic substances two different methods of purification were tested: (i) purification by drying and (ii) purification by sublimation. A DSC measurement was performed to test the impact of the purification method on the organic substances. After the purification process NPG and TRIS was directly used for the alloy preparation.

#### Purification by drying

For purification of NPG and TRIS a heater with a flat glass container filled with the organic material was placed into the glove box (see chapter 3.1). Then the organic compound heated up to 310 K for more than 24 hours. During that time NPG changed its appearance from a white snow-like crystalline material to a white sugar-like powder. TRIS is a white powder and shows no optically visible effects during the drying process.

#### Purification by sublimation

Figure 84 shows a sketch of the used sublimation device. It consists of a double glass bottle with a cooling finger located in the middle axis of one part of the device. The finger is cooled by connecting the fittings with a water supply. Due to the size of the device it is not possible to operate the system within the glove box. Hence the sublimation has to be done outside of the glove box whereas the filling has to be done within the glove box. 10 - 20 g of organic compounds together with 50 vol.% molecular sieve (Aldrich Cat. No. 20.858-2) is filled into the sublimation device. To avoid moisture absorption by the hygroscopic organic compounds during purification a molecular sieve was used within the sublimation device. After the filling the device is carefully removed from the glove box and put into an oil bath. Here it is heated for several hours. During purification, the solid material sublimates and freezes again at the

cooling finger. The applied sublimation parameters are given in Table 12. After the sublimation procedure the purification device is put back into the glove box.

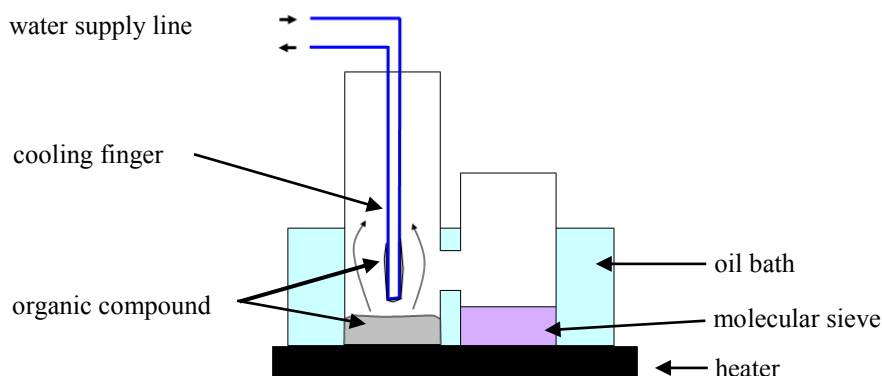


Figure 84: The sublimation device consists of a double glass bottle with a cooling finger located in the middle axis of one part of the device. The organic compound together with 50 vol.% molecular sieve is filled into the device for purification.

The purified material is taken from the cooling finger and the glass device is filled again. Approximately 0.5 g material is prepared by one single sublimation cycle.

Table 12: Sublimation parameters for purification.

Parameters	
Temperature of the oil bath	353 K
Temperature of the cooling finger	283 K
Sublimation time	24 h

### Results and Discussion

TRIS decomposes during the purification by sublimation, which was visible by long dark and light brown threads at the cooling finger. Only NPG shows no optical visible effects. To evaluate the effect of sublimation on NPG, the liquidus temperature of NPG as delivered and the sublimated material was measured by DSC measurement. The exact procedure and evaluation of the DSC measurement [67, 68] was done in the same way as described in details in chapter 4.3.2. For all samples, the difference between the liquidus temperatures before and after purification is very small. The liquidus temperature of the purified material lies within the accuracy of the DSC measurement (see Figure 85). All three curves show a characteristic sharp end of the peak which is characteristic for the used material. All DSC measurements show a smooth increase of the curve from the basic line to the peak maximum. After

purification the material seems to have a higher solidus temperature than the material as delivered, but again, the difference between the different purified materials is within the measurement accuracy. All in all, the difference between the liquidus and solidus temperatures of purification by sublimation and drying is very small and lies within the accuracy of the DSC measurement.

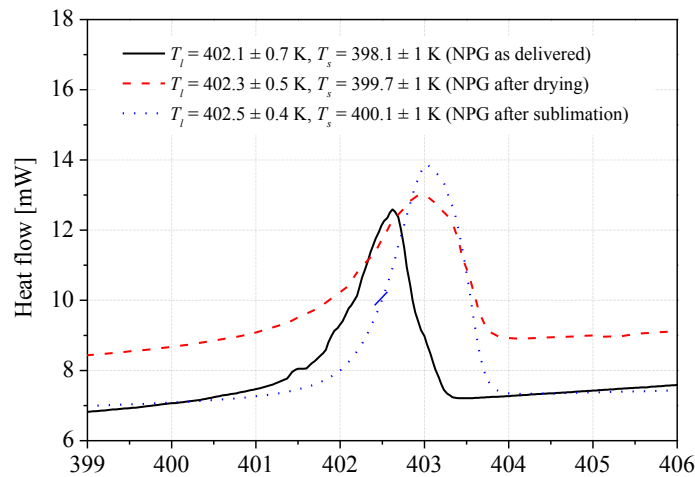


Figure 85: DSC curves for NPG as delivered and for two purified materials. It is obvious that by the drying process a substantial purification can be achieved, visible in the change of the solidus temperature.

Furthermore, the alloy preparation includes an additionally purification method (see chapter 3.1.1), where impurities with lower boiling points are removed by sublimation. For this reason, NPG and TRIS were only purified by long time drying before it was directly used for the alloy preparation.

## A.2 Material Colorization

### Introduction

Plastic crystals are optically isotropic, therefore, the plastic phases [C<sub>I</sub>] and [C<sub>F</sub>] appear black under polarized light. Only the faceted phases [O] and [M] show a wide range of colors under polarized light because they are optically anisotropic. Therefore, it is possible to distinguish between the optical active phase, the faceted phase and the optical inactive phase, the plastic phase (see Figure 14). Under normal white light illumination the faceted phase is dark while the plastic phases [C<sub>I</sub>] and [C<sub>F</sub>] are transparent. However, the two plastic phases [C<sub>I</sub>] and [C<sub>F</sub>] can optically not be distinguished during solidification. In this part of the thesis, the effort to colorize selectively one of both phases is reported.

### Experimental Set-up

The filling was carried out inside a glove box (see chapter 3.1). The dyer was put into a small glass container with NPG and into another glass bottle with TRIS. Afterwards the dryer powder was mixed together with the organic substance by shaking. The glass bottles were sealed and removed from the glove box. The sealed bottles were put separately on a heater and heated up to the melting point of the corresponding material (NPG 401 K, TRIS 443 K). As soon as the organic compounds melt, the dyer colorizes the liquid.

### Results and Conclusions

For all different dyers (Table 13), the organic compounds were still colorizing in the same color during solidification and in the solid state at room temperature. Both organic compounds accept all used dyers in the same way. There was no visible optical difference indicated between NPG and TRIS. The used dyers and their reaction with the organic compounds are given in Table 13. Therefore, it was not possible to increase the optical discriminability by colorization of one of the organic compounds.

Table 13: Dyer and the color effect at the organic compounds TRIS and NPG.

Dyer	Formula	TRIS	NPG
sudan II orange [77]	C <sub>18</sub> H <sub>16</sub> N <sub>2</sub> O	red	red
methyl orange [78]	C <sub>14</sub> H <sub>14</sub> N <sub>3</sub> NaO <sub>3</sub> S	orange	orange
methyl red [77]	C <sub>15</sub> H <sub>15</sub> N <sub>3</sub> O <sub>2</sub>	orange - red	orange - red



## A.3 Boiling Point

### Introduction

The boiling temperature  $T_b$  of pure NPG is given for  $p = 760$  mm Hg (standard pressure) [49] and of pure TRIS for  $p = 10$  mm Hg [49]. The boiling point of pure TRIS cannot be found in the literature at standard pressure. Therefore, the boiling temperature at standard pressure for pure TRIS and selected concentrations were determined (Table 12).

### Experimental Set-up

The samples are filled inside a glove box (argon atmosphere) whereas the further experimental proceeding was done under normal atmosphere. The organic compounds with the required concentration are first put into a glass container. The glass container opening was closed with a metal cap which revealed a small hole for a thermal element. This hole was sealed with silicon and a scotch tap till it was used. The glass container was put on a hot plate of a heater, the scotch tape was removed and a thermo sensor was drilled through the sealed hole. The height of the container, the form of the metal cap and the sealing material silicon enables to neglect a possible increase in pressure inside the glass container. The position of the thermo sensor was chosen next to the bottom of the container. As soon as the liquid material starts to boil the temperature had been recorded. This process was carried out for the two pure compounds and alloy concentrations in steps of 10 %.

### Results and Conclusions

The determination of the boiling point of TRIS gives a temperature at  $553 \pm 2$  K. At the boiling point the material changes the color from transparent to light brown. The same happens to alloys with a high concentration of TRIS, like  $x = 0.1$  or  $0.2$  mol fraction NPG (see Figure 86). All other materials stay transparent during boiling. The obtained values are given in Table 14 and shown in Figure 86. The obtained boiling temperature does not follow a linear relationship with the alloy concentration. The boiling temperatures increase nearly linearly from pure NPG to a concentration of  $0.20$  mol fraction NPG and then increase further till pure TRIS is reached (see Figure 86). TRIS decomposes which is visible in a change of the color of the liquid material in the glass samples from transparent to brown. The same happens do alloys with  $x = 0.10$  and  $0.20$  mol fraction NPG. All other alloys stay transparent in the liquid phase and become white after cooling from the boiling temperature (see the pictures of the samples after the experiment in Figure 86 at room temperature).

Table 14: The boiling temperature of the pure materials and alloys at selected concentrations.

$C_0$	$T_b$	error	$C_0$	$T_b$	error
mol fraction	K	K	mol fraction	K	K
0	553.7	±0.5	0.6	498.2	±2.0
0.1	534.7	±6.5	0.7	491.7	±1.5
0.2	514.7	±2.5	0.8	484.9	±0.3
0.3	509.2	±0.0	0.9	481.7	±0.5
0.4	502.7	±0.5	1	477.7	±0.5
0.5	500.2	±6.0			

Therefore, the process temperature for TRIS and the organic alloys have to be below the boiling point in avoidance of decomposition and coloring of the organic compounds.

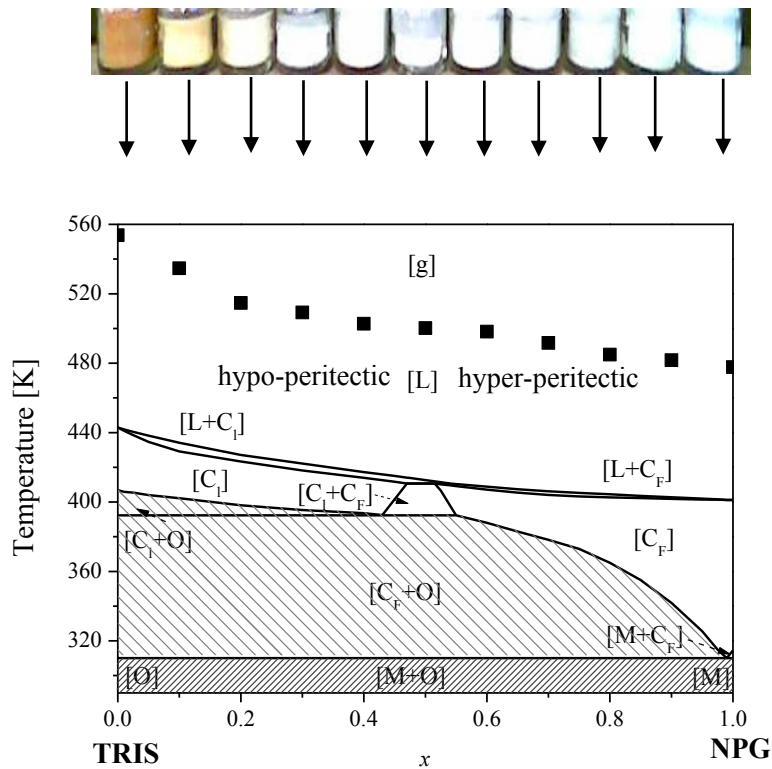


Figure 86: Phase diagram TRIS - NPG. At the top: pictures of the samples after determining the boiling point. Measured boiling points are indicated with black squares in the phase diagram.

## A.4 Raman Spectroscopy

### Introduction

TRIS and alloys with higher TRIS concentration,  $x \geq 0.2$  mol fraction NPG, show a change of the color after being melted and solidified, see chapter A.3. This behavior indicates a probable decomposition of TRIS [64] in the liquid state of TRIS. A decomposition of pure TRIS could be caused by a decrease of the covalent bonds within the molecules. Each bond oscillates with a certain energy which can be measured with Raman spectroscopy. Such a spectrum is an exclusive fingerprint for each material. If an organic material changes its bonds during heating-up, the Raman spectrum changes. Therefore, TRIS as delivered and an alloy with  $x = 0.3$  mol fraction NPG was investigated with Raman spectroscopy before and after solidification investigations in the Bridgman-furnace. The Raman spectra of TRIS can be found in N.N. Brandt et al. [79] whereas B. Granzow [80] published the Raman spectra of the solid and the plastic phase of NPG.

### Experimental Set-up

For the investigation a Dilor LABRAM confocal-Raman spectrometer was used (see Figure 87). TRIS as delivered, unused prepared alloys and used alloys (from the boiling point experiments) were used for the Raman spectroscopy.

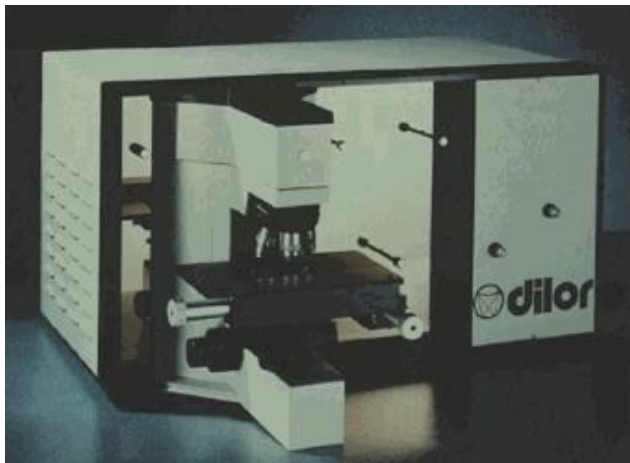


Figure 87:

Dilor LABRAM equipped with a frequency-doubled Nd-YAG laser (100 mW, 532.2 nm) and with a He-Ne laser (633 nm) and diffraction gratings of 1200 and 1800 grooves/mm.

The detection is performed with a Peltier-cooled, slow-scan, CCD matrix-detector. Laser focusing and sample viewing are performed through an Olympus BX 40 microscope fitted with 10X, 50X and 100X long-working distance objective lenses (allowing viewing in reflected- and transmitted-light). Samples can be held at controlled temperatures between 83 K and 873 K using a Linkam THMSG 600 heating-freezing stage. Sample images are acquired by a color video-camera and projected on a video monitor. Both, the Raman

spectra and the sample images, are processed on a 333 MHz Pentium computer.

## Results

The Raman spectra of pure TRIS as delivered and after cooling from the liquid phase to room temperature are given in Figure 88. TRIS as delivered shows a clear spectrum but the same material after heating-up and cooling down shows a shift of the curve to a general higher level indicated by the red line in Figure 88.

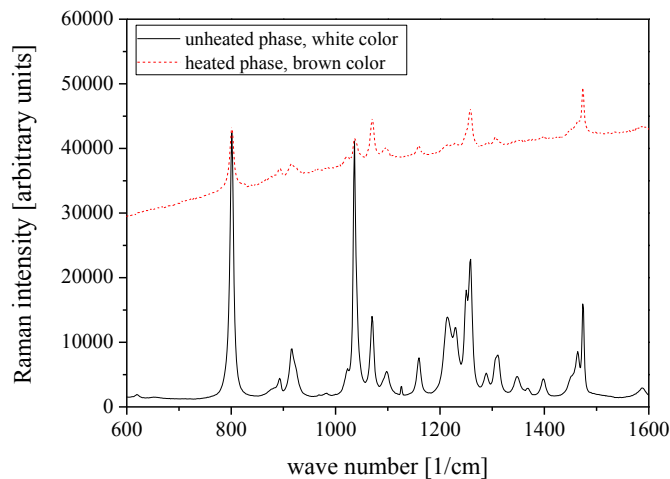


Figure 88: Raman Spectra for pure TRIS as delivered (black line) and after cooling down from the liquid phase (red line). The red line shows a higher intensity level with smaller peaks.

Figure 89 shows the Raman spectra for the alloy with  $x = 0.3$  mol fraction NPG before and after solidification investigation. It is observable that the alloy and the reheated alloy show a higher energy level than the pure organic substances TRIS and NPG. Each peak shows the vibration energy in general, and both curves show the same tenor of peaks, but differ in detail of the Raman intensity.

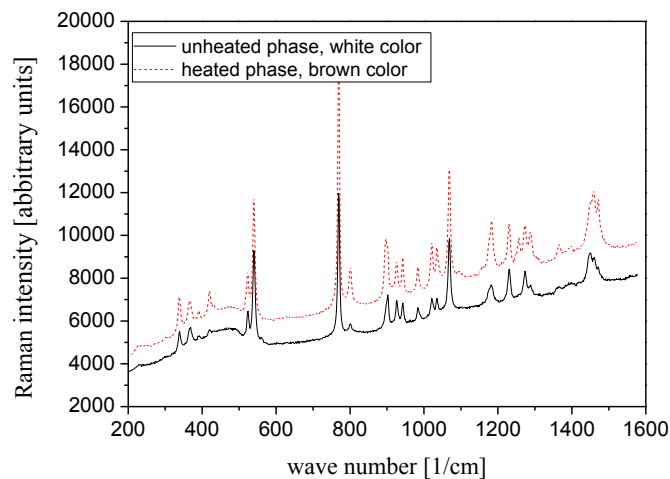


Figure 89: Raman spectrum of an unused alloy  $x = 0.3$  mol fraction NPG and an alloy after being liquid and became brown colored.

### Conclusions

The peaks of the used material are at the same position as the peaks of TRIS as delivered which indicates that the atomic bounding are still intact. After heating-up, TRIS shows a florescence, this can be seen by a shift of the curve to a higher level. During the investigation the material absorbs the energy of the laser and emits it at a higher level. Since the Raman spectroscopy curve differs for TRIS as delivered and molten/frozen TRIS, it is clear that the material changes its properties after heating and cooling.

## A.5 Heat Conductivity

### Introduction

The heat conductivity is one of the fundamental properties of a material. The heat conductivity of a pure material changes with temperature but the heat conductivity of alloys changes with temperature and concentration. Zang et al. [81] investigated the heat conductivity of TRIS as a potential material for thermal storage of energy. In addition, Zhang et al. [82] and Akbulut et al. [83] investigated the heat conductivity of NPG. Furthermore the heat capacity of TRIS and NPG was investigated by Divi et al. [84], Chandra et al. [85], and Ying et al. [86]. Based on this data, the published heat conductivity of the plastic phase lies between 2 to 3 kJ/mol·K for both organic compounds. In this study, it was decided to investigate the heat conductivity of the two pure compounds TRIS and NPG for a comparison with the published values. Additionally, the heat conductivity of an alloy with peritectic concentration was measured.

### Experimental Set-up

The measurement of the heat conductivity was performed with the heat conductivity measuring device type K-system II from the company Advanced CAE Technology Inc. Ithaca, N.Y. USA [87], according to ASTM D5930-97 standard [88]. The measurements were carried out within a temperature range of 373 K and 443 K under normal ambient pressure. The measuring system was based on the concept of a constant infinite linear heat source in the medial axis of a cylindrical sample chamber. Figure 90 shows the bread board construction which was used to estimate the heat conductivity of the organic compounds and its alloy. The measurement was carried out for pure TRIS, pure NPG, and one alloy in the peritectic region with a concentration of  $x = 0.5$  mol fraction NPG (Figure 16 on page 24). For each temperature, three consecutive measurements were performed and an average value for the heat conductivity was calculated. The sample cylinder was filled within the glove box but the experiment itself took place outside of the glove box.

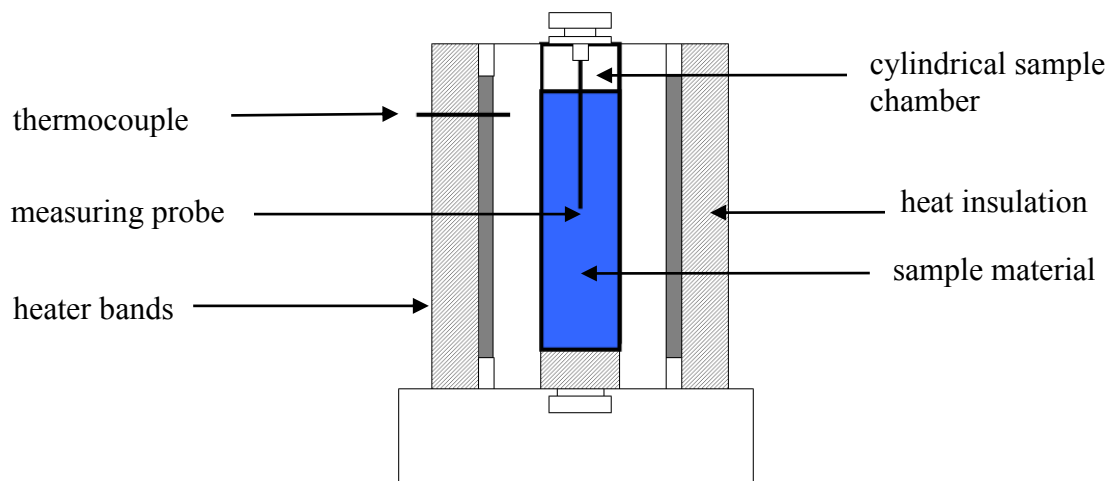


Figure 90: Bread board construction of the K system II to measure the heat conductivity depending on the temperature. For a definite time  $\Delta t$  the sample material is exposed to a definite heat stream  $Q^{\bullet}$ . The sample cylinder is kept during this time at a constant temperature.

### Results

The heat conductivity  $\kappa$  is calculated [88] in a predominated time interval  $(t_2 - t_1)$  with a linear measurement curve:

$$\kappa = \frac{con. \cdot Q^{\bullet}}{4 \cdot \pi \cdot \Delta T} \ln \left( \frac{t_2}{t_1} \right). \quad (\text{Eq. 19})$$

Here,  $\kappa$  is the heat conductivity, con. a sensor constant,  $Q^{\bullet}$  the heat stream, and  $t_i$  the measuring time. After a measurement time of approximately 30 s the sample is cooled down to the next favored temperature and as soon as a stable temperature is reached the next measurement is started. Figure 91 shows the plot of temperature  $T$  versus time  $t$ .

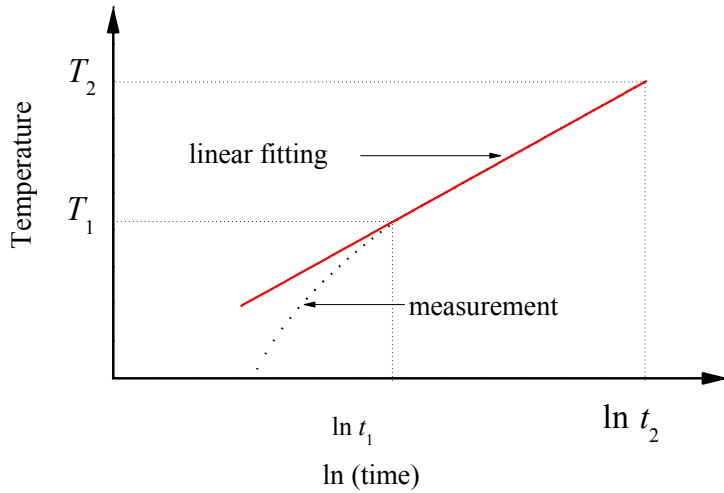


Figure 91:

Temperature versus time and a linear fit to estimate the heat conductivity from the measurement data.

The published results are shown in Figure 92 (rectangular, black squares and red triangles) together with the experimental results (black stars). The investigation shows a non-linear correlation between the temperature and the heat conductivity  $\lambda$  of pure NPG. The investigations of Akbulut et al. [83] and Zang et al. [82] show divergent results for the heat conductivity in the plastic phase (see Figure 16 on page 24). Akbulut investigated the plastic phase of NPG and determined increasing heat conductivity with a decreasing temperature.

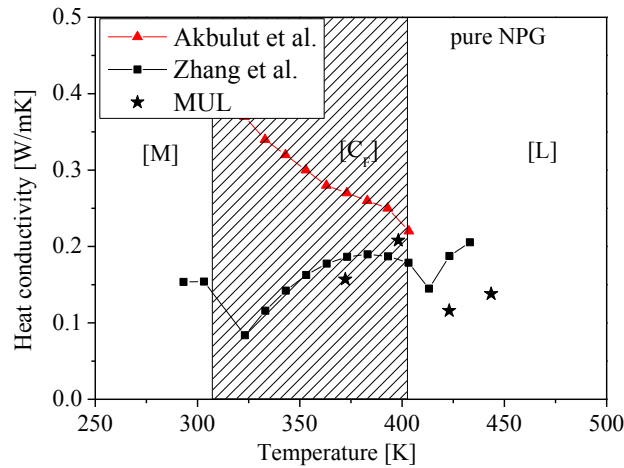


Figure 92: Experimental results of the investigation of the heat conductivity of NPG by Akbulut et al. [83] (red triangles), and Zhang et al. [82] (black squares), compared to the measurement (black stars). The region of the plastic phase is shaded.



However, the investigation done by [82] shows a decrease in heat conductivity in the plastic phase shortly after the transition from the faceted phase to the plastic phase. The heat conductivity is increasing in the plastic phase with increasing temperature. At the melting point  $\lambda$  decreases and increases again in the liquid phase. The obtained experimental results of this performed study are close to the available values of Zhang but don't match it.

The experimentally obtained values of the heat conductivity and the published ones of pure TRIS are shown in Figure 93.

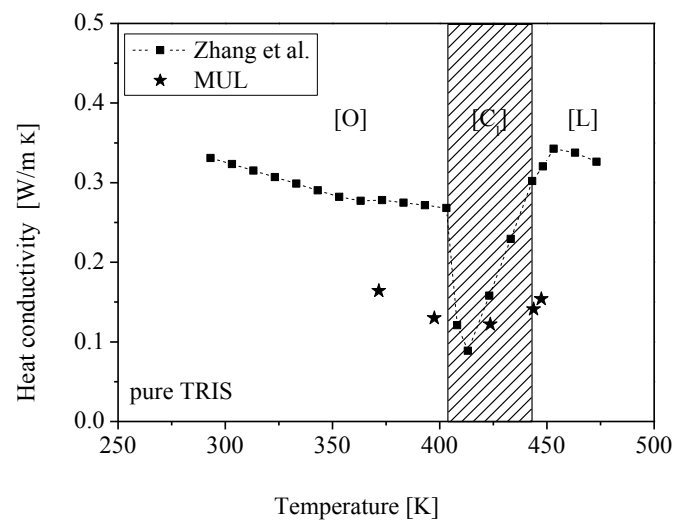


Figure 93: The graph shows the experimentally obtained values for the heat conductivity of TRIS observed in this study (stars) compared to the results (squares) published in [81].

In this figure the heat conductivity in the plastic phase is lower than the one observed in the faceted or liquid phase. The heat conductivity observed in this study shows strong differences to the published one. Only in the  $[C_1]$  region, there is an agreement with the published values. Indeed, our measurements in the liquid- and faceted phases are clearly below the published values.

The investigations of the heat capacity of the alloy ( $x = 0.5$ ) are shown in Figure 94. The graph shows the heat conductivity declining with increasing temperature. The temperature region of the plastic phase is very small at this concentration and only one measured value is available in this region. Therefore, no essential statement can be given for the plastic phase.

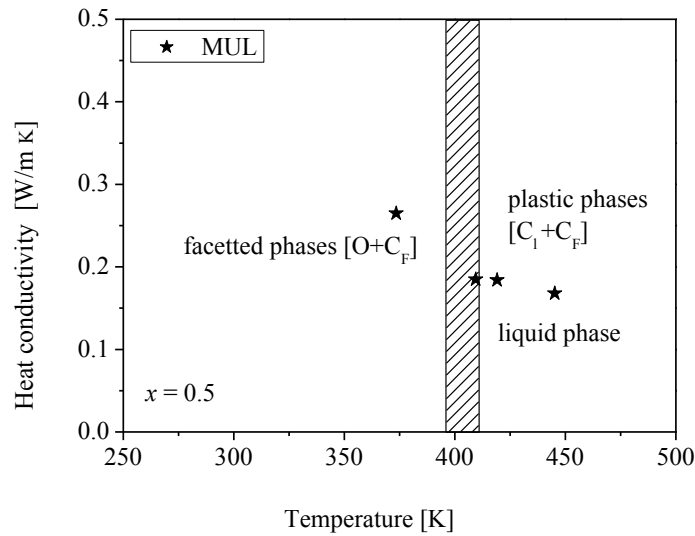


Figure 94: Heat conductivity of an alloy with  $x = 0.5$  mol fraction NPG versus temperature.

The results of the heat conductivity experiments are given in Table 15 with an average error of  $\pm 5\%$ .

Table 15: Measured heat conductivity of the pure organic compounds and  $x = 0.5$  alloy.

$C_0 = 100$ mol. % TRIS		$C_0 = 50$ mol.% NPG		$C_0 = 100$ mol. % NPG	
$x = 0$		$x = 0.5$		$x = 1$	
temperature	$\lambda$	temperature	$\lambda$	temperature	$\lambda$
K	W/m·K	K	W/m·K	K	W/m·K
371.65	0.164	373.45	0.265	372.25	0.157
397.45	0.130	409.45	0.185	398.15	0.208
423.55	0.122	419.15	0.184	423.05	0.116
443.75	0.141	445.25	0.168	443.55	0.138
447.35	0.154				

### Conclusions

All in all the results from various published experiments show dissimilar results. The experimentally obtained heat conductivity of TRIS and NPG in this study fits to the values [82] with an accuracy between 0.05 W/m·K and 0.1 W/m·K which corresponds to an error between 10% and 50%. The deviations between the published values for NPG are much higher.

## A.6 Vapor Pressure

Experimental investigations under micro gravity are planned to carry out on board of the ISS. The tests will be done with the DIRSOL facility which contains glass for the samples, a brittle material. Therefore, the determination of the vapor pressure is necessary under the aspect of security on board of the ISS.

### Introduction

A decisive role for investigations of liquids plays the vapor pressure, because the data about the vapor pressure leads to the enthalpy of vaporization (or heat of vaporization)  $\Delta H_V$  and the vaporization entropy  $\Delta S_V$ . Both energies are criteria for the molecular model of the liquid. The main part of the vaporization enthalpy  $\Delta H_V$  is necessary to break the intermolecular attractive forces and only a small part of the energy is used for the volume work in the gas room. Additionally, the determinations of the vapor pressure of the organic alloys are important for the safety on the ISS.

### Experimental Set-up

Figure 95 shows the experimental bread board where an autoclave is shown with a heating system connected to a pump and a digital pressure gauge [89] which was used for the vapor pressure experiments. The autoclave, including the heating system, can be used in a temperature range from 293 K to 575 K with an accuracy of  $\pm 1\%$  and a thermal Fe-Cu-Ni sensor which measures the temperature inside of the autoclave. The digital pressure gauge is calibrated between 0 kPa and 690 kPa with an accuracy of  $\pm 0.3\%$  and a resolution of 400 Pa. To verify the accuracy of the measurement system a vapor pressure experiment with pure water was carried out and compared with the well known vapor pressure of water. The results of the measurements of the vapor pressure of water fit very well to reported data [90]. For the vapor pressure measurements a mass of 50 g of TRIS and NPG, depending on the alloy composition, was filled into the cylindrical autoclave cup. The sealed autoclave was connected to a pump and a digital pressure gauge. Next, the pressure in the autoclave was reduced to -80 kPa, compared to the surrounding pressure and heated above the melting point (463 K) of pure TRIS to bring both pure compounds TRIS and NPG into the liquid state. Investigations on the vapor pressure at different concentrations were done with  $x = 0.3$ ,  $x = 0.5$  and  $x = 0.7$  mol fraction NPG. Three independent experiments were carried out for all alloys. The alloys were given as a powder mixture into the autoclave. The vapor pressure at room temperature of the pure compounds TRIS and NPG and the alloys are below the

accuracy of the measurement equipment which is limited to 400 Pa. The vapor pressure and the corresponding sample temperature were recorded to determine the equilibrium vapor pressure. As soon as the vapor pressure was stable the temperature was increased to the next temperature level.

It was not possible to obtain a cooling curve of TRIS rich alloys because TRIS dissolves at high temperature.

The vaporization enthalpy  $\Delta H_V$  is temperature depending and decreases with increasing temperature until the critical point, where the vaporization enthalpy  $\Delta H_V$  is zero, is reached due to the equilibrium condition [91].

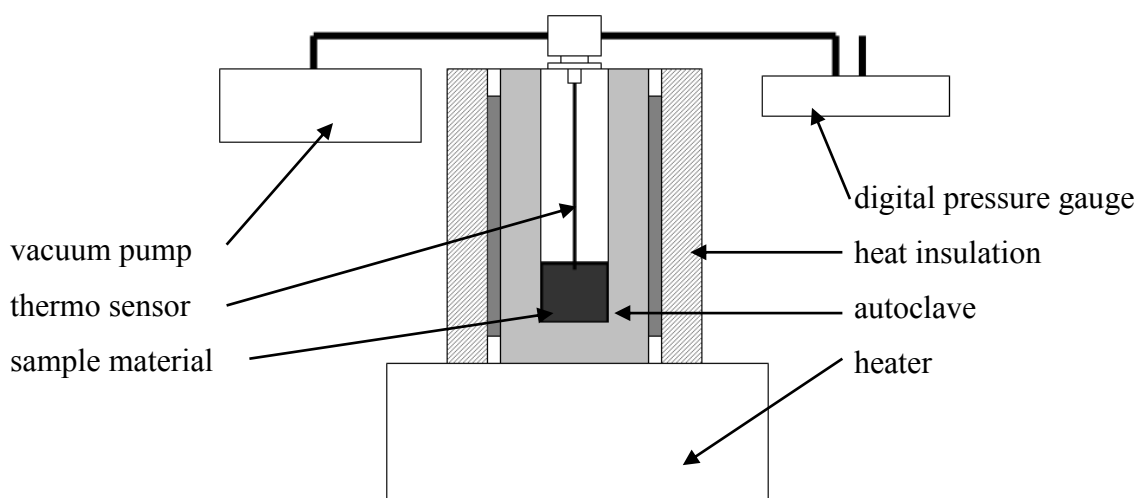


Figure 95: Sketch of the vapor pressure bread board. The sample is put inside of the insulated autoclave and heated up with the heater. The digital pressure gauge is connected to the autoclave and plots the pressure difference to the surroundings.

The vaporization entropy  $\Delta S_V$  of different liquids is in average 88 J/K·mol and is independent from the molecule size which is known as the Trouton rule. Variations from this value can be explained by the presence of hydrogen bonds. Compounds with  $\Delta S_V$  greater than 88 J/K·mol are associated in the liquid phase with hydrogen bonds while compounds below this value are associated with hydrogen bonds in the liquid and in the gas phase [91]. Applying the assumption, that  $\Delta H_V$  is independent from the temperature in a small temperature range, the correlation between the vapor pressure, vaporization enthalpy, and the temperature can be written:

$$\ln p = -\frac{\Delta H_V}{R} \cdot \frac{1}{T} + const. \quad (\text{Eq.20})$$

This equation can be transformed to a simple equation of first order where the slope multiplied by the gas constant  $R$  is equal to the enthalpy  $\Delta H_V$ . The correlation equation for the vapor pressure of NPG is available from the chemical engineering research center (*CHERIC*) [92], which is given by:

$$\ln(p) = -9.023658 \cdot \ln(T) - \frac{5250.162}{T} + 73.99825 + 9.967256 \cdot 10^{-6} \cdot T^2. \quad (\text{Eq. 21})$$

Here,  $p$  is the vapor pressure. Basic information about the vapor pressure at room temperature of the pure compounds TRIS and NPG is available from material data sheets [93, 94]. Both pure compounds are not mixable at room temperature, therefore, the entire vapor pressure can be calculated from the partial vapor pressure of the pure compounds. According to Raoult's law [91] the vapor pressure  $p$  of an ideal solution is dependent on the vapor pressure of each chemical component  $p_A$  and  $p_B$  and the mole fraction of the component  $x_A$  and  $x_B$  as shown in:

$$p = p_A \cdot x_A + p_B \cdot x_B. \quad (\text{Eq. 22})$$

Here,  $p_A$  is partial pressure of the substance A and  $x_A$  the mol fraction of substance A. Figure 96 shows the total vapor pressure of alloys at room temperature (293.15 K) depending on the mol fraction. For more details at low temperature Front et al. [95] reported the pressure – temperature equilibrium curve at the solid state for NPG. Further information about the molar volume changes of NPG and TRIS at atmospheric pressure and pressure – temperature dependencies for the phase transitions of compounds can be found in Tamarit [63]. Thermodynamic data for both compounds were reported at Sturz et al. [52].

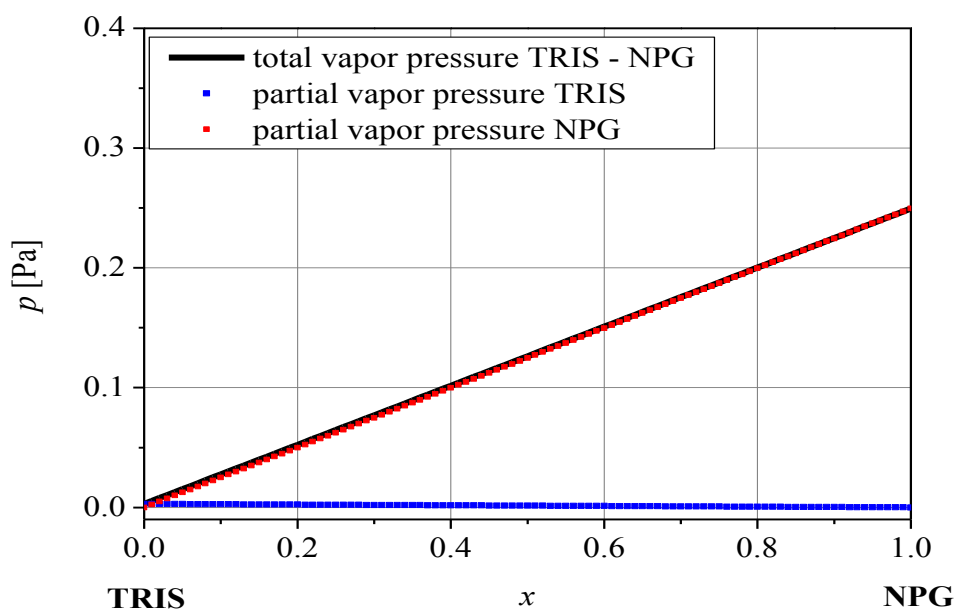


Figure 96: The total vapor pressure of TRIS – NPG (black line) at room temperature depending on the alloy concentration. NPG (red dots) has a 10 times higher vapor pressure as TRIS (blue dots) and as a consequence the total vapor pressure is more or less equal to the partial vapor pressure of pure NPG.

Table 16 gives the physical and chemical properties online available from material safety data sheets of different producers.

Table 16: Material data

Material data		
	TRIS	NPG
formula	$\text{H}_2\text{NC}(\text{CH}_2\text{OH})_3$	$(\text{CH}_3)_2\text{C}(\text{CH}_2\text{OH})_2$
$T_m$ (melting)	$442.7 \pm 1.0$ K	$401.3 \pm 1.0$ K
$T_b$ (as delivered)	492 – 493 K (at 13 hPa) [49]	481 – 482 K [49]
vapor pressure at 293 K	$2.9 \cdot 10^{-3}$ Pa [93]	< 100 Pa [94]
vapor pressure	1300 Pa at 492 K [96]	101.3 kPa at 482 K [97]
$\Delta H_{SSr}$	$34.0 \pm 1.7$ kJ/mol [52]	$12.8 \pm 0.6$ kJ/mol [52]
$\Delta H_m$	$3.7 \pm 0.2$ kJ/mol [52]	$4.4 \pm 0.2$ kJ/mol [52]

To check the experimental results, the vapor pressure equation of NPG from *CHERIC* [92] was used as a reference. Figure 97 compares the experimental values with the calculated values of NPG. A sufficient determination of the vapor pressure at room temperature was not possible since the pressure was below the accuracy of the measurement instrument.

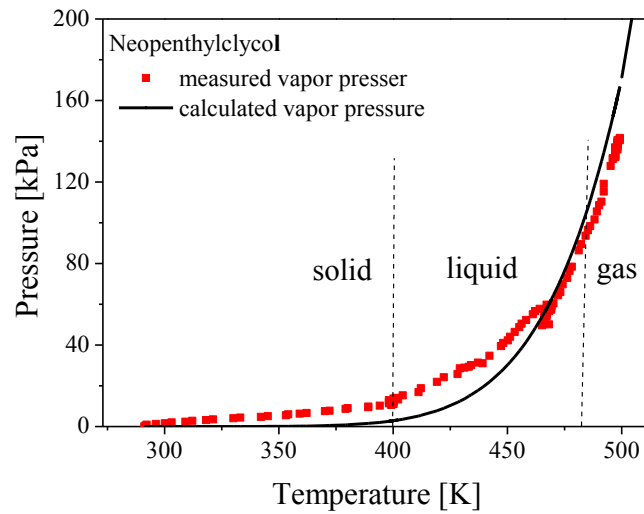


Figure 97: Comparison of the measured vapor pressure of pure NPG (red dots) and the calculated one (black line) available from “*CHERIC*” (chemical engineering research center [92]). The experimental results show a slightly higher vapor pressure in the solid and parts of the liquid state than calculated.

### Results

To enhance the accuracy of the regression analysis the vapor pressure at room temperature has been additionally calculated from equation 27 (see Figure 96). The relation between the logarithm of the vapor pressure and the reciprocal of the temperature is shown in Figure 98 for a sample with a concentration of  $x = 0.7$  mol fraction NPG.

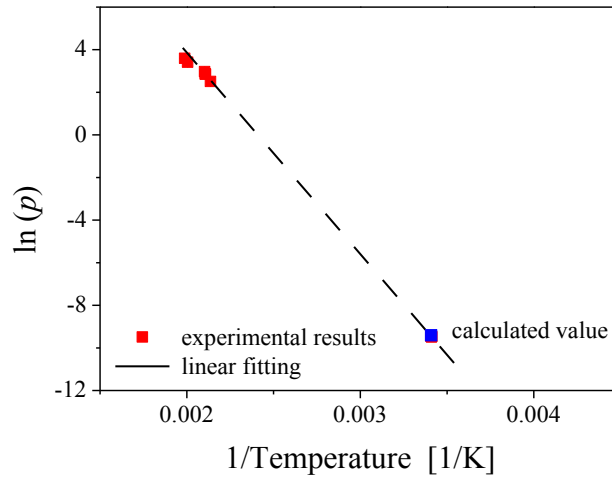


Figure 98: Natural logarithm of the vapor pressure at a temperature of 293 K, 475 K, 478 K and 505 K at a concentration of  $x = 0.7$  mol fraction NPG. The dotted line is the regression analysis for the vapor pressure.

The average value of pressure and temperature was taken from experimental results of the vapor pressure at the same temperature ( $\pm 2$  °K) for the regression analysis. Table 17 gives values of the regression analysis for different investigated concentrations.

Table 17: Results of the regression analysis.

$C_0$ mol.% NPG	$x$ mol fraction	Equation
0	0	$\ln p = -11589 \cdot \frac{1}{T} + 26.7$
30	0.3	$\ln p = -9129.7 \cdot \frac{1}{T} + 21.7$
50	0.5	$\ln p = -9584.9 \cdot \frac{1}{T} + 23.7$
70	0.7	$\ln p = -9621.9 \cdot \frac{1}{T} + 24.3$
100	1	$\ln p = -9368.0 \cdot \frac{1}{T} - 23.9$

$\Delta H_V$  (in [J]) was calculated by multiplying the results given in Table 18 with the gas constant  $R$ . From these values the average values and the deviations have been calculated and plotted in Table 18 together with the phase transition enthalpies published in [52]. To estimate an error bar for NPG, average and deviation of the experimental and the calculated results have



been used.  $\Delta S_V$  has been calculated from  $\Delta H_V$  dividing by the corresponding boiling temperature  $T_b$  (see Table 14). The vaporization enthalpy  $\Delta H_V$  is for NPG and all alloys approximately  $78.4 \pm 1.6$  kJ/mol with the exception of TRIS which has a significant higher  $\Delta H_V$  of  $96.4 \pm 2.3$  kJ/mol.

Table 18: Results of  $\Delta H_V$  and  $\Delta S_V$  for selected concentrations.

		TRIS	x			NPG
		0	0.3	0.5	0.7	1
$\Delta H_{SSV}$ [74]	kJ/mol	$34.0 \pm 1.7$				$12.8 \pm 0.6$
$\Delta H_m$ [74]	kJ/mol	$3.7 \pm 0.2$				$4.4 \pm 0.2$
$\Delta_V H$	kJ/mol	$96.4 \pm 0.5$	$75.9 \pm 0.4$	$79.7 \pm 0.4$	$80.0 \pm 0.3$	$77.9 \pm 0.4$
$T_b$	K	$553.7 \pm 0.5$	$443.4 \pm 0.3$	$500.1 \pm 6$	$491.9 \pm 0.3$	$477.7 \pm 0.5$
$\Delta_V S$	J/K mol	$174.1 \pm 0.2$	$171.1 \pm 0.5$	$159.3 \pm 1.9$	$162.6 \pm 0.1$	$163.1 \pm 0.1$

All alloys and both organic compounds TRIS and NPG show a vaporization entropy  $\Delta_V S$  above 88 J/K mol which proves that the organic compounds are associated in the liquid state by hydrogen bounds but in the gas phase the association is lost [91]. The experimental results don't show strong variations compared to the calculated values except at a concentration of  $x = 0.3$  mol fraction NPG (Figure 99).

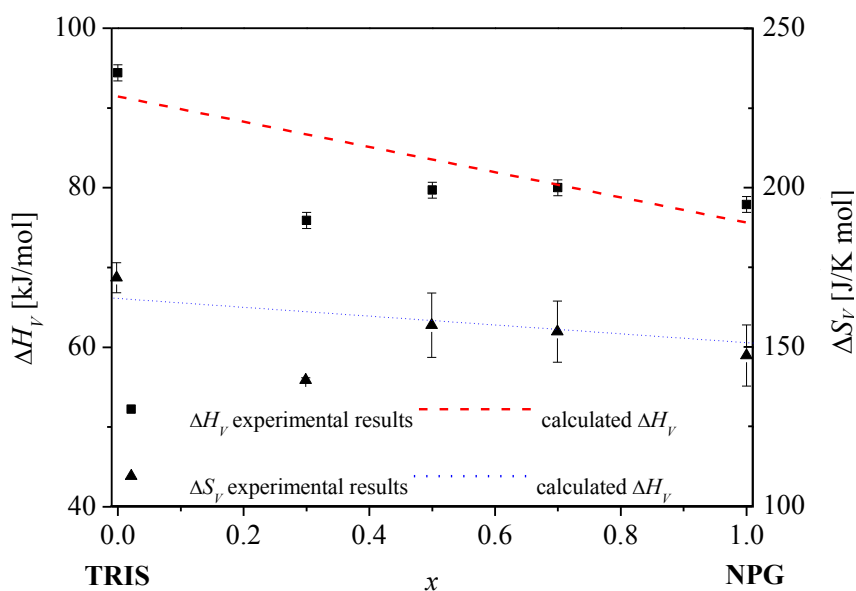


Figure 99: The graph shows the calculated entropy and enthalpy of vaporization (broken lines) in comparison with the experimental results (dots with error bar).

The behavior of the organic material during the experiments itself is also of importance. NPG goes into the gas phase and condensates during the cooling process. Based on the experimental observations the material is still white and appears in the same form as before, see Figure 100.

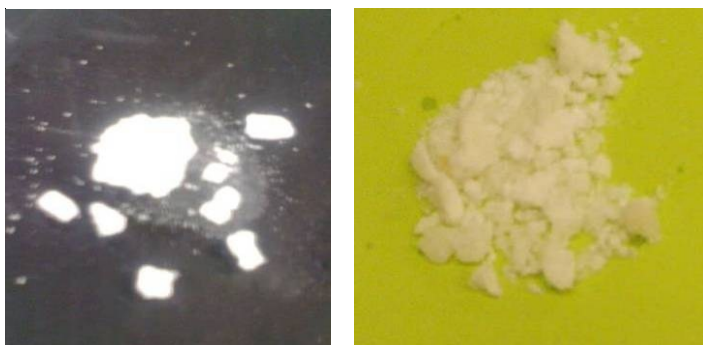


Figure 100:  
NPG before (left hand side) and after (right hand side) the vapor pressure experiment. The organic material shows the same optical appearance although it was gaseous during the experiment.

TRIS decomposes at higher temperature which is mentioned in [64, 65] and chapter A.1, A.3 and A.4 and the vapor pressure increases dramatically if decomposition starts. The form of the organic material changes from white powder to black grains of carbon as shown in Figure 101. Some of the alloys decompose and carbonize, depending on the concentration after more than one hour at higher temperature.

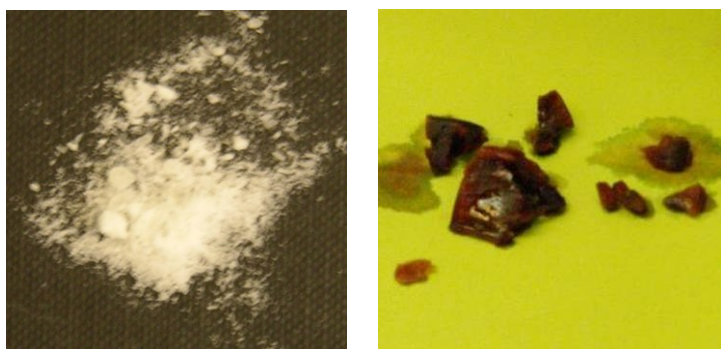


Figure 101:  
TRIS powder before and after the vapor pressure experiment. The organic material transforms during the experiment from white powder (left side) to black grains of carbon (right side).

### Conclusions

The accuracy of the entire vapor pressure experiments was determined by comparing the experimental values of pure NPG with the published values. Due to insufficient accuracy of the measurement instrument at room temperature, published vapor pressures were used for room temperature. NPG shows no decomposition during the experiments but TRIS decomposes at higher temperature and the organic material transforms to pure carbon.

The vaporization enthalpy  $\Delta H_V$  for NPG and all alloys is approximately  $78.4 \pm 1.6$  kJ/mol with the exception of TRIS which has a significant higher  $\Delta H_V$  of  $96.4 \pm 2.3$  kJ/mol. All alloys and both organic compounds TRIS and NPG show a vaporization entropy  $\Delta_v S$  above 88 J/K mol which proves that the organic compounds are associated in the liquid state by hydrogen bounds but in the gas phase the association is lost [91].

## A.7 Dynamic Viscosity

### Introduction

Viscosity is the internal resistance of a fluid to flow. The dynamic viscosity was investigated for the pure compounds TRIS, NPG and one alloy in the hypo-peritectic ( $x = 0.4$ ), peritectic ( $x = 0.5$ ) and hyper-peritectic region ( $x = 0.6$ ) at different temperatures (Figure 102).

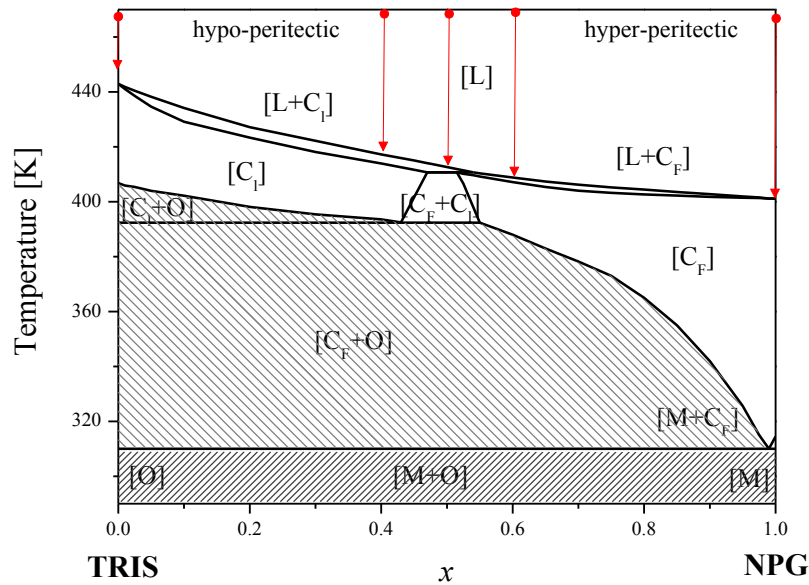


Figure 102: Phase diagram taken from Barrio et al. [50] and the position of the 5 different concentrations in the phase diagram used for viscosity measurements (red arrows).

### Experimental Set-up

The measurement of the dynamic viscosity is carried out with a Brookfield programmable rheometer DV-III Ultra. The Brookfield laboratory viscometer is calibrated within  $\pm 1.0\%$  of the used measurement range and has a repeatability of  $\pm 0.2\%$  [98]. To determine the fluid viscosity the *Couette* system in the Brookfield laboratory viscometer is used. The torque for a rotating cylinder in a certain fluid is measured and the dynamic viscosity of the fluid is recalculated with a software program. The Brookfield rheometer is connected with a temperature sensor and the display is showing directly the dynamic viscosity and the corresponding temperature [99]. The sample materials are placed in 5 different 250 ml beakers filled with the corresponding material. The beakers with the solid sample material were heated in a preheated drying oven to 453 K and kept at this temperature until the sample was completely liquid. Whereby, the required time to melt the sample material depended on

the concentration. For pure NPG it takes about 1 hour, for the 3 alloys approximately 2 hours, and for pure TRIS 3 hours. To avoid vaporization during the melting process the beakers were sealed with glass and foil. All experiments were carried out under normal atmospheric conditions in a gas hood since there was no glove box available with an adequate size to host the necessary equipment. The beaker with the liquid sample material was placed on a hot laboratory heater and protected with glass padding and a foil to avoid cooling from the top as shown in Figure 103.

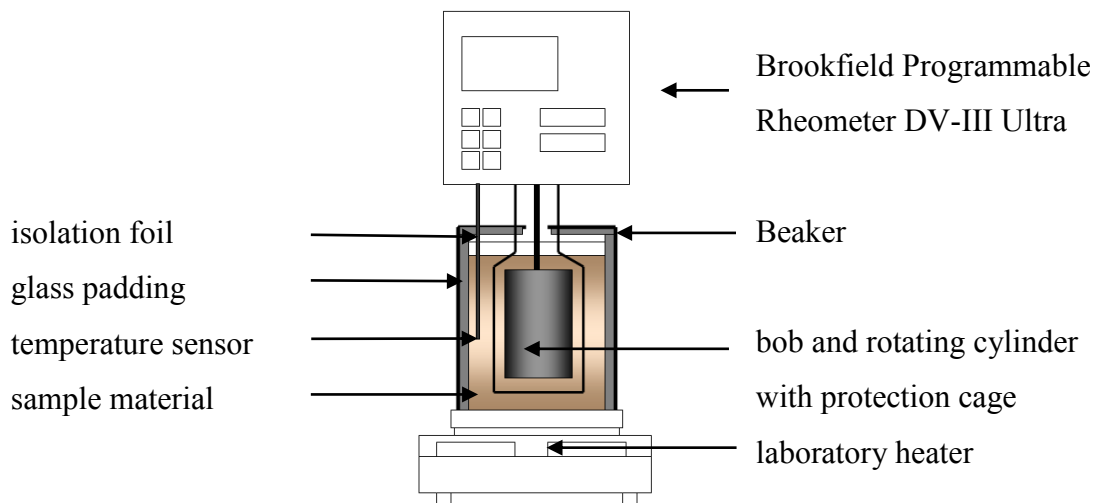


Figure 103: The experimental arrangement for the estimation of the dynamic viscosity. The beaker is completely protected by glass padding and a foil.

The temperature sensor and the rotation cylinder from the viscometer are put into the fluid. The fluid in the beaker was stirred to establish a homogeneous temperature field. As soon as the temperature field is stabilized, the stirring of the liquid alloy is stopped for the measurement. Subsequently the temperature is reduced in discrete steps to measure the viscosity. It was not possible to establish a homogeneous temperature field below 410 K because the material solidified too fast.

## Results

Concentrations between  $0.4 \leq x \leq 0.6$  mol fraction NPG were selected because the investigations for peritectic solidification with the DIRSOL instrument under 1  $\mu\text{g}$  condition will be carried out with alloys in this concentration range. Viscous flow in amorphous materials like glasses or melts is a thermal activated process and depends on the Arrhenius-Andrade equation [91]:

$$\eta(T) = \eta_0 \cdot e^{\frac{Q}{R \cdot T}} \quad (\text{Eq. 23})$$

Here,  $Q$  is the activation energy for viscosity flow,  $\eta_0$  the pre-exponential viscosity (both are approximately constant),  $T$  the temperature in K and  $R$  the molar gas constant. The equation describes the viscosity in a homogeneous temperature field. The logarithm of equation 23 leads to a linear correlation between the viscosity and the temperature:

$$\ln \eta = \ln A + \frac{Q}{R} \cdot \frac{1}{T} \quad (\text{Eq. 24})$$

The values of the so detected dynamic viscosity are given in Figure 104.

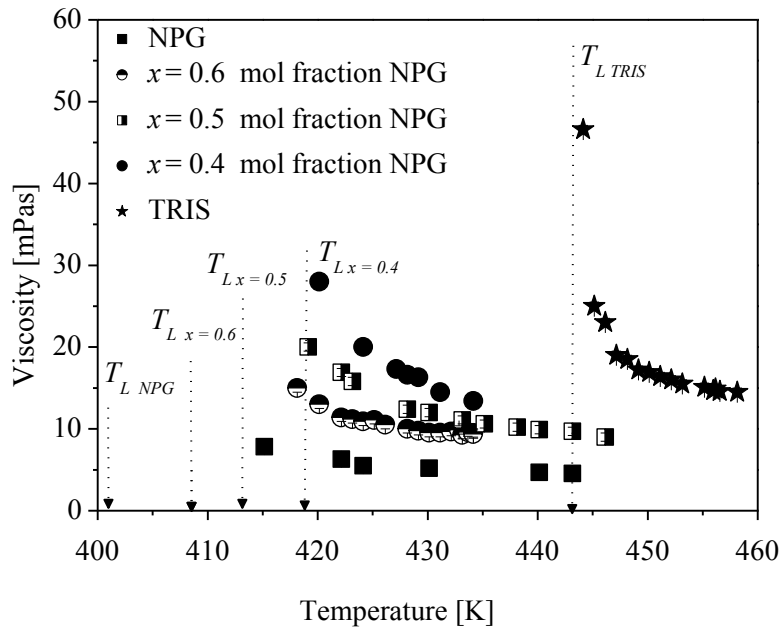


Figure 104: Measured viscosity of selective concentrations of liquid alloys from organic compounds TRIS and NPG. The arrows showing the freezing point taken from the phase diagram TRIS - NPG.

Activation energy and the pre-exponential viscosity are calculated as described in equation 24. The viscosity of pure TRIS, pure NPG and the alloys with  $x = 0.4$  match well with the regression line shown in Figure 105.

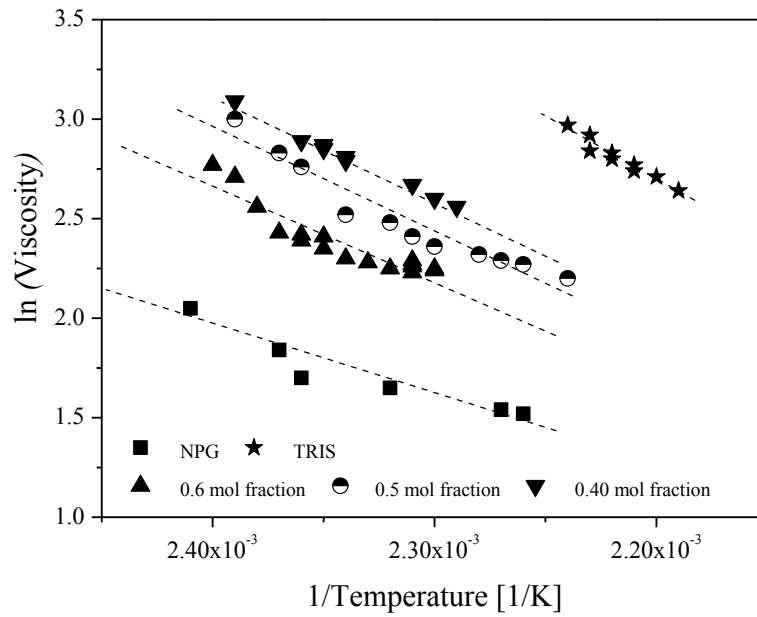


Figure 105: The figure shows the linear correlation between the logarithms of the measured dynamic viscosity of selective concentrations from organic compounds TRIS and NPG and the reciprocal of temperature. The left end of the regression line is equal to the freezing point.

The equations of the regression line are given in Table 19. The viscosity close to the freezing point was calculated from the regression equation.

Table 19: Equation of the viscosity depending on the concentration and the temperature.

$x$	Equation
TRIS	$\ln \eta = 7048.2 \cdot \frac{1}{T} - 12.818$
0.4	$\ln \eta = 5453.1 \cdot \frac{1}{T} - 9.945$
0.5	$\ln \eta = 5209.6 \cdot \frac{1}{T} - 9.5528$
0.6	$\ln \eta = 4781.4 \cdot \frac{1}{T} - 8.8165$
NPG	$\ln \eta = 3251.9 \cdot \frac{1}{T} - 5.8635$

Based on the regression equation, it was possible to calculate the activation energy, which shows a linear increase from NPG to TRIS. The values are given in Table 20.

Table 20: Activation energy and viscosity close to the melting point of the organic material and their alloys.

$x$	$Q$	$\eta$ (close to the melting point)
mol fraction	kJ/mol	m·Pa·s
TRIS	58.6	22.3
0.4	45.3	21.8
0.5	43.3	21.2
0.6	39.7	17.9
NPG	27.0	9.4

The determination of the viscosity is based on one experiment for each concentration. Normally, the accuracy of experiments can be calculated from the deviation of the average value. In this case, it's not possible, therefore, the published values of NEOL [100], a trade mark for NPG of the company BASF, are used as reference material instead. It has to be mentioned that both materials, NEOL from BASF and NPG from Aldrich, have the same CAS number but not exact the same contents. Figure 106 compares the viscosity of NEOL and the experimental results with NPG.

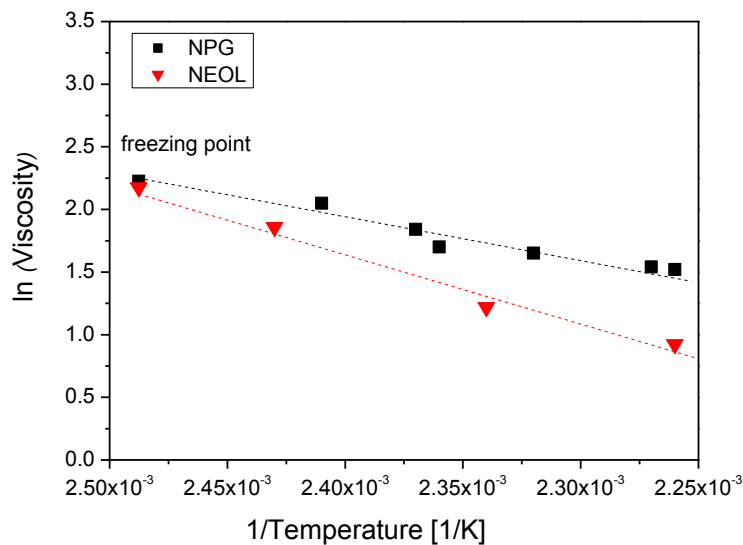


Figure 106: The graph shows the experimental results of pure NPG and the published values of NEOL a trade mark from BASF. The viscosity at the freezing point is for both materials calculated from the regression line.

The viscosity at the freezing point is calculated for both materials. Here, the values show good agreement whereas with rising temperature the viscosity of both materials diverges more and more.



## Conclusions

The values of the dynamic viscosity increase from pure NPG to pure TRIS. The determination of the viscosity close to the freezing point was not possible for all selected concentrations since a measurement below 410 K failed, because of the applied process conditions. From the regression equation, it was possible to calculate the viscosity shortly before the liquid starts to freeze. The experimental values for the viscosity are used to estimate the diffusion coefficient. The accuracy of the values is checked by the comparison of published values and experimental ones.

## A.8 Temperature Gradient

Due to the difference in the heat conductivity of solid and liquid and to the evolution of latent heat at a moving interface, the temperature gradient in the liquid may generally not be equal to the gradient in the solid. The temperature gradient [2] is given in the form,

$$G_T = \frac{G_S \cdot \kappa_S + G_L \cdot \kappa_L}{\kappa_S + \kappa_L}. \quad (\text{Eq. 25})$$

Here,  $G_S$  is the temperature gradient in the solid,  $\kappa_S$  the thermal conductivity in the solid,  $G_L$  the temperature gradient in the liquid, and  $\kappa_L$  the thermal conductivity in the liquid.

[75] published the thermal conductivity ratio of equilibrated liquid phase to solid phase for NPG with 1.07. Since the difference between  $\kappa_L$  and  $\kappa_S$  (0.185 and 0.184 [81, 82]) is small for the peritectic concentration of our system, the temperature gradient for the TRIS – NPG system can be assumed to be  $G_T \approx G_L$ .

### Experimental Set-up

The measurement of the temperature gradient within the adiabatic zone requires a temperature sensor which fits into the size of the glass samples. However, the used long rectangle glass samples of the solidification experiments have to be very thin (100  $\mu\text{m}$  thickness) to reduce the influence of the convection as much as possible. The width and the long length of the glass sample prevent the usage of thermocouples with smaller diameters, like 20  $\mu\text{m}$ . Therefore, the selected special sample size disables the application of a suitable temperature sensor. To measure the temperature gradient, a larger glass sample (0.8 x 3.5  $\text{mm}^2$  instead of 0.1 x 2.0  $\text{mm}^2$ ) is used, filled with a sample of peritectic concentration. An additional adapter has to be used to fit the larger sample into the Bridgman-furnace.

Ni-CrNi thermocouples, type K, were used with a diameter of 200  $\mu\text{m}$  in order to evaluate the temperature gradient between the hot and the cold part of the Bridgman-furnace. Two thermocouples were put into a rectangular sample (0.8 x 3.5  $\text{mm}^2$ ) with a distance of approximately 200  $\mu\text{m}$ . The Bridgman furnace was preheated up to  $T_H = 453 \pm 1 \text{ K}$  and  $T_C = 353 \pm 1 \text{ K}$  because (i) the temperature of the hot zone is limited due to the detected thermal instability of TRIS (by DSC measurement, see Figure 32), and (ii) the interface should be right in the center of the gap. The sample was placed in the furnace and was moved

in steps through the gap. The temperature was recorded at each position after 900 seconds to be sure that the temperature gradient was stable.

### Results and Discussion

The temperature gradient was measured with two separated thermocouples in one sample. The measured temperature inside the sample declines in the last millimeter within the hot copper block because here it is not isolated against the adiabatic zone. Therefore, the maximum observable temperature in the adiabatic gap is below the controlled temperature of the resistant heater in the hot zone of the Bridgman-furnace, see Figure 107.

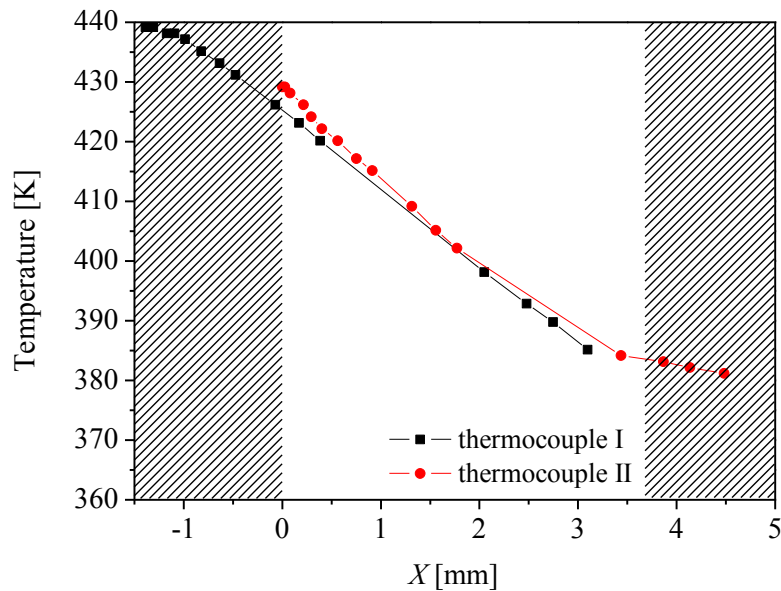


Figure 107: Temperature distribution in the 3.6 mm wide adiabatic gap of the micro Bridgman furnace.

The experimental data shows a linear temperature gradient within the adiabatic zone and confirm the assumed  $G_T \approx G_L$ . This allows the calculation of the current temperature according to the selected position within the adiabatic gape with an accuracy of  $\pm 1.6$  K. The results of the investigation with a temperature sensor give a linear temperature gradient for the liquid and the solid phase with  $G_T = 1.4 \cdot 10^4 \pm 3 \cdot 10^2$  K/m for the selected process conditions ( $T_H = 453 \pm 1$  K and  $T_C = 345 \pm 1$  K) (see Figure 108).

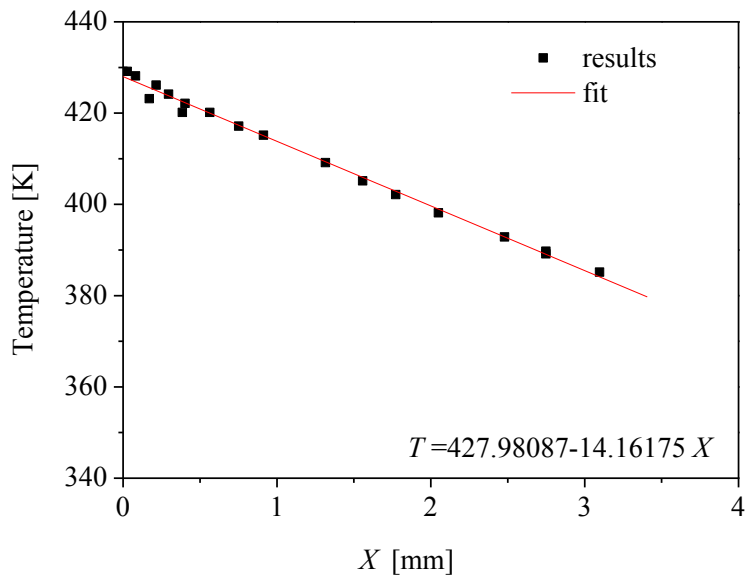


Figure 108: Linear fitting of the temperature field in the gap of the Bridgman furnace.

With the known temperature gradient the current interface temperature of the solid/liquid can be detected, see Figure 109.

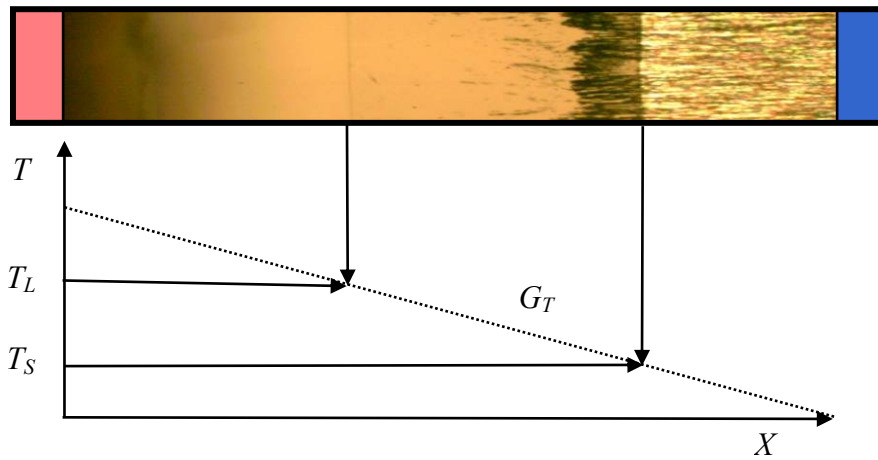


Figure 109: Picture of a sample in a temperature gradient field. The position of the planar solid/liquid ( $T_L$ ) and solid/solid transformation front ( $T_S$ ) can be clearly differentiated.

## A.9 Diffusion Coefficient

### Introduction

The organic peritectic phase diagram TRIS – NPG is used as a model system for *in-situ* observation of layered structures where one or both phases, the primary and the peritectic phase, solidify as a planar front solid/liquid interface. The liquid diffusion coefficient  $D_L$  is needed to analyze the solidification morphology. Liu et al. [101] published a suitable experimental investigation for *in-situ* observation to determine the diffusion coefficient in the liquid. Liquid inclusions, like droplets, can move in a solid matrix within an existing temperature gradient  $G_T$ . The movement, caused by the melting of the solid in contact with the liquid at the hotter temperature and the solidification of the liquid in contact with the solid on the colder temperature side of the liquid. The movement ends at the solid/liquid interface. Melting and solidification within the temperature gradient creates a characteristic migration curve depending on the diffusion coefficient in the liquid. From this characteristic curve it is possible to calculate the diffusion coefficient for a given concentration. Liu et al. [101] shows that the diffusion coefficient  $D_L$  can be calculated from the coefficient  $a$  of the quadratic polynomial velocity curve with:

$$t = a \cdot x(t)^2 + b \cdot x(t) + c \quad . \quad (\text{Eq. 26})$$

Here,  $t$  is the time of the droplet to move through the solid matrix to the solid/liquid interface,  $a$ ,  $b$  and  $c$  are coefficients, and  $x(t)$  the time depending position of the droplet in the matrix. The diffusion coefficient is given by:

$$D_L = \frac{1-k}{2 \cdot a} \cdot \frac{G_S}{G_L} \quad . \quad (\text{Eq. 27})$$

Here,  $a$  is the coefficient from the migration curve.

### Experimental Set-up

The experimental set-up in the Bridgman-furnace is described in chapter 3.1.1 and chapter 3.2 in more detail. The micro Bridgman-furnace is preheated and a glass sample with a selected concentration is put into the furnace. Within the temperature gradient the solid alloy melts and forms a planar solid/liquid interface. Afterwards the sample is pulled with 115  $\mu\text{m/s}$  where

only dendrites with small dendrite arm spacing,  $\lambda_l$ , can grow, see Figure 110. During the growth, the liquid is trapped between the side arms of the dendrites. Depending on the selected concentration, the matrix of the  $\alpha$  phase corresponds to the  $[C_I]$  or  $[C_F]$  phase.

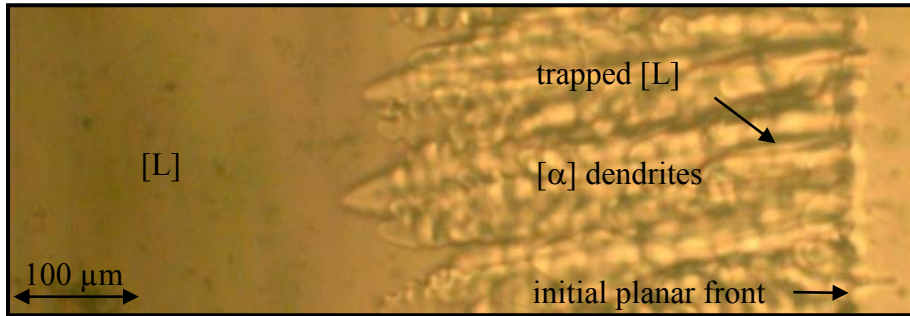


Figure 110: Growth of a dendritic solidification front. On the right side of the picture, the initial planar solid/liquid interface is visible.

After a few seconds the sample is stopped and stays unmoved within the Bridgman-furnace. Now, the dendritic solid/liquid interface changes into a planar front and the entrapped liquid forms droplets. This droplets start to move through the solid matrix, see Figure 111.

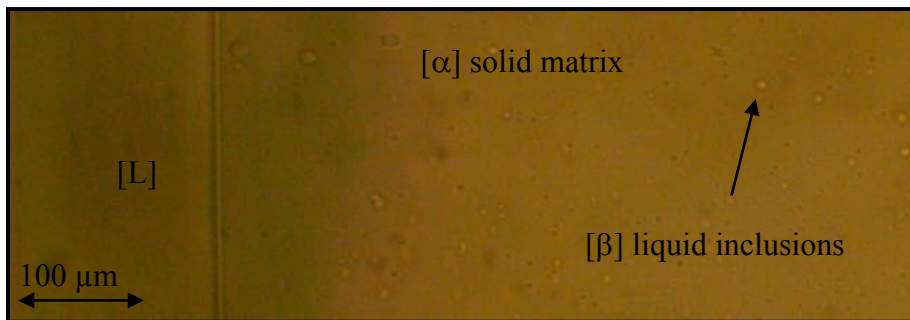


Figure 111: Picture of the organic alloy TRIS - NPG with a mol fraction of  $x = 0.4$  mol fraction NPG in rest. The bubbles are moving from the cold right side to the hot left side and disappear at the solid/liquid interface.

The movement takes place in such a way that one side of the droplet melts whereby the opposite side solidifies simultaneously. For the calculation of the diffusion coefficient in the liquid, the position with time is recorded for selected droplets.

## Results and Discussion

As already mentioned in chapter A.8, it is shown that the temperature gradient  $G_L \approx G_S$ . Up to 10 droplets on different positions within the solid matrix were selected to estimate the migration curve. The position and the time of each individual droplet were recorded until the droplet reached the solid/liquid interface. All droplets show the same characteristic curve (see Figure 112).

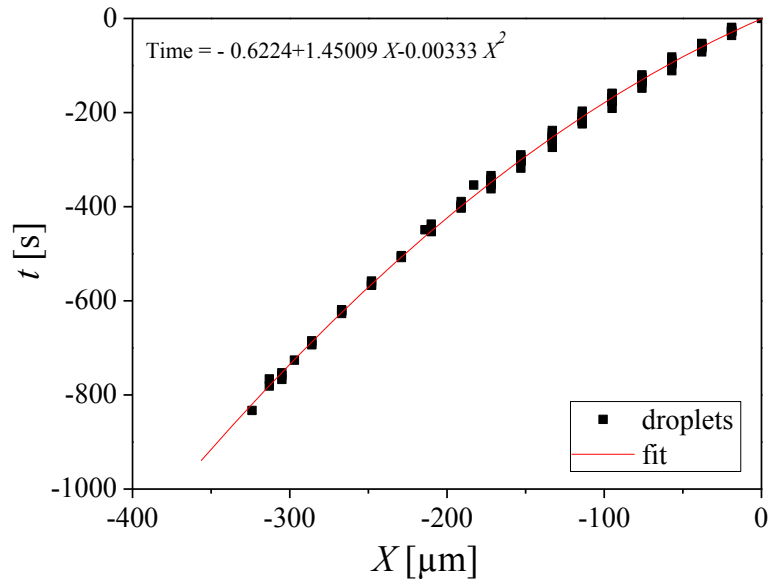


Figure 112: Examples for the diffusion of droplets in alloy with  $x = 0.2$  mol fraction NPG (a). Investigations for different alloy compositions reveal a possible concentration dependency of the diffusion coefficient in the liquid. Note that the exact values may be influenced by convection.

The calculated diffusion coefficients of the entire phase diagram are given in Figure 113. The result shows the average diffusion coefficient of  $2.9 \cdot 10^{-11} \pm 0.8 \cdot 10^{-11} \text{ m}^2/\text{s}$  with a characteristic decrease to the average value of  $2.1 \cdot 10^{-11} \pm 0.6 \cdot 10^{-11} \text{ m}^2/\text{s}$  within the peritectic concentration range of  $0.47 < x < 0.54$  (Table 1). Whereby, the diffusion coefficient makes a jump in the range of  $0.5 < x < 0.6$ , see Figure 113. The calculation of the values depends on the factor  $a$  from the migration curve as well as from the selected distribution coefficient  $k$ .

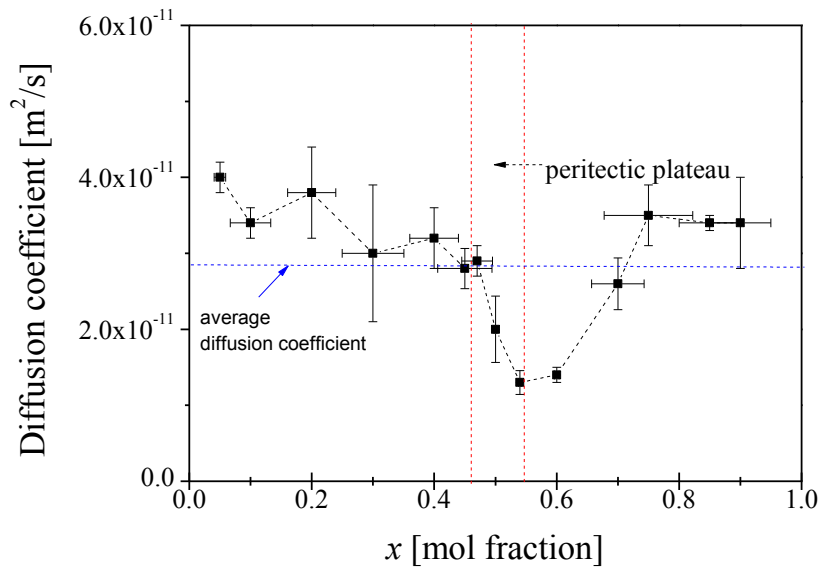


Figure 113: The derived diffusion coefficients  $D_L$  plotted versus the alloy concentration.

Whereas, the estimated factor  $a$  from the migration curve is independent from the phase diagram and only a mathematical factor. Besides, the used distribution coefficient  $k$  depends on the selected phase diagram. Diffusion in the liquid depends on the temperature, the size of the molecules and on the phase that solidifies. During solidification the rejected element enriches in the liquid layer ahead of the solidification front, this behavior is reflected in the distribution coefficient  $k$ . In the phase diagram TRIS - NPG within the range of  $0.4 < x < 0.8$  mol fraction the distribution coefficient  $k$  is nearly consistent. In alloys close to pure elements only few host elements are present which makes diffusion easier. The estimated values of  $D_L$  are shown in Table 6 on page 40.



## A.10 Refractive Index of Liquid with Peritectic Concentration

### Introduction

The refractive index of a material is an important property for optical systems. To investigate the solidification structure of the TRIS - NPG alloys under microgravity the ESA is constructing a Bridgman-furnace in combination with an optical observation system, called DIRSOL (see chapter 1). Therefore, the refraction index is needed to calculate the focal length.

### Experimental set-up

Rectangle samples (see chapter 3.1.2) with a mark are used for the detection of the refractive index for the alloy with peritectic concentration  $x = 0.5$  mol fraction NPG. The empty sample is put into the ZEISS microscope, the microscope is focused onto the mark and the focus positions of the objective are recorded. To measure the refractive index of the liquid with peritectic concentration, the same sample is filled with a peritectic alloy, put into the micro-Bridgeman furnace and heated above the liquidus temperature. Then the focus position of the mark is recorded in the same way as for the empty (i.e. air filled) sample (see Figure 114).

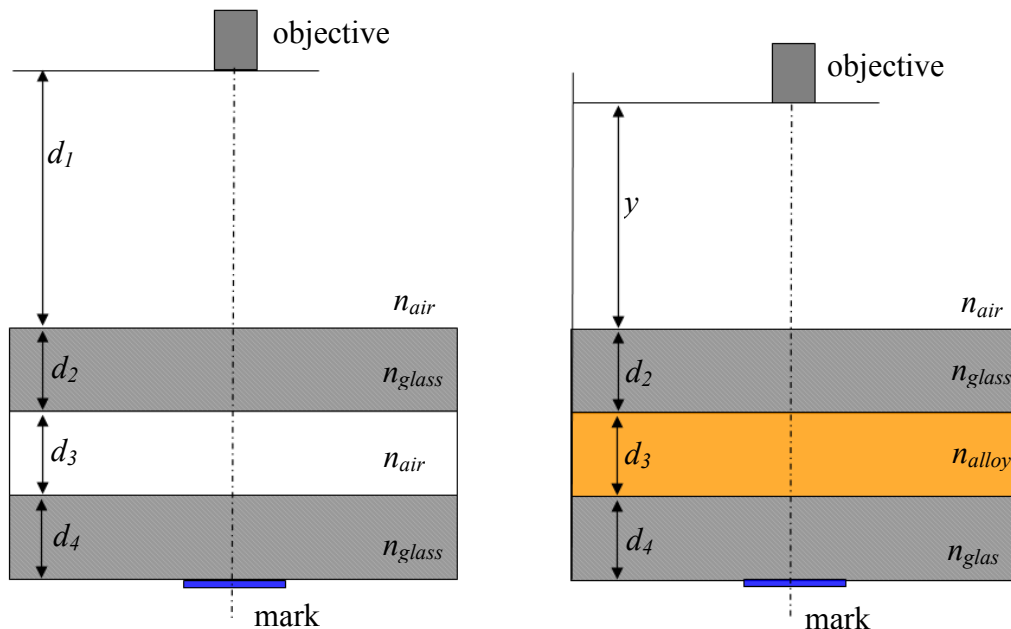


Figure 114: Schematic sketch of the measurement for the refractive index.

From the changes in the focus position the optical index is calculated by the equation given by:

$$\begin{aligned}
& d_1 \cdot n_{air} + d_2 \cdot n_{glass} + d_3 \cdot n_{air} + d_4 \cdot n_{glass} = \\
& y \cdot n_{air} + d_2 \cdot n_{glass} + d_3 \cdot n_{alloy} + d_4 \cdot n_{glass} \quad (\text{Eq. 28}) \\
& n_{alloy} = \frac{n_{air} \cdot (d_1 + d_3 - y)}{d_3}.
\end{aligned}$$

Here,  $n$  is the refractive index, and  $d$  the inner dimension of the glass sample.

## Results

The measurement of the refractive index  $n$  is repeated for air and water (are given in Table 21) to reduce the measurement error.

Table 21: Measured refractive index.

		unit	air	water	$x = 0.5$ mol fraction NPG
temperature	measured	K	293	293	443
$n$	measured	-	0.999	1.39	1.35
	published [102]	-	1.0003	1.33	-